Modeling and Characterization of Au/Liquid and Liquid/Liquid Interfaces for Application in Capacitive-Based Sensing Devices

---

A Thesis

Presented to

the faculty of the School of Engineering and Applied Science

University of Virginia

---

in partial fulfillment
of the requirements for the degree

Master of Science

by

Nicholas J. Francis

May 2018

APPROVAL SHEET

This Thesis
is submitted in partial fulfillment of the requirements
for the degree of
Master of Science

Author Signature: 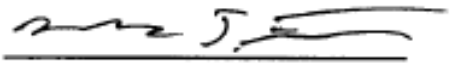

This Thesis has been read and approved by the examining committee:

Advisor: Carl Knospe

Committee Member: Baoxing Xu

Committee Member: David Green

Committee Member: _____

Committee Member: _____

Committee Member: _____

Accepted for the School of Engineering and Applied Science:

Craig H. Benson, School of Engineering and Applied Science

May 2018

Abstract

Capacitive-based MEMS sensing has found use in a wide array of fields; however, the continuing trend of miniaturization necessitates a change in the overall sensing approach of these systems due to the inherent challenges associated with measuring increasingly smaller changes in capacitances. This work seeks to solve this issue through the study of the ultra-high capacitance per unit area of the interface between two immiscible electrolyte solutions (ITIES).

This thesis focuses on the modeling and characterization of the impedance behaviors of the water/1,2-dichloroethane (DCE), gold/water, and gold/DCE interfaces for potential use in capacitive-based microelectromechanical systems (MEMS) sensing devices. Each interface is probed through the use of electrochemical impedance spectroscopy (EIS). Equivalent circuit models are developed for each of these interfaces, and it was found that a modified Randles equivalent circuit best fits the impedance data for both the Au/liquid and water/DCE interfaces. The benefits of using nanoporous gold (NPAu) electrodes as opposed to conventional planar electrodes are discussed and the impacts of initial gold concentration, electrode thickness, and etch time on the NPAu pore structure and impedance behavior of the NPAu/water and NPAu/DCE interfaces are studied in detail. It was found that a pure constant phase element (CPE) model was able to accurately describe the impedance behavior for these interfaces.

Characterization of the impedance data is conducted using a multivariate optimization script developed in MATLAB to simultaneously solve for each variable in the equivalent circuit models through minimization of the difference between the impedance data and the fit given by the equivalent circuit models. The capacitance of the water/DCE interface was found to have a linear dependence on the

interfacial area, with C/A=0.4168±0.042 F/m^2, which is significantly larger than what is observed in a conventional capacitive-based MEMS device. The clear dependence of water/DCE interfacial capacitance on interfacial area for the water/DCE ITIES makes it a promising candidate to couple with input mechanical signals for an ITIES-based sensing device.

Acknowledgements

I would first like to thank my advisor, Dr. Carl Knospe. His thorough support and advisement throughout my time here is greatly appreciated and it is safe to say that without him, this project would not have been possible. I fully appreciate the opportunity to work in his lab during my time at UVA and it is something that I will always fondly look back on.

Next, I would like to thank Dr. Baoxing Xu and Dr. David Green, who served on my thesis defense committee, for the time and effort they put in to the process. I would also like to thank the professors and engineers of the UVML, including Dr. Arthur Lichtenberger, Joe Beatrice, Mike Stogoski, and Alex Lobo for the support and advice throughout the years. I would like to thank the staff in the Mecahnical and Aerospace Engineering Department, particularly Lori Pedersen, Brenda Perkins, Jackie Slaughter-Scott, and Lindsay Grubbs for their help in guiding me throughout the academic process.

I would also like to thank the fellow members of the Capillary Micro Mechatronics Lab, Christina Barth, Xiaoyu Hu, and Marcel Mibus for their support and advice. A special thanks is given to Wilson Ruotolo who worked alongside me for the first year of this project and really helped get this project off the ground.

Lastly, I would like to thank my family and friends for their inspiration and support throughout this process. It means more to me than they could possibly know and I will cherish them always.

Contents

1: Introduction 1
1.1: Microelectromechanical Systems (MEMS): A Brief Introduction 1
1.2: The Interface Between Two Immiscible Electrolyte Solutions (ITIES) 3
1.3: ITIES-Based MEMS Sensing Devices: Theory and Design Considerations 5
1.3.1: Capacitive Sensing with the ITIES 5
1.3.2: Impact of Contact Angle Hysteresis 8
1.3.3: Impact of Minimum Energy Surfaces on Device Performance 10
2: Characterization of the Au/Liquid Interfaces 13
2.1: Study of Different Solvents 13
2.2: Equivalent Circuit Model Development 15
2.2.1: Pure Constant Phase Element Model 20
2.2.2: Transfer Effects Model 31
2.2.3: Adsorption Model 45
2.3: Can ITIES Impedance be Accurately Determined Using Conventional Electrodes? 55
3: Increased Device Sensitivity From Nanoporous Gold 60
3.1: Introduction to Nanoporous Gold 60
3.2: NPAu/Liquid Interface Device Setup and Analysis Methods 64
3.2.1: Materials and Methods 64
3.2.2: Data Analysis 66
3.3: Impact of Manufacturing Parameters on NPAu/Liquid Interfacial Impedance Behavior 69
3.3.1: Initial Gold Concentration 69
3.3.2: Electrode Thickness 79
3.3.3: Etch Time 86
3.3.4: Summary of Results 99
4: Modeling and Characterization of the Water/DCE ITIES 102
4.1: Preliminary Testing of the Water/DCE ITIES 102
4.2: Final Characterization of the Water/DCE ITIES 112
4.2.1: Effectiveness of the Transfer Effects Equivalent Circuit Model 115
4.2.2: Optimization over the High Frequency Regime 121
4.2.3: Impact of Weighting the Optimization Function 128

4.2.4: Summary of Results 137

5: Conclusions and Future Work 140

5.1: Summary of Work and Conclusions 140

5.2: Future Work 144

A: Use of ImageJ Software in Interfacial Area Analysis 148

A1: Determination of the Au/L Interfacial Area Using ImageJ Brightness Threshold Analysis .. 148

A2: Determination of the Water/DCE Interfacial Area Using the ImageJ Contact Angle Plugin 155

B: Appendix C: MATLAB Optimization Scripts for Characterization of the Au/Liquid and Water/DCE Interfaces 162

B1: 'Flat' Au/Water and Au/DCE Optimization 162

B2: NPAu/Water and NPAu/DCE Optimization 165

References 167

List of Tables

Chapter 2

Table 2.1: Non-ideal Behavior of the Au/Water and Au/DCE Interfaces 20
Table 2.2: CPE Model Parameters for the Au/Water and Au/DCE Interfaces..... 28
Table 2.3: Average Q^o/A and α for the Au/Water and Au/DCE Interfaces 29
Table 2.4: MATLAB Optimization of the Pure CPE Model 34
Table 2.5: MATLAB Optimization of the Transfer Effects Model 35
Table 2.6: Transfer Effects Model with R_{ct}=0 41
Table 2.7: Sensitivity of R_{eq} and X_{eq} to Changes in α 43
Table 2.8: Comparison of the Adsorption and Transfer Effects Models 48
Table 2.9: Impact of R_{ad} Starting Point on Optimization Performance 50
Table 2.10: Sensitivity of Adsorption Model to R_{ad} Variation 51

Chapter 3

Table 3.1: Convergence Test of MATLAB Model for Several Different Starting Points 68
Table 3.2: Model Bounds and Starting Points Used for the Various NPAu Tests..... 68
Table 3.3: Effect of Initial Gold Concentration on the Capacitive Behavior of the NPAu/Liquid Interface 75
Table 3.4: Effect of Electrode Thickness on Capacitive Behavior of the NPAu/Liquid Interface . 84
Table 3.5: Average Ligament Diameter an Percent Porosity for Various Etch Times Using DiameterJ 95
Table 3.6: Effect of Etch Time on the Capacitive Behavior of the NPAu/Liquid Interface 98
Table 3.7: NPAu Area Ratio of a 10 Minute Etch Time to a 15 Minute Etch Time 101

Chapter 4

Table 4.1: Interfacial Area Determination of the Water/DCE ITIES 115
Table 4.2: Transfer Effects Model Parameters for the Water/DCE ITIES 117
Table 4.3: Characterization Parameters for the Water/DCE ITIES 135

Appendices

Table B1: Upper Bounds, Lower Bounds, and Starting Points for The MATLAB Optimization of Different Equivalent Circuit Models for the Flat Au/Water and Au/DCE Interfaces 163

List of Figures

Chapter 1

Figure 1.1: Effect of Contact Angle Hysteresis on a Simple Pressure Sensor Design 6

Figure 1.2: Potential Design for Reduction of Contact Angle Hysteresis 9

Figure 1.3: Quadratic Dependence of Capacitance on Nondimensional Acceleration, λ 11

Chapter 2

Figure 2.1: Schematic of a Simple ITIES System 16

Figure 2.2: Equivalent Circuit Model of the Device Depicted in Figure 2.1 16

Figure 2.3: Apparatus Used to Characterize the "Flat" Au/Water and Au/DCE Interfaces 18

Figure 2.4: Typical Image Used to Determine the Area of the "Flat" Au/Liquid Interface 19

Figure 2.5: Typical Raw Impedance Spectrum for the Device Shown in Figure 2.1 20

Figure 2.6: Nyquist Plots for Two Common CPE Configurations 22

Figure 2.7: Equivalent Circuit Describing the Pure CPE Model 25

Figure 2.8: Typical Au/Liquid CPE Model Pseudo-Capacitance Behavior with Frequency 26

Figure 2.9: Typical Raw Impedance Spectrum for a Water Only and DCE Only Device 27

Figure 2.10: Variant Apparatus Used for Increased Au/DCE Interfacial Area 28

Figure 2.11: Equivalent Pseudo-Capacitance vs. Equivalent Area for the "Flat" Au/Water and Au/DCE Interfaces Obtained from a Pure CPE Model 29

Figure 2.12: CPE Model Fit of the Raw Data Impedance of a Water Only and a DCE Only Test 30

Figure 2.13: Nyquist Plots of the CPE Model Fit Compared to Raw Data 30

Figure 2.14: Various Randles Equivalent Circuits Used to Describe Transfer Effects at the Au/Liquid Interface 32

Figure 2.15: Q^{o} and C_{dl} vs. A_{eq} Obtained from the MATLAB Optimization of the CPE and Transfer Effects Models for the Au/Water and Au/DCE Interfaces 36

Figure 2.16: Nyquist Plots for Pseudo-data Generated for the Transfer Effects Model at Various R_{ct} 37

Figure 2.17: Impact of R_{ct} on the Total Equivalent Impedance 38

Figure 2.18: Impact of R_{ct} Variation on the Optimization Function 40

Figure 2.19: Transfer Effects Model with no R_{ct} 40

Figure 2.20: Impact of α Variation on R_{eq} and X_{eq} at Various Frequencies 42

Figure 2.21: Impact of α Variation on the Optimization Function 44

Figure 2.22: Percent Difference between Data and Fit for the Transfer Effects Model 46

Figure 2.23: Equivalent Circuit Describing the Adsorption Model 47

Figure 2.24: Impact of R_{ad} Variation on the Optimization Function 48

Figure 2.25: Effect of R_{ad} Variation on Device Equivalent Resistance 49

Figure 2.26: Percent Difference between Data and Fit for the Transfer Effects and Adsorption Models 53

Figure 2.27: Nyquist Plot Comparison between the Raw Data and Transfer Effects and Adsorption Models 54

Figure 2.28: Dependence of C_{dl} on Interfacial Area for the Au/Liquid Interfaces 55

Figure 2.29: Image of the Water/DCE ITIES 56

Figure 2.30: Impedance Spectrum of the Device Used to Probe the Water/DCE Impedance 57

Figure 2.31: Variant Device Used to Increase Sensitivity to the Water/DCE ITIES 58

Figure 2.32: Transient Behavior of the Device in Figure 2.31 59

Chapter 3

Figure 3.1: Optical Images Depicting the Effect of Initial Gold Concentration on Electrode Structure Post-Etching 71

Figure 3.2: SEM Imaging of the Nanoporous Gold Pore Structure for Different Initial Gold Concentrations 72

Figure 3.3: Raw Impedance Data Comparison for 9 Karat and 12 Karat Electrodes 74

Figure 3.4: Nyquist Plots of Raw Data and Pure CPE Fit for 9 Karat and 12 Karat Nanoporous Electrodes 76

Figure 3.5: Transient Behavior of α, Aeq, and Rsol for 9 and 12 Karat Electrodes 78

Figure 3.6: Transient Behavior of Raw Impedance at f=10 Hz for 9 and 12 Karat Electrodes 78

Figure 3.7: Optical Images Depicting the Effect of Electrode Thickness on 9 Karat Electrode Structure Post-Etching 80

Figure 3.8: SEM Imaging of the Nanoporous Pore Structure for Different 9 Karat Electrode Thicknesses 81

Figure 3.9: Raw Impedance Data Comparison for 3 and 6 Sheet Thick 9 Karat Electrodes 83

Figure 3.10: Transient Behavior of α, Aeq, and Rsol for 3 and 6 Sheet 9 Karat Electrodes 85

Figure 3.11: SEM Imaging of 9 Karat Nanoporous Gold Electrodes for Several Etch Times 87

Figure 3.12: DiameterJ Segmentation of the Filtered SEM Image for a 90 Minute Etch Time 89

Figure 3.13: Manual Thresholding of a NPAu SEM Image Using ImageJ 90

Figure 3.14: DiameterJ Segmentation of a Manually Thresholded NPAu SEM Image 91

Figure 3.15: Comparison of Three Image Processing Methods for Use in DiameterJ 92

Figure 3.16: DiameterJ Output for Pore and Ligament Locations 93

Figure 3.17: Behavior of Average Ligament Diameter and Surface Porosity with Etch Time 97

Figure 3.18: Equivalent Areas and Impedance Behaviors for NPAu Electrodes Etched for 10 and 15 Minutes 99

Chapter 4

Figure 4.1: Simple ITIES Device and its Equivalent Impedance Model 103

Figure 4.2: Transfer Effects Equivalent Circuit Model for the Water/DCE ITIES 104

Figure 4.3: Single Tube Apparatus 105

Figure 4.4: Concentric Tube Apparatus 106

Figure 4.5: Water/DCE ITIES Formed by the Concentric Tube Apparatus 107

Figure 4.6: Water/DCE Interfacial Resistance and Reactance as a Percentage of System Interfacial Impedance 109

Figure 4.7: Nyquist Plots for the Single Tube and Concentric Tube Apparatuses 110

Figure 4.8: MATLAB Optimization for the Single Tube and Concentric Tube Apparatuses 111

Figure 4.9: Big Electrode Apparatus 113

Figure 4.10: Images of the Water/DCE ITIES 114

Figure 4.11: Impedance of the NPAu/water and NPAuDCE Interfaces as a Percentage of Total Interfacial Impedance for the Big Electrode Apparatus 116

Figure 4.12: Basic Optimization Results for the Big Electrode Test 118

Figure 4.13: Dependence of Optimization Function on R_{ct} 120

Figure 4.14: Dependence of R_{ct} on the Water/DCE Interfacial Area 121

Figure 4.15: Impact of Sensitivity Shift during Data Collection on MATLAB Optimization 122

Figure 4.16: Prioritization of MATLAB Optimization to Low Frequency Data Points 125

Figure 4.17: Impact of Optimizing over High Frequencies on Optimization Performance 127

Figure 4.18: Impact of Application of Different Weighting Functions on Optimization Performance 129

Figure 4.19: Comparison of Base, High Frequency, and Weighted Optimizations 130

Figure 4.20: Sensitivity of Model to Changes in R_{ct} 131

Figure 4.21: Impact of Low Frequency, Weighted Optimization on R_{ct} Determination 132

Figure 4.22: Nyquist Plots of System Impedance Obtained From Parameters Effectively Characterizing the Water/DCE ITIES 133

Figure 4.23: Model of Q^o Separated into Contributions form Edge Effects and the Center of the ITIES 136

Appendices

Figure A1: Base image opened in ImageJ 149
Figure A2: Setting a baseline distance to use in setting a length scale 149
Figure A3: Setting the length scale 150
Figure A4: Changing image type to 8 bit grayscale 150
Figure A5: Brightness threshold analysis conducted in ImageJ 151
Figure A6: Adjusting image brightness threshold to select desired area 152
Figure A7: Image after brightness threshold has been applied 152
Figure A8: Setting desired measurements 153
Figure A9: Navigating to the measurement window 154
Figure A10: Displaying results of the measurements obtained by ImageJ 155
Figure A11: Base image of the water/DCE interface 155
Figure A12: Opening the ImageJ contact angle plugin 156
Figure A13: Preferences available in the contact angle plugin 156
Figure A14: Selecting points along the water/DCE interface for the Manual Points Procedure 157
Figure A15: Image after running the Manual Points procedure 158
Figure A16: Geometric representation of Figure A15 159
Figure A17: Measuring Distances to Calculate the Water/DCE Interfacial Area 160

Nomenclature

Arabic

a=dimensional acceleration

$A_{Au/L}$=impedance of an Au/liquid interface

A_{EDL}=double layer area

$A_{w/d}$=Area of the water/DCE interface

A_x=cross-sectional area of the electrolyte path

Bo=Bond number

C=capacitance

C_{dl}=capacitance associated with charge buildup at the edges of the double layer

C_{EDL}=double layer capacitance for an ideally polarized interface

C_r=capacitance of electrode reactions

D=tube inner diameter

E'_{total}=Total system energy after deformation

E_{system}=system energy before deformation

F(ω)=weighting function

f=frequency

g=acceleration due to gravity

g(x)= Function that maps $\boldsymbol{x}$ to $\boldsymbol{x}'$ as a result of an applied acceleration

h=height of the spherical cap forming the water/DCE interface

Im{Z}=imaginary component of impedance

j=the imaginary number

k=curvature

L=characteristic length

l=path length of electrolyte solution

M=arbitrary function

Q^o=pseudo-capacitance of a constant phase element

Q^o_{center}=pseudo-capacitance of the center of the water/DCE ITIES

Q^{o}_{edges}=pseudo-capacitance of the edges of the water/DCE ITIES

Q^{o}_{eq}=equivalent CPE pseudo-capacitance of two Au/liquid interfaces in series

Q^{o}_{w}=pseudo-capacitance of a Warburg element

R=Resistance

r=drop radius; radius of the inscribed circle created by the water/DCD interface

R_1, R_2=Radii of curvature

R_{ad}=adsorption resistance

$R_{Au/d}$=resistance of Au/DCE interface

$R_{Au/w}$=resistance of Au/water interface

r_{cap}=radius of the base of the spherical cap forming the water/DCE interface

R_{ct}=charge transfer resistance

R_{eq}=equivalent resistance of the circuit model

Re{Z}=real component of impedance

R_{fluid}=resistance of a fluid

R_r=resistance of electrode reactions

R_{sol}=solution resistance

$R_{w/d}$=resistance of water/DCE interface

S=arbitrary constant

SA_{cap}=surface area of the spherical cap forming the water/DCE interface

SA_{sphere}=surface area of the sphere created by the imageJ contact angle plugin

$SA_{w/d}$=surface area of the water/DCE interface

t=time since loading

t_{EDL}=double layer thickness

V_{bias}=bias voltage

V_{osc}=oscillation voltage

X=reactance

x=distance from outer edge of stern layer

x= Position vector of a point on the surface of the ITIES before deformation

x'= Position vector of a point on the surface of the ITIES after deformation

x_0=vector of starting points of variables in the MATLAB optimization

X_{eq}=equivalent reactance of the circuit model

$X_{Au/d}$=reactance of Au/DCE interface

$X_{Au/w}$=reactance of Au/water interface

$X_{w/d}$=impedance of water/DCE interface

|Z|=impedance magnitude

$Z_{Au/a}$=impedance of the Au/aqueous interface

$Z_{Au/d}$=impedance of Au/DCE interface

$Z_{Au/L}$=impedance of an Au/liquid interface

$Z_{Au/o}$=impedance of the Au/organic interface

$Z_{Au/w}$=impedance of Au/water interface

Z_{CPE}=impedance of a constant phase element

Z_{data}=impedance of the raw data

Z_{eq}=equivalent impedance of a circuit model

Z_f=impedance due to faradaic processes

Z_{fit}=impedance of the model fit. See also: Z_{eq}

$Z_{interfaces}$=equivalent impedance of all interfaces in a system

Z_{ITIES}=impedance of the interface between two immiscible electrolyte solutions

$Z_{NPAu/d}$=impedance of the NPAu/DCE interface

$Z_{NPAu/w}$=impedance of the NPAu/water interface

Z_w=impedance of a Warburg element

$Z_{w/d}$=impedance of water/DCE interface

Greek

α=constant phase element exponent

$\gamma_{M/N}$=interfacial tension between phases M and N

ΔP=pressure difference across an interface

Δλ=change in nondimensional acceleration

Δρ=density difference between two phases

ε_0=vacuum permittivity

ε_r=dielectric constant

θ=equilibrium contact angle

θ_r=receding contact angle

κ=decay constant that equals one over the Debye Length

λ=nondimensional acceleration

$\mu(\Sigma_{M/N})$=Area of interface M/N before deformation

$\mu(\Sigma'_{M/N})$=Area of interface M/N after deformation

σ=electrical conductivity

Σ_f=sum over frequency

$\Sigma_{M/N}$=Interface between media M and N before deformation

$\Sigma'_{M/N}$=Interface between media M and N after deformation

Ψ=Electric Double Layer Potential

Ψ_0=specified EDL potential at the outer edge of the Stern Layer

ω=angular frequency

Chapter 1: Introduction

This chapter covers an introduction to several topics. First to be covered are microelectromechanical systems, including their classification and a wide range of applications they have found use in. This is followed by an overview of the interface between two immiscible electrolyte solutions (ITIES), covering Gouy-Chapman-Stern electric double layer theory and the mechanisms by which charge is transferred across the interface. Finally, design considerations and the benefits and issues of capacitive-based MEMS sensing utilizing the ITIES are discussed.

Section 1.1: Microelectromechanical Systems (MEMS): A Brief Introduction

Microelectromechanical systems (MEMS) have been met with increasing interest over the past 60 years, growing into the multi-billion dollar industry it is today. This growth has in no small part been perpetuated by their ability to be manufactured using silicon-based microfabrication techniques. Not only does this allow for MEMS technology to be easily implemented into complex integrated circuits, but allows the manufacturing of off-chip MEMS devices to directly benefit from the existing infrastructure of the integrated circuit industry [1]. In these ways, MEMS devices owe their popularity in no small part to the explosion of the integrated circuit industry.

Two prominent categories of MEMS devices that have received significant attention across a wide range of fields are MEMS actuators and sensors. An extensive review by D. J. Bell, *et al.* describes the hierarchy of the numerous MEMS actuators and sensors available on the market [2]. Both actuators and sensors can be broken up into several different “families” based on their operational principles.

Actuators consist of the electrostatic, piezoelectric, thermal, and magnetic families while sensors include the capacitive, optical, and electron tunneling families. Each of these families is made of several classes of different devices [2]. Naturally, different families of devices are better suited for different applications; however, together, the families of actuators and sensors are able to cover an incredible range, making it possible to find a MEMS sensor or actuator suitable for nearly any microscale application.

Further reductions in power drain, cost, and device size have greatly increased the viability of MEMS devices for use in an increasing number of fields. In the automotive industry, they have found use in roll detection, improving fuel economy, and airbag deployment [3,4]. The medical industry has seen the study and development of an impressive array of MEMS devices, known as bioMEMS, over the past several decades which have found extensive application in drug delivery [5] and more recently have been looked at for implementation in prostheses [6]. Lab-on-a-chip devices have received significant attention in particular for medical and biological applications [7-9]. Air flow meters with the ability to detect both flow rate and direction show promise in a several fields, including microfluidics and aerospace [10-12]. Microshear stress sensors in conjunction with a MEMS actuator have been used to reduce drag in turbulent boundary layers through coupling a prediction of the maximum shear stress to the actuator displacement, resulting in shear stress reduction [13]. In more recent years, the use of MEMS in consumer electronics has accelerated [14]. MEMS gyroscopes can be found in smartphones, tablets, and laptops to detect screen orientation. MEMS displays such as LCD and DLP have become common and can be found in a wide array of devices, including televisions and computers. Perhaps one of the most well-known applications of MEMS devices are in the printheads used for inkjet printing.

The continuing trend of miniaturization in the electronics industry has led to the need for smaller MEMS devices. As a result, the size of a conventional three-axis MEMS accelerometer decreased from 12 mm^2 to 2 mm^2 between 2007 and 2011; an 83 percent decrease in just five years [15]. In 2015,

this size threshold decreased further to below a cubic millimeter [16]. Capacitive-based MEMS sensors in particular have difficulties associated with size reduction. These sensors operate on a principle of transduction, converting an input mechanical signal such as pressure or acceleration into a capacitance. As a result, further size reduction of capacitive-based MEMS sensors will require a change in the sensing approach due to the inherent challenges of measuring changes in increasingly smaller capacitances. This project seeks to solve this issue by developing a means to greatly increase measurement sensitivity while reducing overall sensor size through the study and implementation of the interface between two immiscible electrolyte solutions (ITIES).

Section 1.2: The Interface Between Two Immiscible Electrolyte Solutions (ITIES)

The ITIES has been met with increasing interest over the past several decades. These interfaces typically consist of an oil with an organic electrolyte and an aqueous solution of an inorganic salt [17]. Careful consideration of both solutions ensures that the ITIES is ideally polarizable over a range of a couple hundred millivolts, meaning that there is no charge transfer across the interface within this potential window. It is therefore important to choose salts that greatly prefer one phase over the other as to make this polarization window as large as possible since the underlying physics present in the various charge transfer mechanisms can greatly complicate matters.

The ITIES is very thin, having a sub-nanometer thickness as a result of the immiscibility between its two phases. It is this sub-nanometer thickness that makes the ITIES highly attractive for use in mechanical sensing applications, giving rise to the interface's ultra-high capacitance per unit area which has been shown to be capable of achieving values upwards of 100,000 pF/mm^2 [18]. As a result, the

ITIES has the potential to provide accurate measurements related to the change in its interfacial area for very small interfaces. For comparison, a particular capacitive-based microgravity MEMS accelerometer was shown to have a sensitivity of 0.3 pF per g of acceleration for a device area of 22.5mm^2 [19].

Because the ITIES deals with ions in solution, it is important to understand how these ions behave at the interface. Studies by Helmholtz, Gouy and Chapman, and Stern have led to the development of increasingly sophisticated models for the Electric Double Layer (EDL) that is formed at solid/liquid interfaces [20-23]. The Stern model combines the theories of Helmholtz and Gouy and Chapman, dividing the double layer into two distinct regions. The inner, or Stern layer is formed of a monolayer of counterions that form close to the interface in a plane of charge as is seen in Helmholtz double layer theory. The distance between the counterions and the interface surface as well as the distance between counterions within the monolayer is assumed to be the magnitude of their hydrated radii [24]. Due to the uniform distribution of counterions, the change in electric potential within the Stern layer is linear.

Because of the possibility of having ions of different size and charge in each phase, the inner layer does not always neutralize the surface charge at the interface. In these cases, the outer layer of the Stern Model, also known as the diffuse layer, plays a prominent role in the behavior of the EDL and behaves according to Gouy-Chapman theory. In this region, the electric field created by the non-neutralized surface charge results in a concentration gradient of ions in the bulk solution. The ion concentration decreases further away from the interface, eventually reaching the equilibrium concentration of the bulk solution. At this point, the diffuse layer ends, and beyond this point, the electric field created by the excess surface charge at the interface does not affect the bulk solution. Due to the variation in ion concentration within this region, the potential change is nonlinear; however, with several assumptions, the potential takes the form of an exponential decay:

$$\Psi(x) = \psi_0 \exp[-\kappa x] \tag{1.1}$$

where Ψ is the EDL potential, Ψ_0 is the specified potential at the outer edge of the Stern layer, x is the distance from the outer edge of the Stern layer, also known as the Stern Plane, and κ is a decay constant that is equal to one over the Debye Length [25]. Despite being developed for solid/liquid interfaces, Gouy-Chapman-Stern double layer theory also applies to the ITIES, where, instead of having a single double layer, two are placed back to back: one in the aqueous phase and the other in the organic phase.

For any non-ideal ITIES, charge transfer at the interface plays a large role in its behavior. There are three primary mechanisms by which charge can be transferred across the ITIES. In a simple ion transfer reaction, ions are able to transfer from one phase to another due to the difference in energy between the two ion species. Facilitated or assisted ion transfer reactions requires the addition of a complexing agent in the reaction to assist with ion transfer. Electron transfer reactions involve the transfer of electrons across the interface through the interaction of a hydrophilic and hydrophobic redox couple [18]. The actual mechanisms by which charge and ion transfer occurs within the EDL are beyond the scope of this project, however. For the interested reader, Girault provides an in-depth discussion of these three primary charge transfer reactions at the ITIES [26].

Section 1.3: ITIES-Based MEMS Sensing Devices: Theory and Design Considerations

Section 1.3.1: Capacitive Sensing with the ITIES

To see the potential for the use of the ITIES in a MEMS sensor, consider an ideally polarized ITIES with an area of 0.01 mm^2, a thickness of 1 nm and a dielectric constant of 10. The capacitance is given by

$$C_{EDL} = \frac{\varepsilon_0 \varepsilon_r A_{EDL}}{t_{EDL}} \quad (1.2).$$

for an ideally polarized interface. Here, ε_0 is the permittivity of free space, ε_r is the dielectric constant, A_{EDL} is the interfacial area and t_{EDL} is the interface thickness. For the parameters given, the capacitance of the ITIES is 885 pF. Now assume that an applied pressure increases the area of the interface by 1%. The new interfacial capacitance is then 893 pF, a change in capacitance of 8 pF, easily measurable by currently available instrumentation.

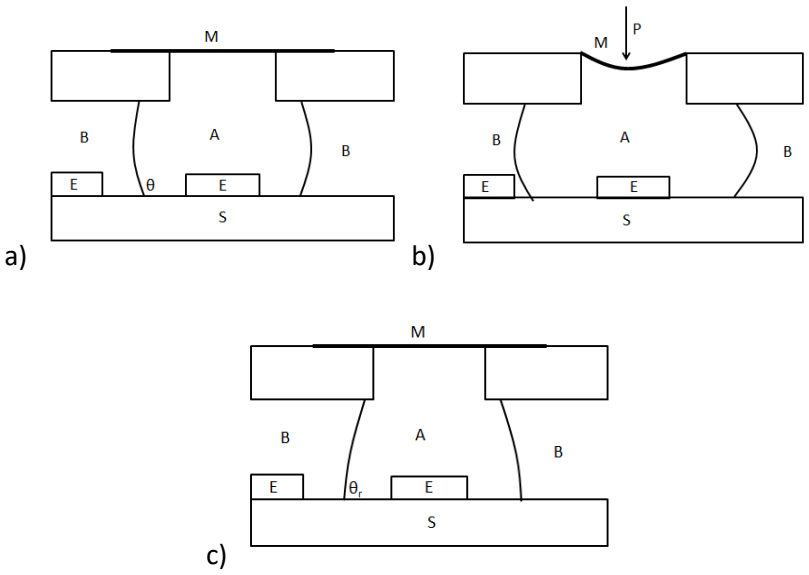

Figure 1.1: Effect of contact angle hysteresis on a simple pressure sensor design. **(a)** Original state before applied pressure. **(b)** Pressure P is applied to membrane M resulting in a change of surface area for drop A and a change in the contact line. **(c)** Pressure P is removed but the contact line does not return to its original state resulting in a different capacitance for the A/B interface than in (a).

The underlying principle of a MEMS sensor based on the ITIES is as follows: If a mechanical input such as an acceleration or pressure is applied to the device, the area, and thus the capacitance, of the ITIES changes as a result of that mechanical input, and it is theoretically possible to determine information about the applied mechanical input from that change in capacitance. Consider a possible pressure sensing device pictured in Figure 1.1. Here, a bridge of liquid A is surrounded by liquid B and spans the membrane M and substrate S. Electrodes E are located in the bulk liquids. The device has an

equilibrium contact angle θ. Because the system is in equilibrium, the contact angle of liquid A can be determined from a balance of the interfacial tensions of the A, B, and S phases, given by

$$\gamma_{A/S} + \gamma_{A/B}\cos(\theta) = \gamma_{B/S} \quad (1.3)$$

where $\gamma_{M/N}$ is the interfacial tension between phases M and N.

The interfacial tension can be calculated through the Young-Laplace equation

$$\Delta P = \gamma(\frac{1}{R_1} + \frac{1}{R_2}) \quad (1.4)$$

where R_1 and R_2 are the radii of curvature, γ is the interfacial tension, and ΔP is the pressure difference across the interface that arises due to the curvature of the interface. It is this pressure difference that causes the deformation of the interface when a mechanical signal is applied. The quantity ($1/R_1$+$1/R_2$) is the curvature, k, of the surface. For a surface with non-simple geometry, k is quite complex and cannot be easily solved without numerical computation; however, for simple geometries such as spherical drops or a meniscus against a flat plate, solutions of the Young-Laplace equation are readily available [27]. Solutions to axisymmetric surfaces such as pendant and sessile drops have also been compiled through the work of Bashforth and Adams [28].

When determining interfacial tension through geometric methods, it is important to consider the extent of the effect gravity has on the shape of the interface compared to the effect of interfacial tension itself. This can be achieved through the non-dimensionalization of the Young-Laplace Equation, which requires scaling x, y, R_1, and R_2 by a characteristic length L. The chosen value of L depends on the geometry of the setup. For example, the diameter of a beaker filled with some liquid is an appropriate length to use. Sometimes, only part of the interface is of interest, causing a different choice of L for the same setup. If, for example, the meniscus of the liquid inside a beaker is being studied, the capillary number would be an appropriate choice for L.

The Bond number is a result of the delineation of surface tension and gravity effects on the interface and can be thought of as the ratio of gravity forces to surface tension forces acting on the interface and is given by

$$Bo = \frac{(\Delta\rho)gL^2}{\gamma} \quad (1.5).$$

Here, Δρ is the density difference between the two phases that form the interface, g is the acceleration due to gravity, L is the characteristic length, and γ is the interfacial tension. For interfaces with large Bo, the effect of gravity in determining the shape of the interface is more important than the effect of interfacial tension. In these situations, the interface will tend to form a flat surface perpendicular to the direction of g. The opposite is true for situations with low (<0.01) Bo, where interfacial tension plays a more dominant role than gravity. In these situations, the surface will generally form a surface of constant curvature, such as a hemispherical cap in a thin capillary tube, resulting in a much easier solution to the Young-Laplace Equation.

Section 1.3.2: Impact of Contact Angle Hysteresis

There are several issues that may arise when designing devices based on the change in capacitance of the ITIES. In consideration of one issue, suppose a pressure P is applied to the membrane as depicted in Figure 1.1b. Because the volume of A is constant, the surface area of the A/B interface changes, causing a corresponding change in capacitance. Once the pressure is removed, the system moves back to equilibrium (Figure1.1c). However, the contact angle in Figure 1.1c is the receding contact angle θ_r, where $\theta_r<\theta$. The interface in Figure 1.1c has not returned to its original orientation in Figure 1.1a and there are now two configurations (and thus two capacitances) corresponding to the same pressure. This phenomenon that the current contact angle depends on its history is known as contact angle hysteresis. The device shown in Figure 1.1 could be highly effective at measuring very

small changes in pressure due to the high capacitance of the A/B interface, but in order to maintain calibration, the system must return back to its original equilibrium position after the mechanical input is removed. Contact angle hysteresis would drastically reduce the repeatability of the device, potentially making it useless for practical sensing applications.

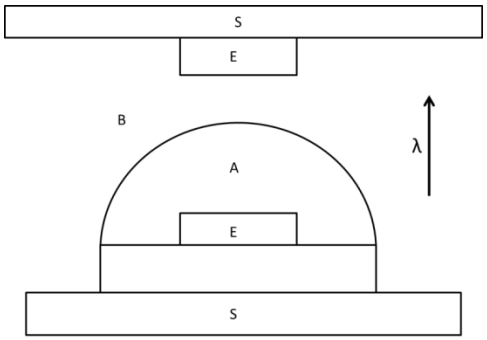

Figure 1.2: Example of a design to potentially reduce contact angle hysteresis. Liquid A sits on top of a microfabricated cylindrical step, preventing it from spreading when an acceleration, λ, is applied.

In order for the devices to be of practical use, contact angle hysteresis must be mitigated or eliminated entirely; however, since contact angle hysteresis depends on the history of the contact angle, it is implausible that it can be entirely removed from the system. Fortunately, many techniques exist that can help reduce the impact hysteresis has on the system. For example, if liquid A is water-based, the substrate surrounding the drop can be functionalized with a hydrophobic functional group to make the electrode surface surrounding the drop hydrophobic. This would keep the drop from spreading when a mechanical signal is applied but special care must be taken to choose a functional group that will not affect the electrical behavior of the system. A potentially easier method would involve geometrically pinning the contact line as shown in Figure 1.2. Here the contact line is pinned by a microfabricated geometric step on the surface. When pressure is applied to the system, the water droplet is unable to spread across the substrate, thereby pinning the contact line and reducing the effect of hysteresis. At

this time, it is unknown which form of pinning would be more effective or the extent to which the effects of hysteresis would be reduced.

Section 1.3.3: Impact of Minimum Energy Surfaces on Device Performance

A droplet subject to no external stimulus will form a minimum energy surface. This can have a profound impact on the performance of a sensor based on the ITIES. As an example, consider the accelerometer shown in Figure 1.2. Here, a sessile drop of liquid A is geometrically pinned by a microfabricated cylindrical step and is surrounded by liquid B. In the absence of an external acceleration, the A/B interface will form a shape $\Sigma_{A/B}$ that minimizes the total energy of the system. This can be expressed as

$$E_{system} = \gamma_{A/B}\mu\left(\Sigma_{A/B}\right) + \gamma_{B/S}\mu\left(\Sigma_{B/S}\right) + \gamma_{A/S}\mu\left(\Sigma_{A/S}\right) \quad (1.6)$$

where $\Sigma_{M/N}$ denotes the interface between media M and N, $\gamma_{M/N}$ is the interfacial tension between M and N and $\mu(\Sigma_{M/N})$ is the corresponding area. Note that specifying $\Sigma_{A/B}$ determines the contact line thereby fixing $\Sigma_{A/S}$ and $\Sigma_{B/S}$. Because the system is at a minimum energy configuration, any perturbation must cause the total energy of the system to increase.

A nondimensional acceleration, λ, is defined such that

$$\lambda = \frac{\Delta\rho r^2}{\gamma_{A/B}} a \quad (1.7)$$

where r is the radius of drop A, Δρ is the difference in densities between media A and B, and a is the physical acceleration felt by the drop. Note that this is the same form as the Bond Number given in Equation 1.5. Due to the small drop radius associated with microscale application, λ will be much less than 1 even for relatively large a. When λ is applied to the system, $\Sigma_{A/B}$ is deformed. Each point on the

undeformed surface can be mapped to a point on the deformed surface. Moreover, for small λ, this mapping is a linear function of λ [29]

$$\boldsymbol{x}' = \boldsymbol{x} + \boldsymbol{g}(\boldsymbol{x})\lambda \quad (1.8)$$

where bold terms represent vectors. Although the points on the surface can be mapped with a linear function of λ, the total energy of the system cannot. Since $\sum_{A/B}$ is a minimum energy surface, the total energy cannot be linear in λ since this would require E_{total} to decrease in one direction. Instead, E_{total} must be quadratic in λ. This ensures that E_{total} will increase if a negative acceleration is applied.

$$E_{total}\left(\Sigma'_{A/B}\right) = E_{total}\left(\Sigma_{A/B}\right) + \lambda^2 M + H.O.T. \quad (1.9).$$

∑' refers to the deformed interface, M is some arbitrary function and H.O.T. represents the higher order terms of the series expansion. This analysis holds only for accelerations that yield λ<<1.

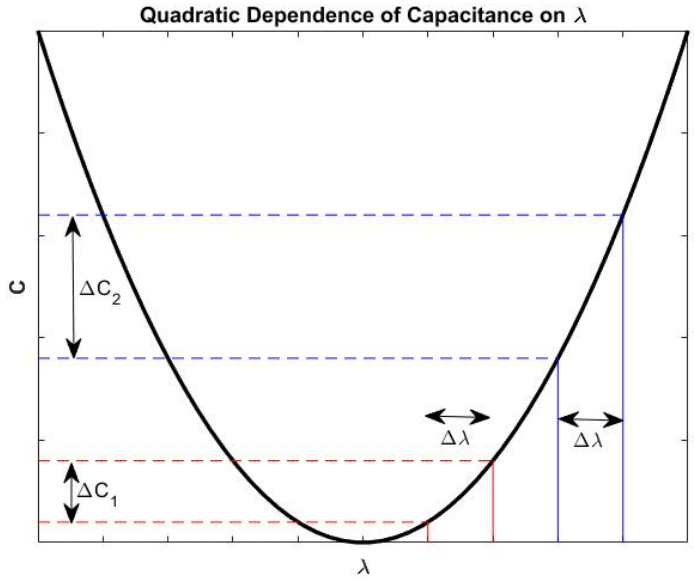

Figure 1.3: The quadratic dependence of capacitance on λ leads to different changes in capacitance for the same Δλ.

It was stated before that specifying $\sum_{A/B}$ (through pinning the contact line or some other mechanism) fixes $\sum_{A/S}$ and $\sum_{B/S}$ and as such, these two interfaces become independent of $\sum_{A/B}$. As a result,

the application of λ to the system will not alter the energies of $\sum_{A/S}$ or $\sum_{B/S}$ and the total energy is a function of $\sum_{A/B}$. The total change in energy as a result of λ can then be expressed as

$$E_{total}(\Sigma'_{A/B}) - E_{total}(\Sigma_{A/B}) = \{\gamma_{A/B}\mu(\Sigma'_{A/B}) + \gamma_{B/S}\mu(\Sigma_{B/S}) + \gamma_{A/S}\mu(\Sigma_{A/S})\}$$

$$-\{\gamma_{A/B}\mu(\Sigma_{A/B}) + \gamma_{B/S}\mu(\Sigma_{B/S}) + \gamma_{A/S}\mu(\Sigma_{A/S})\}$$

$$= \gamma_{A/B}\{\mu(\Sigma'_{A/B}) - \mu(\Sigma_{A/B})\} \quad (1.10).$$

Substituting E'_{total} from Equation (1.9) into Equation (1.10) shows that the change in area of the A/B interface is quadratic in λ:

$$\mu(\Sigma'_{A/B}) - \mu(\Sigma_{A/B}) = \frac{\lambda^2 F}{\gamma_{A/B}} + \cdots \quad (1.11)$$

Because interfacial capacitance is proportional to the interfacial area, this means that the change in interfacial capacitance of the A/B interface must be quadratic in λ as well. This result has significant impact on the overall performance of the sensor. This can be seen in Figure 1.3 which depicts the quadratic dependence of interfacial capacitance with λ. For smaller accelerations, significantly smaller changes in capacitance would be observed. As λ increases, this change in capacitance becomes larger, allowing the device to achieve a higher sensitivity. For example, a specific system accelerated from λ=0 to 0.01, will result in a significantly smaller change in the A/B interfacial capacitance than if the same system was accelerated from λ=0.05 to 0.06 despite Δλ being 0.01 in both cases. As such, the device would have a sensitivity that is dependent on the accelerations it is subjected to. Once again, this analysis only holds for λ<<1.

Chapter 2: Characterization of the Au/Liquid Interfaces

This chapter covers the different solvents studied for the use as the organic phase of the ITIES in this work. Pros and cons of several different solvents are examined. Various equivalent circuit models based on a constant phase element (CPE) and the Randles Equivalent Circuit are also discussed for the Au/liquid double layer. Analysis of several "single liquid" tests is performed with impedance spectroscopy utilizing the various equivalent circuit models discussed as a means to characterize the Au/liquid interfaces. Electrolyte solutions of 1M water-sodium sulfate and 1M 1,2-dichloroethane (DCE)-tetrabutylammonium hexafluorophosphate (TBA) are used as the considered liquid phases. For brevity, the 1M water-Na_2SO_4 solution and the 1M DCE-TBA solutions will be referred to as "water" and "DCE", respectively. Finally, it is tested if the ITIES impedance can be accurately determined from devices made with conventional gold electrodes.

Section 2.1: Study of Different Solvents

Several different organic solvents were studied to determine an apt choice for use in the ITIES. Electrolyte dissolution, cost, toxicity, mutual water solubility and material compatibility were all considered when determining which to use. The ideal organic solvent would be one with high electrolyte dissolution, low cost, low toxicity, low water solubility, and compatibility with a wide array of materials, including glasses and plastics. A solvent with high electrolyte dissolution is necessary in order to minimize the solution resistance of the bulk liquid. Although the ITIES is an interface between two *immiscible* electrolyte solutions, it is rare to have an organic solvent that is completely insoluble in

water. As such, it is important to consider the mutual solubility of the water and organic phases since a higher solubility can cause a break from ideal behavior.

1,2-dichloroethane (DCE), dichloromethane (DCM), nitrobenzene, and 2-nitrophenyl octyl ether (NPOE) have been popular choices for the construction of the organic phase in various ITIES [30-41]. All of these solvents with the addition of 5-Nonanone were considered for use in our ITIES. Due to the very high toxicity of nitrobenzene, it was immediately removed from consideration despite its wide use in other studies. 5-Nonanone is nontoxic, compatible with a wide array of plastics and relatively inexpensive. It also has a very small water solubility of 363 mg/L at 30 degrees C [42] but suffers from low solubility of TBA. NPOE is also nontoxic and compatible with a wide array of materials but is expensive and suffers from low solubility of TBA. DCM is inexpensive and allows for high solubility of TBA but is toxic and attacks most plastics. Further, it has a sizable water solubility compared to the other solvents [43]. DCE is similar to DCM in its benefits and detriments. It is relatively inexpensive and allows for a high solubility of TBA (>1M). On the other hand, it also attacks most plastics and is toxic. Unlike DCM, however, it has a much lower water solubility [44] and has the added benefit of seeing extensive use in the ITIES literature [38-41].

For capacitive-based sensing applications, it is imperative that the impedance of the ITIES dominates the entire impedance behavior of the system. As a result, the ability to hold a high electrolyte concentration in order to minimize the solution resistance is one of the more important parameters for the organic solvent to have. For this reason, NPOE and 5-nonanone were eliminated from contention. The main difference between DCE and DCM are their water solubilities. Since DCE's water solubility was lower than DCM's, it was ultimately decided that DCE would form the organic phase of the ITIES. Although its toxicity and material compatibility are unideal, they can be worked around. Fluoropolymers such as PTFE and FEP are resistant to attack by DCE and can be used in devices, though an inherent problem in doing so is that they have a low surface energy, making it difficult to adhere pieces of the

device to it. Fortunately, fluoropolymer etchants that increase the wettability and adhesion while maintaining the chemical resistance of the polymer are commercially available.

Section 2.2: Equivalent Circuit Model Development

A typical setup of an ITIES experiment is shown in Figure 2.1. Here, the system consists of an organic phase along with an aqueous phase filling a tube between two gold electrodes. An AC perturbation voltage is applied and the impedance behavior of the system can be recorded through the use of electrochemical impedance spectroscopy (EIS). The total impedance of this system comes from four contributions: the resistances associated with the bulk aqueous and organic solutions, the impedance of the Au/aqueous interfaces, the impedance of the Au/organic interface, and the impedance of the ITIES. These impedance contributions can be modeled using an equivalent circuit, with all four elements of the system impedance being in series with one another as shown in Figure 2.2. The equivalent impedance of the system can then be written as

$$Z_{eq} = Z_{Au/o} + Z_{Au/a} + Z_{ITIES} + R_{sol} \quad (2.1)$$

where $Z_{Au/o}$ and $Z_{Au/a}$ are the impedances of the Au/organic and Au/aqueous interfaces, respectively, Z_{ITIES} is the impedance of the a/o ITIES, and R_{sol} is the series combination of the bulk solution resistances of both the aqueous and organic phases.

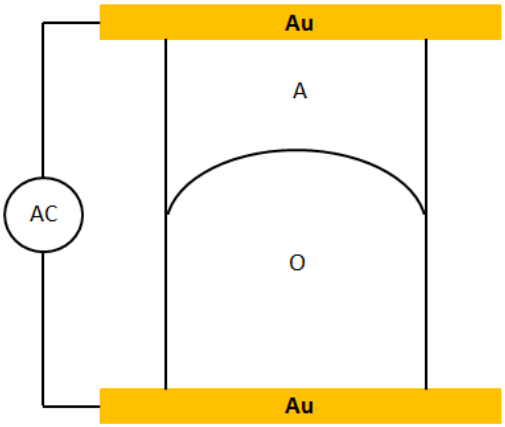

Figure 2.1: Simple ITIES System connected to an AC power supply. Aqueous phase A and organic phase O fill a glass tube. Each phase is in contact with a gold electrode with the ITIES between them.

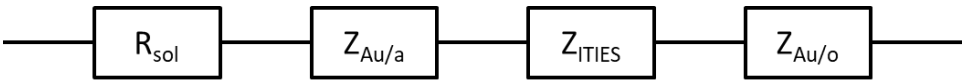

Figure 2.2: Equivalent circuit depicting the four major contributions to the impedance of the device shown in Figure 2.1.

By expressing the system impedance as given in Equation 2.1, it is easy to see that by subtracting out the impedance contributions of the solution resistance and the two Au/liquid interfaces from data collected using impedance spectroscopy, the impedance of the ITIES can be isolated. In order to isolate the ITIES impedance in this way, it is imperative that the impedance contributions of the Au/liquid interfaces and solution resistances are able to be reliably determined, either directly from the system itself or through effective modeling of their impedance behaviors obtained from other experiments. Further, to reduce the impact of any error associated with the subtraction of these impedances, their contribution to the overall system impedance should be small compared to the contribution of the ITIES.

The solution resistance of an electrolyte solution in a length of constant cross-sectional area can be modeled using

$$R_{sol} = \frac{l}{\sigma A_x} \tag{2.2}$$

where l is the length of the tube, σ is the solutions' electrical conductivity, and A_x is the cross-sectional area of the path of the fluid. For microscale applications, l will be inherently small while $1/A_x$ will be inherently large. As such, the most reliable way to reduce the contribution of R_{sol} is by maximizing σ for both the organic and aqueous phases. A straightforward means of accomplishing this is to have a high concentration of salt within each electrolyte solution. Using Equation 2.2 to model R_{sol} is not the only way to accurately approximate it. Another method is to use the real component of the system impedance at high frequencies, where the impedances of the three interfaces are nearly zero. This will be explained in greater depth later in the chapter.

Accurate subtraction of the Au/liquid interfaces is much more difficult. Various effects that can occur within the Au/liquid double layer have the possibility of complicating the equivalent circuit models used to describe these interfaces. In order to develop the equivalent circuit model, impedance data for both the Au/water and Au/DCE interfaces was collected. "Flat" electrodes were fabricated via electron beam vapor deposition on a standard 1"x3" microscope slide prewashed with acetone and methanol then rinsed with deionized water and nitrogen dried. An adhesion layer of 2.5 nm Ti was deposited first followed by 10 nm Au. The electrodes and glass tubing of various inner diameters (ID) ranging from 4-10 mm were cut to size with a desired tube length between 10 and 15 mm. In some tests, Teflon-FEP tubing was used instead. A solvent resistant sealant was used to adhere the tube between the two electrodes. A small hole was left at the top to allow for air to escape during loading. A schematic of the device is given in Figure 2.3.

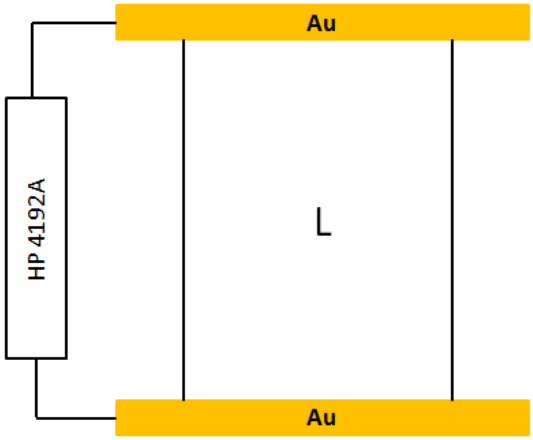

Figure 2.3: Apparatus used to characterize the Au/water and Au/DCE interfaces. Impedance Spectroscopy is performed on the system using a HP 4192A LF Impedance Analyzer

Before loading, the Au/liquid interfacial area for each electrode was determined. A white piece of paper was attached to the back of the bottom electrode on the assembled device. Due to the thinness of the metals deposited on the electrode, the electrode was translucent, allowing enough light to pass through to obtain a good image. To obtain the image, a light was shined through the back electrode. The sealant surrounding the tube on the top electrode blocked light at the edges of what would be the Au/liquid area. An image was taken and the piece of paper was moved to the top electrode and the process was repeated to obtain an image of the bottom electrode. A typical image used to determine the interfacial area is shown in Figure 2.4.

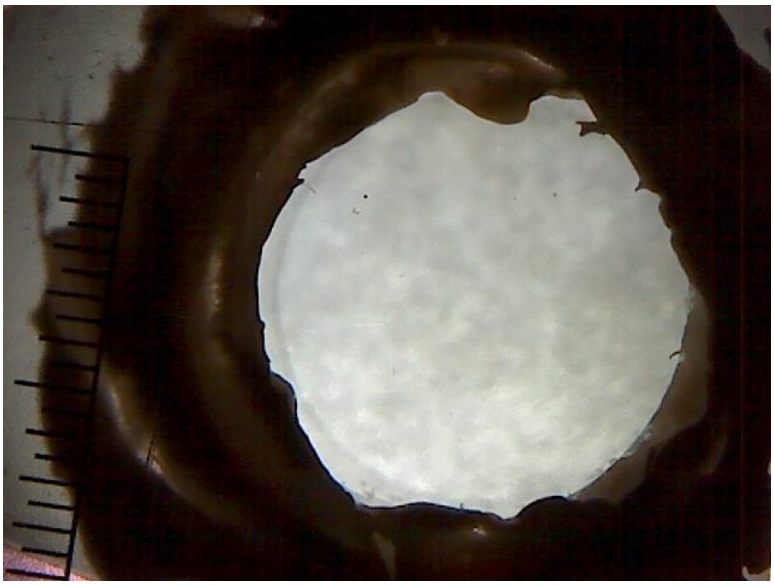

Figure 2.4: Typical image used to determine the area of the Au/liquid interfaces for a given test device. A white sheet of paper is placed on the back side of the device and light is shone through. The area is determined through threshold analysis in ImageJ.

Image analysis was conducted in ImageJ using the threshold image analysis feature. The image was first converted to grayscale and a brightness threshold was then used to measure the Au/liquid area. This process was repeated 3-5 times for each electrode. The results were then averaged to obtain the final Au/liquid interfacial area. A complete overview of this process is given in Appendix A1.

Leads were attached to the electrodes using copper tape and the other ends were hooked up to a HP 4192A LF impedance analyzer. The tube was then filled via syringe with either a 1M water solution or a 1M DCE solution. The 4192A was set to an oscillation level of V_{osc}=50 mV and a bias voltage of V_{bias}=0 V and set to measure resistance and reactance. Data collection was performed by a LabVIEW program that ran a logarithmic frequency sweep from 10Hz to 100kHz with 20 points per decade. Three frequency sweeps were performed for the DCE only tests as a means to check for consistency in recorded values of R and X.

Section 2.2.1: Pure Constant Phase Element Model

Figure 2.5 depicts the raw impedance data obtained from one of the water only and DCE only tests. For an interface treated as an ideal capacitor, the slope of the lines, after subtracting out the solution resistance, should be equal to -1 over the entire frequency range. Due to the impedance associated with the interface being small at high frequencies, however, it is preferable to consider the slope within the low frequency regime where parasitic effect are negligible and any error associated with determining the solution resistance does not have a significant impact on the larger interfacial impedance seen within this frequency range. Table 2.1 clearly shows that the slopes (denoted as -α) of the Au/water and Au/DCE impedance vs. frequency plots do not equal -1. As a result, the Au/liquid interfaces cannot be effectively modeled as an ideal capacitor.

a)

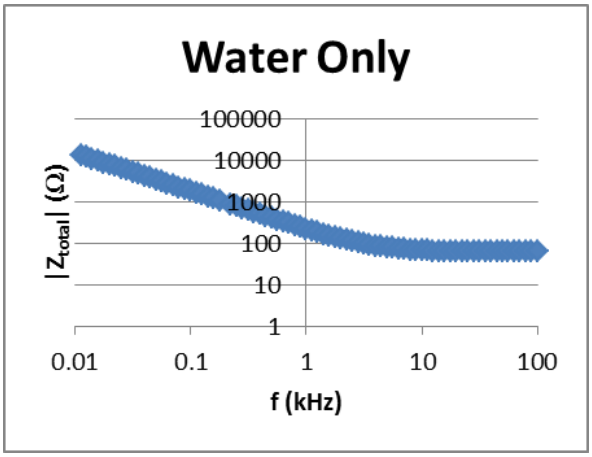

b)

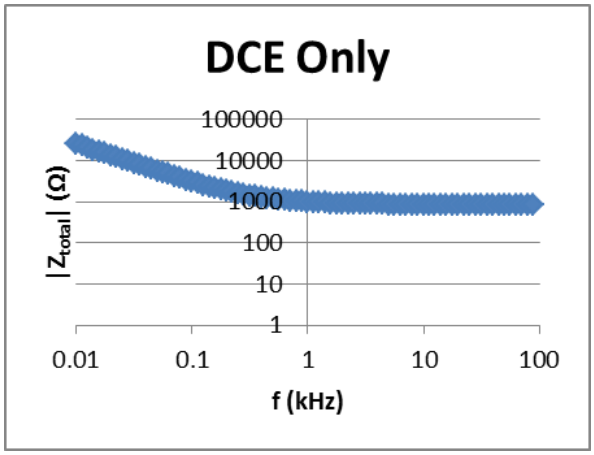

Figure 2.5: Typical impedance spectrum obtained from impedance spectroscopy performed over a frequency range of 10 Hz to 100 kHz. Plots are formed from data obtained from the **(a)** water only and **(b)** DCE only tests performed on the device depicted in Figure 2.3.

Table 2.1: Non-ideal Behavior of the Au/Water and Au/DCE Interfaces

Water Only		DCE Only	
Test	α	Test	α
4mmID 1	0.921	5mmID	0.944
6mmID 1	0.928	6mmID	0.926
6mmID 2	0.924	8mmID 1	0.940
8mmID 1	0.918	8mmID 2	0.956
10mmID 1	0.925	10mmID 1	0.910
10mmID 2	0.929	10mmID 2	0.958
		PTFE Sheet	0.882

A model of non-ideal capacitive behavior attributed to effects causing “capacitance dispersion” within the EDL has been widely used to describe many metal/liquid interfaces. This model is known as a constant phase element (CPE). The impedance of a CPE is similar to that of an ideal capacitor and can be expressed as

$$Z_{CPE} = \frac{1}{Q^o(j\omega)^\alpha} \quad (2.3)$$

where Q^o is referred to as a pseudo-capacitance and α is the CPE exponent constrained by $0 \leq \alpha \leq 1$ and is a measure of how close to ideally the interface behaves. This particular CPE impedance model is used in the case that the metal/liquid interface acts as a blocking electrode, where direct transfer of electrons across the double layer is blocked. By itself, this would mean that the metal/liquid interface would behave ideally, and the plot of its impedance in the complex plane would be a vertical line as depicted in Figure 2.6. However, the addition of other processes occurring at the metal/liquid interface due to capacitive dispersion may cause a reduction in phase angle leading to less ideal behavior. In this case, the plot of interfacial impedance in the complex plane would still yield a straight line but with a phase angle less than π/2 radians.

Q^o has a similar effect on a system as the physical capacitance, and for α=1, Equation 2.3 gives the equation of the impedance of an ideal capacitor with Q^o=C. In general, the units on Q^o are Siemens*seconds$^\alpha$ (S*s$^\alpha$) while the units for a physical capacitance are S*s. In a general case, the value of Q^o is equal to the admittance at ω=1 rad/s.

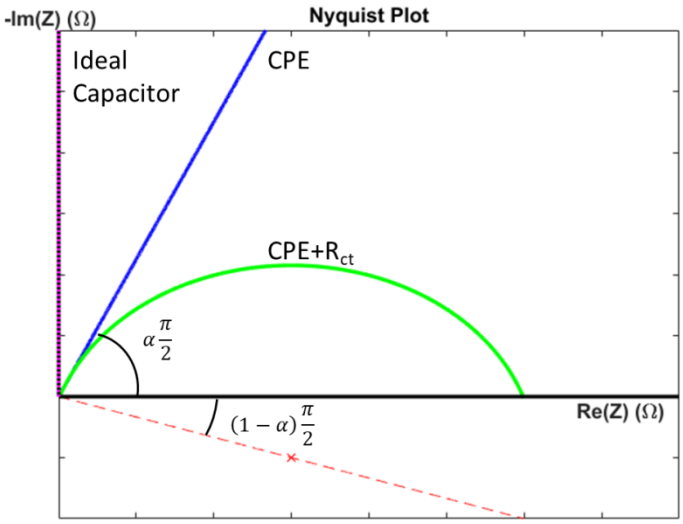

Figure 2.6: Nyquist plots for two common CPE configurations: a single CPE, denoted by the blue curve, and a CPE in parallel with a charge transfer resistance, R_{ct}, denoted by the green semicircle. The red x denotes the center of the semicircle which is depressed by an angle of (1-α)*π/2 where α denotes the CPE exponent.

A major aspect of a CPE's behavior is that the phase angle is less than π/2 and is constant over all frequencies. This can clearly be seen from the Nyquist plot, which plots impedance in the complex plane. For a lone CPE, the Nyquist plot gives a straight line, as depicted from the blue line in Figure 2.6. The angle that this line makes with the Re{Z} axis is equal to α*π/2. As a result, α can easily be determined from trigonometry:

$$\alpha = \tan^{-1}\left(\frac{Re\{Z(\omega_{min})\}-Re\{Z(\omega_{max})\}}{Im\{Z(\omega_{min})\}-Im\{Z(\omega_{max})\}}\right)\frac{2}{\pi} \quad (2.4).$$

Here, $Re\{Z(\omega_{min})\}$ and $Im\{Z(\omega_{min})\}$ are the real and imaginary components of impedance at the minimum value of ω plotted, $Re\{Z(\omega_{max})\}$ and $Im\{Z(\omega_{max})\}$ are the real and imaginary components of impedance at the maximum value of ω plotted, and $\tan^{-1}$ yields an angle in radians. Alternatively, α can be determined as the slope of the log-log plot of interfacial impedance magnitude on the y-axis versus frequency on the x-axis. When calculating α in this way, it is important to only consider the low frequency impedances as looking at high frequencies can introduce errors due to parasitic effects as described above. Note that for α=1, the CPE curve forms a vertical line on the Nyquist plot, showing that as α approaches 1, the

interface behaves increasingly more ideally. An issue of the Nyquist plot is that the values ω are not directly shown in the plot. For a single CPE, ω increases along the curve as you move closer to the origin; however, it is not so easy to gain intuition for how ω behaves in other more complicated CPE systems.

Despite having a non-ideal capacitive behavior, the above CPE model does not account for the possibility of charge transfer across the interface. This can be fixed with the addition of a charge transfer resistance R_{ct}. Since the CPE describes the charging behavior on both sides of the interface and the charge transfer resistance describes any charge that leaks across the interface, R_{ct} must be placed in parallel with the CPE in order to have a model that agrees with the physical system. The total impedance associated with this model is given as

$$\frac{1}{Z_{eq}} = Q^o(j\omega)^\alpha + \frac{1}{R_{ct}} \tag{2.5}$$

where R_{ct} indicates the parallel charge transfer resistance. The Nyquist plot of R_{ct} in parallel with a CPE forms a semicircle which can be seen by the green curve in Figure 2.6. Here, ω increases moving along the semicircle from right to left. The center of the full circle is located at an angle equal to (1-α)*π/2 below the Re{Z} axis. For this configuration, a relationship between the physical capacitance, C, and pseudo-capacitance, Q^o, has been developed by Hsu and Mansfeld [45] and is given by

$$C = Q^o(\omega_{max})^{\alpha-1} \tag{2.6}.$$

Here, ω_{max} is the frequency at which Im{Z} is maximum (i.e. the apex of the semicircle in the Nyquist plot). Equation 2.6 only holds for a CPE and charge transfer resistance in parallel and cannot be used if the electrode is blocking.

Although it sees widespread use in electrochemical analysis, a major shortcoming of the CPE model is that the cause of its behavior being seen in physical systems has yet to be fully understood. Several different postulates have been proposed. Surface roughness is widely thought to play a significant role in CPE behavior [46,47]. There are two primary schools of thought in how surface roughness leads to CPE behavior. First is the idea that due to surface defects, grain boundaries, and

other sources of surface inhomogeneity, the capacitance density varies across the surface of the electrode. Second is that the roughness of the electrode causes a variation of the effective solution resistance along the electrode surface.

Other research has led to conclusions that CPE behavior is unrelated to surface roughness. Bates *et. al.* found no relation between the CPE exponent and the fractal dimension of their Platinum and Silicon-based electrodes; however, they do suggest that the exponent value depends on the shape of the protrusions found on the surface of rough electrodes [48]. Pajkossy instead argues that capacitive dispersion cannot be caused by surface inhomogeneity since these effects show capacitive dispersion occurring at frequencies much higher than what is seen in typical experiments. Instead, he suggests that the behavior is instead due to adsorption effects present at the electrode/liquid interface [49]. Despite the cause of CPE behavior remaining unknown, it fits experimental data remarkably well and any deviations of a physical system with CPE behavior are often dominated by noise and errors associated with experimentation [50].

To characterize the Au/water and Au/DCE interfaces, the data was analyzed using the equivalent circuit model depicted in Figure 2.7. Both the top and bottom Au/liquid interfaces are treated as constant phase element capacitors in series with a solution resistance that accounts for the resistances of both the leads and bulk solution in the tube. With this model, the impedance of the system shown in Figure 2.3 can be described as

$$Z_{eq} = \frac{1}{Q_1^o(j\omega)^\alpha} + \frac{1}{Q_2^o(j\omega)^\alpha} + R_{sol} \quad (2.7),$$

where Q^o_1 and Q^o_2 are the pseudo-capacitances associated with the two Au/liquid interfaces, j is the imaginary number, α is the constant phase exponent, and ω is the angular frequency. For the device in Figure 2.3, both Au/liquid interfaces are identical in all but area and as a result have identical α's. Cross-multiplying these two interfacial capacitance terms yields

$$Z_{eq} = \frac{1}{Q_{eq}^o(j\omega)^\alpha} + R_{sol} \quad (2.8)$$

where $Q^o_{eq}=Q^o_1Q^o_2/(Q^o_1+Q^o_2)$ and is the equivalent pseudo-capacitance of the two Au/liquid interfaces in series. Finally, subtracting R_{sol} from both sides of Equation 2.9 gives the impedance of the system that is associated with the Au/liquid interfaces:

$$Z_{eq} - R_{sol} = \frac{1}{Q^o_{eq}(j\omega)^\alpha} = Z_{interfaces} \quad (2.9).$$

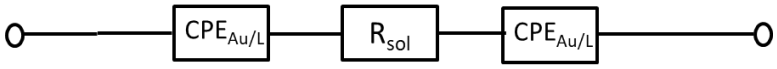

Figure 2.7: Equivalent circuit model of the device used to probe the Au/liquid interface. Both gold/liquid (Au/L) interfaces are assumed to be blocking so the charge transfer resistance is infinite and are modeled as CPE's.

In order to characterize the Au/liquid interface, both the pseudo-capacitance per unit area and α must be determined. α can be determined by looking at a power fit of the form

$$\left|Z_{interfaces}\right| = Sf^{-\alpha} \quad (2.10)$$

where $|Z_{interfaces}|$ is the impedance magnitude of the Au/liquid interfaces, f is the frequency and S is some constant. Equivalently, α is the negative of the slope on a log-log plot of $|Z_{interface}|$ vs. f. Alternatively, α can be determined from Equation 2.4 using the Nyquist plot for the interfacial impedance. With α known, Q^o_{eq} can be determined by solving Equation 2.9 for Q^o_{eq} and taking the norm of the resulting complex number:

$$Q^o_{eq} = \left|\frac{1}{(Z-R_{sol})(j\omega)^\alpha}\right| \quad (2.11).$$

An average value of Q^o_{eq} can be obtained by averaging Q^o_{eq} obtained for each of the low frequency points or, more precisely, over the region where Q^o is constant with frequency. Since the areas of both Au/liquid interfaces are specified, a value for Q^o_{eq}/A_{eq} which, for brevity, will be denoted as Q^o/A from now on can be determined. Here, $A_{eq}=A_1A_2/(A_1+A_2)$ is the equivalent area of both Au/liquid interfaces in series.

Just like the real capacitance, C, of an ideal capacitor, Q^o should be linearly proportional to the interfacial area. As a result, Q^o/A should be constant between tests since the interfaces between tests

conducted for a particular liquid are identical in all but area. This means that Q^{o}/A can be used as a point of reference to ensure that the data between tests is in agreement. Typical plots of Q^{o}_{eq} vs. f for both the Au/water and Au/DCE interfaces using this method are given in Figure 2.8. At low frequencies, Q^{o}_{eq} remains constant but as f increases and parasitic effects become more prominent, Q^{o}_{eq} begins to show some variance.

a)

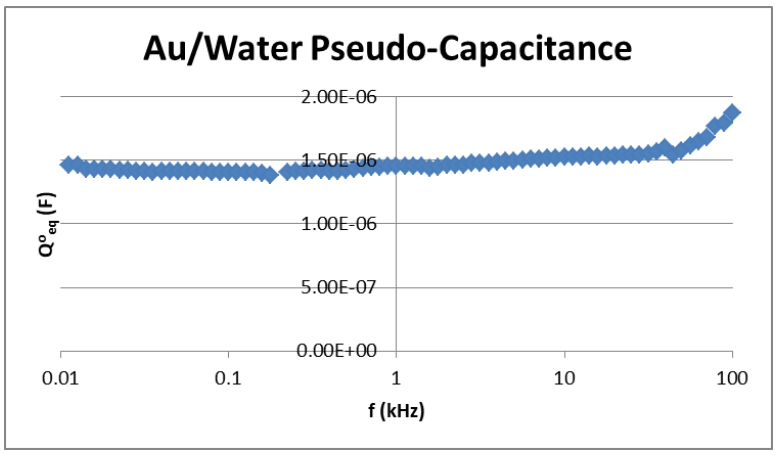

b)

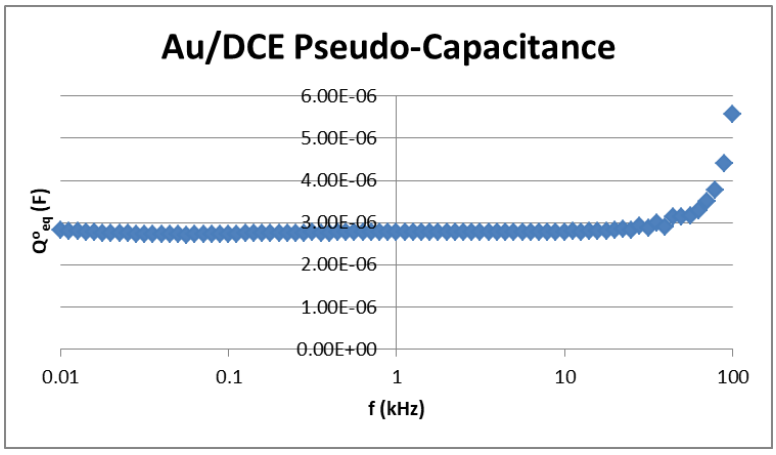

Figure 2.8: Typical behavior of Q^{o}_{eq} over a frequency range for the CPE model of the device in Figure 2.3 calculated from Equation 2.11 for **(a)** the Au/water interface and **(b)** the Au/DCE interface. The increase at high frequencies can be attributed to parasitic effects.

A typical impedance curve for the water only and DCE only tests are depicted in Figure 2.9. Both plots are for a test using a 6mmID glass tube. In both cases, the plot can be broken up into two characteristic regimes: 1) the capacitive regime and 2) the resistive regime. In the capacitive regime, the capacitive behavior of the system is dominant as indicated by the sloped region found in the low

frequency range. As the frequency of oscillation increases, the capacitive response of the system weakens, eventually becoming dominated by the solution resistance. This is seen at the higher frequencies shown in the plots where the impedance values level out.

a) 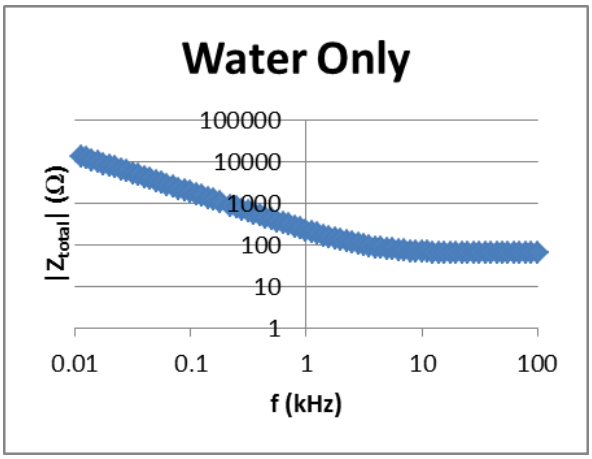

b) 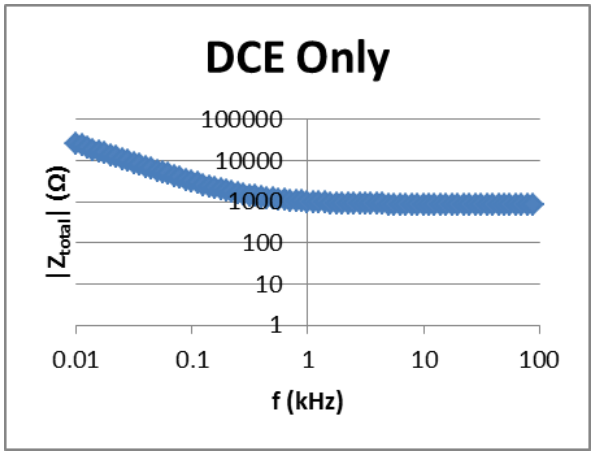

Figure 2.9: Typical impedance spectrum obtained from impedance spectroscopy performed over a frequency range of 10 Hz to 100 kHz. Plots are formed from data obtained from the **(a)** water only and **(b)** DCE only tests performed on the device depicted in Figure 2.3 with identical tube lengths and tube diameters of 6 mm.

It is clear that the capacitive regime of the water only system dominates over a larger frequency range. This is a direct result of the larger electrical conductivity of the water solution. The higher electrical conductivity gives the water solution a much lower solution resistance than that of the DCE solution and as a result, the capacitive Au/water interfaces yield a significantly larger percentage of the overall system impedance. Approximating the solution resistance as the high frequency impedance shows that the solution resistance of the DCE solution is approximately ten times greater than that of the water solution.

Values obtained for α, A_{eq}, Q^{o}_{eq} and Q^{o}/A for both the water only and DCE only tests are listed in Table 2.2. Two separate apparatuses were tested for several tube sizes. All tests were conducted using glass tubing with the exception of the 8mmID DCE test, where an 8mmID FEP tube pretreated with a fluoropolymer etchant to increase adhesion was used instead. The DCE test labeled PTFE sheet had

different geometry than the other tests. Whereas all other tests had the tube directly sealed to the electrode, the PTFE sheet test had two 1/16” treated hollow Teflon squares adhered together. A third treated Teflon sheet was cut with a hole able to snugly fit a 10 mm ID tube and sealed to the other two stacked squares, which were then sealed to an electrode. This was done for both the top and bottom electrodes and the two PTFE reservoirs were connected by the 10 mm ID tube. This was done as a means to obtain much larger electrode areas than the other tube tests. This variant apparatus is depicted in Figure 2.10.

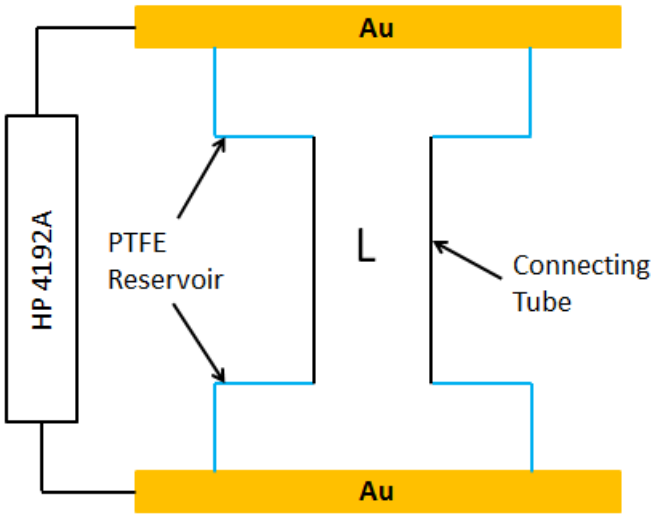

Figure 2.10: “PTFE Sheet” version of the apparatus used in one of the DCE only tests to obtain a larger Au/DCE interfacial area.

Table 2.2: CPE Model Parameters for the Au/Water and Au/DCE Interfaces

Water Only				DCE Only			
Test	A_{eq} (m^2)	Q^o/A ($S*s^\alpha/m^2$)	α	Test	A_{eq} (m^2)	Q^o/A ($S*s^\alpha/m^2$)	α
4mmID 1	4.30E-06	0.102	0.921	5mmID	6.15E-06	0.091	0.944
6mmID 1	1.51E-05	0.088	0.928	6mmID	9.84E-06	0.087	0.926
6mmID 2	1.14E-05	0.125	0.924	8mmID 1	1.74E-05	0.077	0.940
8mmID 1	1.98E-05	0.076	0.918	8mmID 2	1.85E-05	0.083	0.956
10mmID 1	3.68E-05	0.089	0.925	10mmID 1	2.92E-05	0.090	0.910
10mmID 2	3.01E-05	0.100	0.929	10mmID 2	2.96E-05	0.093	0.958
				PTFE Sheet	6.32E-05	0.095	0.882

Table 2.2 shows that A_{eq} is different between test sets with the same size tube. This can be attributed to the sealant spreading when the tube was pressed down onto the electrodes during fabrication. As expected, both Q^o/A and α remain roughly constant for all the tests conducted for both the Au/water and Au/DCE interfaces. The linear relationship between Q^o_{eq} and A_{eq} for both the Au/water and Au/DCE interfaces is shown in Figure 2.11. Average values of Q^o/A and α obtained for both interfaces are given in Table 2.3. As expected, a clear linear behavior is observed for Q^o in A_{eq}.

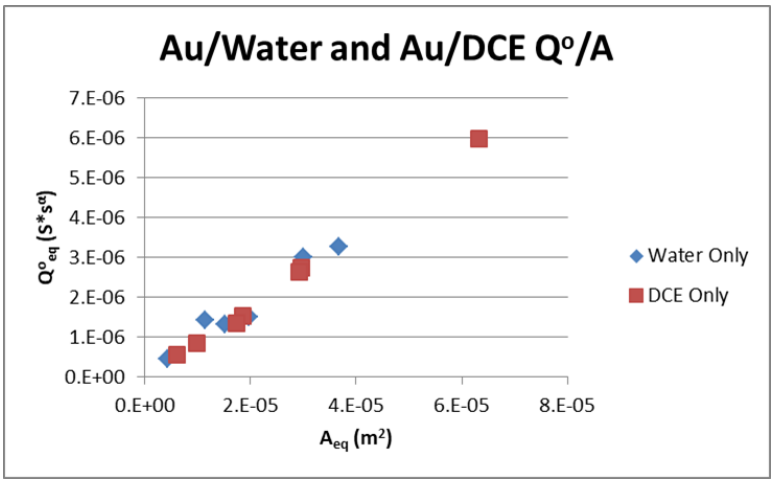

Figure 2.11: Pseudo-capacitance per unit area of the Au/water and Au/DCE interfaces

Table 2.3: Average Q^o/A and α for the Au/water and Au/DCE Interfaces

Au/water		Au/DCE	
Q^o/A ($S*s^\alpha/m^2$)	α	Q^o/A ($S*s^\alpha/m^2$)	α
0.097	0.924	0.088	0.931

Figure 2.12 shows plots of |Z| vs. f for the "10mmID 2" water only test and the "10mmID 1" DCE test. Two curves are given on each plot. The first shows the raw impedance data collected from the test. The second curve shows the fit determined by Equation 2.8 using the parameters for Q^o and α given in Table 2.2. R_{sol} was taken to be the system resistance at f=10 kHz. Although the CPE model fit appears to agree with the data, these plots only show that the impedance *magnitude* fits the raw data. In order to

determine whether the phase angle of the fit agrees with the raw data, the Nyquist plots for the same data in Figure 2.12 were plotted and are shown in Figure 2.13.

a) 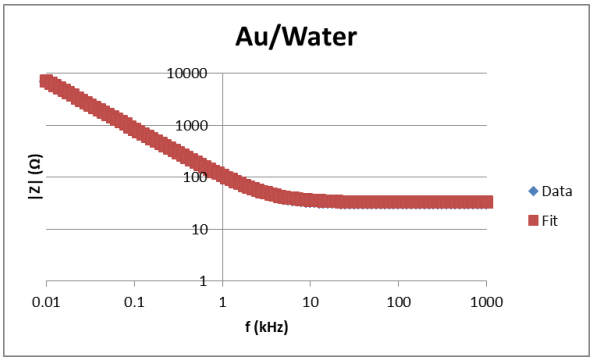

b) 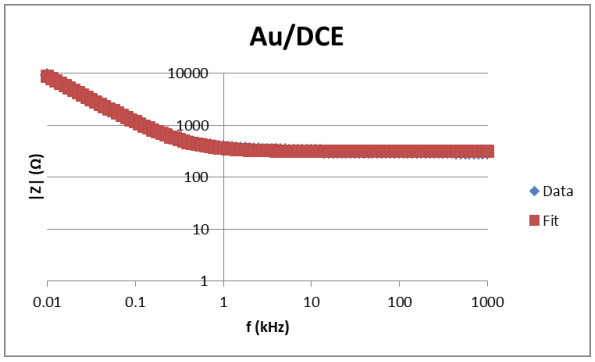

Figure 2.12: CPE model fit of the raw data impedance magnitude for **(a)** the "10mmID 2" water only test and **(b)** the "10mmID 1" DCE only test.

a) 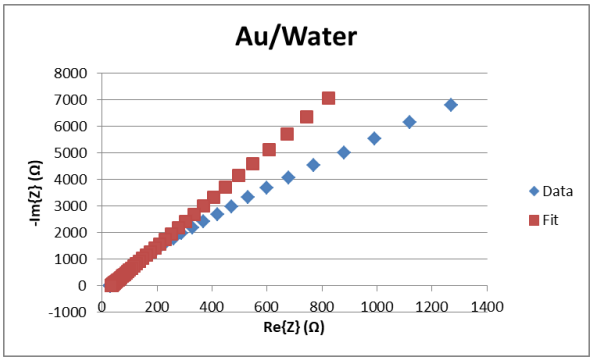

b) 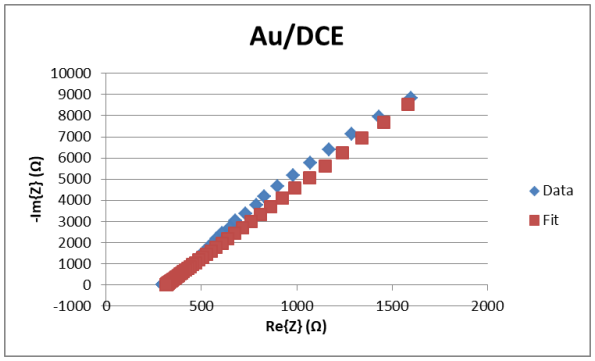

Figure 2.13: Nyquist plots of the CPE model fit compared to the raw data for **(a)** the "10mmID 2" water only test and **(b)** the "10mmID 1" DCE only test. Despite the good fit observed for the impedance magnitude, the CPE model is unable to accurately capture the impedance phase angle.

Figure 2.13 shows that the pure CPE model is unable to effectively model the impedance phase behavior of the Au/liquid interfaces, especially within the low frequency regime. Closer inspection of the Nyquist plots of the raw data shows the presence of a slight bend. Because the Nyquist plot of a lone CPE is that of a straight line, a single CPE element will be insufficient in describing the impedance behavior of the Au/liquid interfaces. A more sophisticated model must be developed in order to accurately capture this behavior.

Section 2.2.2: Transfer Effects Model

Because the lone CPE element cannot effectively describe the behavior of the Au/water and Au/DCE interfaces, modifications have to be made to the equivalent circuit model in order to capture the additional physics occurring within the Au/liquid double layer. Care must be taken when deciding which elements to add into the model. Much like how any mathematical function can be modeled as an infinite sum of sines and cosines, any set of impedance data can be modeled using an infinite number of circuit components; however, no physical intuition can be gained from modeling the data in this manner. Instead, circuit elements must be chosen and inserted into the model in a way that makes sense within the confines of the physical system.

Various additional effects occurring at the Au/liquid interface could impact the impedance behavior at the Au/liquid double layer. Contamination on the surface of the electrode, transfer effects across the double layer, and adsorption of ions to the electrode surface are a few of the processes that can complicate impedance behavior in a way that cannot be captured by a single CPE. Work conducted by Randles on modeling the behavior of high speed electrochemical reactions in the presence of electrically active particles linearly diffusing at flat electrodes [51] yielded an equivalent circuit shown in Figure 2.14a. This model is the Randles equivalent circuit, and consists of a solution resistance in series with a parallel combination of a standard double layer capacitance and a capacitance and resistance in series that describe the electrode interaction. Several modifications have been made to the Randles equivalent circuit to describe various EDL and ITIES systems [36, 39, 41, 52-54]. Two of them are shown in Figure 2.14b and c. It is important that R_r and C_r are placed in parallel with C_{dl} in order to agree with the physical system. This is because while C_{dl} models the charge buildup at each end of the double layer, R_r and C_r model the transfer effects that occur within the double layer. This is carried over into the other two circuit models shown in Figure 2.14 b and c.

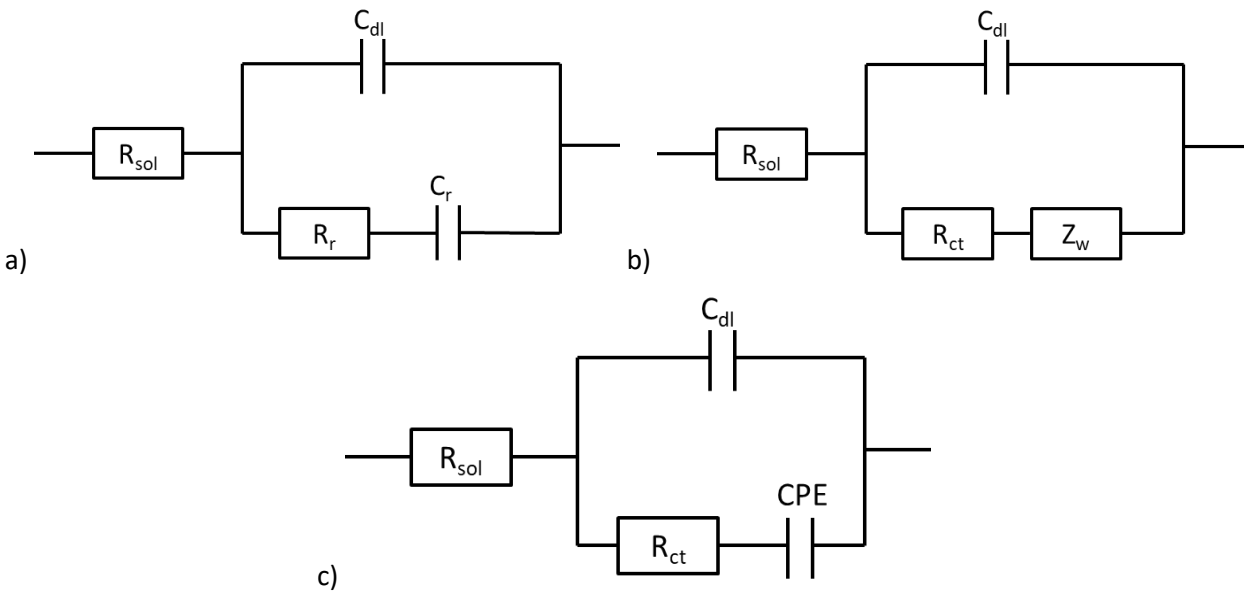

Figure 2.14: a) Equivalent circuit model developed by Randles to describe the behavior of high speed electrochemical reactions in the presence of electrically active particles linearly diffusing at flat electrodes; **b)** Equivalent circuit model that replaces the capacitance associated with the electrode reaction with a Warburg element to describe semi-infinite linear diffusion; **c)** Modification made to b to account for the possibility of anomalous dynamics.

Figure 2.14b depicts a model commonly used to describe the EDL impedance. It is identical to the Randles circuit but with C_r replaced with a Warburg element which is a specific type of CPE with α=0.5. Thus the impedance of a Warburg element can be expressed as

$$Z_w = \frac{1}{Q_w^o (j\omega)^{0.5}} \quad (2.12).$$

Warburg elements are primarily used to describe semi-infinite linear diffusion of ions that may be present at liquid-liquid or liquid-solid electrochemical interfaces and can be thought of as a resistance to ion transport within the mixed phase of the interface. The series combination of R_{ct} and Z_w are often combined into one element, Z_f, denoting the impedance of the faradaic processes occurring within the EDL. Collectively, these two elements describe the effects of charge transfer and ion transport across the interface. Interfaces that have a high resistance to ion transport and charge transfer will have large impedances associated with both R_{ct} and Z_w. Figure 2.14b shows that in this case, the interface will

behave almost identically to an ideal capacitor with a capacitance of C_{dl}. In other words, for systems with a large resistance to ion and charge transfer across the double layer, the electrode will be completely blocking and behave ideally.

In some cases, the dynamics of ions in solution at the electric double layer can break from the standard solution to the Poisson-Nernst-Planck equations. This phenomenon, known as anomalous dynamics, occurs when diffusion forms a nonlinear relationship with time. As a result, fractional exponents arise in the resulting solution to the Poisson-Nernst-Planck equations. This solution can be described effectively by CPE behavior [55], leading to the final model considered in Figure 2.14c. This model replaces the Warburg element in Figure 2.14b with a more general CPE to account for the possibility of anomalous effects. Because the equivalent circuit in Figure 2.14c describes a more general case, it was decided that this model would be fit to the Au/water and Au/DCE data and compared to the results obtained from the pure CPE analysis described in the previous section.

The equivalent impedance of the model shown in Figure 2.14c can be written as

$$\mathrm{Z_{eq}} = \mathrm{R_{sol}} + \frac{1}{C_{dl} j\omega + \frac{1}{R_{ct} + \frac{1}{Q^o (j\omega)^\alpha}}} \quad (2.13),$$

where Q^o and α are the parameters characterizing the CPE, R_{ct} is the charge transfer resistance, C_{dl} is the double layer capacitance of the Au/liquid interface, and R_{sol} is the bulk solution resistance. Unlike the lone CPE model, Z_{eq} is a function of five variables. This can be reduced to four variables by taking the solution resistance to be the raw data resistance at f=10 kHz. The remaining variables are then Q^o, α, C_{dl}, and R_{ct}. Due to the more complicated nature of this model, a new method for fitting the data was developed using MATLAB. This MATLAB optimization uses the built-in fmincon function to simultaneously solve for each of these four variables such that

$$\sum_f |Z_{data} - Z_{eq}| \quad (2.14)$$

is minimum. Here, the sum is over the frequency range of 10 Hz to 10 kHz, corresponding to 60 data points. Z_{data} is the raw data impedance collected from the experiment and Z_{eq} is the impedance of the model fit of Equation 2.13. The function fmincon starts at a vector of specified values of the variables, denoted x_0, and seeks to find a minimum of the multivariate function whose variables are subjected to some constraint, such as an upper or lower bound. The optimization in this work is performed using an interior-point algorithm, although sqp, trust-region-reflective, and active-set algorithms are available as well [56]. An in-depth description of the function's interior point algorithm can be found at [57]. In order to effectively compare the effectiveness of this model to the pure CPE model, a separate script was created using the same methodology to solve for α and Q^o for the lone CPE model once again using Equation 2.14 as the optimization function but with Z_{eq} now given by Equation 2.8. R_{sol} was once again taken to be the raw data resistance at f=10 kHz. The optimization script used for both of these equivalent circuit models are given in Appendix B.

Table 2.4: MATLAB Optimization of the Pure CPE Model

Interface	Test	α	Q^o ($S*s^{\alpha}$)	R_{sol} (Ω)	$\Sigma_f\|Z_{data}-Z_{fit}\|$
Au/water	4mmR&X Round1	0.9138	4.57E-07	146.6	17907.1
	6mmR&X Round1	0.9160	1.41E-06	73.35	3411.6
	6mmR&X Round2	0.9144	1.66E-06	64.21	4027.15
	8mmR&X Round1	0.8953	1.69E-06	51.2	3952.83
	8mmR&X Round2	0.8547	2.28E-06	58.64	3935.18
	10mmR&X Round1	0.9070	3.59E-06	33.2	1485.34
	10mmR&X Round2	0.9084	3.34E-06	32.69	1826.12
Au/DCE	5mmR&X Round2	0.9021	6.89E-07	1266	16171.7
	6mmGlass R&X Round1	0.9474	7.73E-07	847	11632.1
	8mmR&X1 Round2	0.9348	1.72E-06	498.8	7382.82
	8mmFEP R&X Round1	0.9266	1.45E-06	208.1	2908.01
	10mmR&X1 Round2	0.9311	3.15E-06	305.2	2435.91
	10mmglass Round1	0.9184	2.52E-06	311.8	1541.7

Table 2.5: MATLAB Optimization of theTransfer Effects Model

Interface	test	C_{dl} (F)	R_{ct} (Ω)	Q^o ($S*s^\alpha$)	α	R_{sol} (Ω)	$\Sigma_f\|Z_{data}-Z_{fit}\|$
Au/water	4mmR&X Round1	6.81E-08	2.77E-08	4.09E-07	0.8842	146.6	15206.7
	6mmR&X Round1	5.04E-07	6.76E-07	1.11E-06	0.8111	73.35	1360.06
	6mmR&X Round2	3.53E-07	2.22E-04	1.44E-06	0.8650	64.21	3214.11
	8mmR&X Round1	3.20E-07	8.89E+00	1.56E-06	0.8370	51.2	3129.91
	8mmR&X Round2	4.83E-07	8.14E+01	2.19E-06	0.7534	58.64	1499.99
	10mmR&X Round1	1.49E-06	1.33E+01	3.21E-06	0.7231	33.2	181.013
	10mmR&X Round2	1.58E-06	1.84E-07	3.60E-06	0.6391	32.69	563.946
Au/DCE	5mmR&X Round2	3.39E-07	5.26E-01	9.63E-07	0.5464	1266	2723
	6mmGlass R&X Round1	3.37E-07	8.09E+00	5.73E-07	0.8444	847	5839.43
	8mmR&X1 Round2	8.72E-07	5.26E+00	1.76E-06	0.6993	498.8	3398.55
	8mmFEP R&X Round1	4.81E-07	1.00E+01	1.08E-06	0.8580	208.1	2460.47
	10mmR&X1 Round2	1.60E-06	1.03E+01	2.64E-06	0.7227	305.2	1297.8
	10mmglass Round1	1.09E-06	8.14E+02	1.54E-06	0.8210	311.8	1430.75

Tables 2.4 and 2.5 show the results of the MATLAB optimization for the equivalent circuit models described by Equation 2.8 and Equation 2.13, respectively. From the values of $\Sigma_f|Z_{data}-Z_{fit}|$, it is clear that the addition of the modeling of transfer effects at the Au/liquid double layer yields a noticeably better fit of the data; however, this model is not without its issues. First, the values of α should remain constant between tests of the same interface. While this is seen in the MATLAB model for the lone CPE, the newer model including the transfer effects shows a higher variation in values obtained for α. Further, both plots of C_{dl} vs. A_{eq} and Q^o vs. A_{eq} show greater variation from linear behavior than seen for the lone CPE model, as shown in Figure 2.15.

a)

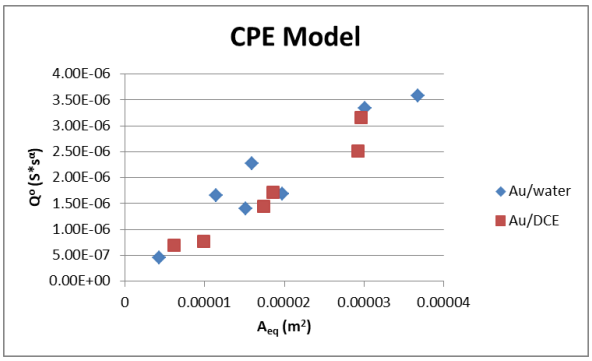

b)

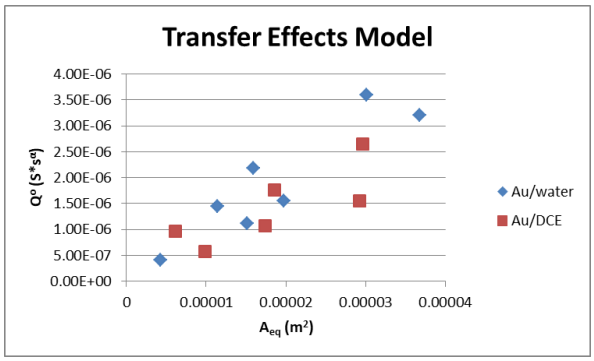

c)

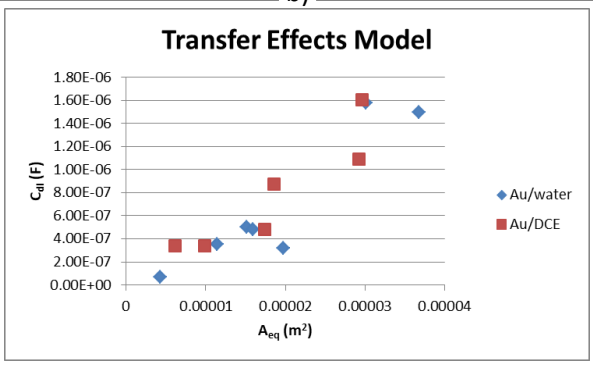

Figure 2.15: Plots of Q^o and C_{dl} vs. A_{eq} obtained from the MATLAB optimization of the lone CPE and transfer effects models. Both transfer effects model plots show larger variation from linear behavior than seen for the CPE model.

Another issue arises when adjusting the starting points for the variables. Starting values for each of the variables used to obtain the results shown in Table 2.5 were 1E-5 F for C_{dl}, 10 Ω for R_{ct}, 1E-6 $S*s^{\alpha}$ for Q^o, and 0.8 for α. While the starting points for C_{dl}, α, and Q^o could all be changed without impacting the final results of the model, the same cannot be said of R_{ct}. The final value of R_{ct} obtained by the model varied greatly based on its starting value. In order to study this more closely, a set of pseudo-data using reasonable values for R_{sol}, C_{dl}, Q^o, and α was generated from Equation 2.13. The values used for R_{sol}, C_{dl}, Q^o, and α were kept constant while R_{ct} was varied over a wide range of values. Values for the four other variables were C_{dl}=1E-6 F, Q^o=5E-7 $S*s^{\alpha}$, α=0.7, and R_{sol}=100 Ω. Before varying R_{ct}, it was first checked whether assuming R_{sol}=R_{eq} at f=10 kHz was appropriate for this particular model. This was easily determined by looking to see if R_{eq} at 10 kHz in fact matched the value inputted for R_{sol}. Results showed that it is reasonable to make this assumption, with the difference between R_{sol} and R_{eq} at 10 kHz being less than 1%.

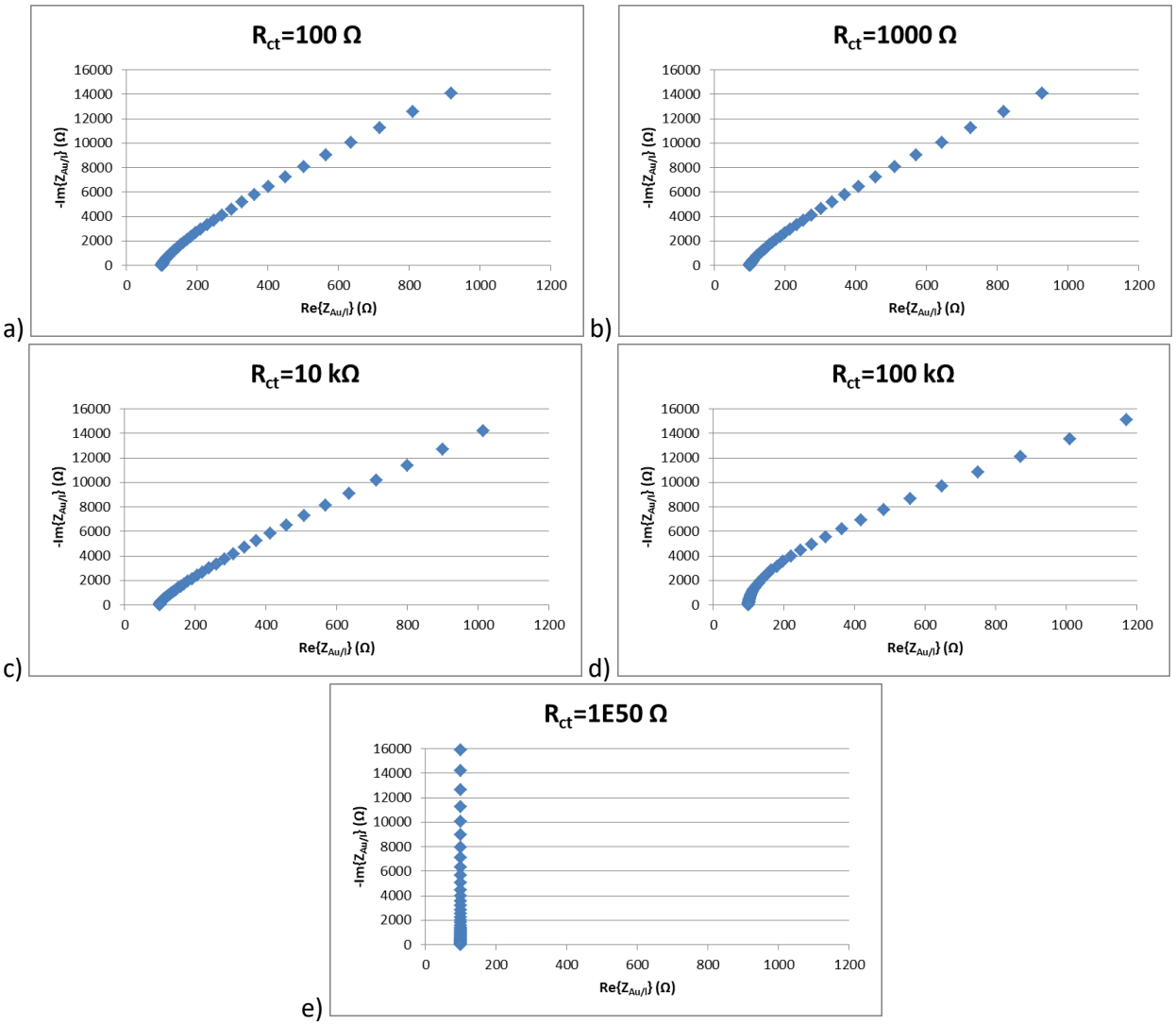

Figure 2.16: Nyquist plots for the pseudo-data generated for the transfer effects equivalent circuit model for **(a)** R_{ct}=100 Ω, **(b)** R_{ct}=1000 Ω, **(c)** R_{ct}=10 kΩ, **(d)** R_{ct}=100 kΩ, and **(e)** as R_{ct} nears infinity.

Figure 2.16 shows the Nyquist plot of the equivalent circuit shown in Figure 2.14c for different values of R_{ct} over a frequency range of 10 Hz-10 kHz using the values for R_{sol}, C_{dl}, Q^{o}, and α given above. In the first four plots, there are two distinct regions within the Nyquist plot. Within the lowest frequency regime, the Nyquist plot forms a straight line, indicative of CPE behavior. As the frequency increases, the interplay between the double layer capacitance and the CPE becomes more prominent, causing a break from the CPE behavior. As the frequency is increased further, the slope of the Nyquist plot becomes steeper, indicating a shift to more ideal behavior. This can be most clearly seen in Figure 2.16d, where

the slope is nearly vertical at the highest frequencies. At these frequencies, the system is dominated by the behavior of C_{dl}. Figure 2.16e shows how the system would behave if R_{ct} were increased to near infinity. The behavior seen in this plot is that of an ideal capacitor in series with a solution resistance. This is to be expected since, in terms of the equivalent circuit model, an infinite charge transfer resistance would prevent any current from passing through the CPE, leading to the double layer capacitance dominating over the entire frequency range. This brings to light the effect of R_{ct} on the behavior of the system: it serves to alter the frequency range over which C_{dl} dominates the system behavior. As R_{ct} increases, The effect of the CPE is diminished until its effect cannot be felt at all when R_{ct} reaches infinity, and, as a result, C_{dl} dominates over a larger frequency range as R_{ct} increases.

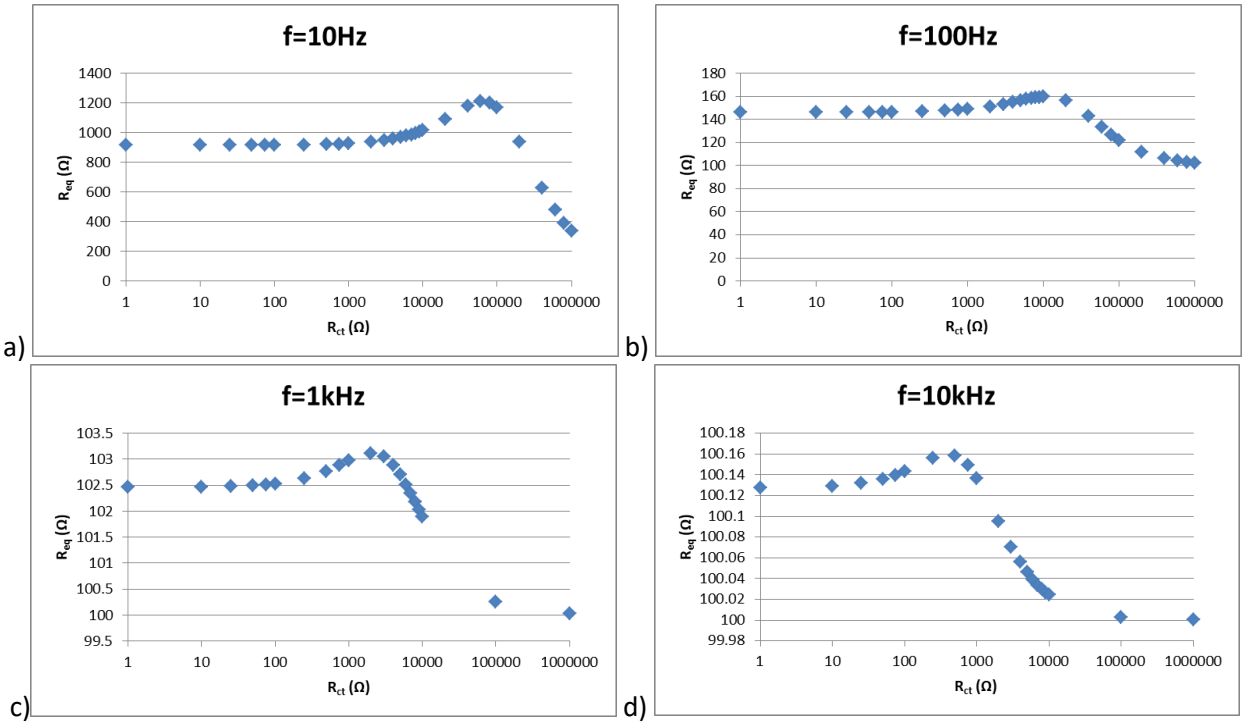

Figure 2.17: Impact of R_{ct} on the total equivalent circuit resistance at **(a)** f=10 Hz, **(b)** f=100 Hz, **(c)** f=1 kHz, and **(d)** f=10 kHz.

Using the same values for R_{sol}, C_{dl}, Q^o, and α given above, the impact of modifying R_{ct} on the equivalent resistance of the circuit model at different frequencies was also studied. R_{ct} was varied between 1 and 1E6 Ω and the value of the system's equivalent resistance was recorded for f=10 Hz, 100

Hz, 1 kHz, and 10 kHz. Plots of R_{eq} vs. R_{ct} are given in Figure 2.17. All four considered frequencies show similar behavior. The hump seen in each plot is related to the interplay between the CPE and C_{dl}. As R_{ct} approaches infinity, the plots converge to R_{sol}. This is to be expected since a large R_{ct} will mitigate the impact that the CPE has on the system and ensure that C_{dl} is dominant. Since the impedance associated with C_{dl} is purely reactive, the only resistive component in the system that contributes noticeably to impedance behavior for a large enough R_{ct} is R_{sol}. It is important to note that for the wide range of R_{ct} considered, the resulting change in R_{eq} is very small. This can explain why the values obtained for R_{ct} in the transfer effects model depended heavily on its starting value. Figure 2.17 shows that R_{eq} is highly invariant to changes in R_{ct} over almost the entire frequency range considered. As a result, it is infeasible that the MATLAB optimization would be able to converge to the solution with the correct R_{ct} value since a small perturbation in R_{ct} would not produce a noticeable change in the equivalent impedance. As such, it should be able to be removed from the equivalent circuit model without greatly impacting the performance of the model.

Because the optimization uses $\Sigma_f|Z_{data}-Z_{fit}|$ as the function to optimize over, it is also useful to consider how $\Sigma_f|Z_{data}-Z_{fit}|$ changes based on R_{ct}. To do this, pseudo-data was generated using the values of C_{dl}, Q^o, R_{sol}, and α obtained from the optimization of the '10mmR&X Round1' Au/water test shown in Table 2.5. Using these values, a fit was generated using Equation 2.13 for various values of R_{ct}. $\Sigma_f|Z_{data}-Z_{fit}|$ was calculated for each selected value of R_{ct} for f in the range of 10 Hz-10 kHz. The results are plotted in Figure 2.18. For large R_{ct}, $\Sigma_f|Z_{data}-Z_{fit}|$ is large but remains relatively constant over a wide range of R_{ct}. As R_{ct} is decreased, the effects of the CPE become more noticeable and $\Sigma_f|Z_{data}-Z_{fit}|$ decreases until a minimum is reached near $R_{ct}=0$. Note that a negative resistance is nonphysical so negative values of R_{ct} are not considered. The minimum occurring near $R_{ct}=0$ directly shows that R_{ct} can be removed without negatively impacting the model performance, as concluded by the previous analysis. Further, this indicates that charge transfer within the EDL plays an insignificant role in the behavior of the system.

a) 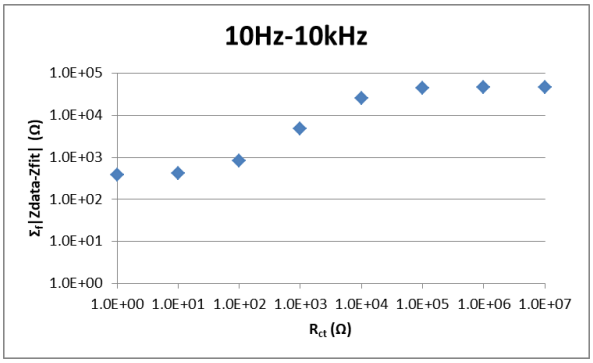

b) 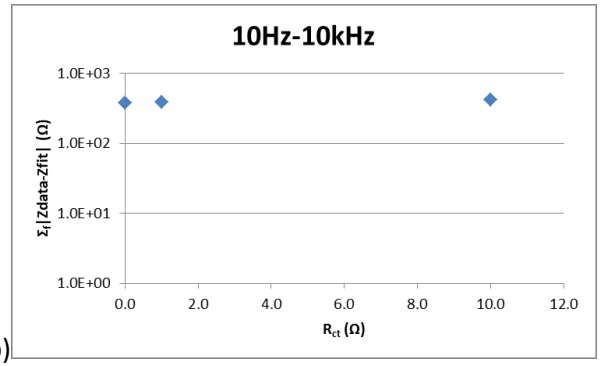

Figure 2.18: (a) Impact of R_{ct} variation on the optimization function. **(b)** Close up of the region containing the minimum in **(a)**. This minimum occurs at R_{ct}=0, indicating that R_{ct} can be removed from the model without any negative impact on model performance.

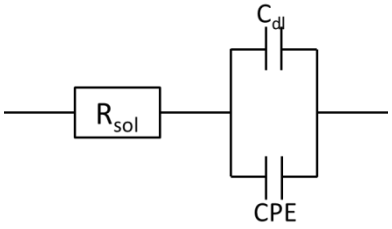

Figure 2.19: Equivalent circuit used to model transfer effects within the Au/liquid double layer after removal of R_{ct}. The large variance in R_{ct} with respect to R_{eq} for the model in Figure 2.14c allows for it to be removed from the circuit without having a significant negative impact on model performance.

Removing R_{ct} from the model yields an equivalent circuit containing a solution resistance in series with a parallel combination of a CPE and C_{dl}, shown in Figure 2.19. The equivalent impedance of this circuit can be written as

$$Z_{eq} = R_{sol} + \frac{1}{C_{dl} j\omega + Q^{o}(j\omega)^{\alpha}} \quad (2.15).$$

Using the same starting values for C_{dl}, Q^{o}, and α as before (C_{dl}=1.5E-5 F, Q^{o}=1E-6 S*s^{α}, and α=0.8) and once again taking R_{sol} to be the raw data resistance at f=100 kHz, the optimization script was modified for this new Z_{eq}. The results for each of the water only and DCE only tests are shown in Table 2.6. Comparison of $\Sigma_f|Z_{data}-Z_{fit}|$ in Tables 2.5 and 2.6 shows that, as expected, removal of R_{ct} does not have a significant impact on the overall performance of the model.

Table 2.6: Transfer Effect Model With R_{ct}=0

interface	test	C_{dl} (F)	Q^{o} ($S*s^{\alpha}$)	α	R_{sol} (Ω)	$\Sigma_f\|Z_{data}-Z_{fit}\|$
Au/water	4mmR&X Round1	8.45E-08	3.99E-07	0.8746	146.6	14538.6
	6mmR&X Round1	5.12E-07	1.10E-06	0.8090	73.35	1448.87
	6mmR&X Round2	4.99E-07	1.30E-06	0.8418	64.21	3000.43
	8mmR&X Round1	4.63E-07	1.37E-06	0.8166	51.2	2535.91
	8mmR&X Round2	7.69E-07	3.72E-06	0.5478	58.64	4346.05
	10mmR&X Round1	1.39E-06	3.05E-06	0.7565	33.2	257.752
	10mmR&X Round2	1.40E-06	2.88E-06	0.7312	32.69	354.769
Au/DCE	5mmR&X Round2	3.76E-07	2.14E-06	0.3338	1266	8419.65
	6mmGlass R&X Round1	3.85E-07	6.51E-07	0.7795	847	5257.71
	8mmR&X1 Round2	9.02E-07	1.84E-06	0.6767	498.8	3098.12
	8mmFEP R&X Round1	4.83E-07	1.08E-06	0.8566	208.1	2466.87
	10mmR&X1 Round2	1.60E-06	2.65E-06	0.7224	305.2	1297.31
	10mmglass Round1	1.71E-06	1.77E-05	0.0177	311.8	6595.06

Unfortunately, the issue of relatively large α variance between tests remains unresolved with the removal of R_{ct}. In order to study this in more detail, the pseudo-data was modified, removing R_{ct} from the equivalent impedance model. Values for Q^{o} and C_{dl} were once again held fixed at 5E-7 $S*s^{\alpha}$ and 1E-6 F, respectively. R_{sol} was taken to be 100 Ω. Values of R_{eq} and X_{eq} were recorded at f=10 Hz, 100 Hz, 1 kHz, and 10 kHz for alphas between 0 and 1 with a step size of 0.05. Plots of R_{eq} and X_{eq} versus alpha at each of the four frequencies are given below.

a)

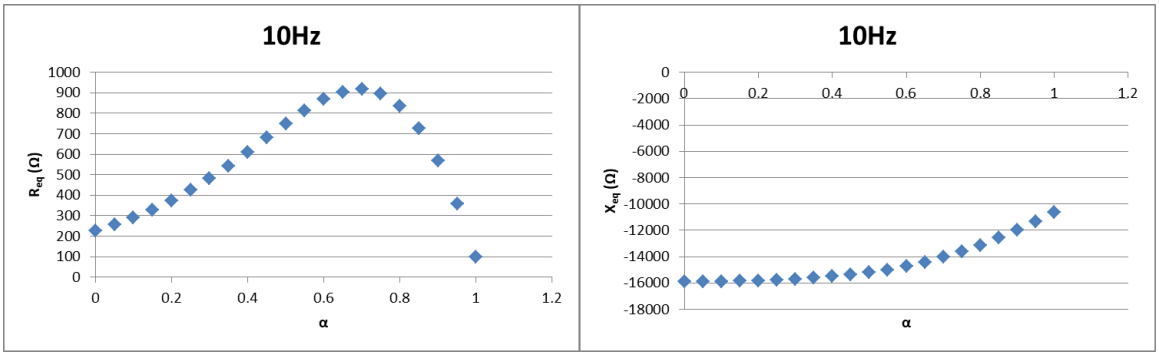

b)

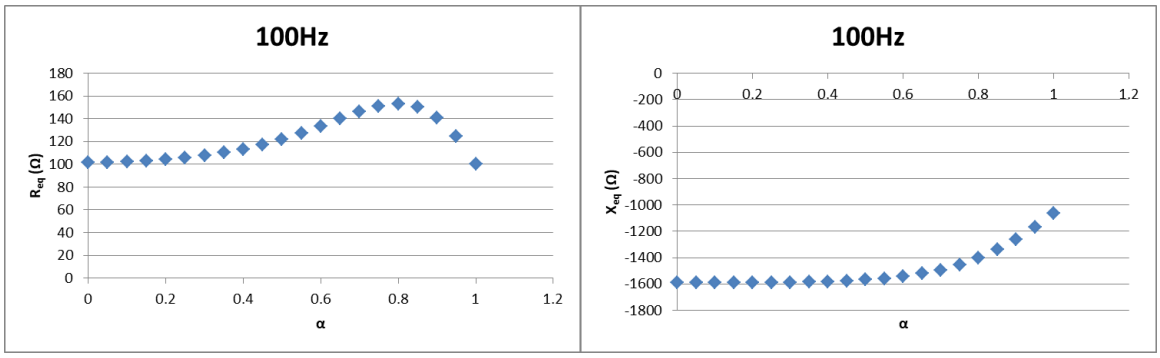

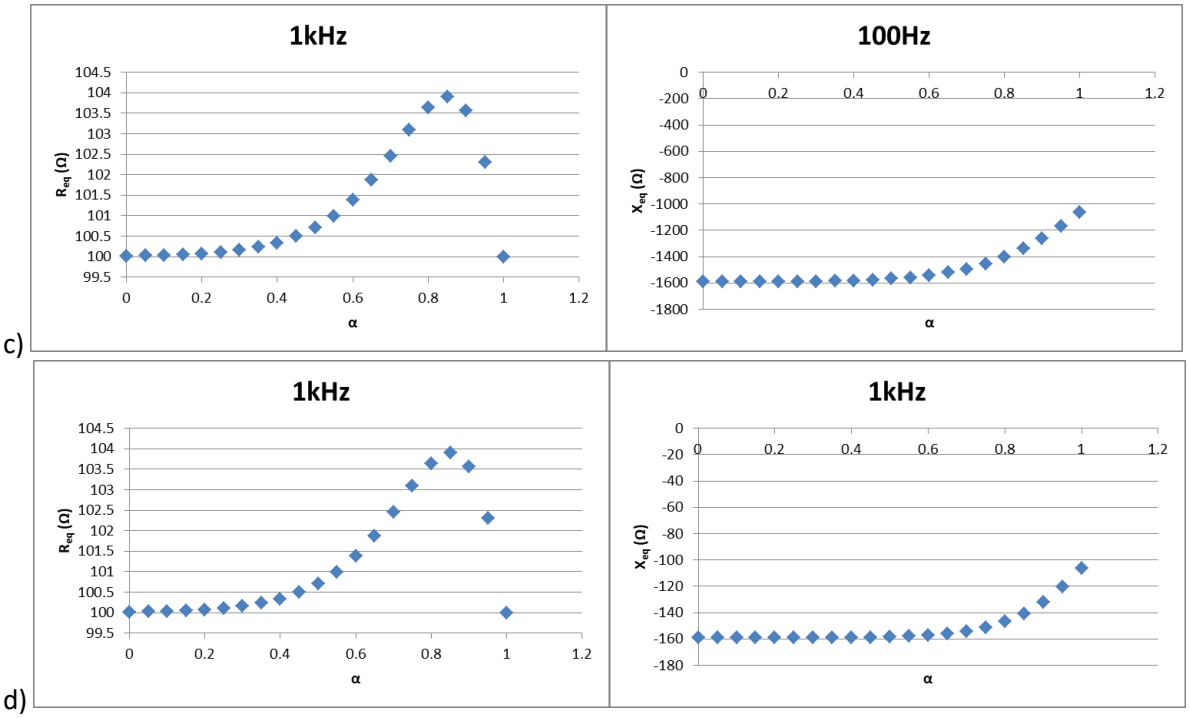

Figure 2.20: Pseudo-data generated to study the effect of varying α on R_{eq} and X_{eq} at **(a)** 10 Hz, **(b)** 100 Hz, **(c)** 1 kHz, and **(d)** 10 kHz for the model given by Figure 2.18 and Equation 2.15.

Because R_{sol}=100 Ω is closer to what is seen for the water only tests, additional analysis was conducted using R_{sol}=700 Ω in order to use a value more applicable to the DCE only tests. Values of C_{dl} and Q^{o} were kept the same as before since these are expected to be roughly the same order of magnitude between the water only and DCE only tests. Similar plots for this R_{sol} were also generated but are excluded here as they follow the same general behavior as what is seen in Figure 2.20. Table 2.6 shows a range of α's obtained for both the Au/water and Au/DCE interfaces by the R_{ct}=0 model. Neglecting the obvious outliers, α was in the range of 0.73-0.87 for the water only tests and in the range of 0.67-0.85 for the DCE only tests. Using the plots of R_{eq} and X_{eq} versus α along with the two values of α defining the range obtained from the water only or DCE only tests, R_{eq} and X_{eq} were determined at the four different frequencies. The results are shown in Table 2.7.

Table 2.7: Sensitivity of R_{eq} and X_{eq} to Changes in α

Water Only (R_{sol}=100 Ω); α_{min}=0.73, α_{max}=0.87						
frequency	R_{eq}, α_{min} (Ω)	R_{eq}, α_{max} (Ω)	X_{eq}, α_{min} (Ω)	X_{eq}, α_{max} (Ω)	$(R_{\alpha min}-R_{\alpha max})/R_{\alpha max}$*100%	$(X_{\alpha min}-X_{\alpha max})/X_{\alpha max}$*100%
10Hz	905.86	646.48	-13839.9	-12284.13	40.12	12.66
100Hz	148.47	145.72	-1474.53	-1301.88	1.89	13.26
1kHz	102.77	103.74	-152.69	-136.25	-0.94	12.07
10kHz	100.15	100.29	-15.7	-14.8	-0.14	6.08
DCE only (R_{sol}=700 Ω); α_{min}=0.67, α_{max}=0.85						
frequency	R_{eq}, α_{min} (Ω)	R_{eq}, α_{max} (Ω)	X_{eq}, α_{min} (Ω)	X_{eq}, α_{max} (Ω)	$(R_{\alpha min}-R_{\alpha max})/R_{\alpha max}$*100%	$(X_{\alpha min}-X_{\alpha max})/X_{\alpha max}$*100%
10Hz	1510.16	1325.99	-14238.34	-12587.59	13.89	13.11
100Hz	743.01	750.26	-1508.06	-1341.24	-0.97	12.44
1kHz	702.17	703.91	-155.08	-140.62	-0.25	10.28
10kHz	700.11	700.3	-15.72	-14.56	-0.03	7.97

By looking at how much R_{eq} and X_{eq} vary over the region of α's obtained from the MATLAB optimization, insight can be gained into how sensitive the model is to changes in α. If the variation is small, then a wide range of α's would correspond to roughly the same R_{eq} and X_{eq}, and, as a result, it would be expected that α would play a diminished role in the behavior of the system. In this case, the optimization would have difficulty telling the difference between one α and another, yielding a wide variation in obtained values. Conversely, if R_{eq} and X_{eq} vary widely over the considered ranges of α, then the exact value of α plays a more significant role in the overall behavior of the system.

In consideration of R_{eq}, Table 2.7 shows that variation in R_{eq} over the specified range of α is only significant at the lowest frequencies. The difference seen between R_{eq} for the water only and DCE only version of the pseudo-data can be attributed to the larger solution resistance used for the DCE pseudo-data. Despite its significance at low frequencies, the change in R_{eq} between the maximum and minimum α's rapidly drops off, becoming insignificant by f=100 Hz. The same cannot be said for X_{eq}. The percent changes obtained for X_{eq} are comparable between the R_{sol}=100 Ω and R_{sol}=700 Ω versions. This makes sense, as the values of Q^o and C_{dl} were kept the same for both versions. Of greater significance, though, is that the change in X_{eq} between the maximum and minimum α's remains a significant percentage of X_{eq} throughout the entire frequency range considered. As a result, it would be expected that the model would give less variation in α than what is actually observed.

The variation of $\Sigma_f|Z_{data}-Z_{fit}|$ with respect to various different α's was also considered using a similar form of analysis used to study the variation of $\Sigma_f|Z_{data}-Z_{fit}|$ with respect to R_{ct}. This analysis, however, used R_{ct}=0. R_{sol} was taken to be R_{data} at 10 kHz for the "10mmR&X Round1" water only test and values of Q^o and C_{dl} were once again obtained from the MATLAB optimization of the "10mmR&X Round1" water only test shown in Table 2.6. These values were then used to generate Z_{fit} for various considered values of α to monitor the changes observed for $\Sigma_f|Z_{data}-Z_{fit}|$. This analysis was conducted for f=10 Hz-10 kHz.

a) 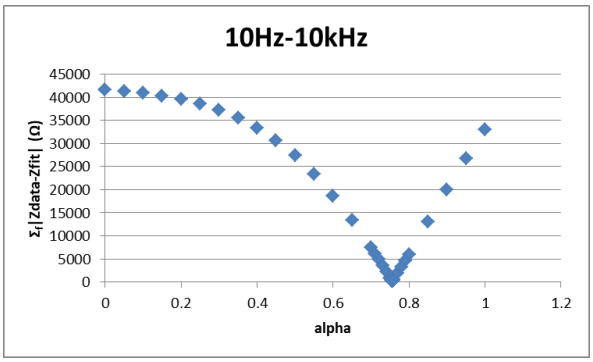

b) 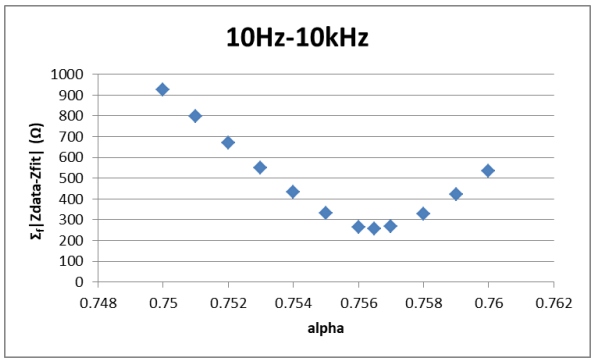

Figure 2.21: (a) Impact of α variation on the optimization function. Data is generated from the values of R_{sol}, Q^o, and C_{dl} from the "10mmR&X Round1" water only test shown in Table 2.6. **(b)** Close-up of the region containing the minimum in (a).

Figure 2.21 shows how changing α impacts the optimization function $\Sigma_f|Z_{data}-Z_{fit}|$. Figure 2.21a shows that only one minimum occurs over the entire applicable range of α. Due to the lack of other local minima in this range, the optimization will converge to the value of α that globally minimizes $\Sigma_f|Z_{data}-Z_{fit}|$. This is also seen in Figure 2.21b, which shows that the minimum function value occurs for the same α as solved for by the optimization given for the appropriate test in Table 2.6. Further, immediately surrounding this minimum, the behavior is approximately quadratic and the changes in the values of the optimization function are large enough to where the optimization should be significantly sensitive to α.

The above analysis shows that the variance observed in α is likely not caused by numerics. Instead, it is likely that the variance in α is due to physical differences between the electrodes used in

each test. Since each electrode was manufactured using the same procedure, two primary possibilities could be the cause. First is the presence of contamination on the surface of the electrode. Although each electrode was cleaned using the same method, it is possible for contamination to remain on the surface post-cleaning or to accrue on the surface during device fabrication. Further, each electrode will likely not have the exact same amount of contamination as the others, which would give rise to the variation observed in α. Second is electrode aging. It has been observed over the course of this project that "flat" electrodes left to sit long enough begin to exhibit color change, going from gold to a silvery-grey that is likely associated with the Titanium forming the adhesion layer. This is a result of diffusion of titanium into the gold. This process happens over the course of weeks or months, but results in electrodes that have varying composition based on their age. Since these devices were manufactured over the course of several weeks, the electrodes may have slightly different compositions between devices, resulting in the variation in α.

Section 2.2.3: Adsorption Model

In order to determine how the model is performing throughout the entire frequency range, it becomes useful to consider the values of R_{data}-R_{fit}, X_{data}-X_{fit} and $|Z_{data}$-$Z_{fit}|$ as a percentage of R_{data}, X_{data}, and Z_{data} at each individual frequency point. Doing so allows for easy interpretation of where the model fits the data well and where improvements can be made. Figure 2.22 shows the results of this process for the "8mmR&X Round1" water only test and "10mmR&X1 Round2" DCE only test conducted for the Transfer Effects model with R_{ct} removed and R_{sol} taken as the raw solution resistance at 10 kHz. Note that the imaginary component has been divided by $|X_{data}|$ since X_{data} is negative across the entire considered frequency range.

a)

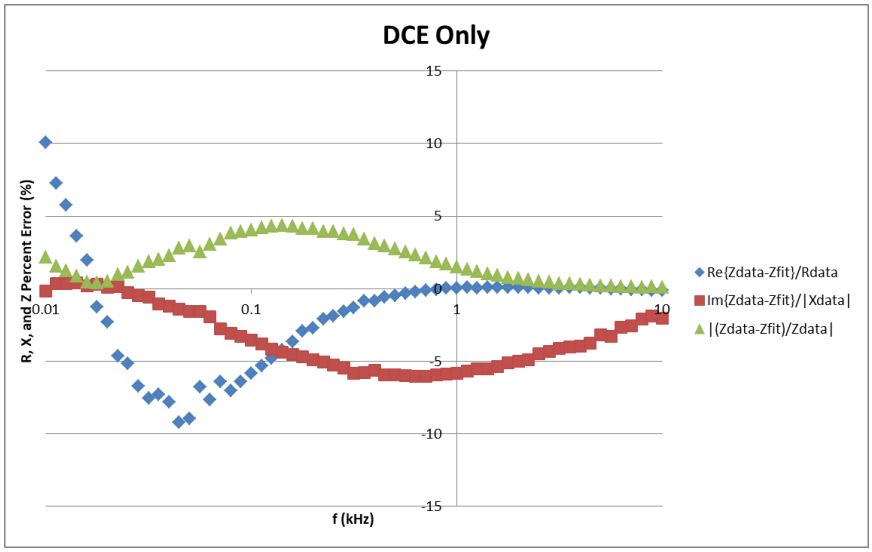

b)

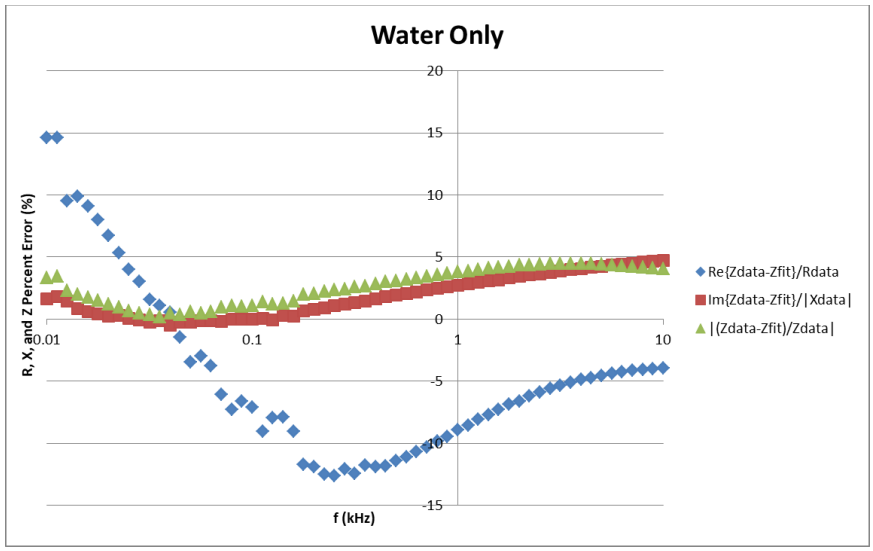

Figure 2.22: Percent difference for R, X, and Z between the data and fit for **(a)** the "10mmR&X Round2" DCE only test and **(b)** the "8mmR&X Round1" water only test.

For both tests considered, differences between the data and fit for X and Z remain within 5% with the exception of the region between 0.2 and 2 kHz in the DCE only test, where the maximum difference in X reaches 6%. The fit in R is much worse in both cases, particularly at low frequencies where maximum differences of 10% and 15% occur at 10Hz for the water only and DCE only tests, respectively. This suggests that the Transfer Effects model does not accurately capture the behavior of the real component of impedance of the Au/water and Au/DCE double layers.

Because of the better fitting of X, it is likely that another purely resistive process remains unaccounted for. The most obvious candidate is specific adsorption of the ions in solution to the gold electrode surface. In terms of the equivalent circuit model, this process occurs in parallel with both the double layer charging capacitance and the CPE describing transfer effects within the EDL. The addition of an adsorption resistance, R_{ad}, yields the equivalent circuit model shown in Figure 2.23.

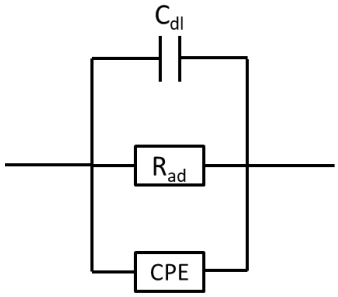

Figure 2.23: Equivalent circuit model (called the 'Adsorption Model') accounting for the effects of double layer charging (C_{dl}), adsorption of ions onto the gold electrode (R_{ad}), and the effects of ion transport through the EDL (CPE).

The equivalent impedance of the adsorption model is

$$Z_{eq} = R_{sol} + \frac{1}{C_{dl}j\omega + Q^o(j\omega)^{\alpha} + \frac{1}{R_{ad}}} \quad (2.16).$$

This equation was substituted into the MATLAB optimization, which is now a function of 4 variables: C_{dl}, R_{ad}, Q^o, and α. With x defined as x=[C_{dl}, R_{ad}, Q^o, α], lower bounds, upper bounds, and starting points of each variable were set as lb=[0,0,0,0], ub=[1E-2,1E7,1E-2,1], and x_0=[1E-5,1E6,1E-6,0.8], respectively. The updated optimization was performed over a frequency range of 10 Hz-10 kHz for each test with the results summarized in Table 2.8 and compared to the results obtained for the transfer effects model (no R_{ct}) discussed in the previous section. Comparison of $\Sigma_f|Z_{data}-Z_{fit}|$ between the two different models shows that the addition of R_{ad} yields a closer fit for all tests with the exception of the 10 mm Au/w tests; however, the optimization for each test using the Adsorption model yielded a final R_{ad} equivalent to its starting point.

Table 2.8: Comparison of the Adsorption and Transfer Effects Models

Adsorption Model							
interface	test	C_{dl} (F)	R_{ad}	Q^o ($S*s^\alpha$)	α	R_{sol} (Ω)	$\Sigma_f\|Z_{data}-Z_{fit}\|$
Au/w	4mmR&X Round1	1.80E-07	1.00E+06	3.63E-07	0.7747	146.6	6850.3
	6mmR&X Round1	4.73E-07	1.00E+06	1.08E-06	0.8293	73.35	983.184
	6mmR&X Round2	3.46E-07	1.00E+06	1.39E-06	0.8737	64.21	2879.36
	8mmR&X Round1	4.03E-07	1.00E+06	1.42E-06	0.8298	51.2	1942.9
	8mmR&X Round2	5.18E-07	1.00E+06	2.21E-06	0.7401	58.64	448.145
	10mmR&X Round1	1.33E-06	1.00E+06	3.02E-06	0.7688	33.2	330.664
	10mmR&X Round2	1.83E-06	1.00E+06	6.56E-06	0.4342	32.69	2145.36
Au/DCE	5mmR&X Round2	3.67E-07	1.00E+06	1.18E-06	0.4514	1266	5206.73
	6mmGlass R&X Round1	3.31E-07	1.00E+06	5.72E-07	0.8455	847	4356.72
	8mmR&X1 Round2	7.19E-07	1.00E+06	1.62E-06	0.7757	498.8	4137.72
	8mmFEP R&X Round1	4.93E-07	1.00E+06	1.05E-06	0.8578	208.1	2023.66
	10mmR&X1 Round2	1.76E-06	1.00E+06	2.97E-06	0.6509	305.2	827.004
	10mmglass Round1	1.62E-06	1.00E+06	6.29E-06	0.2662	311.8	5087.92
Transfer Effects Model							
interface	test	C_{dl} (F)	Q^o ($S*s^\alpha$)	α	R_{sol} (Ω)	$\Sigma_f\|Zdata-Zfit\|$	
Au/w	4mmR&X Round1	8.45E-08	3.99E-07	0.8746	146.6	14538.6	
	6mmR&X Round1	5.12E-07	1.1E-06	0.8090	73.35	1448.87	
	6mmR&X Round2	4.99E-07	1.3E-06	0.8418	64.21	3000.43	
	8mmR&X Round1	4.63E-07	1.37E-06	0.8166	51.2	2535.91	
	8mmR&X Round2	7.69E-07	3.72E-06	0.5478	58.64	4346.05	
	10mmR&X Round1	1.39E-06	3.05E-06	0.7565	33.2	257.752	
	10mmR&X Round2	1.4E-06	2.88E-06	0.7312	32.69	354.769	
Au/DCE	5mmR&X Round2	3.76E-07	2.14E-06	0.3338	1266	8419.65	
	6mmGlass R&X Round1	3.85E-07	6.51E-07	0.7795	847	5257.71	
	8mmR&X1 Round2	9.02E-07	1.84E-06	0.6767	498.8	3098.12	
	8mmFEP R&X Round1	4.83E-07	1.08E-06	0.8566	208.1	2466.87	
	10mmR&X1 Round2	1.6E-06	2.65E-06	0.7224	305.2	1297.31	
	10mmglass Round1	1.71E-06	1.77E-05	0.0177	311.8	6595.06	

a)

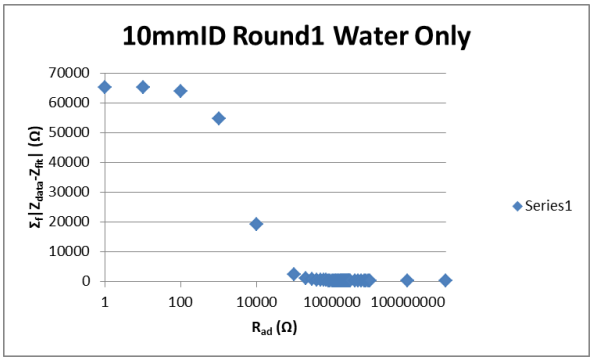

b)

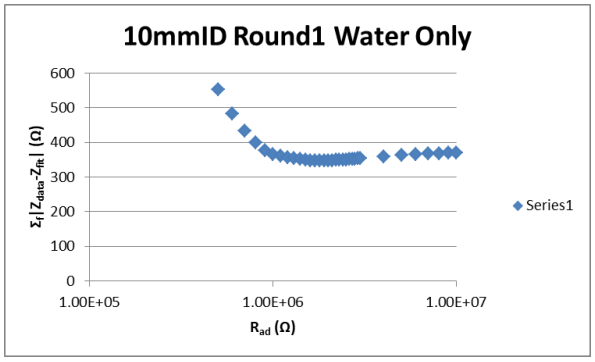

Figure 2.24: (a) Impact of R_{ad} variation on the optimization function. **(b)** Close up of the region containing the minimum in **(a)**. The small changes in $\Sigma_f|Z_{data}-Z_{fit}|$ over a large range of R_{ad} directly around the minimum make it difficult for the optimization to find the exact minimum.

To obtain a better idea of how the model behaves with respect to R_{ad}, pseudo-data was once again generated for the '10mmR&X Round1' Au/w test using the values for C_{dl}, Q^o, α, and R_{sol} given in

Table 2.8. The considered frequency range was 10 Hz-10 kHz. The results, depicted in Figure 2.24, show that the optimization function is minimized for R_{ad}=1.9E6 Ω. Directly surrounding this minimum, however, $\Sigma_f|Z_{data}-Z_{fit}|$ remains relatively constant, changing by approximately 1 Ω for a corresponding change in R_{ad} of ±3E5 Ω away from the minimum. This can be further seen in Figure 2.25, which shows how various values of R_{ad} impact the system's equivalent resistance at frequencies of 10 Hz, 100 Hz, 1 kHz, and 10 kHz. Each plot shows large changes in R_{eq} for small R_{ad}, but for large values, particularly near the minimum in Figure 2.24b, the resulting change in R_{eq} is negligible.

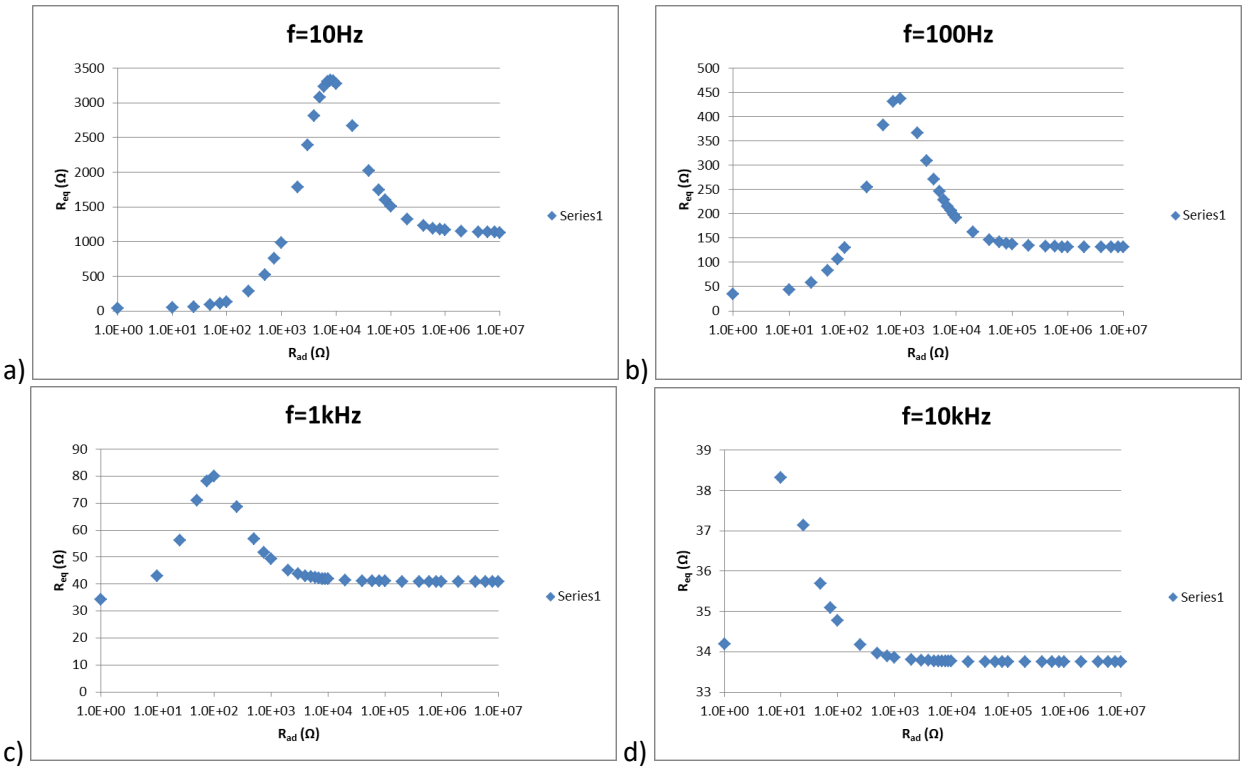

Figure 2.25: Pseudo-data generated to study the effect of varying R_{ad} on R_{eq} at **(a)** 10 Hz, **(b)** 100 Hz, **(c)** 1 kHz, and **(d)** 10 kHz for the model given by Figure 2.23 and Equation 2.16

It is important to note that while the location of the minimum may not necessarily occur for the same R_{ad} as the plots in Figure 2.24 for different sized interfaces of the same type, the general behavior should remain consistent. The pseudo-data shown in Figure 2.24b indicates that changes in $\Sigma_f|Z_{data}-Z_{fit}|$

remains noticeable until roughly R_{ct}=1E6 Ω. Below this value, the optimization function increases rapidly. In contrast, the optimization function increases very slowly above this value.

Table 2.9: Impact of R_{ad} Starting Point on Optimization Performance

$R_{ad,start}$ (Ω)	C_{dl} (F)	$R_{ad,end}$ (Ω)	Q^o ($S*s^\alpha$)	α	R_{sol} (Ω)	$\Sigma_f\|Z_{data}-Z_{fit}\|$
1	1.00E-06	9.16E+04	2.41E-06	0.8688	33.2	796.941
10	9.51E-07	7.54E+04	2.38E-06	0.8781	33.2	1025.53
100	2.28E-06	2.81E+04	1.32E-12	0.6583	33.2	4986.89
1000	2.28E-06	2.82E+04	2.35E-07	0.0000	33.2	4986.03
1.00E+04	2.28E-06	2.82E+04	1.53E-09	0.0331	33.2	4986.83
2.00E+04	2.23E-06	2.00E+04	2.65E-13	1.0000	33.2	6137.63
3.00E+04	1.68E-06	3.00E+04	9.58E-07	0.8937	33.2	3869.84
4.00E+04	1.84E-06	4.00E+04	1.55E-06	0.7388	33.2	3103.08
5.00E+04	5.98E-07	5.00E+04	2.36E-06	0.9277	33.2	1872.95
6.00E+04	6.67E-07	6.00E+04	2.46E-06	0.9105	33.2	1379.03
7.00E+04	8.99E-07	7.00E+04	2.34E-06	0.8900	33.2	1161.6
8.00E+04	5.82E-07	8.00E+04	2.67E-06	0.9062	33.2	902.411
9.00E+04	9.90E-07	9.00E+04	2.43E-06	0.8694	33.2	904.085
1.00E+05	8.79E-07	1.00E+05	2.55E-06	0.8767	33.2	679.954
2.00E+05	1.63E-06	2.00E+05	3.15E-06	0.6890	33.2	979.737
3.00E+05	1.40E-06	3.00E+05	2.89E-06	0.7615	33.2	377.041
4.00E+05	1.98E-06	4.00E+05	7.61E-06	0.4059	33.2	2589.07
5.00E+05	1.97E-06	5.00E+05	7.41E-06	0.4162	33.2	2482.26
6.00E+05	1.42E-06	6.00E+05	2.93E-06	0.7562	33.2	171.223
7.00E+05	1.51E-06	7.00E+05	3.15E-06	0.7222	33.2	355.212
8.00E+05	1.48E-06	8.00E+05	3.24E-06	0.7249	33.2	510.453
9.00E+05	1.32E-06	9.00E+05	2.91E-06	0.7775	33.2	307.262
1.00E+06	1.33E-06	1.00E+06	3.02E-06	0.7688	33.2	330.664
1.00E+07	1.29E-06	1.00E+07	2.93E-06	0.7828	33.2	460.957
1.00E+08	1.30E-06	1.00E+08	2.95E-06	0.7801	33.2	444.728
1.00E+09	1.49E-06	1.00E+09	3.31E-06	0.7179	33.2	393.614
1.00E+10	1.59E-06	1.00E+10	3.42E-06	0.6878	33.2	376.666
1.00E+50	1.51E-06	1.00E+50	3.24E-06	0.7161	33.2	202.158
1.00E+99	1.51E-06	1.00E+99	3.24E-06	0.7161	33.2	202.158
R_{ct}=0 transfer effect model	**1.39E-06**		**3.05E-06**	**0.7565**	**33.2**	**257.752**

Table 2.9 shows the impact of the starting point of R_{ad} on the optimization of the "10mmID Round1" water only test. For starting values of R_{ad}<6E5 Ω, values obtained by the optimization for C_{dl}, Q^o, and α are unable to be reliably determined. Above this point, however, the values obtained for each of these variables show remarkable consistency despite the wide range of R_{ad} considered.

Despite the consistency of the optimization variables above a starting R_{ad} of 6E5 Ω, the optimization function values varies by several hundred Ohms depending on the starting value used for R_{ad}; however, most of this variation is not attributable to the chosen starting value of R_{ad} as evident by

Figure 4.24b. Instead, it must be a result of the slight differences in C_{dl}, Q^o, and α obtained between the different starting values of R_{ad}, indicating that the optimization of the system still has good sensitivity to the other optimization variables. Due to the low sensitivity to R_{ad}, it might be expected that it could be removed from the model without greatly impacting the optimization as was done for R_{ct} in the Transfer Effects model; however, Table 2.8 shows that this is not the case. Inclusion of R_{ad} provides a noticeably better optimization fit for nearly every test. The lack of sensitivity to R_{ad} at larger values does, however, indicate that the determination of the starting point of R_{ad} in the optimization can be less rigorous in this range since a relatively wide range of R_{ad} values will correspond to roughly the same solution to the optimization.

Table 2.10: Sensitivity of Adsorption Model to R_{ad} Variation

interface	test	**Varying R_{ad}**		**Optimization Script**		$\sum_f(\lvert Z_{data}-Z_{fit}\rvert)$	R_{ad} % diff.
		R_{ad} at min (Ω)	$\sum_f(\lvert Z_{data}-Z_{fit}\rvert)$ (Ω)	R_{ad} (Ω)	$\sum_f(\lvert Z_{data}-Z_{fit}\rvert)$ (Ω)	% diff. (%)	(%)
Au/w	4mmR&X Round1	1.20E+06	6.36E+03	1.00E+06	6850.3	7.39	-18.18
	6mmR&X Round1	7.00E+05	684.1531	1.00E+06	983.184	35.87	35.29
	6mmR&X Round2	7.00E+05	2.76E+03	1.00E+06	2879.36	4.38	35.29
	8mmR&X Round1	7.00E+05	1.82E+03	1.00E+06	1942.9	6.46	35.29
	8mmR&X Round2	1.10E+06	4.33E+02	1.00E+06	448.145	3.49	-9.52
	10mmR&X Round1	1.90E+06	347.7579	1.00E+06	330.664	-5.04	-62.07
	10mmR&X Round2	1.00E+07	2.05E+03	1.00E+06	2145.36	4.55	-163.64
Au/DCE	5mmR&X Round2	1.40E+06	4.72E+03	1.00E+06	5206.73	9.76	-33.33
	6mmGlass R&X Round1	9.00E+05	4.33E+03	1.00E+06	4356.72	0.55	10.53
	8mmR&X1 Round2	4.00E+05	3.84E+03	1.00E+06	4137.72	7.51	85.71
	8mmFEP R&X Round1	7.00E+05	1.97E+03	1.00E+06	2023.66	2.89	35.29
	10mmR&X1 Round2	9.00E+05	8.18E+02	1.00E+06	827.004	1.07	10.53
	10mmglass Round1	6.00E+05	5.06E+03	1.00E+06	5087.92	0.46	50.00

To test this hypothesis, values of C_{dl}, Q^o, R_{sol}, and α were taken for each test from the Adsorption model section of Table 2.8. R_{ad} was defined in MATLAB as a vector starting at 1E5 Ω and ending at 1E7 Ω with a step of 1E5 Ω. For each element in R_{ad}, the optimization function value $\sum_f\lvert Z_{data}-Z_{fit}\rvert$ was determined using a frequency range of 10 Hz-10 kHz. The minimum optimization function value and the corresponding value of R_{ad} were recorded for each test and compared to the optimization function value and R_{ad} obtained by the optimization script for each test. The results are shown in Table 2.10. Despite

the large differences observed between the values of R_{ad} as determined by the two different methods, the differences between the optimization function values between the two methods are, for the most part, relatively small. This shows that choosing a value for the starting point of R_{ad} in the MATLAB optimization that does not exactly line up with the actual R_{ad} that minimizes the optimization function does not have a large impact on the optimization itself. Consideration of this along with the values of R_{ad} that yielded the actual minimum (i.e. R_{ad} at min. for Varying R_{ad}), it was decided that a starting value of R_{ad}=1E6 Ω is appropriate to use for each of the tests.

As R_{ad} approaches infinity, the equivalent circuit of the adsorption model converges to the equivalent circuit of the transfer effects model with R_{ct}=0. Thus it is expected that optimization of the adsorption model for a large R_{ad} will yield a similar solution to that obtained by the transfer effects model. The last row of Table 2.9 shows the results from the optimization of the "10mmID Round1" water only test using the transfer effects model with R_{ct} not included. Although the values of the corresponding variables of the adsorption model for starting R_{ct} of 1E50 and 1E99 Ω are similar to those given by the transfer effects model, there is still a noticeable difference. These differences are purely numeric, resulting directly from the optimization of the data. These slight differences only cause a small difference of 56 Ω over a frequency range of 10 Hz-10 kHz in the final value of the optimization function and are not considered to be significant.

a)

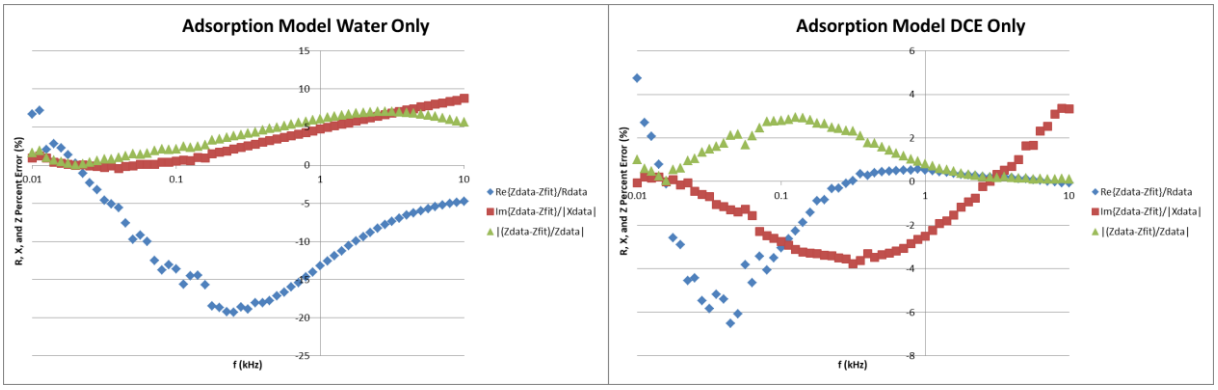

b)

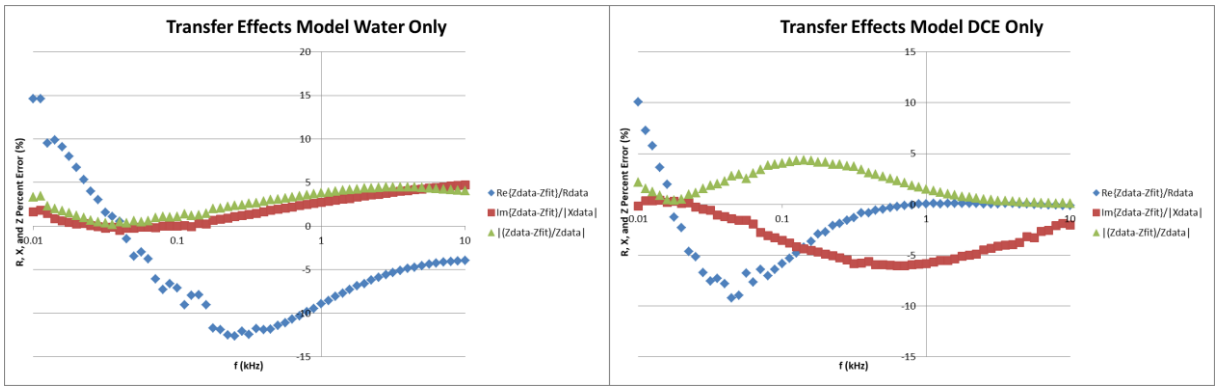

Figure 2.26: R, X, and Z percent errors of the "8mmR&X Round1" Au/water and "10mmR&X Round2" Au/DCE interfaces for the **(a)** Adsorption model and the **(b)** Transfer Effects model.

Figure 2.26 depicts plots of the percent error between the data and fit of the "10mmR&X Round2" DCE only test and "8mmR&X Round1" water only test for both the Transfer Effects and Adsorption models. Note that the Adsorption model of the water only test has a noticeably worse error in R, particularly over the 0.1-1 kHz range. As a result, it might seem odd that the adsorption model yielded a smaller optimization function value than the Transfer Effects model; however, the better fit seen in the low frequency regime can explain this. The adsorption model provides a better fit in R for a frequency range of roughly 10-50 Hz: a much smaller impedance range than the 0.1-1 kHz range over which its performance is worse than the Transfer Effects model. Recall that the optimization model function is $\sum_f |Z_{data}-Z_{fit}|$. Since the raw data impedance is largest at low frequencies, the better fit at low f in the adsorption model makes up for the worse error seen at middle frequencies due to the lower system impedances in this range.

Fortunately, the real component of the Au/liquid interfacial impedances is much smaller than the imaginary component. For example, the "8mmR&X Round1" water only test has $R_{Au/w}$=2849 Ω and $X_{Au/w}$=-14100 Ω, meaning that the real component of the impedance only makes up 20% of the impedance magnitude of the Au/water interface in this test. Likewise, the "10mmR&X Round2" DCE only test has $R_{Au/d}$=1136 Ω and $X_{Au/d}$=-6600 Ω, meaning that the real component of the impedance only makes up 17% of the impedance magnitude of the Au/DCE interface in this test. A result of this is that larger errors in R will not have as large an impact on model performance as larger errors in X will. This can clearly be seen in Figure 2.26, where the behaviors and magnitude of the errors seen in the X and Z curves are nearly identical.

a)

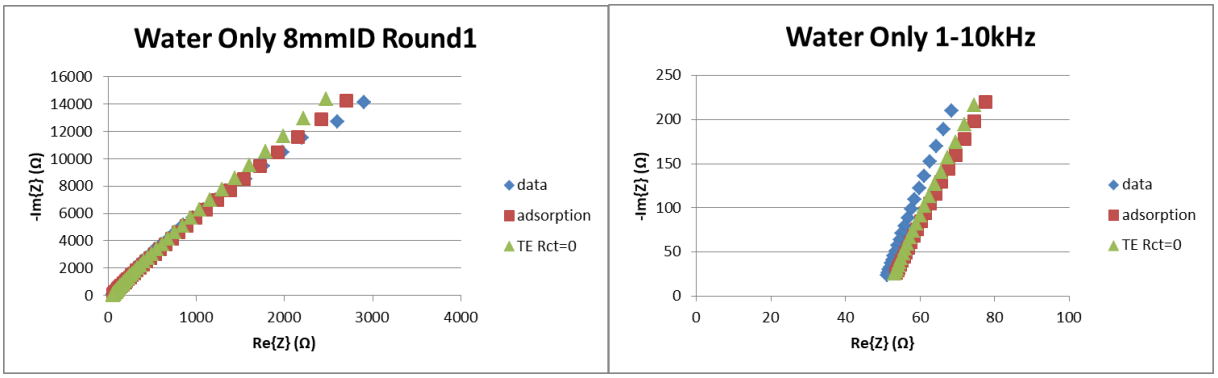

b)

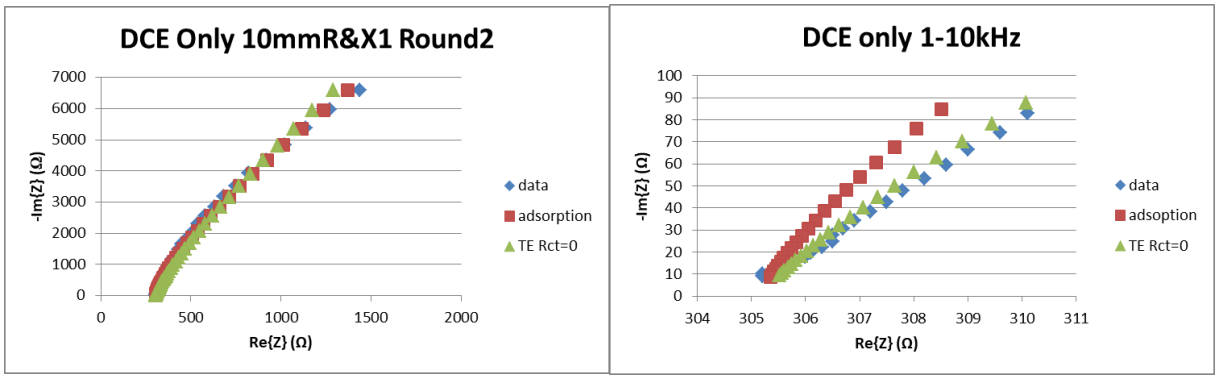

Figure 2.27: Nyquist plots of the raw data and fits obtained by the Adsorption and Transfer Effects models for **(a)** the 8mmID Round1 water only test and **(b)** the 10mmID Round2 DCE only test. The first plots in (a) and (b) cover a frequency range of 10 Hz-10 kHz while the second plots focus on 1-10 kHz.

The last remaining question is as follows: which equivalent circuit model best describes the Au/water and Au/DCE interfaces? Unfortunately, there does not appear to be a clear answer. While the

transfer effects model behaves reasonably well at frequencies above 100 Hz, it suffers from a poor fit in R at low frequencies where the interfacial impedances are largest. Similarly, while the Adsorption model exhibits less error in the low frequency regime, it suffers from large error in R over a wider range of mid-range frequencies. Both models, however, appear to perform decently at high frequencies, with perhaps the Transfer Effects model performing slightly better when considering the Nyquist plots in Figure 2.27. The solution to the above question is that determining which model to use ultimately comes down to what frequency range a device is expected to operate in. For example, if the device is to be operated at a low frequency, C/A obtained by the adsorption model would be more appropriate to use due to the smaller error provided by the model within this frequency range. A plot of C_{dl} versus area obtained for both the Transfer Effects and Adsorption models is shown in Figure 2.28.

a) 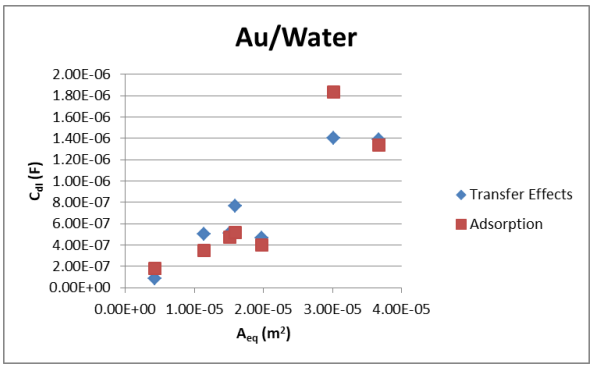

b) 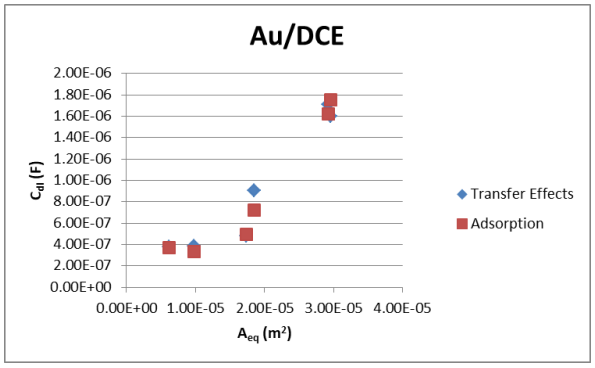

Figure 2.28: Dependence of C_{dl} on interfacial area for the **(a)** Au/water and **(b)** Au/DCE interfaces. Data is plotted for both the Transfer Effects and Adsorption models.

Section 2.3: Can ITIES Impedance be Accurately Determined Using Conventional Electrodes?

With a model developed for the Au/water and Au/DCE interfaces, all impedance contributions in the ITIES device described in Figures 2.1 and 2.2 with the exception of the ITIES can be accounted for. The equivalent impedance of this device with the 1M water and 1M DCE solutions can be expressed as

$$Z_{eq} = Z_{Au/d} + Z_{Au/w} + Z_{ITIES} + R_{sol} \quad (2.17).$$

Setting Z_{eq} equal to the raw data impedance Z_{data} and isolating the ITIES impedance yields

$$Z_{data} - Z_{Au/w} - Z_{Au/d} - R_{sol} = Z_{ITIES} \quad (2.18).$$

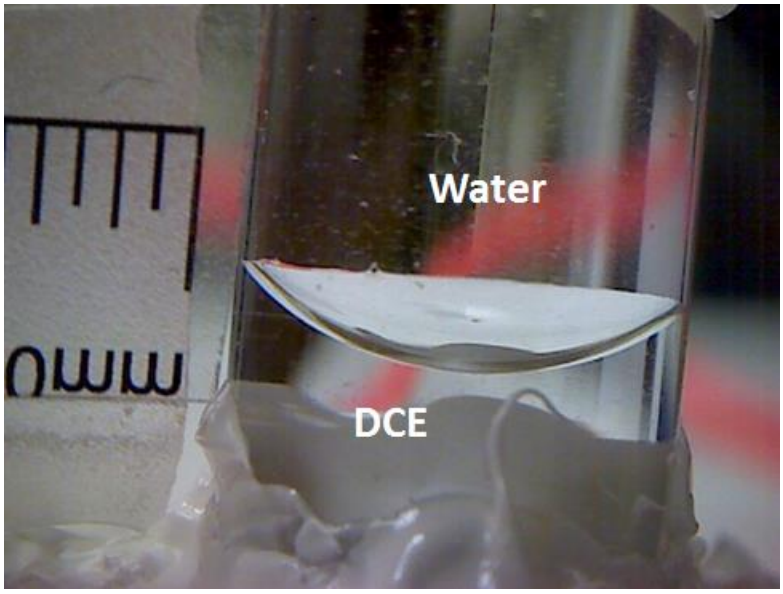

Figure 2.29: Image of the water/DCE interface. The interfacial area was determined using the available ImageJ contact angle plugin as described in Appendix A2.

The device described by Figure 2.1 was constructed using the same method that was used to construct the devices described in Figure 2.3 that were used to study the Au/water and Au/DCE interfaces. Figure 2.29 shows an image obtained for the water/DCE interface. Using the ImageJ contact angle plugin as described in Appendix A2, the area of this interface can be determined. Further, the brightness threshold analysis technique described in Appendix A1 can be used to determine the Au/liquid interfacial areas. By using these areas along with the impedance model developed for the flat Au/liquid interfaces and taking R_{sol} as the high frequency raw data resistance, the impedance contribution of the water/DCE ITIES can be backed out.

It has been stated that in order for a particular device to be sensitive to changes in the ITIES, the ITIES impedance must make up a large fraction of the device's total impedance. Figure 2.30 shows the

raw data impedance spectrum of one of the tests conducted using the above apparatus. At f=10 Hz, where the impedance of the ITIES is expected to be largest, subtracting out the other impedance contributions showed that the water/DCE interface accounted for only roughly half of the device's resistance and only 14% of its total reactance. Because the impedance contribution of the ITIES is comparatively small, especially in X, any errors present from utilizing the equivalent circuit model for the Au/liquid interfacial impedances are magnified. As a result of this, subtracting out the impedance contributions of the Au/water and Au/DCE interfaces along with R_{sol} resulted in an ITIES interfacial impedance with negative R and positive X values over parts of the considered frequency range for some tests, indicating that too much impedance was being subtracted out. Because of this inconsistency, no reliable data on the water/DCE interface was able to be collected from this device.

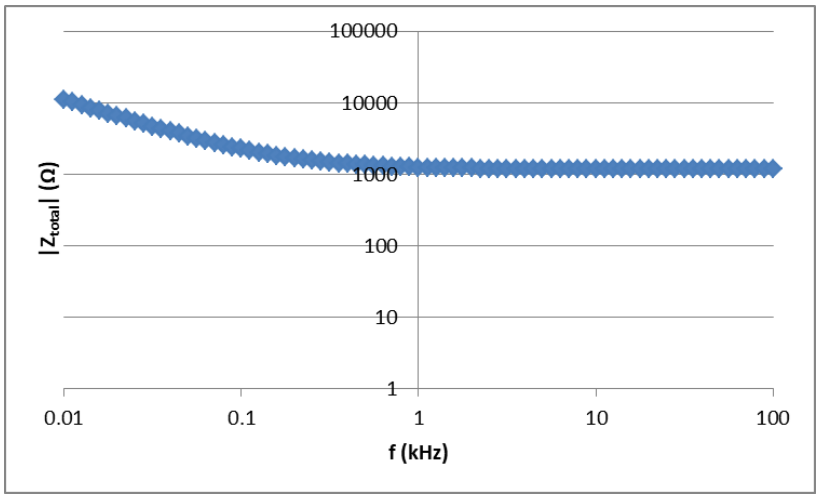

Figure 2.30: Impedance spectrum of the preliminary device used to probe the water/DCE ITIES

A second attempt to back out the water/DCE interfacial impedance was conducted using the device shown in Figure 2.31. To construct this device, slots were cut out of the sides of two separate BD Luer Lok syringes. Gold electrodes prepared as described above were cut to size and inserted into the slots face down and sealed into place. A small capillary tube with an inner diameter of 1.5 mm and outer diameter of 1.8 mm was adhered to the tip of each syringe. Leads were attached to the gold electrodes

using copper tape. A reservoir was created by cutting and sealing glass slides together. Both syringes were filled with water until the electrodes were submerged while the reservoir was filled with DCE. The tips of the capillary tubes were submerged in the DCE and oriented to make the water drops form as close together as possible. Drops were formed by adjusting the plunger on each syringe. Impedance spectroscopy was performed as previously described.

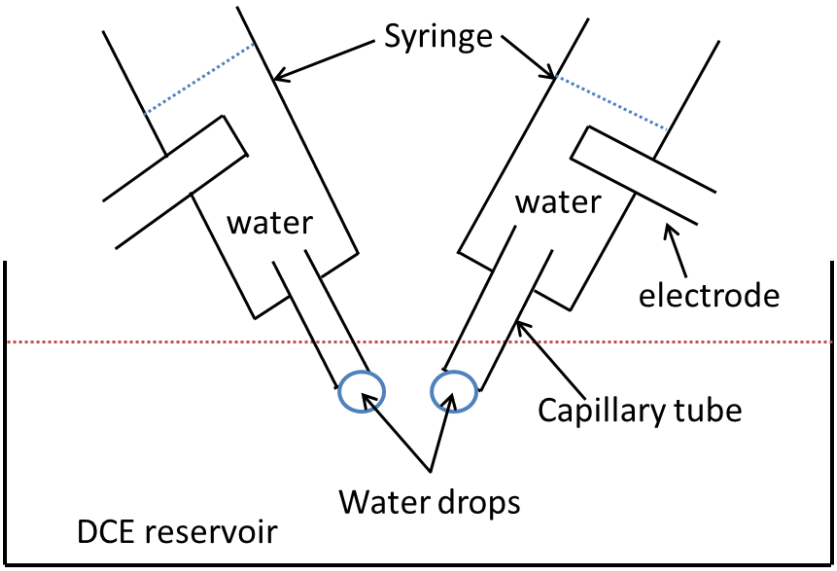

Figure 2.31: "Two syringe" apparatus used as a variation of the design in Figure 2.1. The device was designed to have a smaller water/DCE interfacial area and fewer interface types to increase sensitivity to the water/DCE interface.

This device had the benefits of both Au/liquid interfaces being Au/water and allowed for the formation of much smaller water/DCE interfaces; however, it did suffer from an increased solution resistance. Fortunately, since the solution resistance is easily able to be accurately backed out, this was not expected to have a large impact on the device's performance. Unfortunately, the apparatus was unable to be used for an unforeseen reason which can be seen clearly seen in the right water/DCE interface shown in Figure 2.32. Pressure differentials within the syringe as well as the evaporation of the DCE within the reservoir caused the size of the drops to grow and shrink over time. As such, the size of the interface did not remain constant over the course of a given test and no reliable data was able to be obtained.

a)

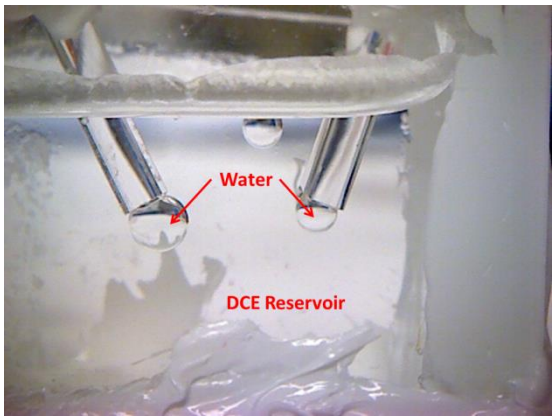

b)

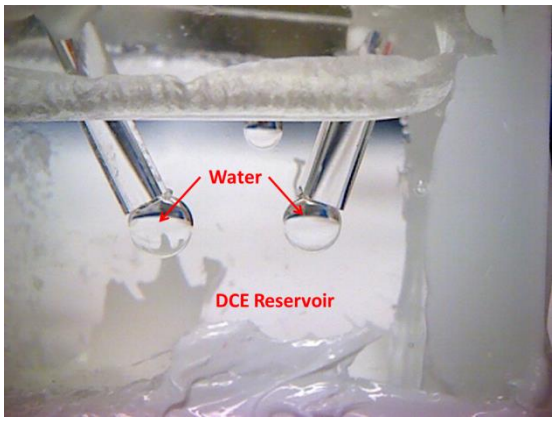

Figure 2.32: (a) Image taken of the two water/DCE interfaces right before the test was run. **(b)** Image taken when the test was complete (roughly two minutes later). Both water drops have increased in size and the height of the DCE reservoir has slightly decreased.

In order to fix the water/DCE sensitivity issue, design changes must be made in order to increase the impedance fraction of the water/DCE interface. Since the interfacial impedance is inversely proportional to area, this can be accomplished by decreasing the surface area of the ITIES and increasing the surface area of the Au/liquid interfaces. Fortunately, an entire class of materials, known as porous materials, has an extraordinarily high surface area to volume ratio. When implemented in a device, this property of porous materials would allow the planar surface area of the electrodes to remain the same while drastically increasing the total area of the Au/liquid interfaces. The following chapter discusses a method by which this is accomplished through the use of nanoporous gold.

Chapter 3: Increased Device Sensitivity From Nanoporous Gold

This chapter gives an overview of nanoporous gold (NPAu), including fabrication methods and applications. Implementation of NPAu to increase device sensitivity to the ITIES is discussed. Characterization of the NPAu/water and NPAu/DCE interfaces are conducted using an optimization method in MATLAB to model the data obtained from impedance spectroscopy. The impact of several NPAu manufacturing parameters on NPAu pore structure and impedance behavior of the NPAu/water and NPAu/DCE interfaces, including electrode thickness, initial alloy gold concentration, and etch time are studied.

Section 3.1: Introduction to NPAu

NPAu refers to a three dimensional gold structure of nano- to micro-scale pores and ligaments. It is formed through a process of selective dissolution of a metal constituent of a gold alloy which is typically accomplished through placing the alloy into an acidic solution. Erlebacher *et al*. proposed a continuum model that clearly demonstrates and describes the fundamental physics involved in the development of porosity throughout the dealloying process [58,59]. Their simulation showed that as the silver is dissolved, gold adatoms are left behind on the surface. These adatoms diffuse on the surface, joining together into clusters. As the gold adatoms diffuse, they expose more unalloyed material to the etching solution and the dissolution front penetrates further into the bulk material. This releases more gold adatoms onto the surface which then diffuse to the clusters formed previously. As the process

continues, the gold clusters get undercut, leading to the eventual development of an interconnected pore structure throughout the material.

Typical fabrication of NPAu begins with a gold alloy. Several different binary gold alloys have been used to fabricate NPAu, including Au-Zn, Au-Ni, Au-Al, and Au-Ag [60-65]. The Au-Ag alloy has been extremely popular due to the abundance of highly selective etching techniques available for silver. A review by Seker *et. al.* discusses various fabrication and characterization methods used with NPAu [66]. The rest of this section will focus specifically on the Au-Ag alloy.

Electroplating, sputtering, and vapor deposition have all been used to create the base Au-Ag alloy used in NPAu [67-69]. The use of sputtering gives a large amount of control over the end properties of the deposited film due to the wide array of control variables available to the user; however, it is impractical to deposit thick films using this technique due low deposition rates. Further, costs can be quite large due to materials being wasted throughout the process. Like sputtering, evaporation allows for precise control over film thickness and composition but suffers from high costs due to wasted material and slow deposition speeds. Electroplating allows for the creation of thicker thin films but has difficulty in creating consistent films between different batches. These three techniques have the added advantage that they can benefit from conventional microfabrication techniques.

The use of white gold leafs as an inexpensive source of the Au-Ag alloy has also received attention [70-73]. These sheets of Au-Ag alloy are typically in the range of 100-200 nm thick and the composition of the gold leaf is denoted by its karat. For example, 12 karat white gold leaf is composed of 50% gold and 50% silver by weight. Although the use of white gold leaf allows for the cheap construction of thin NPAu electrodes, it suffers from incompatibility with current microfabrication techniques. Further, the composition is restricted to the karats produced by manufacturers. Although thicker samples can be formed by stacking multiple leafs together and heat treating under pressure, the process can be time-consuming.

Formation of the porous gold structure from the Au-Ag alloy is performed through a process of selective etching of silver in an acid solution. Two common methods of silver etching include exposing the Au-Ag alloy to nitric acid and the application of an anodic potential during dissolution in perchloric acid. The latter gives more control over the resulting porosity due to the larger number of control variables available. For example, modifying the applied potential during etching can either increase or decrease the silver dissolution rate as compared to the gold diffusion rate. Nitric acid, however, has the advantage of not requiring the setup of circuitry for the dissolution process and is useful in cases where application of a potential is not ideal [66].

Methods by which the pore size can be controlled via dissolution in nitric acid do exist, increasing this method's viability for use in NPAu fabrication. Chen, *et. al.* found that for their $Au_{0.35}Ag_{0.65}$ alloy the resulting average pore size increased from 18 nm after 15 min of dealloying in 70% concentrated nitric acid to 50 nm after 8 hours [74]. Others have also seen that increasing the etch time increases the porosity of the NPAu [70,75]. Increasing the dealloying temperature has also been shown to increase pore size [76]. Increasing the nitric acid concentration increases the dissolution rate of silver in relation to the gold surface diffusion rate, resulting in finer porosity [77].

The diffusion of gold during dealloying is the primary cause for the coarsening of the pore structure described in the methods above. As silver is removed, a fine pore structure starts to form in the alloy; however, a very fine porosity is not energetically favorable for the remaining gold. As a result, the gold in contact with the acid solution diffuses in such a way as to coarsen the pore structure in order to reach a more energetically favorable state. Fortunately, the coarsening can be quenched by removing from acid and rinsing in deionized water. Once removed from the acid, the coarsening of the pore structure stops and the structure remains stable in air for several months [70]. Coarsening of the pore structure can be undesirable in many applications due to the resulting decrease in the surface area to volume ratio. As a result, it is often desirable to increase the silver dissolution rate compared to the gold

diffusion rate, which allows for a finer porosity to be achieved. It is this high surface area to volume ratio that makes porous structures popular in a wide array of fields. In particular, high surface area NPAu electrodes are desirable for electrochemical sensing applications due to the increased sensitivity they can provide.

The initial composition of the Au-Ag alloy also plays a large role in porosity formation. Lu *et al.* created a sample through simultaneous magnetron sputtering of gold and silver in such a way that a concentration gradient of gold to silver varied across the diameter of the sample [68]. After dealloying in 32.5% nitric acid for 10 hours they found that the resulting porosity of the NPAu could be broken into three regions. Region 1 consists of alloys with an initial gold composition between 37-45 atomic %. In this region, the dealloying of the silver is incomplete, with lines of nanopores separated by large regions of unalloyed film. Region 2 consists of alloys with an initial gold concentration between 26-36 atomic %. This region contains mostly alloyed films, with extensive regions of porosity and small islands of unalloyed film. Alloys with initial gold composition between 22-26% make up region three. In this region, the film is fully dealloyed but cracks ranging between 200-1200 nm have developed throughout the film [68].

The reduction of film thickness due to volume contraction (shown to be up to 30% [78]) as well as the coarsening of the pore structure during the dealloying of the Au-Ag system gives rise to increased stress within the NPAu structure, leading to crack formations [77]. Further, in contrast to the ductile nature of bulk gold, NPAu is quite brittle on the macroscale despite maintaining its ductile nature on the microscale [79]. As a result, cracking is common within NPAu films and can be a major concern in the fabrication process. This is particularly true for sensing applications, where interconnectivity of the pore network is paramount. In order to reduce the impact of cracking on the NPAu system, a heat treatment can be performed on the alloy prior to dealloying. Seker *et al.* showed that annealing at 300 degrees C significantly reduced the presence of cracking in the resulting NPAu structure as compared to an

untreated sample for each of the three compositions studied [80]. Initial alloy composition also plays a significant role in the cracking behavior of NPAu structures, with alloys containing greater amounts of silver exhibiting significantly more cracking [68,81]. If cracking throughout the sample is unavoidable or not particularly problematic, deposition of the Au-Ag alloy onto a pre-deposited gold thin film substrate ensures connectivity by having nanoporous regions disconnected by cracks stick to the same conductive gold base.

NPAu electrodes have found use in various electrochemical sensing applications, becoming a popular replacement to standard planar electrodes due to their high surface area to volume ratio. This allows for sensors of much higher sensitivity than sensors of the same size that utilize planar electrodes. The ability to precisely control the pore structure of NPAu has made it desirable for use in drug delivery, where controlling the pore size can limit the rate at which medicine is introduced into the body over time [82,83]. It has also found use in increasing sensitivity of measurement instruments. Hieda *et al.* increased the sensitivity of a quartz crystal microbalance by a factor of 40 with no loss to the quality factor or resonant frequency stability by replacing the planar gold electrodes with NPAu [84].

Section 3.2: NPAu/Liquid Interface Device Setup and Analysis Methods

Section 3.2.1: Materials and Methods

NPAu electrodes were fabricated using a 1”x3” microscope slide substrate cleaned with an acetone and methanol rinse followed by a DI water rinse and nitrogen dried. A 2.5 nm titanium adhesion layer followed by 25 nm gold were deposited via e-beam vapor deposition. The slide was then cut into

pieces which were once again cleaned utilizing the method described above. A single sheet (~120 nm thick) of transfer type white gold leaf was cut to size and placed face down onto the pre-deposited gold. A bare microscope slide was placed on top of the paper backing of the gold leaf and the entire setup was placed between two C-clamps used to apply pressure. This was then baked in an oven at 130 degrees C for 90 minutes to ensure that the gold leaf would stick to the deposited gold. The electrodes were allowed to cool to room temperature before removing pressure and the backing from the gold leaf. They were then placed in a nitric acid solution (70% HNO_3, 30% DI water) to etch away the silver. The samples were then placed in a beaker filled with DI water and placed under a faucet of running DI water and allowed to sit for five minutes before removing and drying with a nitrogen gun. The end result is an electrode with a nanoporous gold structure sitting atop a flat gold substrate.

A glass tube cut and sanded to approximately 15 mm in length was cleaned before adhering one end to the NPAu electrode that would form the bottom of the device with a solvent resistant sealant. After allowing the sealant to set, the top NPAu electrode was placed, leaving a small opening to allow air to escape during loading and the device was placed in a C-clamp to hold the system securely in place. A coat of sealant was applied to the edge between the outer tube and NPAu electrode to ensure no fluid would leak out. A lead was attached to each electrode with copper tape, with the other ends hooked into an HP 4192A LF Impedance Analyzer. Either a 1M water-Na_2SO_4 or 1M DCE-TBA solution was loaded into the tube via syringe. This is an apparatus that is identical to the one used to characterize the flat Au/water and Au/DCE interfaces as described in Section 2.2. Impedance spectroscopy with V_{osc}=50 mV and V_{bias}=0 V was performed using a LabVIEW program set to run a logarithmic frequency sweep over a frequency range of 10 Hz-100 kHz with 20 points per decade. The measurement mode was set to record the system's resistance and reactance.

Section 3.2.2: Data Analysis

An added difficulty associated with the introduction of NPAu into a device is that it is no longer feasible to determine the Au/liquid interfacial area using optical techniques. Instead, chemical techniques such as obtaining a nitrogen adsorption isotherm for the electrode and applying BET theory to back out the specific surface area must be employed; however, these techniques run the risk of potentially altering the electrode surface which may impact the behavior of the NPAu/liquid EDL. Fortunately, knowing the exact surface area of the NPAu/liquid interface is not critical, as the ultimate purpose of introducing NPAu electrodes is to drastically decrease the impedance of the Au/liquid interfaces compared to the water/DCE ITIES. Useful information can still be gained from knowledge of the area of the interface, however. Introduction of a pore structure may cause transient responses within a given test over a period of time as the liquid penetrates into the pore structure. By looking at the transient response of this interface, information about how long the device must sit until the NPAu/liquid interfaces behave in a steady or quasi-steady manner can be determined. Fortunately, an exact determination of interfacial area is not required to accomplish this. An estimate can be used just as effectively.

To this end, the NPAu/liquid interface is assumed to behave like a single CPE. While the interface is likely more complicated than this as seen for the 'flat' Au/liquid interfaces in Chapter 2, the model provided a relatively good fit for the impedance magnitude of the 'flat' electrode systems. Further, the area of the interface can readily be implemented as a variable into the optimization by multiplying the denominator of the CPE impedance by a creative one: A_{eq}/A_{eq}:

$$Z_{fit} = \frac{1}{\left(\frac{Q^o{}_{eq}}{A_{eq}}\right) A_{eq}(j\omega)^{\alpha}} + R_{sol} \qquad (3.1).$$

Here, $Q^o{}_{eq}/A_{eq}$ is the equivalent pseudo-capacitance per unit area of the two NPAu/liquid interfaces in series, $A_{eq} = A_1A_2/(A_1+A_2)$ is the equivalent area of the two nanoporous electrodes in the test, j is the

imaginary number, ω is the angular frequency, α is the CPE exponent, and R_{sol} is the solution resistance. Because Q^o for a CPE is expected to increase linearly in A, Q^o/A can be treated as a constant in the optimization, enabling A_{eq} to be treated as a variable.

In order to use this method, a reasonable value for Q^o/A must be selected. Fortunately, the value of Q^o/A is not expected to be too different between the NPAu/liquid and 'flat' Au/liquid interfaces. As a result, the values obtained from the tests conducted in Chapter 2 can be used to effectively approximate Q^o/A for the NPAu/liquid interfaces. The values obtained from the pure CPE model in Table 2.3 were chosen as the approximation for the NPAu/liquid interfaces due to the strong linear behavior exhibited by the plot of Q^o vs. A. Although values of Q^o for the other equivalent circuit models could have been used, the larger variation seen between tests makes it more difficult to obtain a reliable value of Q^o/A. Once again, the actual equivalent circuit model of these interfaces is likely more complicated than a lone CPE; however, the model being discussed here is not meant to fully characterize the NPAu/liquid interfaces, but rather allow for the approximation of the interfacial area to estimate how long the device must sit until the Au/liquid impedances can be treated as quasi-steady.

With a specified value of Q^o/A, Equation 3.1 is a function of three variables: A_{eq}, R_{sol}, and α. The MATLAB optimization technique describe in Chapter 2 was used to simultaneously solve for these three variables by minimizing the following optimization function over the considered frequency range:

$$function = \sum_f \left| Z_{data} - Z_{fit} \right| = \sum_f \left| Z_{data} - \frac{1}{\left(\frac{Q^o}{A}\right) A_{eq} (j\omega)^{\alpha}} - R_{sol} \right| \quad (3.2).$$

The sum is performed over the specified frequency range f and Z_{data} denotes the raw impedance data collected from the experiment.

Several starting points for all three variables were chosen to check if the model would converge to the same solution regardless of what starting values were used. Since a good estimation of the end values for R_{sol} and α were known from study of the raw data, special attention was payed to A_{eq} during this process. In all cases, the model obtained reasonable values for R_{sol}, A_{eq}, and α that were within

numerical error of one another. This is shown for two particular tests in Table 3.1: one with only water and another with only DCE with electrodes formed from three stacked sheets of 12 karat gold leaf etched for 30 minutes in 70% DI water. Table 3.2 shows the upper bounds, lower bounds, and starting points used for each variable in all of the future NPAu/water and NPAu/DCE tests. The full MATLAB script used is given in Appendix B2.

Table 3.1: Covergence Test of MATLAB Model For Several Different Starting Points

Water Only					
Lower Bounds			**Upper Bounds**		
α	A_{eq} (m^2)	R_{sol} (Ω)	α	A_{eq} (m^2)	R_{sol} (Ω)
0	0	0	1	1.00E-03	200
Starting values			**Model Output**		
α	A_{eq} (m^2)	R_{sol} (Ω)	α	A_{eq} (m^2)	R_{sol} (Ω)
0.8	1.00E-04	40	0.8939	1.145E-04	38.69
0.5	1.00E-05	10	0.8940	1.144E-04	38.70
0.9	5.00E-04	25	0.8940	1.144E-04	38.70
0.05	9.00E-04	190	0.8939	1.145E-04	38.69
0.6	1.00E-07	100	0.8941	1.144E-04	38.77
DCE Only					
Lower Bounds			**Upper Bounds**		
α	A_{eq} (m^2)	R_{sol} (Ω)	α	A_{eq} (m^2)	R_{sol} (Ω)
0	0	0	1	1.00E-03	1000
Starting values			**Model Output**		
α	A_{eq} (m^2)	R_{sol} (Ω)	α	A_{eq} (m^2)	R_{sol} (Ω)
0.6	1.00E-04	600	0.8931	2.186E-04	491.90
0.9	1.00E-06	50	0.8926	2.192E-04	491.39
0.2	5.00E-04	850	0.8932	2.185E-04	491.90
0.05	1.00E-05	200	0.8932	2.185E-04	491.90
0.45	5.00E-07	0	0.8932	2.186E-04	491.89

Table 3.2: Model Bounds and Starting Points Used for the Various NPAu Tests

Water Only					
Lower Bounds			**Upper Bounds**		
α	A_{eq} (m^2)	R_{sol} (Ω)	α	A_{eq} (m^2)	R_{sol} (Ω)
0	0	0	1	1.00E-03	200
DCE Only					
Lower Bounds			**Upper Bounds**		
α	A_{eq} (m^2)	R_{sol} (Ω)	α	A_{eq} (m^2)	R_{sol} (Ω)
0	0	0	1	1.00E-03	1000
Water Only Starting Points			**DCE Only Starting Points**		
α	A_{eq} (m^2)	R_{sol} (Ω)	α	A_{eq} (m^2)	R_{sol} (Ω)
0.8	1.00E-04	40	0.6	1.00E-04	600

Section 3.3: Impact of Manufacturing Parameters on NPAu/Liquid Interfacial Impedance Behavior

As described in Section 3.1, a wide array of variables within the manufacturing process can have a significant impact on the structure and pore morphology of the NPAu electrodes; however, little is known about how these variances within the manufacturing process affect the capacitive and impedance behavior of the NPAu/water and NPAu/DCE interfaces. In this section, the impact of electrode thickness, etch time, and initial gold concentration on the impedance behavior of systems consisting of only 1M water-Na_2SO_4 solution and only 1M DCE-TBA solution are studied and discussed. The transient behavior of the impedance spectrum is also discussed.

Section 3.3.1: Initial Gold Concentration

White gold leafs with initial gold concentrations of 12 karat (50 at. % Au), 9 karat (37.5 at. % Au), and 6 karat (25 at. % Au) were used to study the effect of initial gold concentration on the impedance

behavior of the NPAu/water and NPAu/DCE interfaces. Both the 12 karat and 6 karat gold leafs were transfer type while the 9 karat was loose-leaf. Electrodes were manufactured by first depositing a 2.5 nm Ti adhesion layer onto a glass substrate followed by 25 nm Au via e-beam vapor deposition. The "flat" gold substrates were cut to size and washed in acetone followed by methanol and then rinsed in DI water and nitrogen dried. In order to stack multiple sheets of the 12 and 6 karat leafs, two swatches of the gold leaf were cut to size and then placed face-to-face. The sheets were then placed between two microscope slides, compressed between two C-clamps, and baked for 90 minutes at 130 °C. The samples were then allowed to cool to room temperature before releasing the pressure and removing the backing from one of the sheets. This process was repeated until the desired number of sheets had been stacked. One final round of this procedure was conducted to adhere the stacked sheets to the substrate.

Due to the 9 karat leafs being loose-leaf, a different stacking method had to be implemented. To do this, the pre-deposited gold substrate was placed face-down directly onto the 9 karat leaf. It was then pressed down for roughly 20 seconds to get the leaf to stick to the surface. A razor was used to cut through the leaf surrounding the substrate, allowing for the sample and the newly adhered sheet of gold leaf to be lifted away, leaving the rest of the leaf intact. This process was repeated until the desired number of sheets had been stacked before being baked using the above described method.

The samples were then etched in a 70% nitric acid, 30% DI water solution to remove the silver from the leaf, leaving behind a porous gold structure. While the 6 and 12 karat samples were etched for 30 minutes, the 9 karat samples were only etched for 15 minutes. This was because after 15 minutes of etching, the color of the 9 karat electrodes had stopped changing. As etching progresses, the sample gets darker in color, indicating the continuing removal of silver from the system. Once all of the silver has been removed, the color stops changing. Unfortunately, the color change could not be easily seen for the 6 karat samples due to the lack of interconnectivity of the gold leaf seen in the samples which

made it difficult to determine exactly when the color stopped changing. As a result, they were etched for the full 30 minutes.

a) 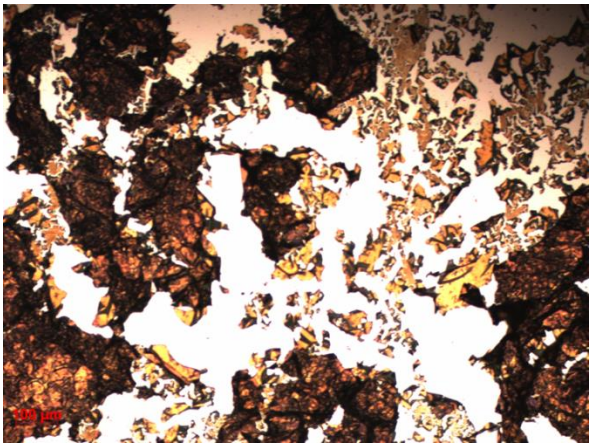 b) 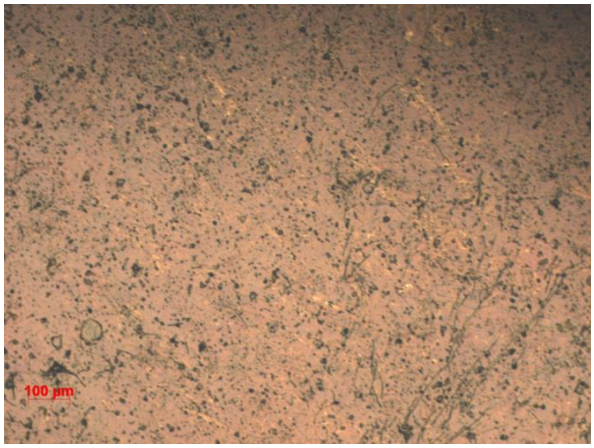

c) 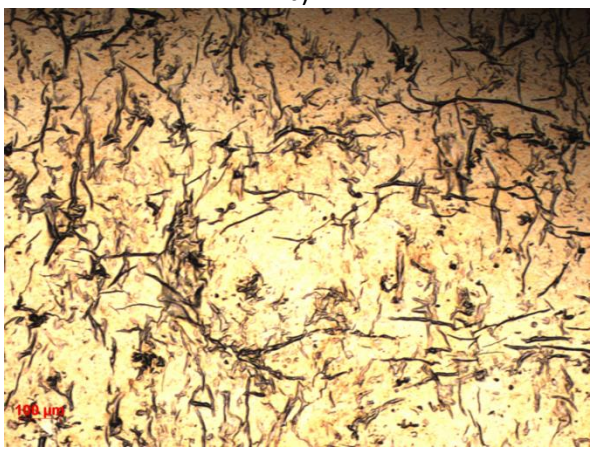

Figure 3.1: Optical microscope images of electrodes formed from three stacked sheets of **(a)** 6 karat, **(b)** 9 karat, and **(c)** 12 karat etched in 70% nitric acid for 30 minutes in the case of (a) and (c) and 15 minutes in the case of (b).

Figure 3.1 shows optical images of the three sheet 6, 9, and 12 karat electrodes after etching. The 6 karat electrode shows several islands of darker regions surrounded by lighter regions. These white-appearing regions are areas where the gold substrate has been exposed during the etching process. Around the edges of the dark islands are regions of lighter-colored smaller islands. These are regions where a single sheet of the gold leaf remains, the rest having been either diffused or etched away. The dark islands are regions where multiple sheets have survived the etching process. Careful inspection shows that cracking is present throughout each of these islands. The discontinuity between

the porous regions of this sample is due to the low initial gold concentration of the sample. As the initial gold concentration is increased, the structure is better able to hold itself together throughout the etching process as can be seen from the 9 karat sample in Figure 3.1b. The 9 karat sample exhibits a rough and much more interconnected structure that appears to have plateaus and holes throughout. As the gold concentration is increased further, the effect of dealloying becomes less pronounced, and the 12 karat sample doesn't seem too different from the gold leaf pre-etching except for a slight change in color and a large number of cracks present across the surface.

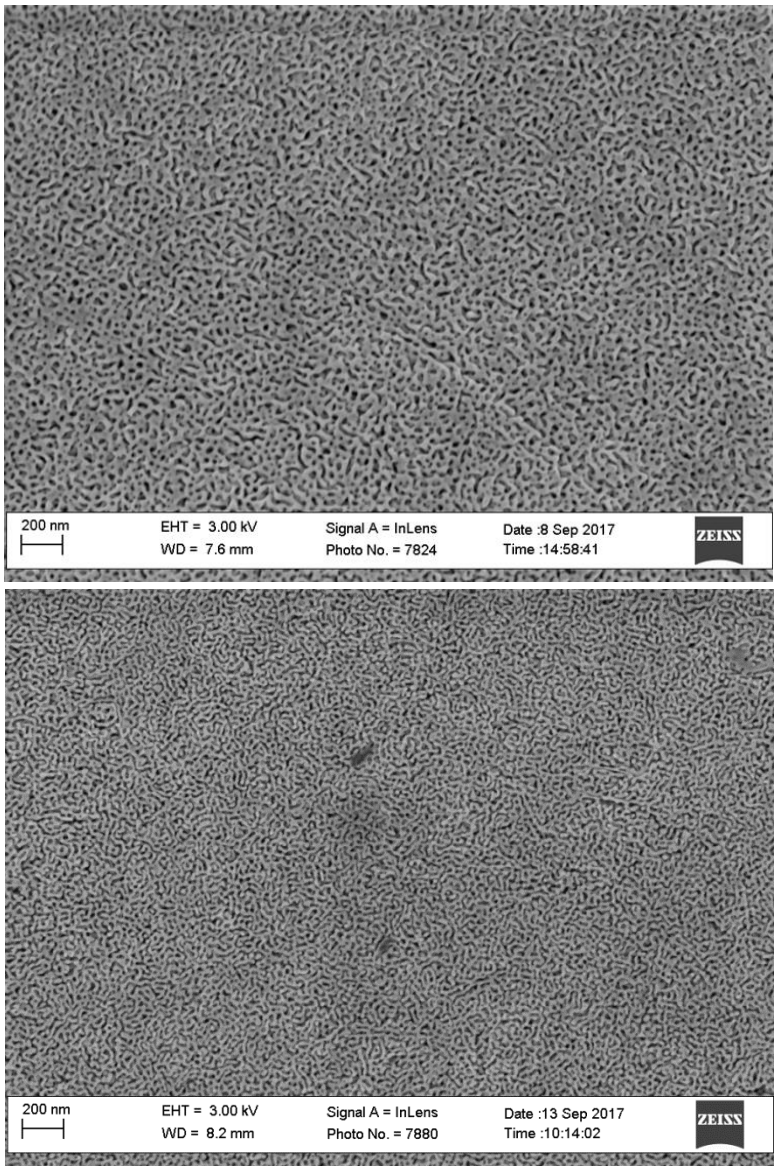

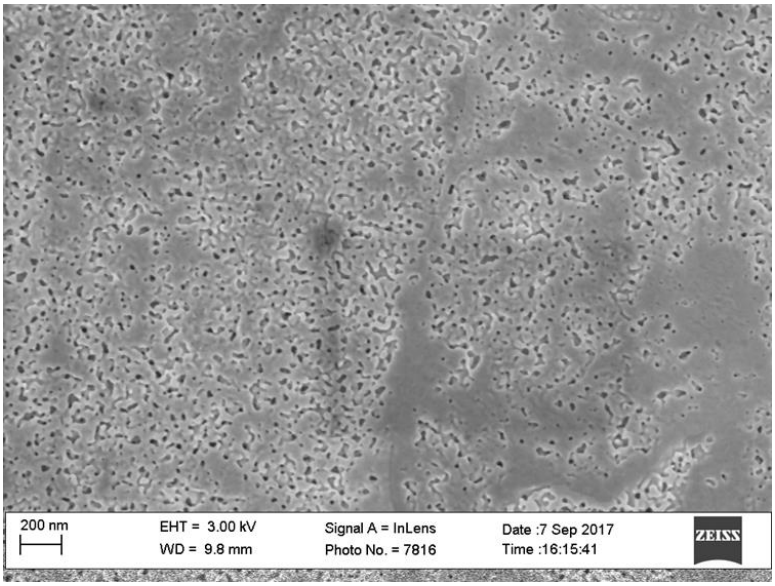

c)

Figure 3.2: SEM images of the Nanoporous pore structure of **(a)** 6 karat, **(b)** 9 karat, and **(c)** 12 karat gold leaf.

In order to see the nanoporous structure, Scanning Electron Microscopy (SEM) images of the three samples were taken and can be seen in Figure 3.2. To obtain the image of the 6 karat nanoporous structure shown in Figure 3.2a, the SEM was focused onto a region where multiple stacked sheets remained. Within this region is a fully porous nanostructure. Within the 12 karat sample, the porous structure is no longer seen throughout. Instead, the sample is filled with regions of unalloyed material with little to no pore density. Further, in regions where some porosity has formed, many of the pores are discrete, forming pinholes, and, as such, lack the interconnectivity of the porous regions seen in the 6 karat and 9 karat samples. Despite the porous structure observed for the 6 karat sample, it is removed from future analysis due to the lack of connectivity present at the optical level. These findings are in good agreement with [68]. Note that while the pore sizes seen for the 6 karat and 9 karat samples are noticeably different, they cannot be effectively compared here due to the difference in etch time between the two samples.

Impedance spectroscopy was performed on devices constructed from the three sheet 9 and 12 karat electrodes over a frequency range of 10 Hz to 100 kHz with V_{bias}=0 V and V_{osc}=50 mV. Tests were

run at several different times to look at any transient behavior that might be present. It is important to note that time was kept in a way that did not include the time that passed while a test was running (~1 minute 40 seconds per test) and was started when the device was first loaded. The devices were filled with either the 1M water solution or the 1M DCE solution. Figure 3.3 shows the raw impedance data collected for both water only and DCE only tests for devices utilizing the 9 karat and 12 karat electrodes at t=50 min. At low frequencies, the 9 karat electrode appears to perform better than the 12 karat, having roughly half the impedance at f=10 Hz for the water only. Although this is not as prominent in the DCE tests, the impedance of the nine karat device is still less than what is observed for the 12 karat device in the low frequency range. As expected, both the 9 karat and 12 karat impedances converge to roughly the same value as f increases and the impedance contributions of the NPAu/liquid interfaces go to zero. Unfortunately, as indicated by the sloped region between 10 and 100 Hz in Figure 3.3, the impedances for all four devices dominate the total system impedance within this frequency range. Ideally these impedances should be reduced further to maximize sensitivity to the water/DCE interface.

a)

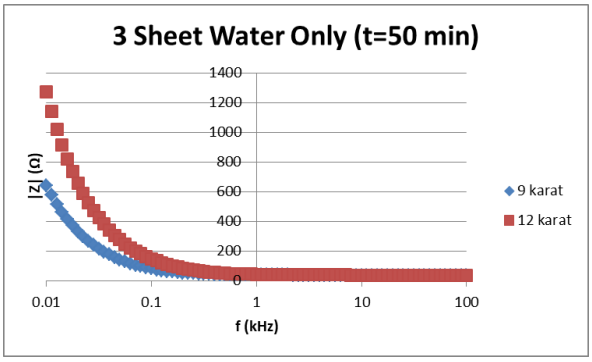

b)

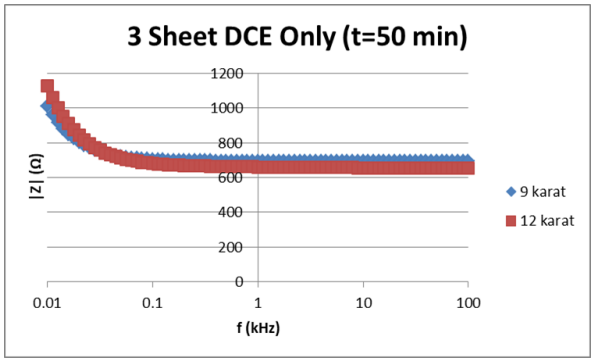

Figure 3.3: Raw impedance data obtained for three sheet thick 9 karat (15 min etch) and 12 karat (30 min etch) electrodes for **(a)** water only and **(b)** DCE only tests. Data was collected 50 minutes after loading.

In addition to studying the effects of initial gold concentration on the impedance and capacitive behaviors of the NPAu/liquid interfaces, these tests were also taken as an opportunity to compare two different methods of interface characterization for the pure CPE model. First of these is the MATLAB optimization model. Second was the direct calculation of α and R_{sol} from the raw impedance data. For

this method, R_{sol} was taken to be the raw data resistance at f=10 kHz and α was determined by subtracting out R_{sol} from Z_{data} and obtaining the exponent of a power fit of the plot of $|Z_{data}-R_{sol}|$ vs. f. The results are shown in Table 3.3. All four tests show good agreement between α and R_{sol} obtained from the MATLAB model and CPE analysis for each test, indicating that the optimization is behaving as intended.

Table 3.3: Effect of Initial Gold Concentration on the Capactive Behavior of the NPAu/liquid Interface

9 karat							12 karat						
3 sheet 15min etch water only:							**3 sheet 30 min etch water only:**						
MATLAB Model					**Raw Data Calculations**		**MATLAB Model**					**Raw Data Calculations**	
t (min)	α	A_{eq} (m^2)	R_{sol} (Ω)	$\Sigma_f\|Z_{data}-Z_{fit}\|$ (Ω)	α	Rsol (Ω)	t (min)	α	A_{eq} (m^2)	R_{sol} (Ω)	$\Sigma_f\|Z_{data}-Z_{fit}\|$ (Ω)	α	R_{sol} (Ω)
0	0.937	2.73E-04	39.2	112.462	0.948	39.31	0	0.955	1.58E-04	39.6	195.4	0.974	39.77
5	0.949	2.93E-04	39.2	92.5769	0.951	39.26	5	0.947	1.57E-04	40.1	72.1141	0.947	40.28
10	0.953	3.00E-04	39.1	45.1591	0.954	39.21	10	0.951	1.49E-04	40.2	68.5752	0.953	40.42
25	0.957	3.06E-04	39.2	33.4391	0.958	39.27	20	0.953	1.49E-04	40.4	63.815	0.955	40.5
30	0.958	3.08E-04	39.3	31.8386	0.958	39.36	30	0.950	1.57E-04	40.4	126.303	0.953	40.4
40	0.959	3.07E-04	39.4	30.7045	0.958	39.39	40	0.943	1.66E-04	40.1	116.299	0.944	40.08
50	0.959	3.05E-04	39.5	31.0456	0.959	39.46	50	0.954	1.57E-04	40.1	54.2236	0.956	39.98
60	0.959	3.03E-04	39.5	32.7538	0.959	39.45	60						
70	0.958	3.01E-04	39.5	33.2099	0.958	39.52	70						
3 sheet 15min etch DCE only:							**3 sheet 30 min etch DCE Only**						
MATLAB Model					**Raw Data Calculations**		**MATLAB Model**					**Raw Data Calculations**	
t (min)	α	A_{eq} (m^2)	R_{sol} (Ω)	$\Sigma_f\|Z_{data}-Z_{fit}\|$ (Ω)	α	Rsol (Ω)	t (min)	α	A_{eq} (m^2)	R_{sol} (Ω)	$\Sigma_f\|Z_{data}-Z_{fit}\|$ (Ω)	α	R_{sol} (Ω)
0	0.943	3.84E-04	685.0	113.585	0.949	685.5	0	0.877	4.48E-04	624.0	99.6671	0.876	623.4
5	0.950	3.71E-04	692.4	50.288	0.953	692.6	5	0.892	4.10E-04	633.3	163.203	0.890	631.9
10	0.950	3.59E-04	695.7	41.2541	0.953	695.8	10	0.898	3.85E-04	638.8	167.997	0.897	637.4
20	0.950	3.45E-04	697.1	45.577	0.953	697.3	20	0.905	3.51E-04	646.3	167.062	0.904	644.8
30	0.951	3.36E-04	696.2	49.6163	0.955	696.3	30	0.909	3.30E-04	652.2	166.01	0.910	650.5
40	0.951	3.30E-04	696.3	44.0786	0.955	696.4	40	0.913	3.16E-04	656.6	168.286	0.914	654.7
50	0.951	3.29E-04	696.0	46.1686	0.954	696.1	50	0.913	3.12E-04	658.8	182.231	0.918	656.9
60	0.951	3.26E-04	695.2	47.9531	0.955	695.3	60	0.916	3.07E-04	660.9	171.665	0.917	659
70	0.952	3.22E-04	694.8	48.8231	0.955	694.9	70	0.917	3.03E-04	662.7	174.443	0.917	660.8

Perhaps the most surprising aspect of Table 3.3 is $\Sigma_f|Z_{data}-Z_{fit}|$. While the fit is noticeably worse for the 12 karat tests, the pure CPE model does a remarkably good job of fitting the 9 karat data. This can be more clearly seen in the Nyquist plots in Figure 3.4, which shows the impedance data plotted from 10 Hz-100 kHz for each of the four devices in Table 3.3 at t=40 min. In these plots, the pure CPE fit is able to capture the impedance behavior of the system over the entire frequency range considered. Despite having implemented the pure CPE model as a means of only approximating the interfacial behavior in order to study its transient response, the pure CPE equivalent circuit effectively models the NPAu/water and NPAu/DCE interfaces. While this does not necessarily indicate that transfer and adsorption effects do not occur at the NPAu/water and NPAu/DCE interfaces, it does mean that the

anomalous effects that cause CPE behavior completely dominate the behavior of these interfaces. As a result, a lone CPE in series with a solution resistance is capable of effectively describing the system's behavior and this model will be used throughout the rest of the chapter.

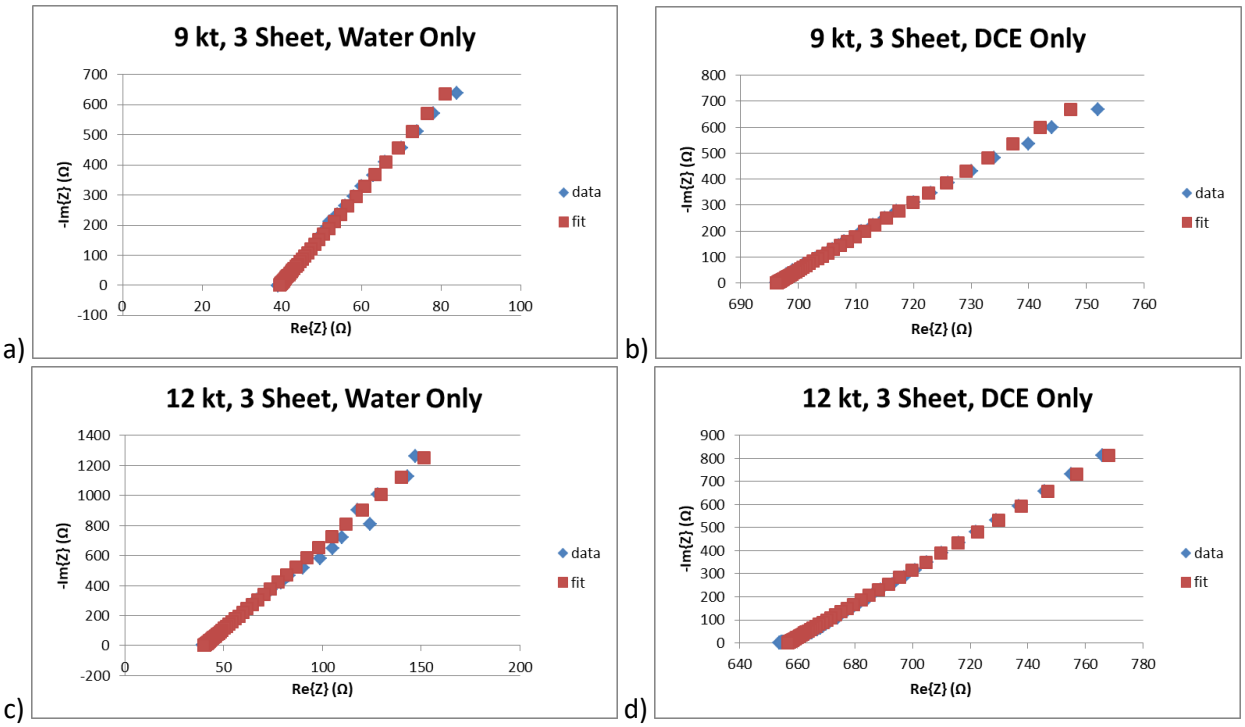

Figure 3.4: Nyquist plots of the raw data and fit obtained by a CPE in series with a solution resistance for 3 sheet thick nanoporous electrodes with initial gold concentration of **(a)** 9 kt with 1M water solution, **(b)** 9 kt with 1M DCE solution, **(c)** 12 kt with 1M water solution, and **(d)** 12 kt with 1M DCE solution.

Another interesting observation is the apparent transient behavior of $\Sigma_f|Z_{data}-Z_{fit}|$ seen most clearly in both of the 9 karat tests. As time since the device loading increases, there is a sharp decrease in the optimization function value that eventually levels off around 40 minutes after loading. This behavior likely has to do with the time it takes for the fluids to fully penetrate into the NPAu pore structure. Directly after loading, the fluids have barely entered the pores at all and the interface more closely resembles the electrodes used in the 'flat' Au/liquid tests in Chapter 2, albeit much rougher. As the fluids wick further into the pore structure, the CPE behavior becomes more dominant until the transfer and adsorption effects are completely overshadowed by CPE behavior. Although why the CPE

effects dominate the behavior of the NPAu interfaces is beyond the scope of this project, these results seem to indicate that it has something to do with the pore structure. This would agree with the idea that surface roughness and topography are a cause for CPE behavior as discussed in Chapter 2 and in [46-48]. This would also explain why $\Sigma_f|Z_{data}-Z_{fit}|$ does not appear to depend on time in the 12 karat electrode tests in Table 3.3, where a fully developed pore structure is not observed.

The data in Table 3.3 shows that α is not greatly affected by changing the initial gold concentration. Further, α's obtained from these nanoporous electrode tests are in relatively good agreement with the values obtained for the pure CPE model of the "flat" Au/water (α=0.924) and Au/DCE (α=0.931) interfaces given in Table 2.3. This suggests that the pore structure of the electrode has little impact on α. The slight differences between α's obtained for the 9 karat tests and the 12 karat tests are likely a result of residual silver present in the unalloyed regions within the 12 karat electrodes. As expected, changing the initial gold concentration does not change the solution resistance in any way. Any differences in R_{sol} between the 9 karat and 12 karat tests can be attributed to slightly different tube lengths caused by inconsistency in sanding the tubes used in the different tests to the same length. As would be expected from the SEM images given in Figure 3.2, A_{eq} for the 9 karat water only test is between 1.5-2 times greater than the 12 karat test; however, this is not the case for the DCE only tests, where A_{eq} for both the 12 karat and 9 karat tests are comparable.

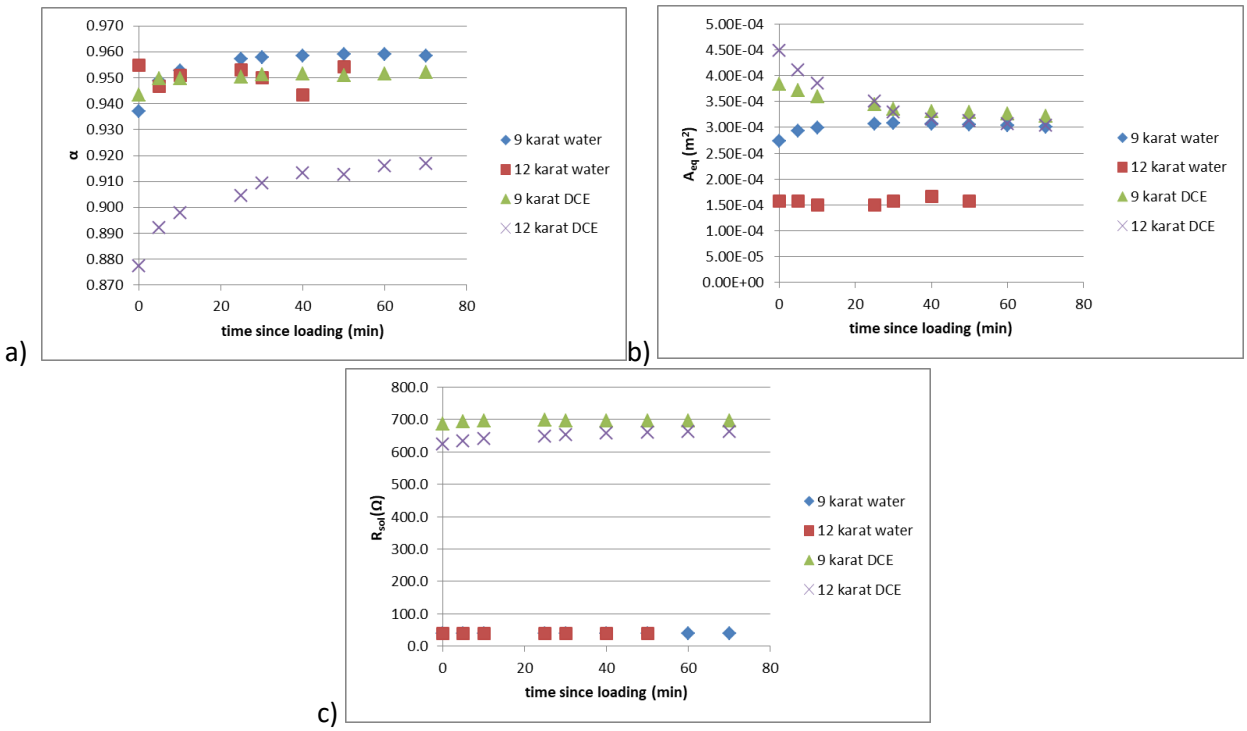

Figure 3.5: Transient response of **(a)** α, **(b)** A_{eq}, and **(c)** R_{sol} for three sheet thick 9 and 12 karat electrodes.

Figure 3.5 graphically depict how α, R_{sol} and A_{eq} obtained with the MATLAB model change with respect to the amount of time that has passed since loading. The plots of both A_{eq} and α both show that there is a brief "start-up" period, where the parameters obtained from the model vary as a result of a change in system impedance between different tests. This can be most clearly seen in Figure 3.6 which shows how the raw system impedance at f=10 Hz changes over time.

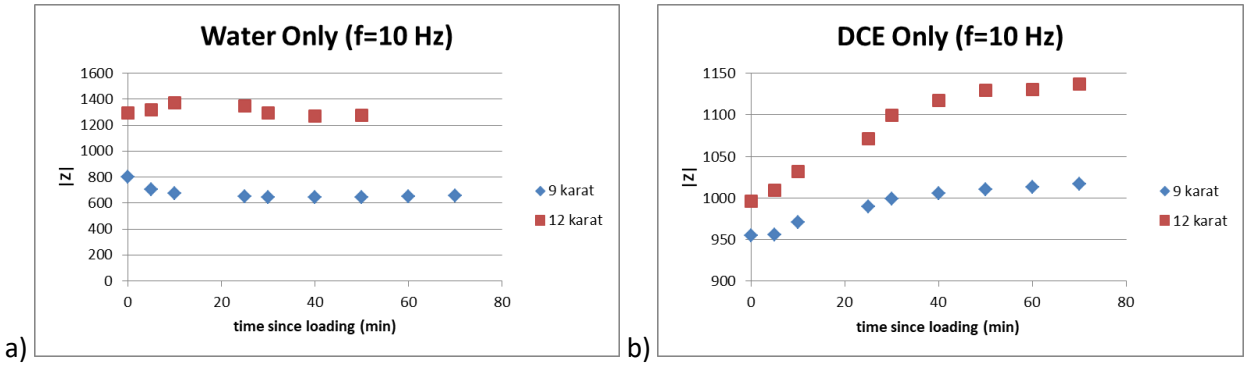

Figure 3.6: Transient behavior of raw impedance data at f=10 Hz for 12 and 9 karat **(a)** water only devices and **(b)** DCE only devices.

Once removed from the nitric acid etching solution and quenched in DI water, the pore structure of the NPAu electrodes, and therefore its area, is not expected to change in time. This is clearly not the case as can be seen in Figure 3.5b. With the exception of the 9 karat water only test, each test shows a slight decrease in A_{eq} as the time since loading increases. While the time it takes for the liquid to fully wick into the pore structure has a noticeable effect, this cannot be the cause of this startup behavior in A_{eq} due to the resulting *increase* in the Au/liquid area this would result in as time passed.

One hypothesis for this decrease is that as time passes and more tests are run, more ions adsorb to the gold surface. This would have the effect of decreasing the effective capacitance of the NPAu/liquid interface by increasing the thickness of the NPAu/liquid double layer. Since Q^o/A is considered constant in the MATLAB optimization, a decrease in capacitance would be interpreted as a decrease in interfacial area. In this hypothesis, despite not having a significant impact on the raw impedance behavior, the effects of adsorption still impact the system. Although this variance in A_{eq} with time is not ideal, it can be worked around. An individual frequency sweep from 10 Hz to 100 kHz takes roughly 130 seconds to run, and, as can be seen in Figure 3.5b, the decrease in A_{eq} begins to slow at around 1 hour after loading for most cases. By waiting to run a test until the change in A_{eq} has become negligible, values of α, R_{sol}, and A_{eq} that can be appropriately approximated as quasi-steady can be obtained.

Section 3.3.2: Electrode Thickness

In order to study how electrode thickness impacts the capacitive and impedance behaviors of the NPAu/water and NPAu/DCE interfaces, multiple 9 karat gold leaf sheets (~120 nm thickness per sheet) were stacked atop one another using the method described in Section 3.3.1. The electrodes were etched for 15 minutes in a 70% nitric acid 30% DI water solution. Impedance spectroscopy was

performed as described in Section 3.2.1. Tests were performed at several different times after loading the device up to t=70 minutes after loading to consider any transient behavior.

a)
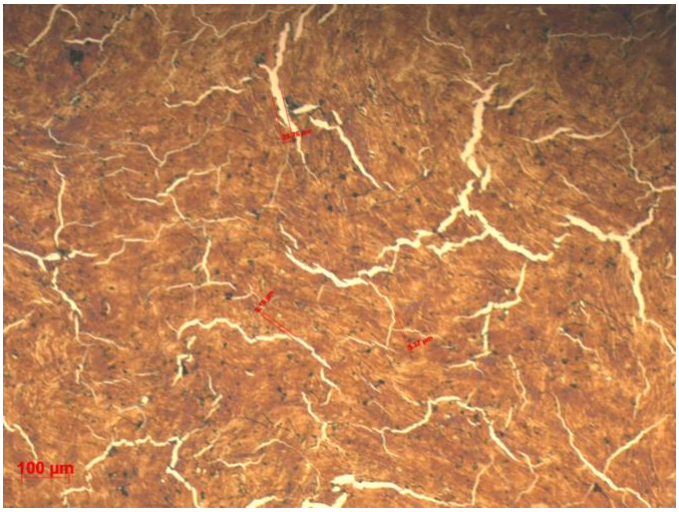

b)
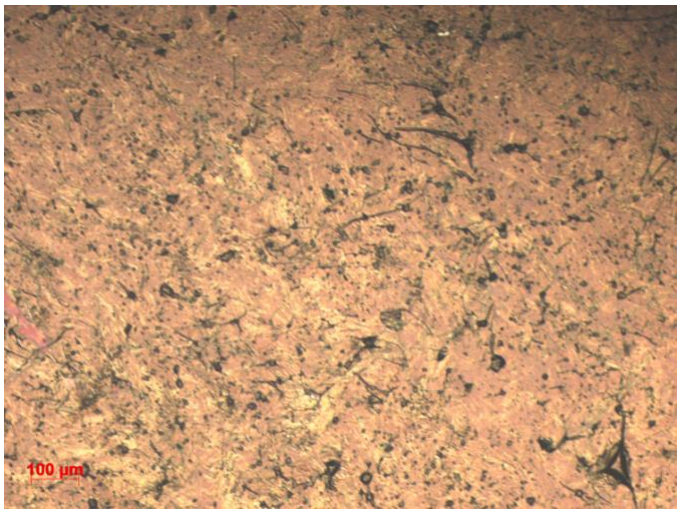

c)
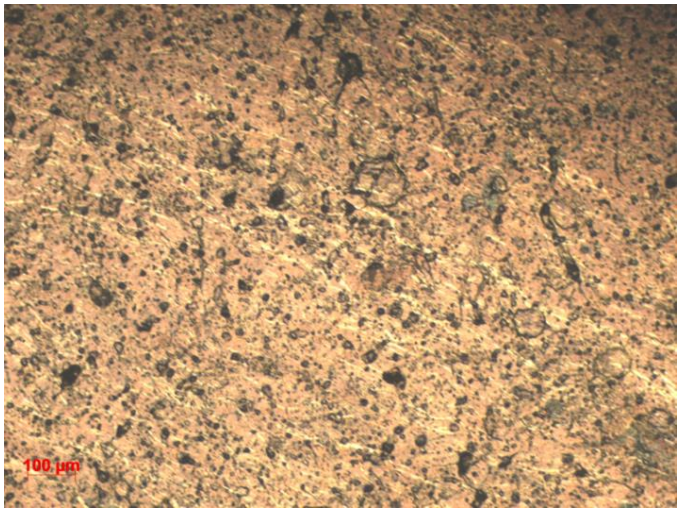

Figure 3.7: Effect of electrode thickness on the evolution of porosity. Electrodes formed from stacking **(a)** single sheet (~120 nm thick), **(b)** three sheets (~360 nm thick), and **(c)** 6 sheets (~720 nm thick) of 9 karat white gold leaf.

Figure 3.7 shows optical microscope images of electrodes formed from 9 karat gold leaf with thicknesses of one sheet, three sheets, and six sheets. As with the 6 karat electrodes shown in Figure 3.1, the single sheet 9 karat electrode has cracks throughout, exposing the bare gold substrate beneath; however, unlike the six karat electrodes, the cracks are smaller and are not dense enough to create a largely disconnected structure of etched leaf. As the thickness is increased, the number of cracks decreases and the sample forms one continuous structure. Hills and valleys are present throughout the surface of the three sheet thick sample in Figure 3.7b, and their numbers increase as the electrode is made even thicker, as evident in the six sheet thick structure in Figure 3.7c. These hills and valleys are formed by the gold diffusion that occurs during the etching process.

a) 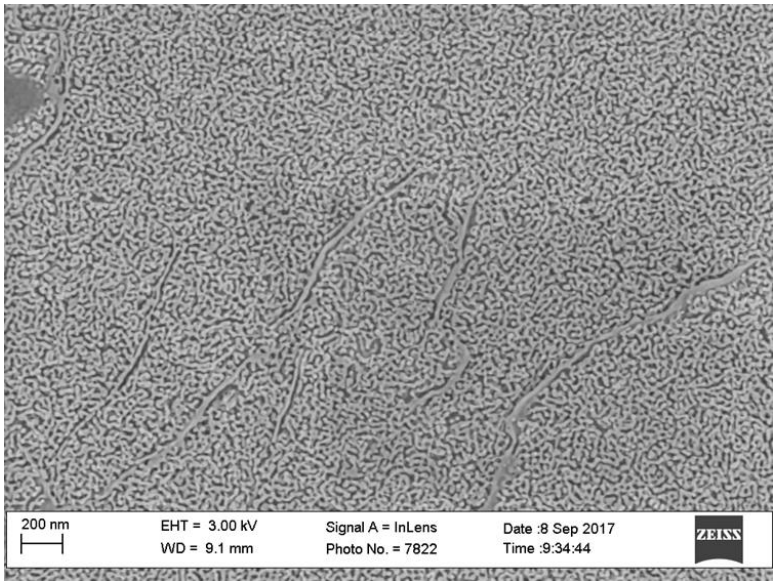

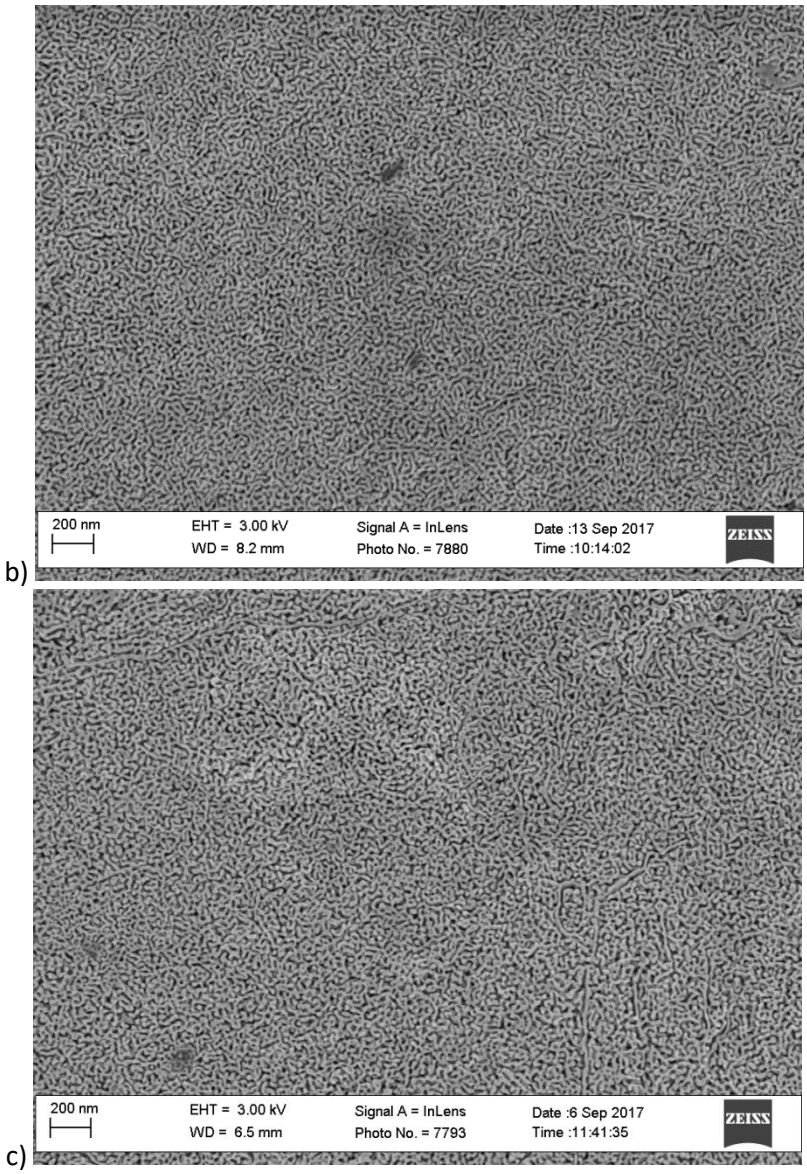

Figure 3.8: SEM images of **(a)** 1 sheet, **(b)** 3 sheet, and **(c)** 6 sheet thick NPAu electrodes formed from 9 karat white gold leaf.

SEM was performed on the three different 9 karat samples to observe the nanoporous structure found in each and the resulting images can be seen in Figure 3.8. As expected, all three samples show an extensive pore structure throughout. Visual examination Figure 3.8 suggests that modifying the sample thickness does not have an impact on the pore structure of the resulting NPAu. This does not, however, mean that increasing the electrode thickness will not have an impact on the impedance and capacitive behaviors of the Au/liquid interfaces. Increasing the thickness of the electrode increases the area of the

pore structure available thereby increasing the area of the NPAu/liquid interfaces. This in turn would result in noticeably lower interfacial impedances for thicker electrodes.

a)

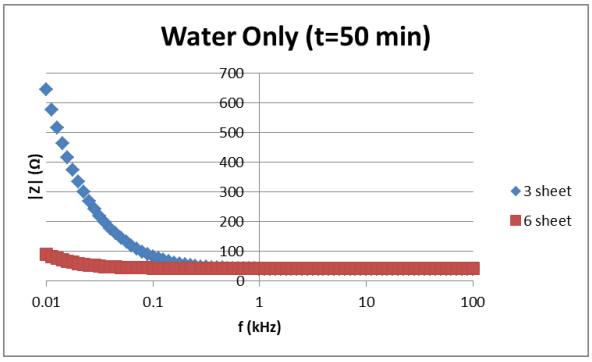

b)

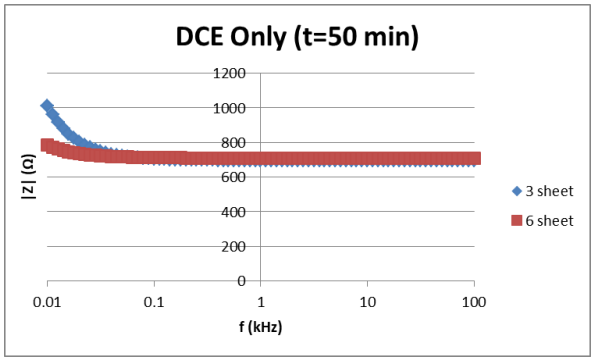

Figure 3.9: Effect of electrode thickness on raw data impedance for **(a)** water only test device and **(b)** DCE only test device. Data was collected at t=50 min after loading.

The raw impedance data obtained for t=50 minutes for each of the 3 sheet and 6 sheet tests is shown in Figure 3.9. The low frequency impedance behavior of the 3 sheet thick electrodes and 6 sheet electrodes is noticeably different. For the three sheet electrode tests, the capacitive behavior of the Au/water interface is noticeable over the 10 Hz-100 Hz frequency decade while the Au/DCE impedance is only noticeable over nearly half the same frequency range. The capacitive regime of the NPAu/liquid interfaces in both six sheet test devices dominate over a much smaller frequency range than the corresponding three sheet devices. For a device attempting to probe the water/DCE ITIES, this behavior is paramount since the capacitive impedance of the Au/liquid interfaces needs to be significantly smaller than the impedance of the water/DCE ITIES in order to obtain sufficient sensitivity to the water/DCE ITIES as described in Section 2.3. As such, the 9 karat electrodes formed from six sheets of stacked gold leaf are a strong candidate for use in devices aimed at probing the water/DCE ITIES.

Table 3.4: Effect of Electrode Thickness on the Capactive Behavior of the NPAu/liquid Interface

3 Sheet Water Only					6 Sheet Water Only				
t (min)	α	A_{eq} (m^2)	R_{sol} (Ω)	$\Sigma_f\|Z_{data}-Z_{fit}\|$ (Ω)	t (min)	α	A_{eq} (m^2)	R_{sol} (Ω)	$\Sigma_f\|Z_{data}-Z_{fit}\|$ (Ω)
0	0.937	2.73E-04	39.2	112.462	0	0.967	1.13E-03	41.5	19.9239
5	0.949	2.93E-04	39.2	92.5769	5	0.966	1.58E-03	42.1	14.2737
10	0.953	3.00E-04	39.1	45.1591	10	0.966	1.92E-03	42.1	13.6659
25	0.957	3.06E-04	39.2	33.4391	20	0.969	2.17E-03	42.2	12.2618
30	0.958	3.08E-04	39.3	31.8386	30	0.971	2.29E-03	42.2	11.4642
40	0.959	3.07E-04	39.4	30.7045	40	0.971	2.36E-03	42.2	11.4358
50	0.959	3.05E-04	39.5	31.0456	50	0.971	2.40E-03	42.2	11.3103
60	0.959	3.03E-04	39.5	32.7538	60	0.971	2.44E-03	42.2	11.0587
70	0.958	3.01E-04	39.5	33.2099	70	0.972	2.44E-03	42.7	10.1862
3 Sheet DCE Only					**6 Sheet DCE Only**				
t (min)	α	A_{eq} (m^2)	R_{sol} (Ω)	$\Sigma_f\|Z_{data}-Z_{fit}\|$ (Ω)	t (min)	α	A_{eq} (m^2)	R_{sol} (Ω)	$\Sigma_f\|Z_{data}-Z_{fit}\|$ (Ω)
0	0.943	3.84E-04	685.0	113.585	0	0.940	1.06E-03	688.8	46.0623
5	0.950	3.71E-04	692.4	50.288	5	0.948	9.53E-04	694.0	45.8769
10	0.950	3.59E-04	695.7	41.2541	10	0.946	9.29E-04	697.9	39.995
20	0.950	3.45E-04	697.1	45.577	20	0.943	9.02E-04	703.8	36.7789
30	0.951	3.36E-04	696.2	49.6163	30	0.943	8.74E-04	706.6	34.7318
40	0.951	3.30E-04	696.3	44.0786	40	0.943	8.54E-04	708.6	34.3365
50	0.951	3.29E-04	696.0	46.1686	50	0.943	8.35E-04	709.8	30.4564
60	0.951	3.26E-04	695.2	47.9531	60	0.940	8.33E-04	707.8	32.2742
70	0.952	3.22E-04	694.8	48.8231	70	0.940	8.25E-04	699.2	33.7649

Table 3.4 summarizes the values obtained for α, A_{eq} and R_{sol} obtained for three sheet thick and six sheet thick 9 karat electrodes. The data shows that increasing the electrode thickness does not have a significant effect on α. This makes sense, since increasing the thickness of the pore structure should not alter the effects causing CPE behavior. As expected, increasing the electrode thickness significantly increases the interfacial area. For the water only test, $A_{eq,6sheet}/A_{eq,3sheet}$ attains a maximum value of just over 8 at t=70 minutes, indicating that doubling the pre-etch electrode thickness increased the NPAu/water interface by roughly a factor of 8; a profound increase. For the DCE tests, $A_{eq,6sheet}/A_{eq,3sheet}$ reaches a maximum value of just over 2.75 at t=0 minutes and evens out to a value of roughly 2.5 at t=70 minutes. The reason for the stark difference between $A_{eq,6sheet}/A_{eq,3sheet}$ for the water and DCE tests is not entirely understood. One hypothesis is that the larger ions in the DCE solution have greater difficulty penetrating into the pore structure resulting in a smaller interface between the NPAu and the

DCE electrolyte solution. Also as expected, R_{sol} does not depend upon changing electrode thickness, and any differences between tests can be attributed to inconsistencies in sanding down the glass tubes to the same length. The fit of the CPE model also improves upon increasing the electrode thickness, lending more credibility to the hypothesis discussed in Section 4.3.1.

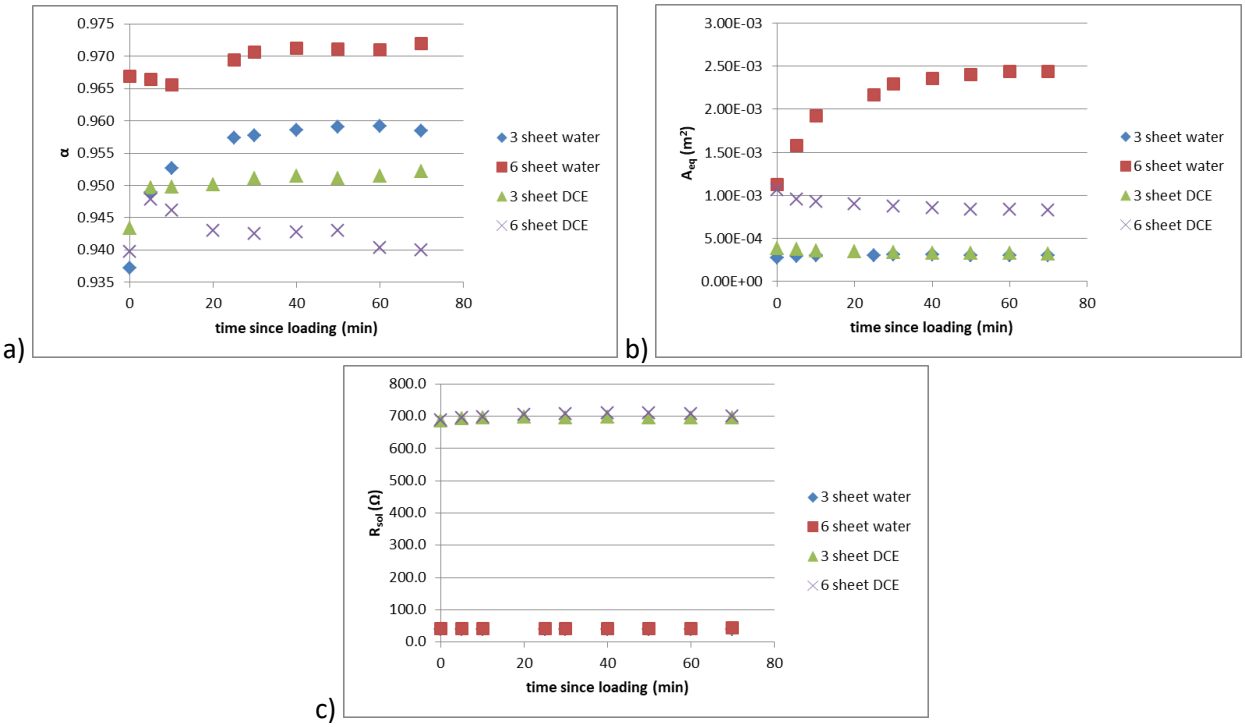

Figure 3.10: Transient response of **(a)** α, **(b)** A_{eq}, and **(c)** R_{sol} for 3 sheet and 6 sheet thick electrodes formed from 9 karat gold leaf.

Figure 3.10 shows the transient behavior of α, A_{eq}, and R_{sol}. As with the tests on initial gold concentration, there is a "start-up" period where the overall device impedance, and thus α, $A_{eq,}$ and R_{sol} noticeably changes between tests. However, by t=60 min, each parameter levels out and steady values for α, A_{eq}, and R_{sol} are obtained. Thus, as described in Section 3.3.1, quasi-steady values of α, R_{sol}, and A_{eq} can be obtained.

Section 3.3.3: Etch Time

The last manufacturing parameter considered was the effect of etch time on NPAu porosity. The initial gold concentration used in electrode construction was 9 karat and its thickness was that of 6 stacked gold leaf sheets and was manufactured in the same manner as the other 9 karat electrodes described in Section 3.3.1. This electrode, however, was etched for various different etch times, including 5, 10, 15, 30, 45, 60, and 90 minutes of total etch time. Initially, the sample was submerged in the 70% nitric acid solution for 5 minutes. The sample was then removed and placed in a bath of DI water with fresh DI water constantly running into the bath for 2 minutes. The sample was then removed and dried via nitrogen gun before taking SEM images of the surface. Once imaging was complete, the sample was placed back in the nitric acid solution until the next desired total etch time was reached. The acid solution was not refreshed at any point throughout the test.

As the pore structure coarsens, the surface area of the porous structure is expected to decrease. Because a large NPAu/liquid surface area is desired for an ITIES device, a fine pore structure is ideal; however, care must be taken to ensure that the electrode is fully dealloyed, and, as such, this sets a lower limit on a useable etch time. Figure 3.11 shows SEM images of the NPAu pore structure at etch times of 5, 10, 15, 30, 45, 60, and 90 minutes. Note that these images have been processed using image noise reduction techniques and filters in ImageJ to decrease some slight blurriness present in some of the initial images. All images were processed using the exact same method. As shown in Figure 3.11a, an etch time of 5 minutes appears to still have some unalloyed regions present on the sample, so despite having the finest pore structure of all the etch times tested, it is unable to be used.

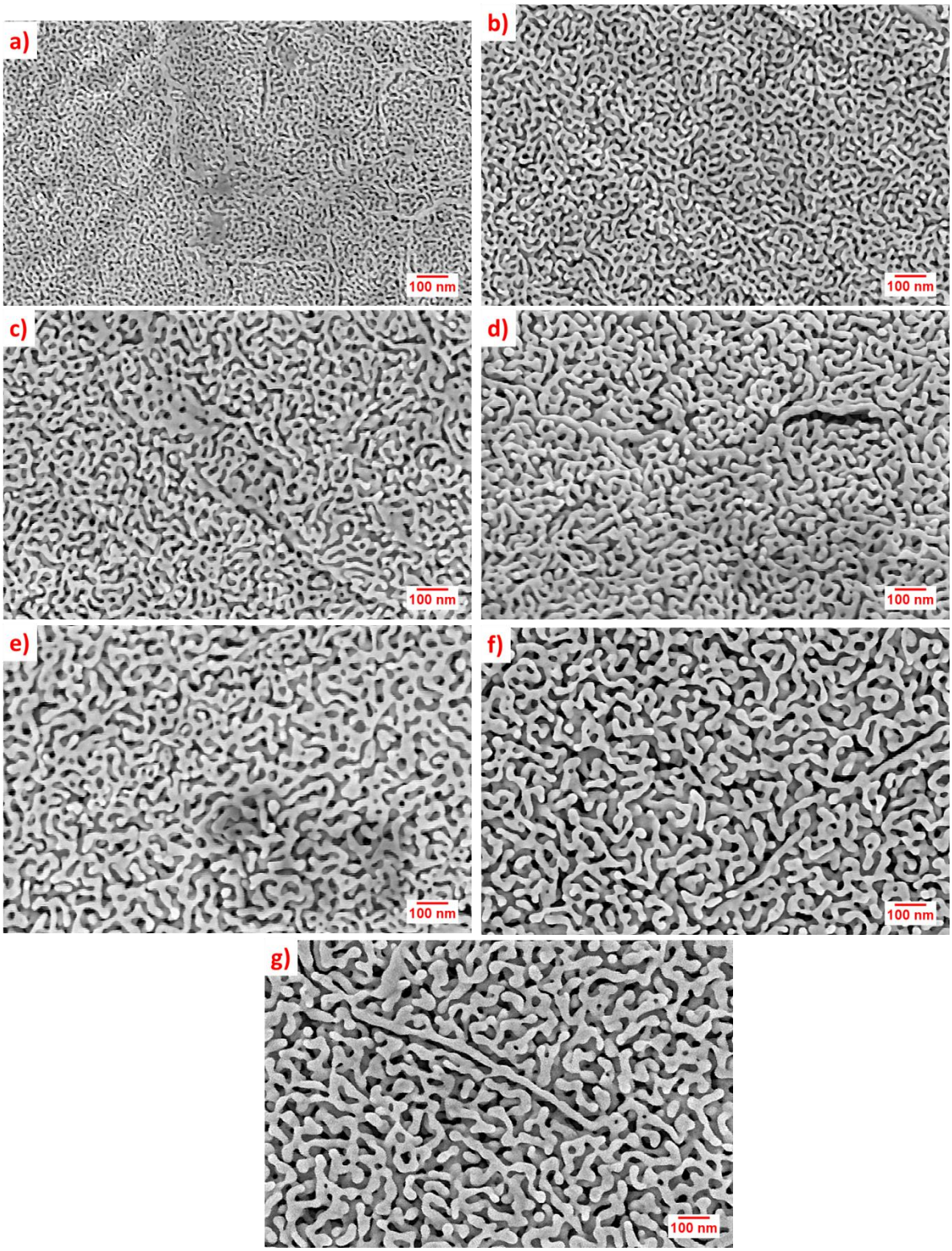

Figure 3.11: SEM images for **(a)** 5, **(b)** 10, **(c)** 15, **(d)** 30, **(e)** 45, **(f)** 60, and **(g)** 90 minute etch times in a 70% HNO_3 30% DI water solution

It is clear from inspection of Figure 3.11 that the NPAu pore structure drastically changes based on etch time. As the etch time increases, the gold ligaments coarsen and the ligaments even appear to move further apart from on another to a certain extent: likely a cause of volume contraction during the etching process. In order to fully characterize how the pore structure evolves with etch time, more intricate analysis must be conducted. This was accomplished through the use of a plugin for ImageJ known as DiameterJ [85,86]. This plugin operates in two phases. First, the base image is segmented into a binary image with grey values of 0 (black) and 255 (white) only. In this image, the white pixels represent the ligaments while the black pixels represent the background. Several different segmentations are provided during this first step and it is left to the user to select which one most closely matches the original image. Once an appropriate segmentation has been obtained, analysis of the segmented image is conducted, providing information about the distribution of fiber sizes, average pore area, percent porosity and more. A full description of the plugin's capabilities as well as a link to an in-depth training module can be found in [86].

Because DiameterJ was initially developed for creating histogram of microfiber diameters, it was initially unsure how the plugin would perform in analyzing a nanoporous structure. Nanoporous systems can be noticeably more complicated due to the random nature of the pore structure and the higher pore density than would be seen in analysis of a typical image of microfibers. To study DiameterJ's performance, three separate methods of image processing were conducted before running through DiameterJ. First, a scale was added directly to the image through ImageJ using the scale bar present from the SEM tag bar. Doing this allows for information about the scale to be carried in the image regardless of any processing that may be done so long as the image is saved as a '.tif' file. With the scale set, the image was cropped to remove the SEM tag bar and noise reduction techniques and filters were applied to clean up the image. The first method of processing through DiameterJ involved taking the

filtered images shown in Figure 3.11 and running them through the segmentation software. The resulting segmentation that yielded the best agreement was chosen to run through DiameterJ. It is important to note that in order to effectively compare the results between different base images, the same segmentation should be chosen for each image. Fortunately, every image that was run through the segmentation for each of the three methods considered was best described by Segmentation S1, indicating that the Statistical Region Merging algorithm used in the segmentation provided the best results [87]. Figure 3.12 provides a side-by-side look at the filtered 90 minute etch time given in Figure 3.11g and the resulting best segmentation. Once again, white regions in the segmentation correspond to ligaments present on the surface while black regions correspond to holes.

a) 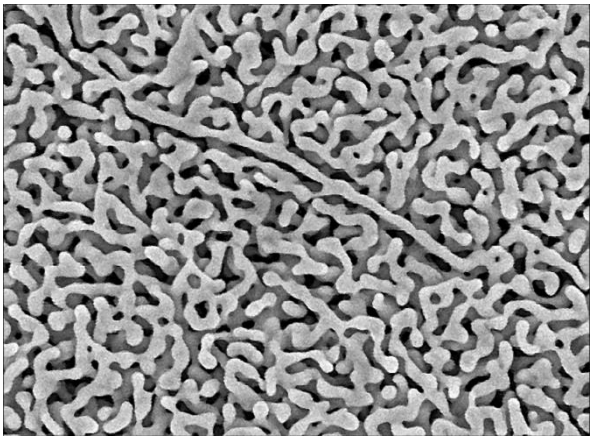 b) 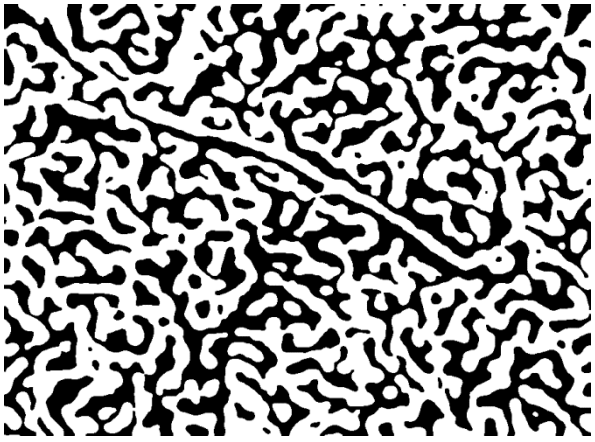

Figure 3.12: (a) Filtered and **(b)** segmented image of the 90 minute etch time sample.

While appropriate segmentations were able to be acquired using this method for etch times of 45, 60, and 90 minutes, the segmentation program was unable to generate any reasonable segmentations for etch times below 45 minutes. As such, a separate means of segmenting the images was considered. This was accomplished using the “adjust threshold” feature of ImageJ. This feature operates by having the user select a range of grey values between 0 (black) and 255 (white) to separate the foreground from the background. Careful inspection of the filtered images in Figure 2.11 showed that grey values between 0 and 102 most closely corresponded to the regions of pores present

throughout the images. Applying this threshold converts the image to binary, with black regions representing pores and white regions representing ligaments on the surface. In order to be consistent between images, a threshold range of 0-102 was applied to all images analyzed using this method. Figure 3.13 shows the image of the 90 minute etch time surface before and after applying this threshold range.

a) 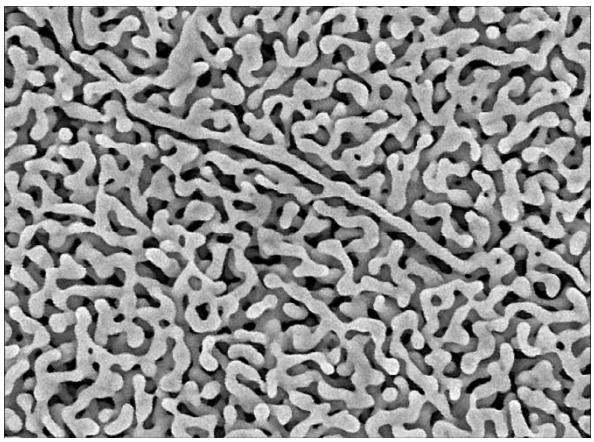 b) 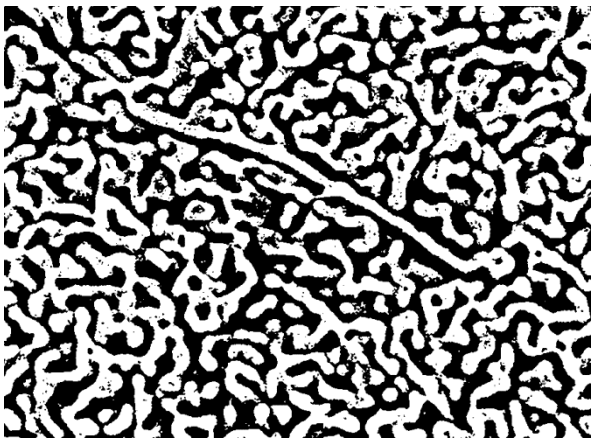

Figure 3.13: (a) Filtered image of the 90 minute etch time surface. **(b)** Image given in (a) after applying a threshold range of 0-102. Black regions correspond to pores and white regions correspond to ligaments on the surface.

Careful inspection of Figure 3.13 shows the presence of several small black regions present on some of the ligaments. Thus while this method of thresholding is able to capture the bulk of the information about the pore structure, some noise is introduced as a result of the thresholding. In an attempt to reduce this noise, these thresholded images were run through the DiameterJ segmentation program. The results of the segmentation can be seen in Figure 3.14. This image shows the thresholded image of the 90 minute etch time surface overlain with the best segmentation (S1) obtained for the image. Grey regions in this image indicate regions where the two images are different. Inspection of Figure 3.14 shows that the grey regions largely overlap with the regions of noise seen in the thresholded image while the overarching structure of the segmented image remains almost identical to the

thresholded image. This means that the segmentation has successfully reduced the noise present in the thresholded image while keeping the overall pore structure in line with its physical state.

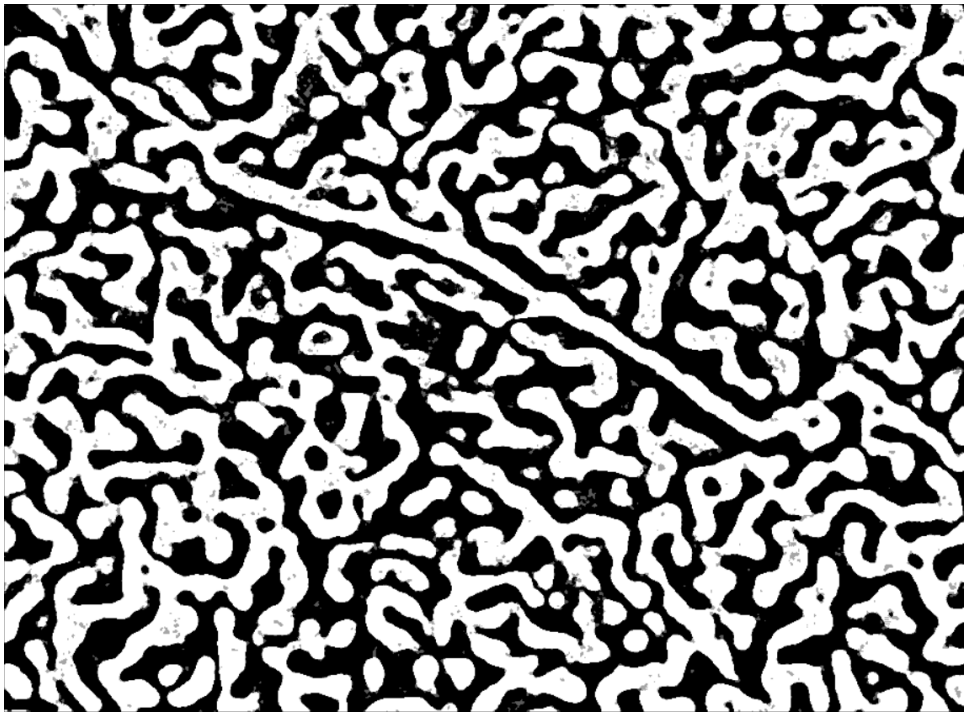

Figure 3.14: Thresholded image of the 90 minute etch time surface overlain with the best segmentation obtained by the DiameterJ segmentation program. Grey regions correspond to differences between the two images.

In summary, three separate images depicting the surface of NPAu for various etch times have been generated to run through DIameterJ. The first images is generated by running the filtered images shown in Figure 3.11 through the DiameterJ segmentation program and choosing Segmentation S1 as the segmentation that best matches the starting image; however, successful segmentations were only able to be obtained for etch times of 45, 60, and 90 minutes. The second image is generated by manually thresholding the filtered image in ImageJ to include pixel grey values between 0-102. This method introduces some noise into the image. The third image seeks to eliminate the noise seen in image 2 by running the thresholded image through the DiameterJ segmentation program. The resulting images maintain the overall pore structure seen in the image while greatly reducing the noise. Only the 5 minute etch time test was unable to obtain a good segmentation using this method; likely a result of

the incredibly fine pore structure present resulting from such a short etch time. Figure 3.15 shows all three of these segmented images for the 90 minute etch time surface as well as the base filtered image.

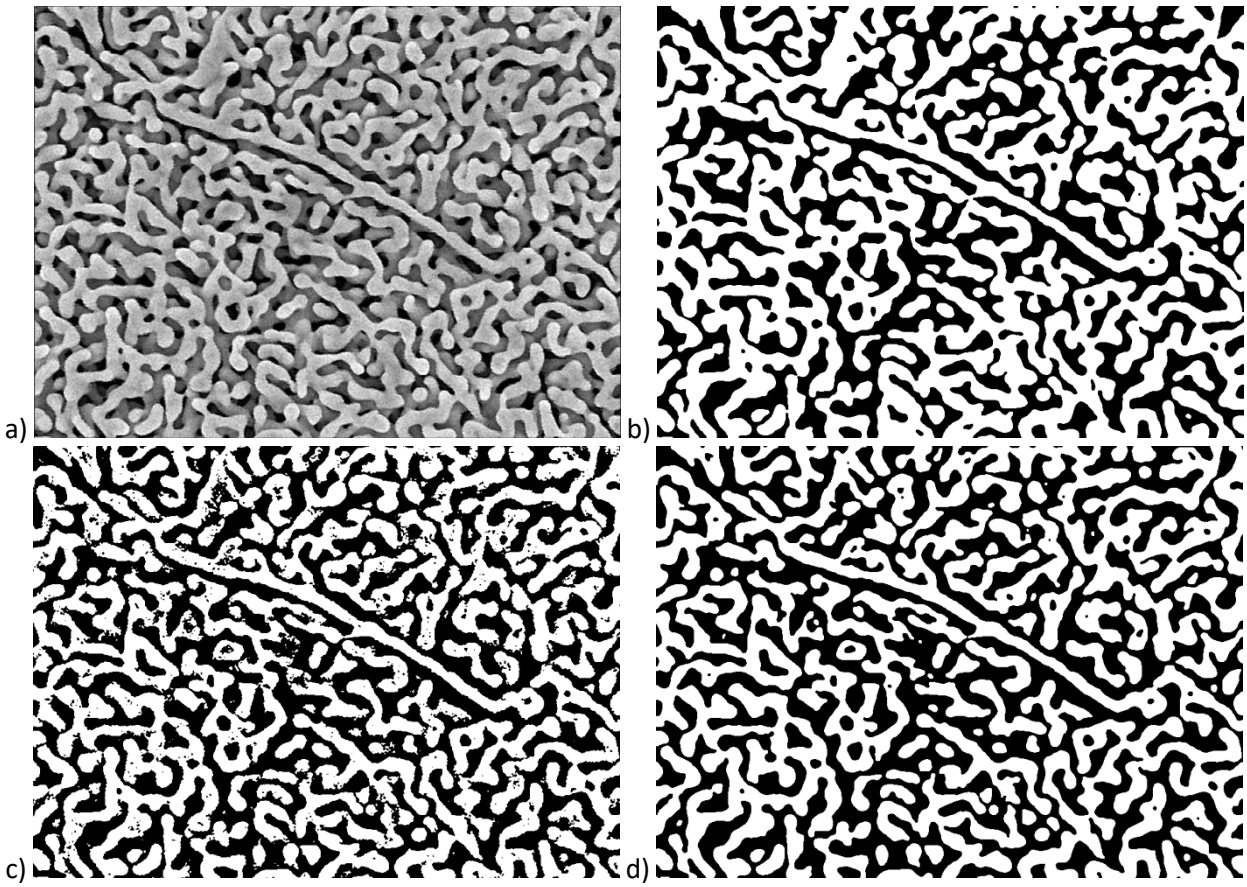

Figure 3.15: (a) Base filtered image. **(b)** Best segmentation obtained by running the filtered image in (a) through the DiameterJ segmentation program. **(c)** Thresholded image obtained by adjusting the threshold of the filtered image in (a) to include grey values in the range of 0-102. **(d)** Best segmentation upon running the thresholded image in (c) through the DIameterJ segmentation program. All images describe the 90 minute etch time NPAu surface.

Upon running an image through DiameterJ, information about the global average ligament diameter, global average pore size, and percent porosity can be obtained. Further, histograms are generated for the various ligament diagrams seen throughout the surface. Because one method by which DiameterJ determines ligament diameter is by performing a Gaussian fit on the radius data and finding the resulting mean value of the curve, each histogram of radius data was checked for behavior seen in a normal distribution. The skewness and kurtosis of these distributions were also considered for

good measure. In all cases, a normal distribution was observed, and the ligament diameter and associated standard deviation were taken from DiameterJ's interpretation of the data using a Gaussian distribution.

Another output of DiameterJ includes a set of four images depicting the center lines of the ligaments determined by DiameterJ, how they align with the segmented image, and a map of all the pores detected by DiameterJ. These images are a useful tool to ensure that DiameterJ is accurately describing both the ligaments and the pores present in the image. Outputs for the 10 minute etch surface and the 90 minute etch surface are given in Figure 3.16. The top left quadrant shows the segmented image run through DiameterJ. The top right quadrant shows the center lines of the ligaments found by DiameterJ. The bottom left quadrant overlays the ligament centerlines on top of the input image and the bottom right quadrant shows the pores determined by DiameterJ.

a) 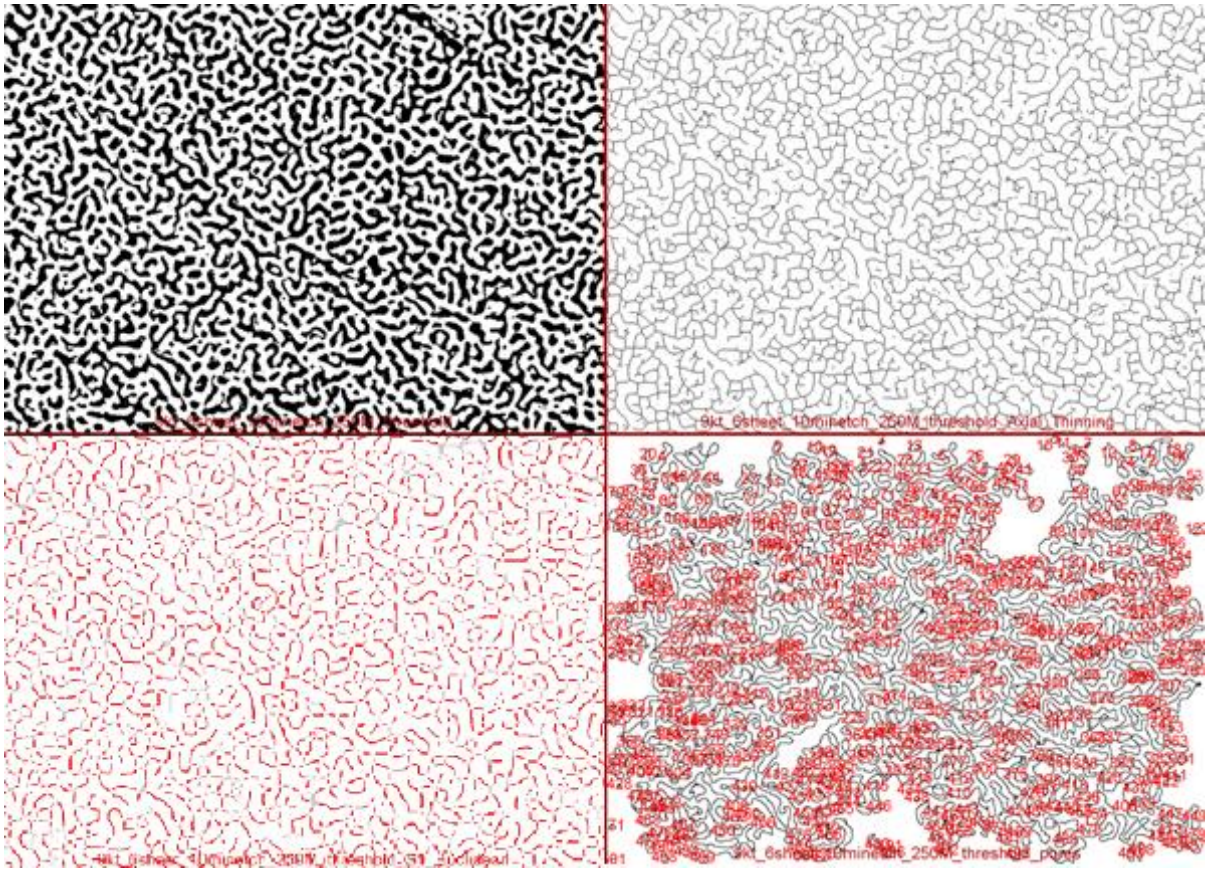

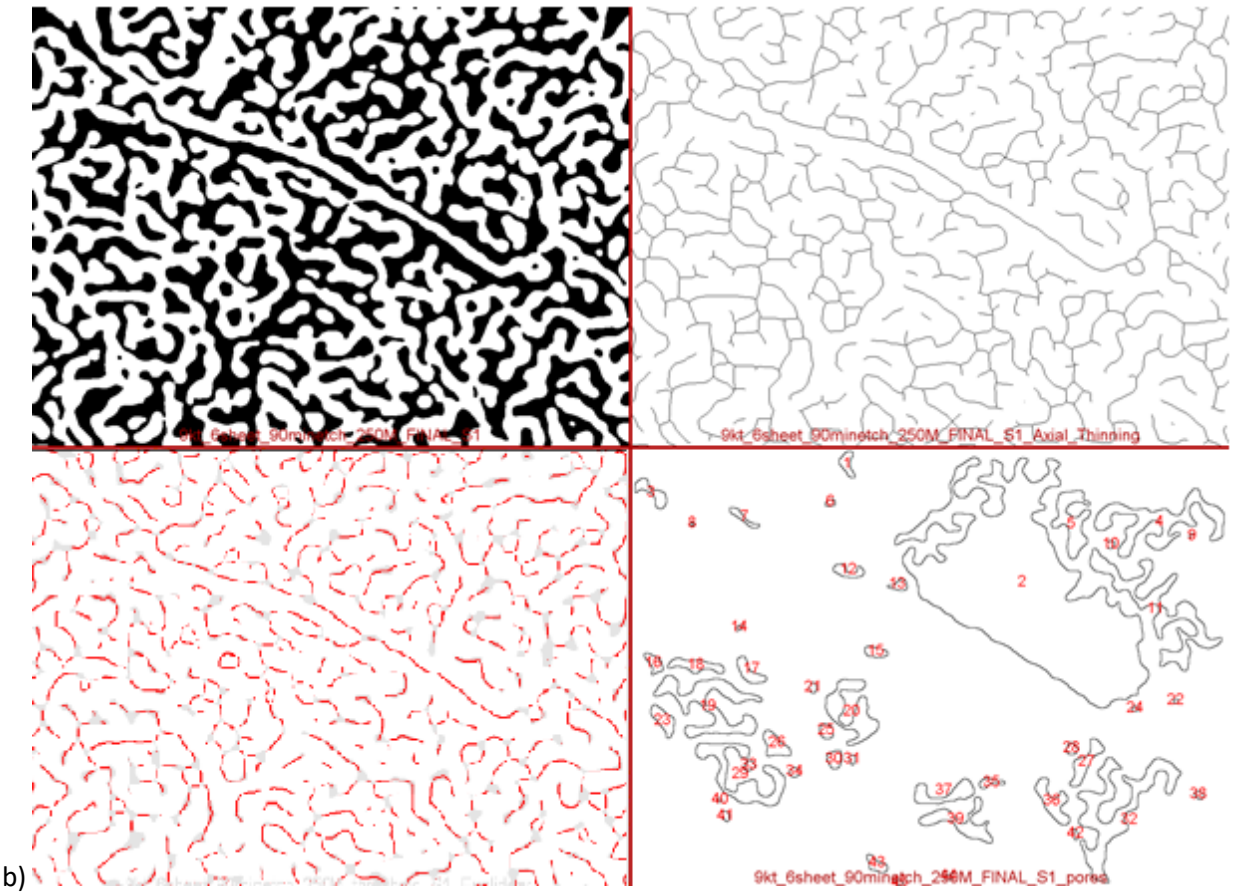

b)

Figure 3.16: Output images from DiameterJ for the **(a)** 10 minute etch surface thresholded in ImageJ and run through DiameterJ and **(b)** the 90 minute etch surface with the filtered image in Figure 3.11 run though the segmentation. The bottom left quadrant makes it evident that DiameterJ is unable to effectively find all of the pores present in the image.

Examination of the bottom left quadrant of these images for each tests shows that DiameterJ does a reasonable job of finding the ligaments in the image. It is important to note in these images that DiameterJ does not draw centerlines at intersections between ligaments. Unfortunately, the pore structure in all cases is unable to be effectively described by DiameterJ. This is likely a result of the high density of pores present throughout each image. As a result, no useable information about the pore size or diameter can be determined through the use of DiameterJ; however, information about the average ligament size and the percent porosity can still be reasonably determined.

It may seem odd that while DiameterJ is able to reasonably determine information about the porosity of the surface despite being unable to accurately capture all of the present pores in a given image. The method by which DiameterJ calculates the percent porosity of the surface is completely independent from how it determines where pores are located on the surface. Percent porosity is measured by counting the total number of black pixels present in the image and dividing by the image's total number of pixels. This is equivalent to using the measurement capability in ImageJ to determine the area fraction of a thresholded or segmented image. For example, the area fraction of the segmented threshold image of the 90 minute etch time surface as calculated by ImageJ is 47.99% while the percent porosity determined by DiameterJ for this same image is also 47.99%.

Table 3.5: Average Ligament Diameter and Percent Porosity for Various Etch Times Using DiameterJ

etch time (min)	Measurement	Segmentation of filtered images	Threshold images	Segmentation of threshold images
5	Mean Ligament Diameter (nm)		9.3	
	Ligament Diameter SD (nm)		3.4	
	Diameter Skewness		0.1097	
	Diameter Kurtosis		0.336	
	percent porosity (%)		0.1963	
10	Mean Ligament Diameter (nm)		10.3	12.6
	Ligament Diameter SD (nm)		4.1	2.9
	Diameter Skewness		-0.1115	0.2634
	Diameter Kurtosis		-0.5042	0.57
	percent porosity (%)		0.416	0.3954
15	Mean Ligament Diameter (nm)		10.5	16.0
	Ligament Diameter SD (nm)		7.0	4.2
	Diameter Skewness		0.2055	0.3963
	Diameter Kurtosis		-0.643	0.7944
	percent porosity (%)		0.3376	0.3144
30	Mean Ligament Diameter (nm)		12.2	18.1
	Ligament Diameter SD (nm)		7.8	5.0
	Diameter Skewness		0.0642	0.0812
	Diameter Kurtosis		-0.8108	0.4753
	percent porosity (%)		0.3118	0.2891
45	Mean Ligament Diameter (nm)	17.2	8.6	19.4
	Ligament Diameter SD (nm)	5.4	10.4	5.9
	Diameter Skewness	0.1626	0.403	0.0413
	Diameter Kurtosis	0.2404	-0.913	-0.0106
	percent porosity (%)	0.4246	0.3385	0.3247
60	Mean Ligament Diameter (nm)	20.5	10.4	18.8
	Ligament Diameter SD (nm)	5.7	10.5	5.7
	Diameter Skewness	0.0368	0.2029	0.0507
	Diameter Kurtosis	0.4194	-1.1316	0.0719
	percent porosity (%)	0.4228	0.4756	0.4796
90	Mean Ligament Diameter (nm)	23.2	11.5	20.9
	Ligament Diameter SD (nm)	6.7	9.9	7.0
	Diameter Skewness	0.0503	0.4056	0.0077
	Diameter Kurtosis	0.3378	-0.756	-0.299
	percent porosity (%)	0.4231	0.4792	0.4799

Values obtained for average ligament diameter and standard deviation, percent porosity, and the ligament radius histogram skewness and kurtosis obtained for the various etch times considered are given in Table 3.5. Note that the segmentation of thresholded images appeared to best match the original image. As expected, the 5 minute etch surface exhibits both the smallest ligament diameter and the smallest porosity. A maximum porosity of 48% is seen for the 90 minute etch time surface, also in agreement with expectations. Figure 3.17 shows how increasing etch time affects both ligament diameter and porosity. Of particular interest is the complex behavior of the surface porosity. While it is expected that for very low etch times that the porosity will be low, it was initially hypothesized that the porosity would continually increase as etch time increased until eventually leveling off once a stable state had been reached. Instead, Figure 3.17b shows that the surface porosity undergoes periods of increase and decrease with etch time. This behavior indicates the presence of competing mechanisms.

As the dealloying of the initial exposed surface nears completion after 5 minute etching, pores on the surface become more interconnected, resulting in an increase in porosity; however, as the dissolution front penetrates further into the solution, gold diffusion begins coarsening ligaments on the surface, causing porosity to be reduced indicated by the region between 10 and 30 minutes of etch time. Inspection of Figure 3.11 shows that while the ligaments tend to increase in thickness for longer etch times, they also appear to move further apart from one another, especially for etch times beyond 30 minutes. One possibility for this is the presence of volume contraction as the pore structure underneath the surface continues to reorganize. The increase in separation between ligaments results in an increase in porosity despite the coarsening of the ligaments. As the etch time is increased further, this increase is expected to level out as the structure below the surface stabilizes; however, ligament coarsening will not necessarily stop, meaning that for etch times greater than 90 minutes, it is possible that a decrease in porosity will be present.

a)

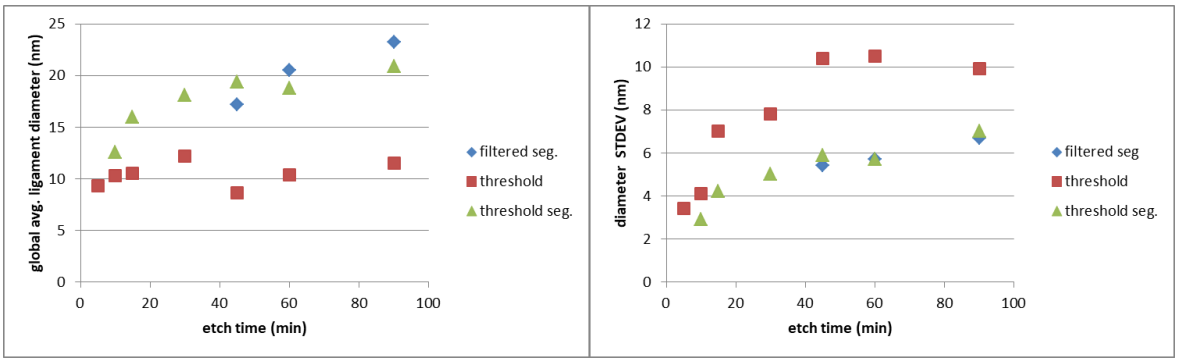

b)

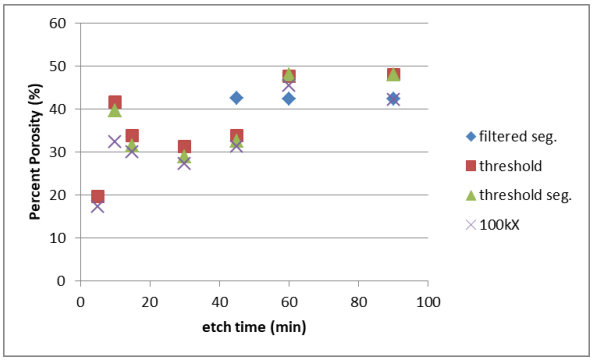

Figure 3.17: Behavior of **(a)** average ligament diameter and its standard deviation and **(b)** percent porosity with etch time. While the nature of porosity development is more complex than initially expected, clear coarsening of the pore structure is present for increasing etch times.

Data for water only and DCE only devices formed from 9 karat 6 sheet electrodes etched for 15 minutes was obtained from the prior electrode thickness tests. As such, devices constructed from electrodes etched for 10 minutes were tested to compare the viability of a 10 minute acid etch versus a 15 minute etch. Due to the finer pore structure present in the 10 minute etch sample, it is expected that the device impedances will be lower than those obtained for the 15 minute etch devices.

Table 3.6 shows the comparison of α, A_{eq}, and R_{sol} obtained from the MATLAB model for the 15 minute etch and 10 minute etch tests. As expected, modifying the etch time does not have any noticeable effect on α or R_{sol}; however, there is a noticeable decrease in A_{eq} obtained going from a 10 minute etch time to a 15 minute etch time. This agrees with the expectation that the pore structure coarsens as the etch time is increased. Note that the 10 minute etch water only tests for t=60 min has $\Sigma_f|Z_{data}-Z_{fit}|=1169.89\ \Omega$, which is significantly higher than what is seen in all other tests. Since the raw

impedance data of this experiment does not appear to be overtly different from the other times tested for this particular electrode, this is likely a failure in the optimization model to converge to the correct solution, as evident from the noticeably different values obtained for α and A_{eq}.

Table 3.6: Effect of Etch Time on the Capacitive Behavior of the NPAu/liquid Interface

15 min Etch, 6 Sheet, Water Only					**10 min Etch, 6 Sheet, Water Only**				
t (min)	α	A_{eq} (m^2)	R_{sol} (Ω)	$\Sigma_f\|Z_{data}-Z_{fit}\|$ (Ω)	t (min)	α	A_{eq} (m^2)	R_{sol} (Ω)	$\Sigma_f\|Z_{data}-Z_{fit}\|$ (Ω)
0	0.967	1.13E-03	41.5	19.9239	0	0.964	4.22E-03	38.6	13.6704
5	0.966	1.58E-03	42.1	14.2737	5	0.966	4.69E-03	38.8	7.19119
10	0.966	1.92E-03	42.1	13.6659	10	0.966	4.78E-03	38.7	6.86483
20	0.969	2.17E-03	42.2	12.2618	20	0.968	4.80E-03	38.8	6.66216
30	0.971	2.29E-03	42.2	11.4642	30	0.968	4.82E-03	38.8	6.82445
40	0.971	2.36E-03	42.2	11.4358	40	0.968	4.80E-03	38.9	6.75487
50	0.971	2.40E-03	42.2	11.3103	50	0.969	4.76E-03	39.6	6.79358
60	0.971	2.44E-03	42.2	11.0587	60	0.895	6.15E-03	38.8	1169.89
70	0.972	2.44E-03	42.7	10.1862	70	0.969	4.67E-03	41.2	6.71977
15 min Etch, 6 Sheet, DCE Only					**10 min Etch, 6 Sheet, DCE Only**				
t (min)	α	A_{eq} (m^2)	R_{sol} (Ω)	$\Sigma_f\|Z_{data}-Z_{fit}\|$ (Ω)	t (min)	α	A_{eq} (m^2)	R_{sol} (Ω)	$\Sigma_f\|Z_{data}-Z_{fit}\|$ (Ω)
0	0.940	1.06E-03	688.8	46.0623	0	0.955	1.41E-03	699.7	97.6337
5	0.948	9.53E-04	694.0	45.8769	5	0.938	1.37E-03	711.3	36.0768
10	0.946	9.29E-04	697.9	39.995	10	0.933	1.33E-03	717.2	41.4878
20	0.943	9.02E-04	703.8	36.7789	20	0.919	1.35E-03	714.6	41.2391
30	0.943	8.74E-04	706.6	34.7318	30	0.920	1.30E-03	700.3	34.3907
40	0.943	8.54E-04	708.6	34.3365	40	0.922	1.26E-03	683.7	30.2029
50	0.943	8.35E-04	709.8	30.4564	50	0.888	1.46E-03	683.8	110.262
60	0.940	8.33E-04	707.8	32.2742	60	0.926	1.20E-03	682.7	36.4092
70	0.940	8.25E-04	699.2	33.7649	70	0.924	1.19E-03	686.1	39.9909

Figure 3.18a graphically depicts the differences obtained for A_{eq} in both the water only and DCE only tests. Figure 3.18b shows how this resulting decrease in A_{eq} from the 10 minute etch tests to the 15 minute etch tests effects the estimated interfacial impedance data obtained by subtracting R at f=10 kHz from the complex impedance for each test. At f=10 Hz, the interfacial impedance of the 10 minute etch water only test is roughly half that obtained for the 15 minute etch water only test. Although this is not as profound in the DCE only tests, the maximum difference in interfacial impedance between the 10 minute etch and 15 minute etch tests is still significant, with the interfacial impedance of the 10 minute etch test being roughly ¾ the impedance of the 15 minute etch test at f=10 Hz. Thus, electrodes etched for 10 minutes can provide noticeably smaller impedances for the Au/liquid interfaces than electrodes etched for 15 minutes while also ensuring that nearly all residual silver has been removed during the

etching process. These results indicate that a 10 minute etch time will yield electrodes that will enable greater sensitivity to the water/DCE ITIES when used in a device constructed to probe the liquid/liquid interface than a 15 minute etch time. Since increasing etch time leads to further coarsening of the pore structure, etching for more than 15 minutes is expected to increase interfacial impedance and, as such, impedance analysis for NPAu electrodes etched longer than 15 minutes is omitted.

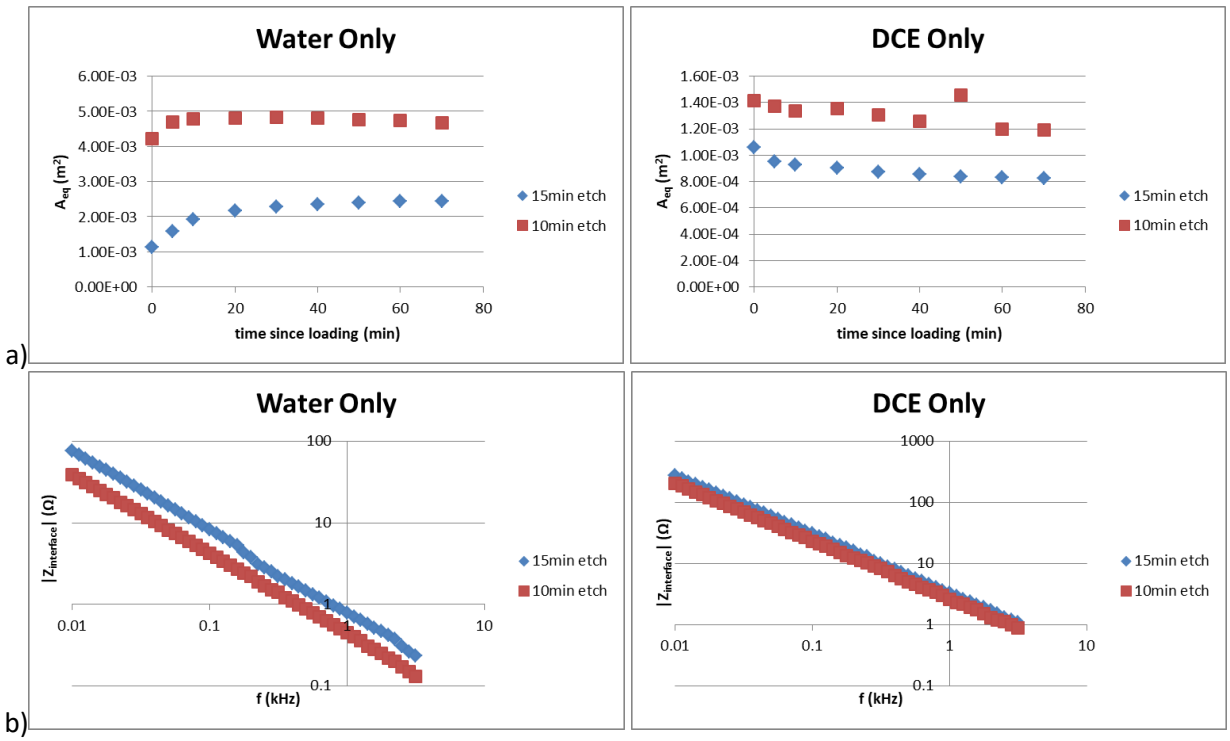

Figure 3.18: (a) Difference in obtained values of A_{eq} for electrodes etched for 10 minutes and 15 minutes for both water only and DCE only tests. **(b)** Difference in obtained interfacial impedance for electrodes etched for 10 minutes and 15 minutes for both water only and DCE only tests.

Section 3.3.4: Summary of Results

Through the study of the effects of initial gold concentration, electrode thickness, and etch time, knowledge has been gained as to which electrodes should be most useful in a device focused on probing the water/DCE ITIES. Tests studying the effects of initial gold concentration (Section 3.3.1) showed that the NPAu/water and NPAu/DCE interfaces can be successfully modeled using a lone CPE despite the

complicated nature of the 'flat' Au/liquid interfaces seen in Chapter 2. SEM images of electrodes of the same thickness but of different initial gold concentrations showed that 12 karat gold leaf does not form a fully porous structure, leaving several unalloyed regions amid lightly porous regions. On the other extreme, 6 karat gold leaf, while forming porous regions throughout, was unable to provide a uniform sheet distribution throughout, leaving behind islands of nanoporous regions surrounded by the bare gold substrate. As a result, 6 karat electrodes were removed from future consideration. 9 karat gold leaf was able to provide porosity throughout the sample while maintaining uniform coverage. Impedance analysis conducted on devices formed from 9 karat and 12 karat electrodes showed that increasing the initial gold concentration from 9 karat to 12 karat noticeably decreased the area of the Au/liquid interface and 12 karat electrodes were removed from future consideration as a result.

Studying the effect of electrode thickness (Section 3.3.2) showed that electrode thickness played no role in the porosity of the resulting NPAu, with 1 sheet, 3 sheet, and 6 sheet 9 karat electrodes having nearly identical porosity on the surface. However, impedance analysis showed that increasing electrode thickness had a significant impact on the area of the NPAu/liquid interface due to the increased thickness of the pore structure. While the impedances of the 3 sheet NPAu/liquid interfaces dominated over the low frequency regime for both the water and DCE tests, increasing the thickness to 6 sheets made the solution resistance dominant over most of the entire frequency range studied.

The effects of etch time (Section 3.3.3) showed significant coarsening of the pore structure with increasing etch time in agreement with the literature. For a 9 karat and 6 sheet thick electrode, the resulting percentage of void regions located on the surface of the sample showed a complicated behavioral trend with etch time. This is a result of two competing mechanisms present within the pore structure evolution: increase in pore size due to merging of pores and the resulting coarsening of the ligaments between pores. Because a coarser pore structure results in a smaller total surface area, a

coarser pore structure is expected to decrease the area of the Au/liquid interface. This would result in an increase in interfacial impedance which is undesirable for the proposed application. As a result, shorter etch times will provide a greater benefit to the sensitivity of devices aimed at probing the water/DCE ITIES due to the increased NPAu/liquid area they contain. The presence of residual silver after etching prevents the use of an etch time that is too short, however. SEM images and results of the optimization for the etch time test show that an etch time of 10 minutes would be ideal for use. This can be seen in Figure 3.12 as well as Table 3.7, which depicts the ratio of A_{eq} obtained for the 10 minute etch tests to the 15 minute etch tests. The results of the three tests described in Section 3.3 show that electrodes formed from six stacked sheets of 9 karat white gold leaf etched for 10 minutes in a 70% HNO_3, 30% DI water solution are the ideal candidate for use in devices aimed at isolating the water/DCE ITIES. Electrodes formed with these specifications are used in the next chapter and beyond unless otherwise stated.

Table 3.7: NPAu Area Ratio of a 10 Minute Etch Time to a 15 Minute Etch Time

	Water Only			**DCE Only**		
	15 min etch	**10 min etch**		**15 min etch**	**10 min etch**	
t (min)	A_{eq} (m^2)	A_{eq} (m^2)	$A_{eq}(10)/A_{eq}(15)$	A_{eq} (m^2)	A_{eq} (m^2)	$A_{eq}(10)/A_{eq}(15)$
0	9.61E-04	3.61E-03	3.75	1.06E-03	1.41E-03	1.33
5	1.35E-03	4.00E-03	2.98	9.53E-04	1.37E-03	1.44
10	1.64E-03	4.08E-03	2.49	9.29E-04	1.34E-03	1.44
20	1.85E-03	4.10E-03	2.22	9.02E-04	1.35E-03	1.50
30	1.96E-03	4.12E-03	2.10	8.74E-04	1.30E-03	1.49
40	2.01E-03	4.10E-03	2.04	8.54E-04	1.26E-03	1.47
50	2.05E-03	4.06E-03	1.98	8.35E-04	1.46E-03	1.75
60	2.08E-03	4.05E-03	1.95	8.33E-04	1.20E-03	1.44
70	2.08E-03	3.99E-03	1.92	8.25E-04	1.19E-03	1.45

Chapter 4: Modeling and Characterization of the Water/DCE ITIES

This chapter discusses the characterization of the water/DCE ITIES. First, an appropriate equivalent circuit model to use is discussed followed by the analysis of data collected from two different preliminary apparatus systems. Construction of a third apparatus system based on the results seen in the preliminary tests is discussed. Finally, several analyses are conducted on the data collected from this third apparatus in order to effectively characterize the water/DCE ITIES. These analyses include examining the impact of optimizing over high frequency data exclusively and weighting the optimization function by a frequency-dependent function to ensure the optimization is able to perform well over a wide frequency range. The behavior of pseudo-capacitance Q^o with respect to interfacial area is also discussed.

Section 4.1: Preliminary Testing of the Water/DCE ITIES

The simple ITIES device and its equivalent circuit depicted in Figure 4.1 consist of impedances from four primary sources: the solution resistance, R_{sol}, the impedance of the Au/water and Au/DCE interfaces, $Z_{Au/w}$ and $Z_{Au/d}$, and the impedance of the water/DCE ITIES, Z_{ITIES}. With the characterization of the Au/water and Au/DCE interfaces complete, attention can now be focused on the water/DCE ITIES.

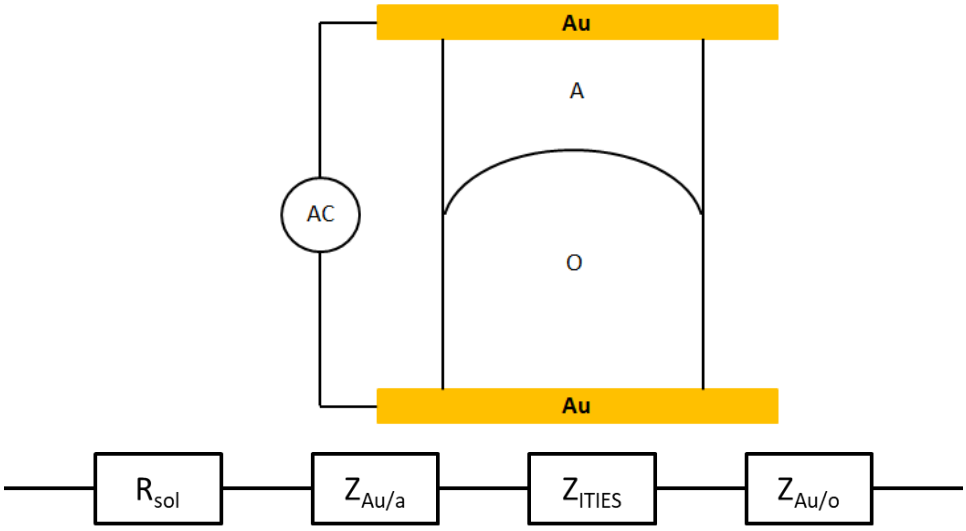

Figure 4.1: Simple ITIES device and its equivalent impedance model. With the characterization of the Au/water and Au/DCE interfaces complete, only the water/DCE interface remains.

First, an equivalent circuit model must be developed for the ITIES. Several different equivalent circuit models were developed to describe the Au/water and Au/DCE interfaces in Chapter 2. By considering the differences between an Au/liquid and a liquid/liquid interface, it is possible to directly use or make modifications to these models already considered in the characterization of the Au/liquid interfaces. Like for the Au/liquid interfaces in Chapter 2, it is unlikely that a lone CPE would be able to effectively model the impedance of the ITIES. While adsorption was shown to have an impact at the Au/liquid interfaces, adsorption is not expected to occur at the ITIES since there is no surface for the ions within the ITIES to adsorb to. Ion transport effects within the ITIES and charge transfer effects across the ITIES are still expected to both be present and have a significant impact on the behavior of the water/DCE interface. As such, the Transfer Effects model given in Figure 2.14c is used as the preliminary model of the water/DCE interface. This equivalent circuit is reproduced in Figure 4.2, below.

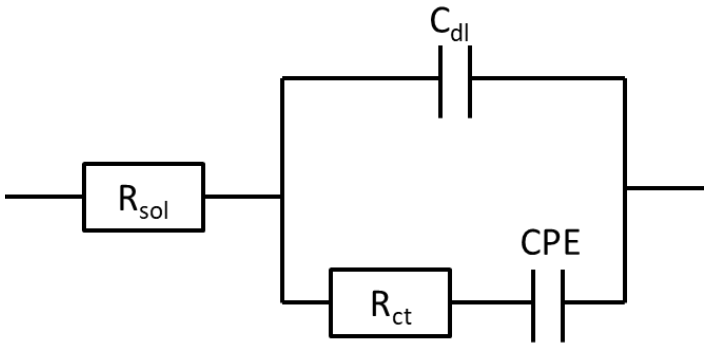

Figure 4.2: Transfer Effects equivalent circuit used to model of the water/DCE ITIES. The effects of charge transfer and ion transport at the ITIES are included in the model by the series combination of the CPE and charge transfer resistance, R_{ct}.

With the equivalent circuit model decided, two different apparatuses were constructed to conduct preliminary tests on the water/DCE interface. The first of these was the simple ITIES device shown in Figure 4.3. The device was placed in a C-clamp for stability. Both electrodes were made of NPAu and manufactured from 6 stacked sheets of 9 karat white gold leaf etched for 10 minutes in 70% concentrated nitric acid as described in Chapter 3. The tube had an inner diameter of 8 mm and was made of Teflon-FEP. Construction of the device was the same as described for the single liquid tests in Chapter 3. The device was loaded by first adding the DCE solution to fill roughly one-third of the tube. Water was then added to the tube until roughly three quarters of the tube was filled. A third syringe was then used to suck out the liquid at the top to ensure that no DCE slipped through above the water while the water was first being added. More water solution was then added until the device was fully loaded. Impedance spectroscopy was performed over a frequency range of 10 Hz-10 kHz with V_{bias}=0 V and V_{osc}= 100 mV. The water/DCE interfacial area was kept constant through the three tests.

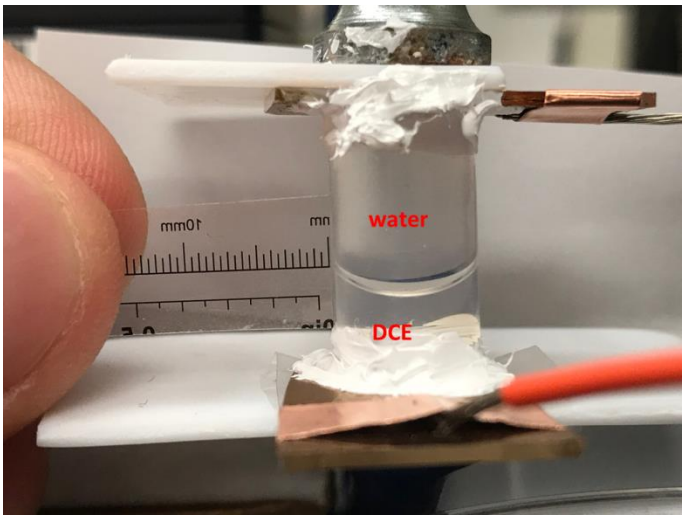

Figure 4.3: Single tube constructed to probe the water/DCE ITIES.

The second apparatus was constructed from two glass tubes, one with inner diameter of 6 mm and the other with a diameter of 10 mm. Although this device is more complicated, it has the additional benefits of pinning the contact line of the water/DCE interface and increasing the area of the NPAu/water interface. Electrodes were manufactured the same method as in the first device. The length of the 6 mm ID tube was 10 mm and the length of the 10 mm ID tube was 15 mm. To construct, the smaller tube was first adhered to the bottom electrode using a solvent resistant sealant. A thin acrylic sheet was cut with a hole of equal size of the outer diameter of the small tube. A small coating of sealant was applied around the outside of the base of the small tube and the acrylic sheet was slid down around the tube and pressed to the sealant, adhering the sheet to the bottom electrode. This sheet is necessary to ensure that the liquid in the outer tube does not contact both electrodes, thereby creating a short in the device's circuit. It is important to note that while acrylic is susceptible to attack by DCE, the DCE in the device is confined to the inner tube and as such does not come into contact with the acrylic at all. The larger outer tube was then adhered to the top of this acrylic sheet and the second electrode was sealed to the top of this tube. A small hole was left open to allow for air to escape during loading. The device was placed in a C-clamp for stability. A schematic of this device is shown in Figure 4.4.

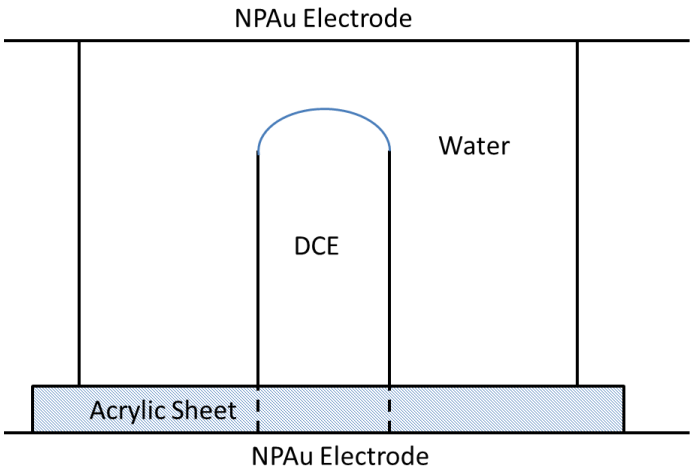

Figure 4.4: Schematic of the concentric tube apparatus used to probe the water/DCE ITIES.

The device was loaded via syringe by first filling the inner tube roughly halfway with DCE. The inner tube was not filled all the way with DCE because upon adding water, this would likely cause some of the DCE to break away from the inner tube and end up in the outer tube. A second syringe was then used to load the water until above the top of the inner tube. At this point, the inner tube was filled the rest of the way with DCE and a bulged interface was created. More water was then added to completely fill the device. An image of the water/DCE interface formed by this device is shown in Figure 4.5. Impedance spectroscopy was performed three separate times for each of the two devices. The frequency range considered was 10 Hz to 100 kHz with V_{osc}=100 mV and V_{bias}=0 V. The water/DCE interfacial area was kept constant through the three tests.

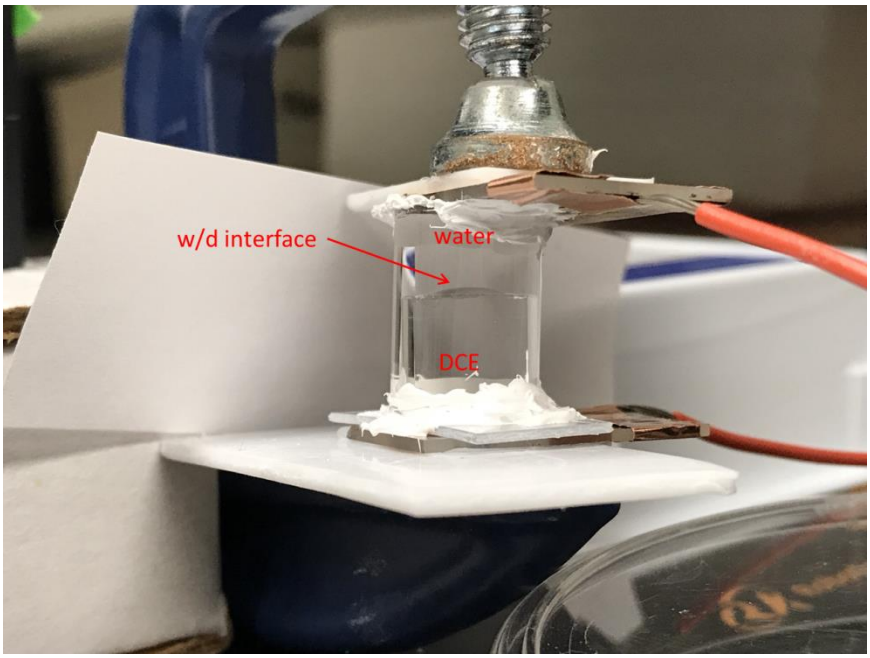

Figure 4.5: Water/DCE ITIES formed by the concentric tube apparatus. The contact line of the interface is pinned by the top of the inner tube's wall.

In order to isolate the impedance of the water/DCE interface from the raw data impedance obtained for both devices, the impedances of the NPAu/water and NPAu/DCE interfaces were subtracted out. Because of the inability to exactly determine the electrode/liquid interfacial areas through optical methods as described in Chapter 3, the impedance model developed for the NPAu/L interfaces (Equation 3.1) could not be used to approximate the impedance contributions of the NPAu/L interfaces used in these apparatuses. Instead, impedance values obtained from the water only and DCE only NPAu tests in Chapter 3 were used to approximate the impedance contributions of the NPAu/L interfaces in the two preliminary test devices described above. While the Chapter 3 water and DCE only tests had two NPAu/water and NPAu/DCE interfaces, respectively, it was assumed that both the top and bottom electrodes in the device had identical area and the impedances obtained for these interfaces were divided by two to obtain the impedance contribution of a single electrode.

Since the planar areas of the NPAu/L interfaces in the Chapter 3 tests are not the same as the areas used here, they must be altered by an area factor to account for the difference in size. For

example, the tubes used in the Chapter 3 NPAu/water and NPAu/DCE interface tests had an inner diameter of 8 mm while the outer tube in Figure 4.5 had an inner diameter of 10 mm and the inner tube had an inner diameter of 6 mm. Since the cross-sectional areas of these tubes are different than in the Chapter 3 tests, the impedances have to be multiplied by a constant to account for this difference in area. Since the NPAu/liquid interfacial impedance is inversely proportional to its area (Equation 3.1), a ratio of

$$\frac{1/Z_1}{1/Z_2} = \frac{A_1}{A_2} \tag{4.1}$$

was used. Here, a subscript of 1 indicates the Chapter 3 tests and a subscript of 2 indicates the single tube and concentric tube apparatuses in Figures 4.3 and 4.5. Note that A in Equation 4.1 indicates the planar area of the electrode, that is to say $(\pi/4)D^2$, where D is the inner diameter of the tube.

With the area modifications made to the Chapter 3 NPAu/water and NPAu/DCE interfacial impedances, these values were subtracted out from the raw data impedance in these preliminary water/DCE interface tests and the resulting impedances were run through the MATLAB optimization. The solution resistance was taken to be the raw data resistance at f=10 kHz. While this method of accounting for the NPAu/liquid interfacial impedances is rather inexact, it was expected that the impedance contributions of these interfaces would make up a significantly smaller fraction of the total system impedance than the water/DCE ITIES. As a result, the error associated with determining the NPAu/liquid interfacial impedances would negligibly impact the characterization of the water/DCE interface.

a)

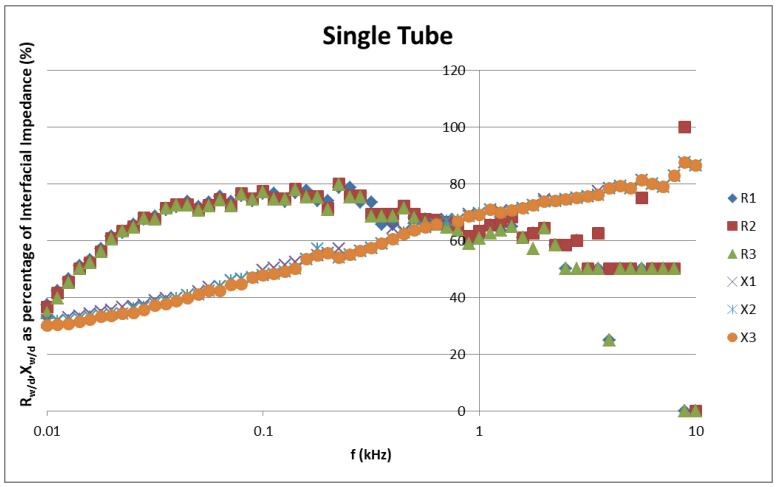

b)

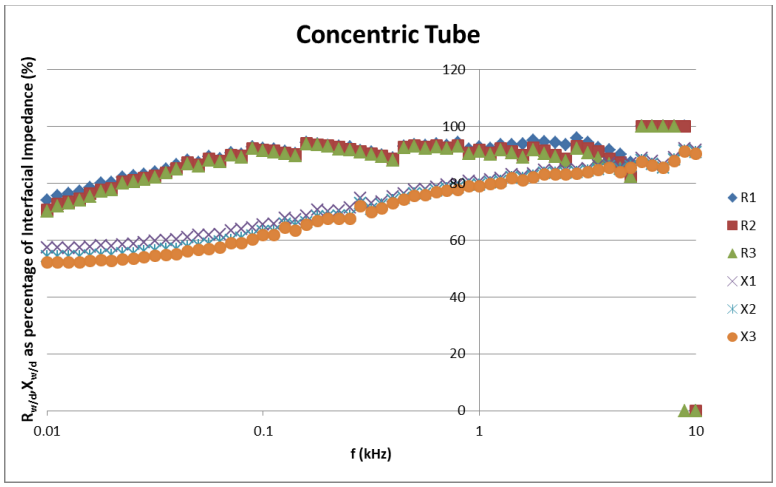

Figure 4.6: Water/DCE interfacial resistance and reactance as a percentage of total system interfacial impedance of the **(a)** single tube apparatus and **(b)** concentric tube apparatus.

Analysis of the raw data impedance collected for both of the above apparatuses shows that the above assumption cannot be made. $R_{w/d}$ and $X_{w/d}$ were first isolated by subtracting out the impedances of the NPAu/water and NPAu/DCE interfaces and R_{sol} from the raw data impedance. Figure 4.6 shows $R_{w/d}$ and $X_{w/d}$ as a percentage of interfacial resistance and reactance of the device (i.e. $R_{Au/w}+R_{Au/d}+R_{w/d}$ and $X_{Au/w}+X_{Au/d}+X_{w/d}$) for both the single tube and concentric tube apparatuses. At a frequency of 10 Hz, the water/DCE interface accounted for approximately 38% of resistance and 31% of reactance for the single tube apparatus and 72% of the total resistance and 55% of the total reactance for the concentric tube apparatus. While both of these are noticeably better in X than what was obtained for the initial

water/DCE interface in Section 2.4, where $X_{w/d}$ made up 14% of the device reactance and $R_{w/d}$ made up 50% of device resistance, the impedances of the Au/water and Au/DCE interfaces are still too large compared to the water/DCE impedance to assume that the method used to subtract them out would introduce negligible error. While the components of $Z_{w/d}$ do increase to nearly 80% of the total interfacial impedance of the system, this is only true over a very small range of frequencies. In order to effectively characterize the water/DCE interface, a larger frequency range would be required.

a) 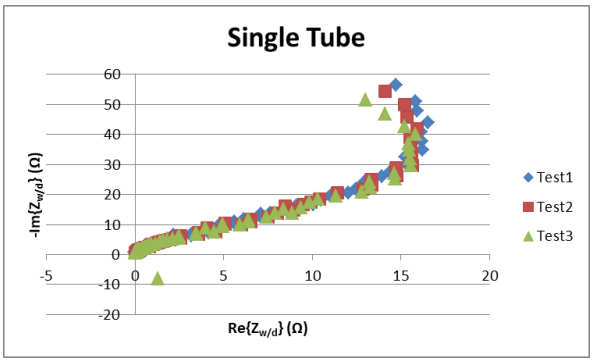

b) 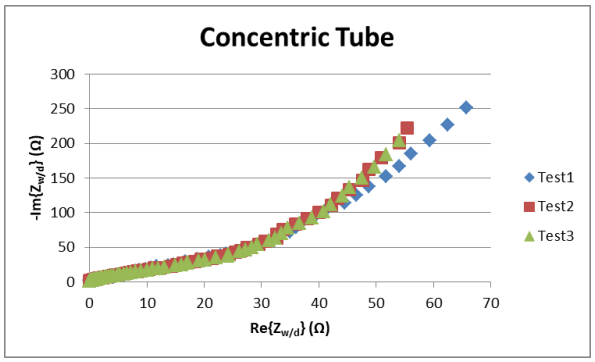

Figure 4.7: Nyquist plots of the water/DCE interfacial impedances calculated for the **(a)** single tube and **(b)** concentric tube apparatuses.

The consequence of subtracting out the impedances of the NPAu/water and NPAu/DCE interfaces using the above described method when $Z_{w/d}$ does not make up a sufficiently large enough part of the total system interfacial impedance can be explicitly seen by considering the resulting Nyquist plot of the water/DCE interface. The Nyquist plot of the single tube test given in Figure 4.7a is particularly clear. Here, the low frequency response of the water/DCE interface is clearly nonphysical, with the resistance bending back on itself. Specifically, this likely indicates that too much resistance has been subtracted out when attempting to account for the NPAu/water and NPAu/DCE impedances. It would be improbable that any reasonable information about the water/DCE interface could be gained from the equivalent circuit analysis of this data. While the Nyquist plot for the concentric tube apparatus looks more reasonable, the uncertainty caused by the subtraction of the NPAu/L impedances would

make it difficult to tell if the equivalent circuit modeling of the data would yield an accurate characterization of the water/DCE interface.

a)

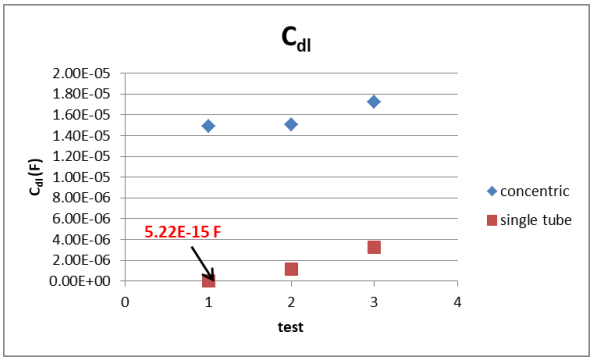

b)

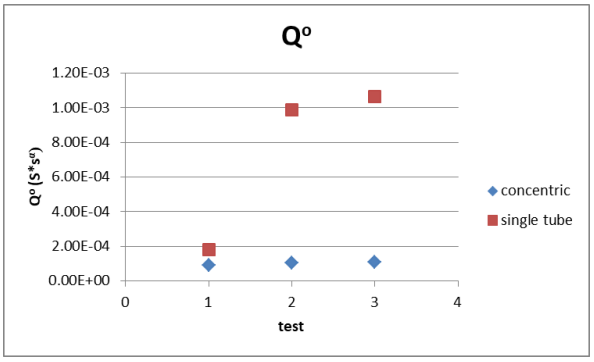

c)

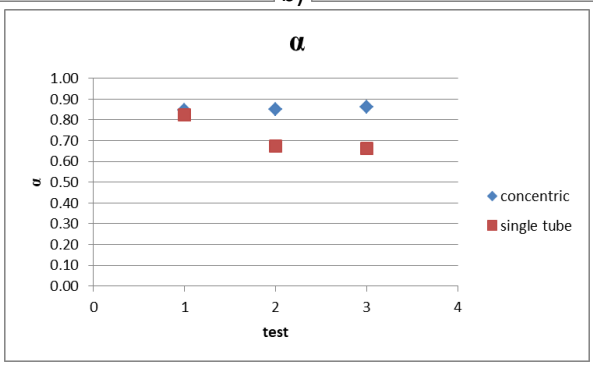

Figure 4.8: (a) C_{dl}, **(b)** Q^o, and **(c)** α obtained by the MATLAB optimization for the water/DCE interface for the single tube and concentric tube apparatuses. The water/DCE interface had the same area between tests conducted for each individual apparatus. The tolerance range is expected to be large due to the subtraction of the Au/liquid interfacial impedances.

In order to see how inaccuracies in determining the NPAu/liquid impedances affect the characterization of the water/DCE interface, each collected data set was run through the MATLAB optimization. Figure 4.8 depicts the resulting values of C_{dl}, Q^o, and α obtained for each of the three tests conducted for the single tube and concentric tube apparatuses. Because the water/DCE interfaces have the same area between the three tests conducted for a particular device, values of Q^o, α, and C_{dl} are expected to be the same for each test. This is clearly not the case for the single tube tests. While tests 2 and 3 yield roughly similar results, test 1 gives significantly different values for $C_{dl,}$ Q^o, and α. In particular, optimization of the data yielded C_{dl} on the order of 10^{-15} F for test 1 which is a clearly nonphysical value. This indicates that the errors introduced from subtraction of the NPAu/liquid

impedances prevent the MATLAB optimization from consistently and accurately minimizing the optimization function to obtain an appropriate characterization of the water/DCE interface. The concentric tube apparatus, on the other hand, performs noticeably better: a direct consequence of the larger percentage of system impedance that the water/DCE interface makes up. Although the values of the variables obtained by the optimization seem reasonable, it is uncertain whether they accurately characterize the water/DCE interface.

Section 4.2: Final Characterization of the Water/DCE ITIES

Both of the previous tests showed that the area of the Au/liquid interfaces must be further increased compared to the area of the water/DCE interface in order to gain enough sensitivity to effectively probe the water/DCE ITIES. To this end, a third apparatus that greatly increases the Au/liquid interfacial area with respect to the water/DCE ITIES was constructed. Electrodes were once again fabricated using six stacked sheets of 9 karat white gold leaf etched for 10 minutes in a 70% Nitric acid, 30% DI water solution as described in Chapter 3.

The device was constructed from two glass reservoirs stacked atop one another with a PTFE sheet in between. The reservoirs were constructed by cutting strips from standard 1”x3” microscope slides and sanding them down to heights of 10 mm. Four strips were required to make one reservoir, and each strip was 1 inch in length. Each strip was adhered together using a solvent resistant sealant. A small gap was left between two of the strips in the bottom reservoir to allow space for a syringe to be inserted for loading purposes. This gap was filled with sealant to ensure that no liquids would leak out during loading. The PTFE sheet separating the two reservoirs had a 4 mm diameter hole cut into its

center to allow for a tube with outer diameter of 4 mm to be sealed in place, connecting the two reservoirs. To piece the device together, both the top and bottom reservoirs were adhered to their respective electrodes. A small hole was left in the top reservoir to allow for air to escape during loading. The PTFE sheet (with the 4mm tube already adhered in place) was oriented to have the tube protrude into the top reservoir and then adhered to the bottom reservoir. The top reservoir was then sealed in place and the entire device was placed between a C-clamp. A schematic of this device is given in Figure 4.9.

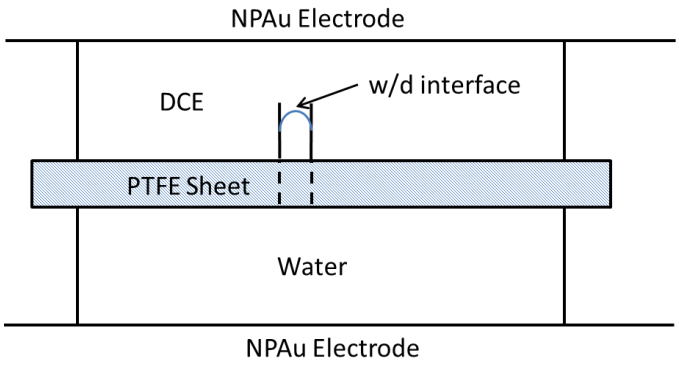

Figure 4.9: 'Big Electrode' apparatus used to probe the water/DCE ITIES.

To load the device, water was added via syringe to the bottom reservoir until it was entirely filled and water began entering the tube connecting the two reservoirs. At this point, DCE was added to the top reservoir until the tube was completely submerged. More water was added until the water/DCE interface could be easily seen. Loading was finished by adding more DCE to completely fill the top reservoir. In order to adjust the position and shape of the interface between different tests, water was either added to or removed from the system through the bottom reservoir. Both water/DCE interfaces formed within the tube and outside the top of the tube were considered to obtain data for a wide range of interfacial areas. Images of both of these are given in Figure 4.10.

a) 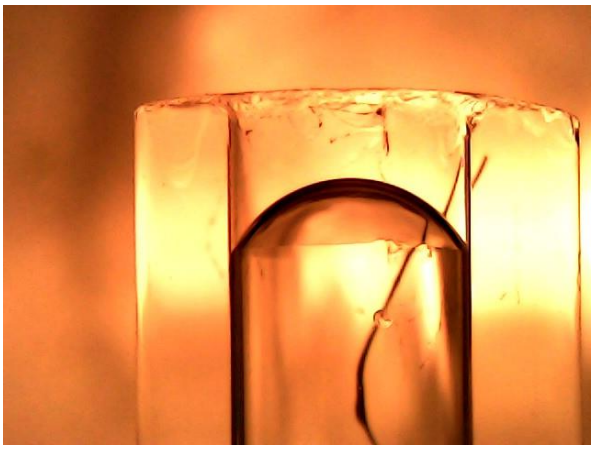 b) 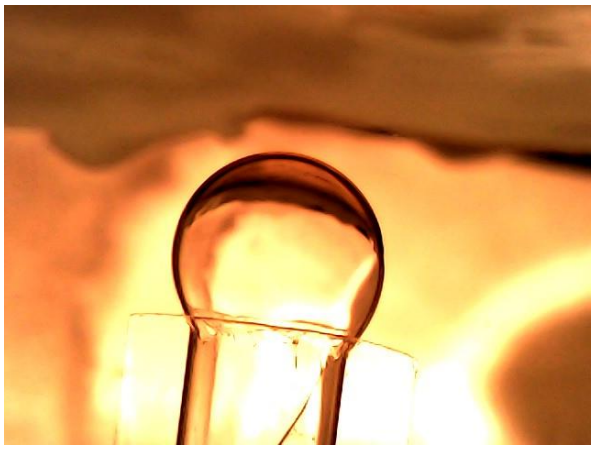

Figure 4.10: Images obtained of the water/DCE interface **(a)** inside and **(b)** outside the tube connecting the two reservoirs in the 'Big Electrode' apparatus. The tube inner diameter was measured to be 2.22 mm. The fluid outside the tube is DCE.

The ImageJ contact angle plugin was utilized to determine the water/DCE interfacial area. In order to accomplish this, a scale needed to be set on the image. Unlike the previous two apparatuses where a ruler could be held to the side and included the image, this apparatus is unable to effectively include a ruler to use for scale. To account for this, the inner diameter of the tube was measured to be 2.22 mm before constructing the device. The presence of total internal reflection in Figure 4.10 allows for a precise determination of where the inner wall of the tube is and allows for a scale to be accurately set. The process by which the water/DCE interfacial areas were determined is described in detail in Appendix A2. This process was conducted three times for each image and the results were averaged together. Note that while Tests 3-6 only had a single image taken at the end of the data collection, Tests 7-16 had images taken at the start and end of data collection. In these tests, the areas calculated in the before and after images were averaged together as well, including a total of 6 calculations of the water/DCE interfacial area. The average value obtained for A_{eq} for each test is given in Table 4.1. Error in determining $A_{w/d}$ in each test is taken as one standard deviation of the three areas determined for each of the 'before' and 'after' images.

Table 4.1: Interfacial Area Determination of the Water/DCE ITIES

test	A_{start} (mm^2)	A_{end} (mm^2)	$A_{average}$ (mm^2)	test	A_{start} (mm^2)	A_{end} (mm^2)	$A_{average}$ (mm^2)
3		4.319	4.319±0.10	10	23.520	24.359	23.940±0.56
4		4.593	4.593±0.10	11	4.922	5.395	5.158±0.28
5		6.181	6.181±0.02	12	5.111	5.233	5.172±0.11
6		16.010	16.010±0.40	13	5.141	5.248	5.195±0.15
7	14.247	13.571	13.909±0.41	14	6.721	6.511	6.616±0.17
8	13.185	14.148	13.667±0.54	15	10.264	10.879	10.572±0.42
9	22.901	23.713	23.307±0.46	16	13.305	13.275	13.290±0.23

Section 4.2.1: Effectiveness of the Transfer Effects Equivalent Circuit Model

Due to the much larger ratio of Au/liquid interfacial areas to the water/DCE interfacial area, it is assumed that the impedance contribution of the NPAu/water and NPAu/DCE interfaces make up a negligible portion of the total system impedance and are removed from the system. With this assumption, the impedance of the system becomes

$$Z_{eq} = Z_{w/d} + R_{sol} \quad (4.2).$$

The validity of this assumption can be confirmed by looking at $R_{NPAu/w}$+$R_{NPAu/d}$ and $X_{NPAu/w}$+$X_{NPAu/d}$ as a percentage of the interfacial impedances of the system ($Z_{NPAu/w}$+$Z_{NPAu/d}$+$Z_{w/d}$). Estimations of the NPAu/water and NPAu/DCE impedances were determined using the same method as described in Section 4.1, with the planar areas of the NPAu/water and NPAu/DCE interfaces being 1 in^2. The resulting percentages of total system impedance that R and X make up for the NPAu/liquid interfaces are given in

Figure 4.11 for Test 10. Note that this test was found to have the largest ITIES interfacial area. As such, the impedance contribution of the ITIES in this test will be the smallest of any of the tests. Therefore, the impedance contribution of the NPAu/water and NPAu/DCE interfaces in Test 10 will be the largest of all tests.

Over the entire frequency range considered, both the real and imaginary impedance components of the sum of both NPAu/liquid interfaces make up at most 2% of the impedance of the total interfacial impedance of the system, indicating that the NPAu/liquid interfacial impedances can be approximated as zero while introducing little error into the characterization of the water/DCE interface. Further, optimization performed after subtracting out $Z_{NPAu/w}$ and $Z_{NPAu/d}$ yields values of C_{dl}, Q^{o}, α, and R_{ct} that are for the most part less than 5% different from those obtained with the NPAu/liquid impedances are neglected entirely. Tests 6, 8, and 16 do show significantly larger differences between C_{dl} and R_{ct}, but for reasons explained later, these differences are expected to be nonphysical and instead a result of numerical errors.

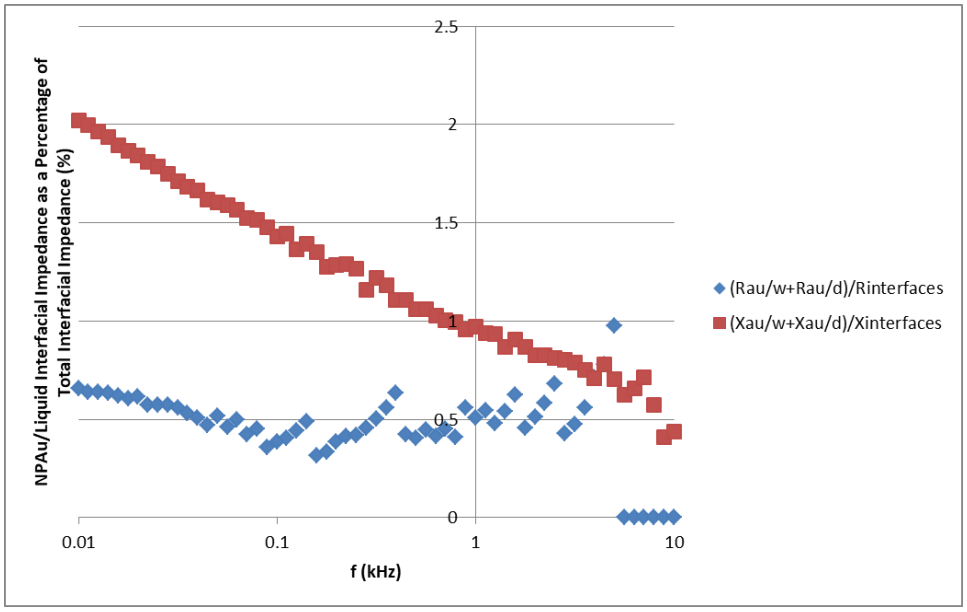

Figure 4.11: Impedance of the NPAu/water and NPAu/DCE interfaces as a percentage of the total interfacial impedance of the system for Test 10.

It is also once again assumed that the solution resistance is equal to the raw impedance data at f=10 kHz. Because this assumption was used effectively in the transfer effects model for the Au/liquid interfaces, it is expected to perform well again here. Nevertheless, this assumption was validated by generating a set of pseudo-data for the transfer effects model in Figure 4.2 using the model parameters obtained by the optimization for Test 16. The solution resistance output by the optimization parameters for this test was R_{sol}=469.6 Ω. The generated pseudo-data for Test 16 yielded R_{sol}=469.8 Ω.

Table 4.2: Transfer Effects Model Parameters for the Water/DCE ITIES

R_{ct} Included (10Hz-10kHz)						
test	C_{dl} (F)	R_{ct} (Ω)	Q^o ($S*s^{\alpha}$)	α	R_{sol} (Ω)	$\Sigma_f\|Z_{data}-Z_{fit}\|$
3	7.52E-06	194.7	5.65E-05	0.717	2180	602.84
4	4.91E-06	126.8	6.42E-05	0.675	2239	460.35
5	4.50E-06	155.6	6.56E-05	0.685	1105	371.629
6	5.34E-06	20.2	7.97E-05	0.716	456.1	70.8313
7	8.32E-06	41.8	7.75E-05	0.702	455.9	47.2033
8	6.71E-06	29.9	7.98E-05	0.706	454.2	44.4472
9	9.11E-06	16.8	8.00E-05	0.718	410.2	19.9496
10	9.26E-06	17.0	7.98E-05	0.718	409.3	24.8932
11	8.50E-16	7.1	9.05E-05	0.613	1110	600.021
12	5.64E-15	1.25E-06	8.70E-05	0.625	1065.4	554.019
13	1.90E-06	70.2	7.74E-05	0.638	1080	280.476
14	4.33E-06	48.5	7.89E-05	0.674	546.6	116.063
15	2.72E-13	1.01E-06	8.42E-05	0.730	486.3	83.5695
16	6.27E-06	29.6	8.40E-05	0.697	469.6	40.5817
R_{ct} Excluded (10Hz-10kHz)						
test	C_{dl} (F)	R_{ct} (Ω)	Q^o ($S*s^{\alpha}$)	α	R_{sol} (Ω)	$\Sigma_f\|Z_{data}-Z_{fit}\|$
3	2.38E-06		7.54E-05	0.680	2180	721.52
4	1.08E-06		7.43E-05	0.669	2239	586.158
5	1.07E-06		8.65E-05	0.636	1105	661.65
6	6.03E-14		8.14E-05	0.752	456.1	75.9604
7	7.49E-07		7.99E-05	0.753	455.9	76.6845
8	1.17E-10		8.16E-05	0.752	454.2	54.7745
9	1.71E-06		7.95E-05	0.775	410.2	33.5932
10	1.99E-06		7.94E-05	0.775	409.3	34.8999
11	3.95E-14		9.56E-05	0.601	1110	653.247
12	1.90E-13		8.69E-05	0.625	1065.4	554.051
13	1.47E-13		8.66E-05	0.624	1080	502.111
14	9.96E-13		8.20E-05	0.700	546.6	193.145
15	2.12E-09		8.43E-05	0.730	486.3	83.5005
16	5.67E-14		8.51E-05	0.741	469.6	64.7866

The MATLAB optimization was run over a frequency range of 10 Hz-10 kHz for each test using the Transfer Effects model with R_{ct} both included and excluded. Starting points when excluding R_{ct} were x_o=[1E-5, 1E-6, 0.8] (x=[C_{dl}, Q^o, α]) and the corresponding lower and upper bounds were lb=[0,0,0,0] and ub=[1E-2,1E7,1E-2,1], respectively. Excluding R_{ct}, the starting points were x_o=[1E-5,10,1E-6, 0.8] (x=[C_{dl},R_{ct},Q^o,α]) with lower and upper bounds of lb=[0,0,0] and ub=[1E-2,1E-2,1], respectively. The results of both cases can be seen in Table 4.2. Plots of the behavior of C_{dl}, Q^o, and α for this data are provided in Figure 4.12. It is important to note that tests with the water/DCE interface located within the tube as in Figure 4.10a (Tests 3-5, 11-13) had reduced sensitivity during data collection compared to tests with the interface located outside the tube as in Figure 4.10b. This is due to the increased solution resistance associated with the longer DCE path length increasing the system resistance enough to trigger the 4192A to jump to the next sensitivity range. As a result, these tests exhibit noticeably larger optimization function values than tests with the water/DCE interface located outside of the tube.

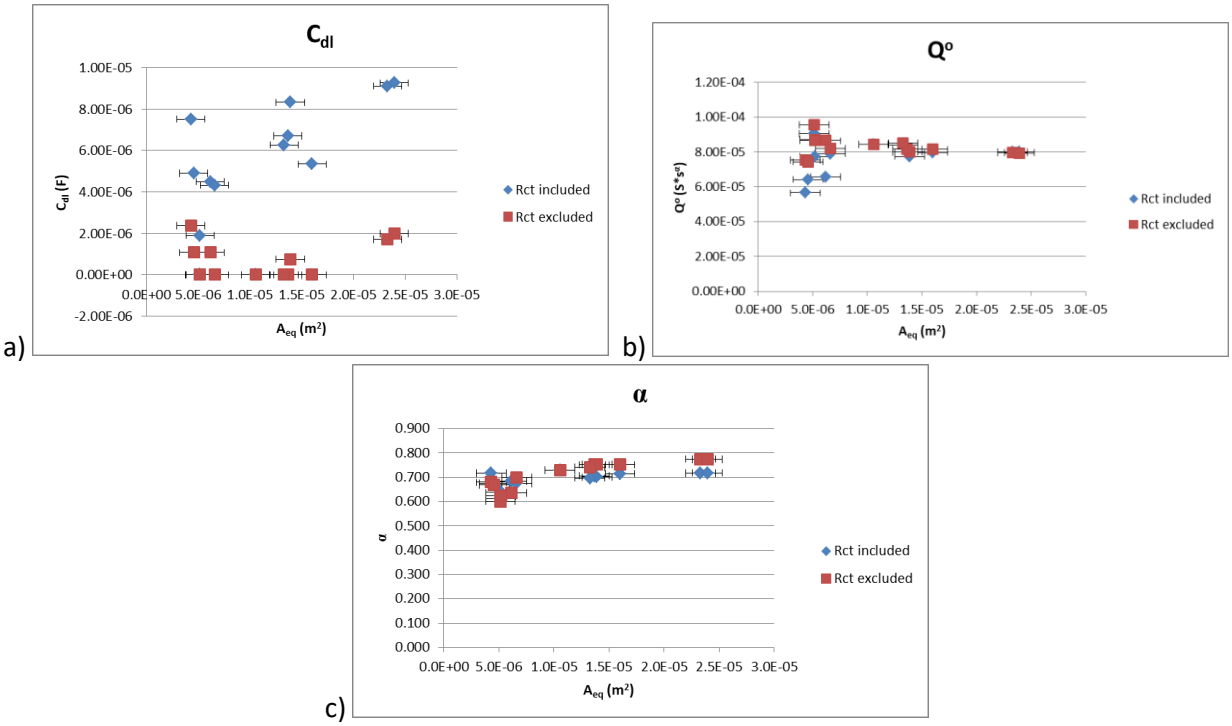

Figure 4.12: (a) C_{dl}, **(b)** Q^o, and **(c)** α obtained from MATLAB optimization of the transfer effects equivalent circuit model for the water/DCE ITIES both including and excluding the presence of R_{ct}. The optimization was run over a frequency range of 10 Hz-10 kHz.

It is clear from the examination of the optimization function values in Table 4.2 and the nonphysical values obtained for C_{dl} seen in Figure 4.12 upon excluding R_{ct} from the model that inclusion of R_{ct} yields a better fit than excluding it. This brings to light a significant difference between the model developed for the Au/L interfaces and the w/d ITIES. While charge transfer was shown to have a negligible effect on the impedance behavior of the Au/L interfaces, charge transfer may play an important role in the impedance behavior of the w/d ITIES. To study the impact of R_{ct} on the impedance behavior of the w/d ITIES, pseudo-data was generated for Test 16 using the values obtained for Q^o, α, and R_{ct} obtained in Table 4.2 for various values of R_{ct} ranging from 1 Ω to 1E7 Ω in order to study the impact of R_{ct} on $\sum_f |Z_{data}-Z_{fit}|$ for the water/DCE ITIES.

The resulting plot shows a single minimum located near 30 Ω, as can be seen in Figure 4.13. Above this value, the optimization function value dramatically increases until finally leveling off as R_{ct} approaches 1E5 Ω. For R_{ct} less than the minimum R_{ct}, the optimization function value increases before quickly leveling off as R_{ct} approaches zero. This overall behavior indicates that for a starting point of R_{ct} less than 1 kΩ, the optimization should converge to the global minimum. Comparison of the minimum obtained by the pseudo-data to the result obtained by the MATLAB optimization for Test 16 shows that this is the case. The above pseudo-data analysis yielded a minimum optimization function value for R_{ct}=30 Ω while the optimization yielded R_{ct}=29.6 Ω. This was also tested for a starting point of R_{ct}=1 kΩ. Figure 4.14 shows that the change in starting point of R_{ct} has little impact on the final value obtained by the optimization.

a)

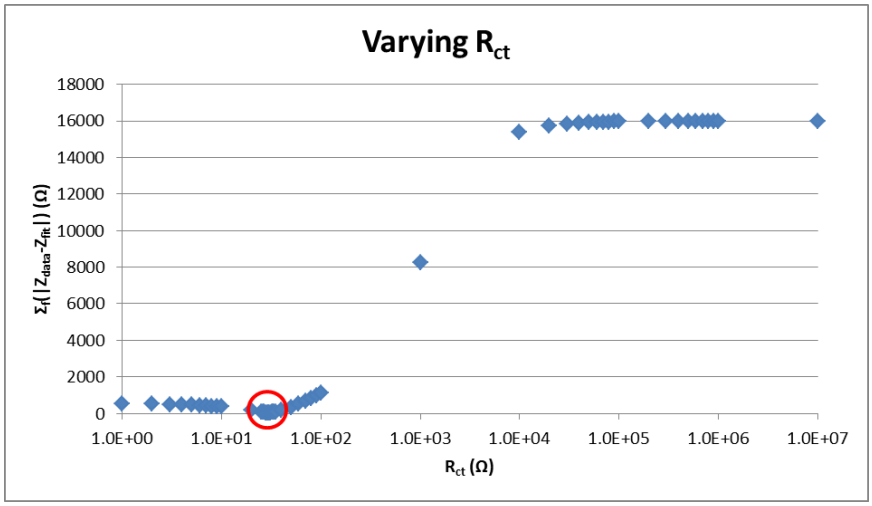

b)

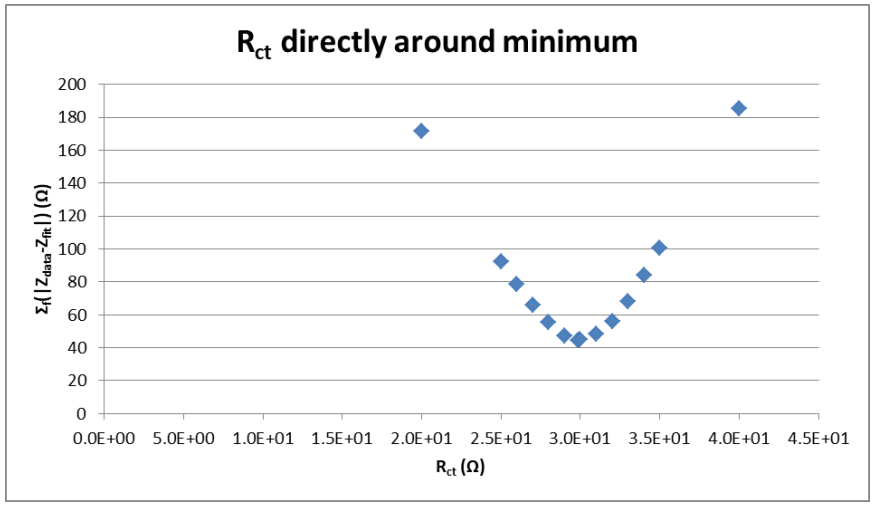

Figure 4.13: (a) Pseudo-data spectrum generated for Test 16 showing the behavior of the optimization function value for various R_{ct}; **(b)** Close-up of the red circled region depicting the local minimum over the considered R_{ct} spectrum in (a).

An interesting result of Table 4.2 is that the values obtained for R_{ct} are noticeably different from one another. Since the optimization is expected to yield the appropriate value for R_{ct}, this indicates that there must be some dependence with the interfacial area. This can be seen in Figure 4.14, which neglects the R_{ct} outliers given in Tests 12 and 15. For areas smaller than 5 mm^2 in size, R_{ct} increases dramatically. As the area of the interface increases, the value of R_{ct} levels out. This behavior looks similar of that seen for the resistance of a path of fluid. Recall that the resistance of a path of fluid can be expressed as

$$R_{fluid} = \frac{l}{\sigma A} \tag{4.3}$$

where l, in this case, would correspond to the thickness of the water/DCE interface, σ is the electrical conductivity associated with the water/DCE interface, and A is the cross-sectional area of the resistance path that would be most similar to the area of the water/DCE ITIES. Increasing the area of the resistance path by increasing the area of the ITIES then results in a decrease in resistance associated with that fluid path.

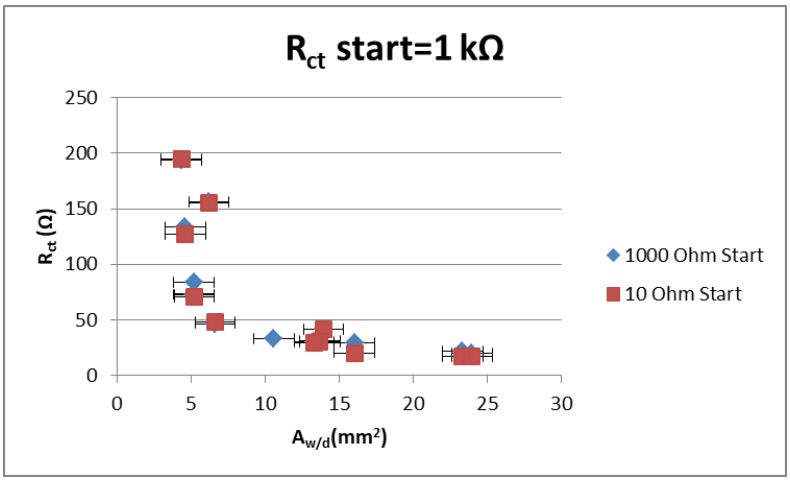

Figure 4.14: Dependence of R_{ct} on the area of the water/DCE interface given the results of the optimization shown in Table 4.2. Obvious outliers are neglected.

Section 4.2.2: Optimization over the High Frequency Regime

As can be seen in Table 4.2 for Tests 11, 12, and 15 for included R_{ct}, the optimization returns several nonphysical values for C_{dl}. Further, while the sensitivity difference might be able to explain this behavior for Tests 11 and 12, it is unable to explain why Test 15 behaves in this manner. While the increase of C_{dl} in $A_{w/d}$ can clearly be seen in Figure 4.12a, there is still a significant amount of variation present between tests. Due to how the HP 4192A operates, the sensitivity of the impedance data changes by one decimal place at f=446.68. As a result, impedances at frequencies greater than or equal to this point have improved sensitivity than the points below it. That is to say, for example, that tests with a sensitivity of 1 Ω below f=446.68 Hz will have a sensitivity of 0.1 Ω above this frequency.

It was hypothesized that this sensitivity shift could be responsible for some of the scatter seen in the plots of C_{dl}, Q^{o}, and α versus water/DCE interfacial area. To test this, the optimization was run two additional times for each test: once over the frequency range of 10-398.1 Hz and once over the frequency range of 446.68 Hz-10 kHz. The results are shown in Figure 4.15, which depicts the differences in how C_{dl}, Q^{o}, α, and R_{ct} behave when the optimization is run above and below the sensitivity shift. An interesting result of this test is that it becomes abundantly clear that C_{dl} dominates at high frequencies, as evident by the much lower amount of variance present in the 'above' data series. Likewise, the CPE dominates in the low frequency regime, allowing for more consistent values of Q^{o} and α to be obtained by the optimization. This behavior was also seen when considering the Nyquist plot of pseudo-data generated for the Transfer Effects model of the Au/water and Au/DCE interfaces in Figure 2.16.

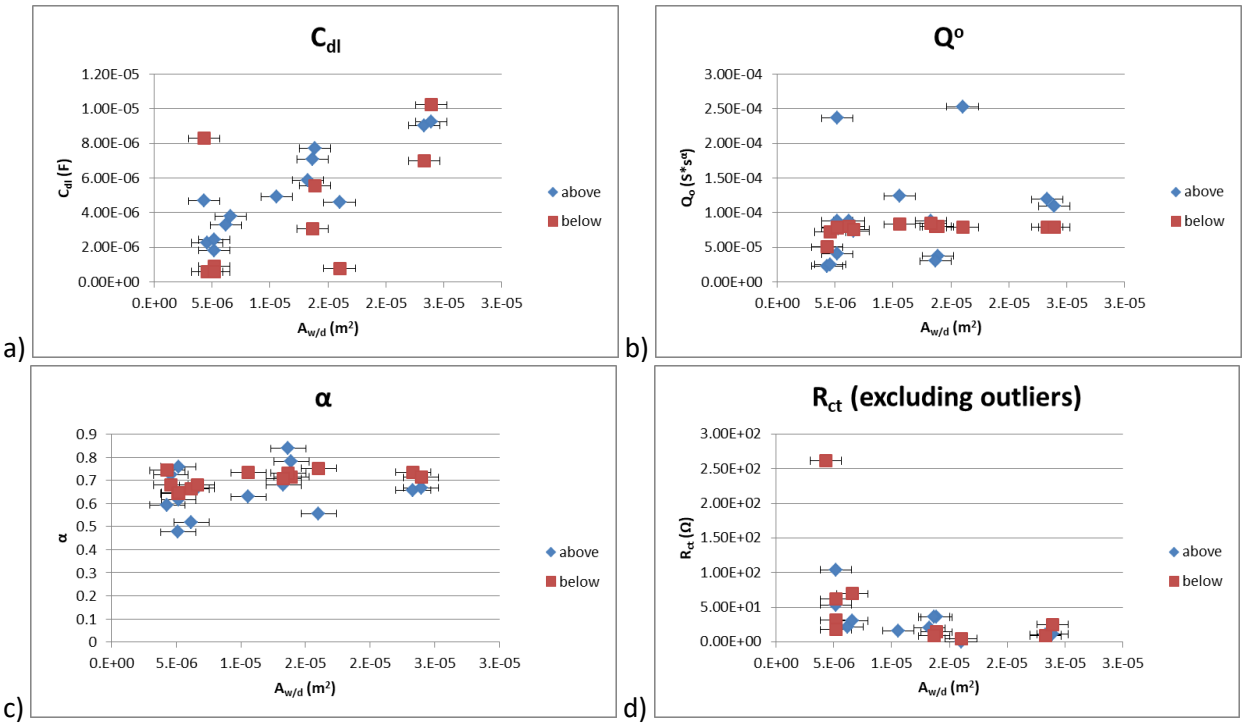

Figure 4.15: Differences in behavior of **(a)** C_{dl}, **(b)** Q^{o}, **(c)** α, and **(d)** R_{ct} for optimizations run for frequencies above and below the sensitivity shift present in the HP 4192A.

While there are still some outliers, the variance between tests is much smaller than what was seen for the optimization run over 10 Hz-10 kHz and the increase of C_{dl} with respect to the water/DCE

interfacial area can easily be seen for the frequency range above the sensitivity shift. Conversely, both Q^o and α are much more uniform when optimizing below the sensitivity shift. Since the CPE is expected to dominate the interface's impedance behavior at low frequencies, it makes sense that optimizing over high frequencies would yield much less sensitive results for Q^o and α. Similarly, optimizing over low frequencies would yield significantly less sensitive results for C_{dl}.

Surprisingly, Q^o remains constant in water/DCE interfacial area. This is especially odd considering that the transfer effects model for the 'flat' Au/water and Au/DCE interfaces *did* show a loose dependence of Q^o on interfacial area (Figure 2.15). While the cause of this behavior change is currently unknown, it is not expected to greatly impact the characterization of the water/DCE interface; however, it is something that should be studied in closer detail in future work. A hypothesis for this behavior is discussed later in the chapter. In any case, the unclear variation with respect to interfacial area reduces the plausibility of Q^o as being an effective measurement variable to use in an ITIES-based sensing device.

Note that the plots of R_{ct} vs. $A_{w/d}$ in Figure 4.15d remain noisy regardless of whether the frequency ranges above or below the sensitivity shift is considered. Table 4.2 shows that the values of R_{ct} obtained by the optimization remain relatively small. This combined with the CPE being dominant at low frequencies indicates that the impact of R_{ct} on the system will be most noticeable at lower frequencies; however, the impedance of R_{ct} is much less than that of the CPE within this frequency range. This results in R_{ct}'s contribution to the behavior of the system to be overshadowed by the CPE. As the frequency range is increased, C_{dl} begins to dominate the behavior of the system as the contributions of R_{ct} and the CPE grow weaker. As a result, the contribution of R_{ct} is overshadowed by other system effects regardless of the frequency range considered. While R_{ct} does impact the interface's behavior, its effect is mitigated by other more dominant effects and, as a result, the system is not sensitive enough to changes in R_{ct} to be able to obtain specific values, resulting in the variance seen in Figure 4.15d.

Note that the above analysis is only true for small enough R_{ct}. Reduction of the ITIES area will result in a rapid increase in R_{ct} as evident by Figure 4.15d, and, as R_{ct} increases in magnitude, its effect becomes more and more prominent in overall interfacial behavior. While this may initially seem like an issue, it may actually help increase sensitivity to C_{dl} when the interfacial area is on the microscale. To see this, it becomes useful to consider the equivalent circuit model in Figure 4.2. Because R_{ct} is in series with the CPE, it has the effect of shielding the rest of the system from the CPE. Small R_{ct}'s are unable to effectively block the CPE behavior since $Z_{CPE}>>R_{ct}$ at low frequencies where the CPE effect is strongest. As R_{ct} becomes more comparable to Z_{CPE}, however, it is able to more effectively block the CPE, reducing the frequency range over which it dominates. In the limit where $R_{ct}>>Z_{CPE}$, the effect of the CPE is almost entirely blocked and the reactance of C_{dl} is able to dominate over a much larger frequency range. For microscale interfaces, it is then plausible that C_{dl} will play the prominent role in interfacial impedance behavior over a large frequency range.

Figure 4.16 effectively shows that the variance seen in values of C_{dl}, Q^o, and α by the optimization is a direct result of the frequency range that is considered. This is because different components of the equivalent circuit model dominate the impedance behavior of the water/DCE ITIES at different frequencies. Because the impedance of the water/DCE ITIES is largest at low frequencies, the optimization will tend to favor the low frequency data, since the function being minimized depends on $|Z_{data}-Z_{fit}|$. For example, a 5% error between the model and fit at f=10 Hz will correspond to a larger value of $|Z_{data}-Z_{fit}|$ than a 5% error between the model and fit at f=1 kHz. As a result, the optimization will prioritize the variables associated with the CPE since they dominate system behavior at low frequencies. This means that as long as the low frequency regime is included in the optimization, the resulting values of Q^o and α will maintain greater sensitivity at the cost of reduced sensitivity to C_{dl} regardless of whether the high frequency regime is included. Conversely, optimizing over higher frequencies will increase sensitivity to C_{dl} while decreasing sensitivity to Q^o and α.

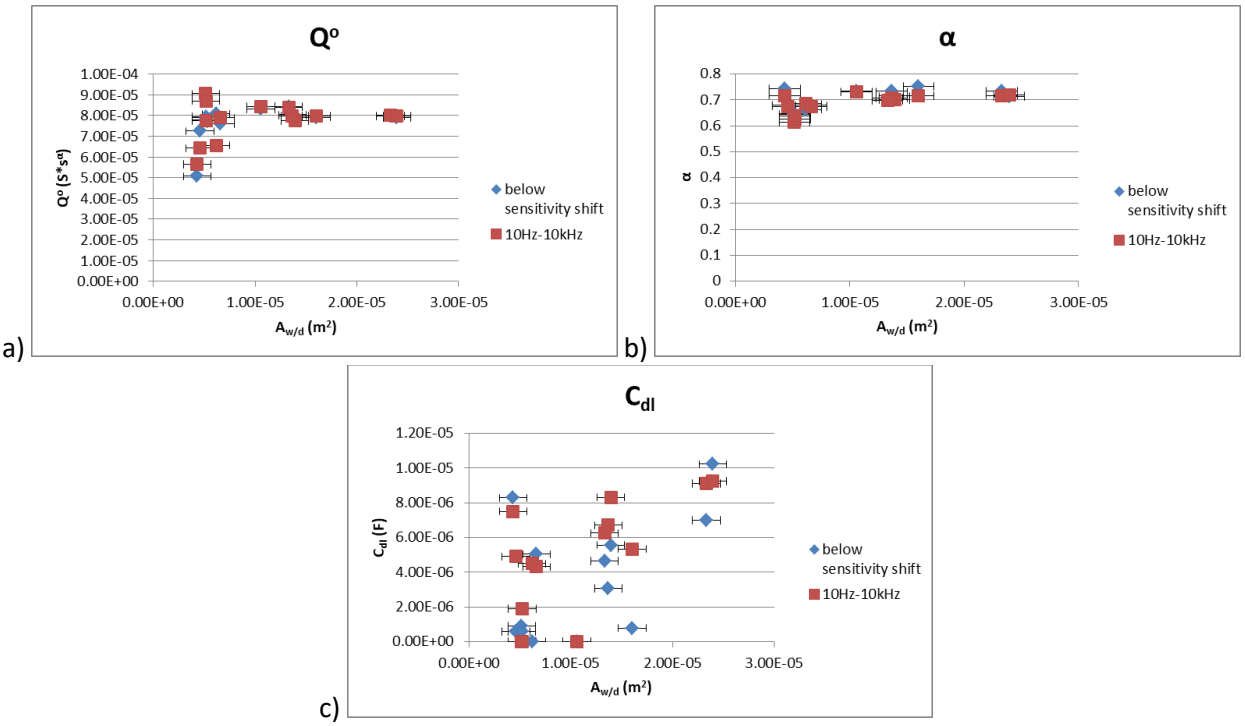

Figure 4.16: Prioritization of the MATLAB optimization to low frequency data leads to increased sensitivity to the variables associated with the CPE at the cost of sensitivity to C_{dl} whenever the low frequency regime is included in the optimization.

Since the transfer effects model was also used for characterization of the 'flat' Au/water and Au/DCE interfaces, it is to be expected that the optimization for these interfaces will perform in a similar manner at it does for the water/DCE interface. While there is variance present in the plot of C_{dl} vs. $A_{Au/liquid}$ in Figure 2.15c, it is significantly less than what was seen when optimizing the water/DCE ITIES over the same 10 Hz-10 kHz frequency range. This can be explained through examination of the values of Q^o obtained by the optimization for each interface. In the case of the Au/water and Au/DCE interfaces, Q^o is on the order of 10^{-6} where as it is on the order of 10^{-4} for the water/DCE ITIES. The impedance of each interface using the transfer effects model can be expressed as

$$Z_{eq} = R_{sol} + \frac{1}{C_{dl} j\omega + \frac{1}{R_{ct} + \frac{1}{Q^o (j\omega)^{\alpha}}}} \qquad (4.4).$$

Using the respective values for Q^o and noting that R_{ct}=0 for the Au/liquid interfaces and R_{ct} ~ 100 Ω for the water/DCE ITIES, this approximately reduces to

$$Z_{Au/L} = \frac{1}{Cjw+10^{-6}} \quad (4.5)$$

for the Au/water and Au/DCE interfaces and

$$Z_{w/d} = \frac{1}{Cjw+10^{-4}} \quad (4.6)$$

for the water/DCE ITIES.

For both the Au/L and water/DCE interfaces, C_{dl} is on the order of 10^{-6} F. Since Q^o>C_{dl} for the water/DCE ITIES, the impedance of the interface will be dominated by Q^o over a larger frequency range, leading to less sensitivity in determining C_{dl} when optimizing over a frequency range that includes low frequencies. On the other hand, Q^o ~ C_{dl} for the Au/liquid interfaces so Q^o will dominate the system impedance over a smaller frequency range. This will lead to increased sensitivity in determining C_{dl} when optimizing over a frequency range that includes low frequencies. The transfer effects model for the Au/liquid interfaces is able to provide more consistent results for C_{dl} than it is for the water/DCE ITIES when considering frequency ranges that include low frequencies.

The behavior of the optimization poses a question as to its overall effectiveness. If different components of the equivalent circuit dominate over different frequency ranges, it cannot necessarily be assumed that the optimization will perform without issue over a wide frequency range. While this is certainly something that needs to be considered (and will be in the following sub-section), it may still be possible to obtain an accurate representation of C_{dl} with the optimization in its present form. Figure 4.15a shows that only considering the frequency range above the data sensitivity shift greatly reduces the variance seen in C_{dl}. Since C_{dl} dominates the interface's impedance behavior at high frequencies, it is possible that only optimizing over the high frequency range would yield consistent results for C_{dl}. This would, however, come at a cost of reduced sensitivity of Q^o and α as was seen in Figure 4.15 b and c. This may not be a significant issue, however, as it has been shown in Figures 4.12 and 4.16 that Q^o has a

minimal relationship with the water/DCE interfacial area, making it non-ideal as a measurement parameter for an ITIES-based measurement device. As a result, any variations in Q^{o} and α may not be particularly important so long as a clear behavior of C_{dl} with interfacial area can be obtained.

The MATLAB optimization was rerun for each test utilizing frequency ranges of 1-10 kHz (21 data points), 10-100 kHz (21 data points), and 31.662-100 kHz (11 data points). The values of C_{dl} obtained through optimization over each frequency range for each test was compared to the values obtained when optimizing over 10 Hz-10 kHz (81 data points) and the frequency range above the sensitivity shift (0.44668-10 kHz; 28 data points). Inspection of Figure 4.17 shows that optimizing over higher frequencies greatly reduces the amount of variance seen in C_{dl} between tests. Further, all frequency ranges considered with the exception of f=31.622-100 kHz yielded very similar values for $C_{dl}/A_{w/d}$. It is important to note that the outlying data set was only optimized using a total of 11 frequency points, and as such, not as much confidence can be held in the optimization since very few data points were considered. Note that this plot excludes the results from Tests 3-5 and 11-13 due to the reduced sensitivity during data collection.

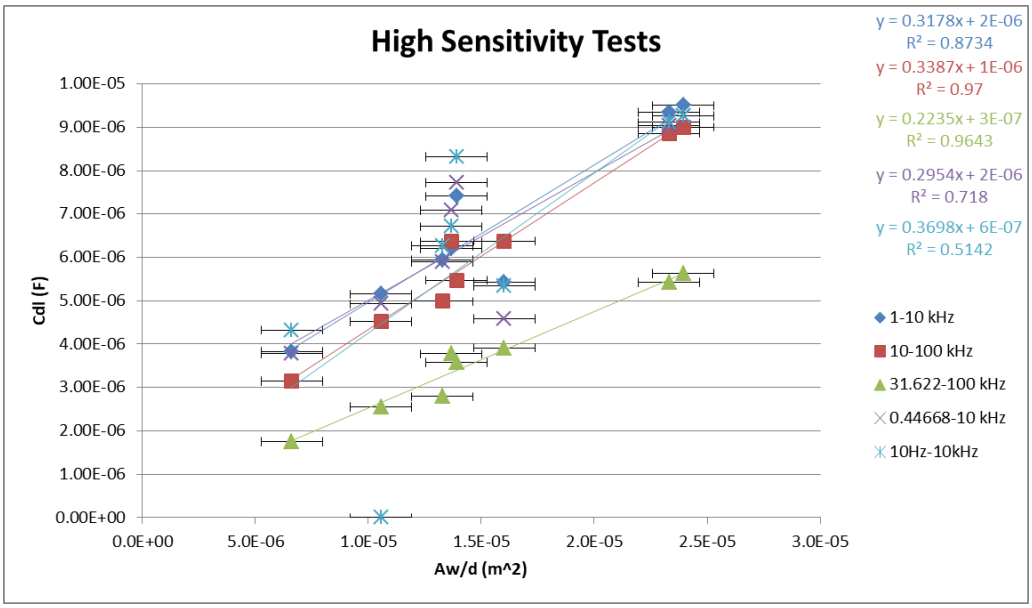

Figure 4.17: Effect of optimizing over higher frequencies on the variance seen in C_{dl}.

Section 4.2.3: Impact of Weighting the Optimization Function

An issue with the above optimization approach is that sensitivity to the CPE is sacrificed for greater sensitivity to C_{dl}. This was due to the CPE and C_{dl} dominating system behavior over different frequency regimes. It has been previously said that because the impedance of the water/DCE ITIES is largest at low frequencies, the optimization will tend to favor the low frequency data, since the function being minimized depends on $|Z_{data}-Z_{fit}|$. In order to make the optimization more sensitive to data points at higher frequencies, the optimization function was multiplied by a weighting function:

$$\sum_f F(\omega)|Z_{data} - Z_{fit}| \quad (4.7).$$

The weighting function, F(ω), is a function of angular frequency and is chosen in such a way as to either increase the importance of $|Z_{data}-Z_{fit}|$ at high frequencies or decrease its importance at low frequencies, thereby making the entire considered frequency range important in the optimization.

Three preliminary weighting functions were tested: $F(\omega)=\omega$, $F(\omega)=\omega^{0.5}$, and $F(\omega)=1/|Z_{data}(\omega)|$. $F(\omega)=\omega$ was chosen as an option due primarily to its simplicity. Since ω increases linearly in f, the impact of the data points at higher frequencies should be brought more into line with the lower frequency data points. $F(\omega)=\omega^{0.5}$ was chosen as a second option in case $F(\omega)=\omega$ was too aggressive in weighting the high frequency data points. $F(\omega)=1/|Z_{data}(\omega)|$ was chosen since it most closely resembles what would be seen in a standard procedure for the normalization of data. Because impedances are larger at low frequencies, the impact of low frequency data will be lessened, ensuring that the entire frequency range is impactful in the optimization. With this third choice of a weighting function, the optimization function of Equation 4.7 takes a form akin to that of the sum of percent errors between the raw data impedance and the fit at each considered frequency.

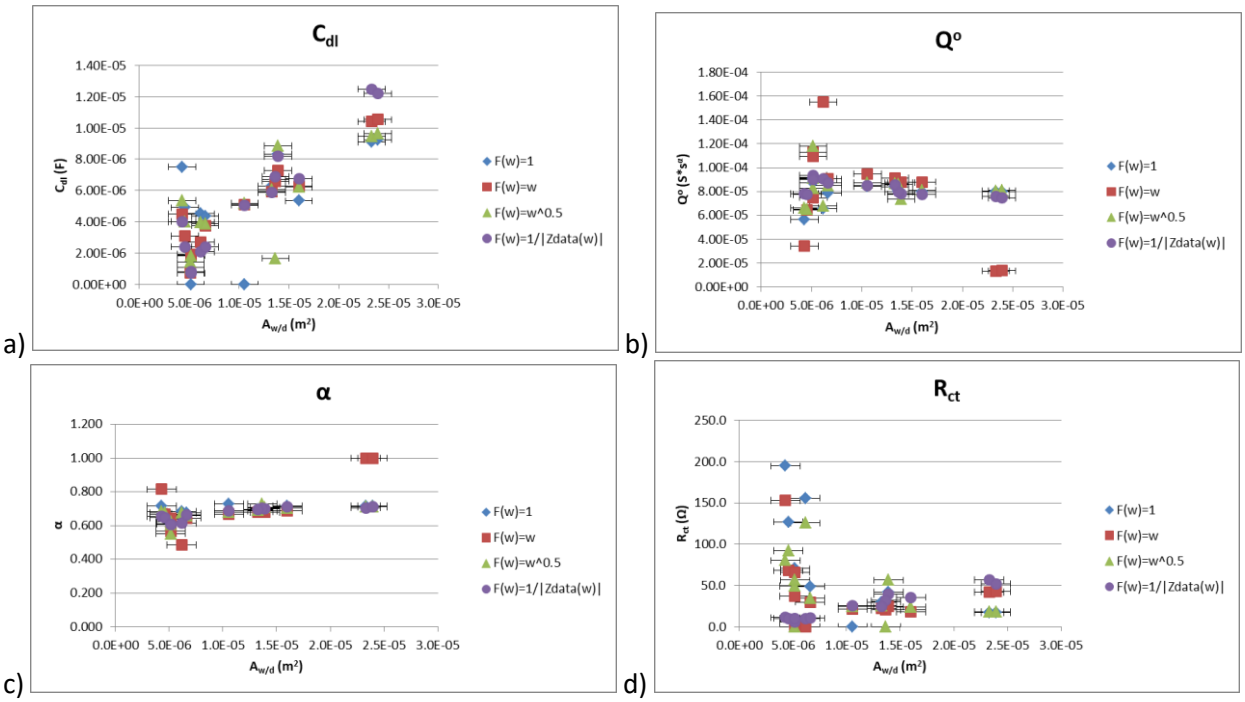

Figure 4.18: Impact of different weighting functions on behavior of the MATLAB optimization. F(ω)=1 corresponds to no weight being applied to the optimization function.

Figure 4.18 shows the impact of applying the three different weighting functions to the optimization function when optimized over a frequency range of 10 Hz-10 kHz. In each of these plots, a weighting function of F(ω)=1 corresponds to what was obtained by the optimization with no weight applied. All three weighting functions provided cleaner behavior for C_{dl}. While F(ω)=ω exemplifies this, it also yields increase variance in the CPE parameters, indicating that the weight has been shifted too far to higher frequencies to the point where impact of the low frequency data points is being mitigated. In contrast, $F(\omega)=\omega^{0.5}$ yields consistent values for the CPE parameters while exhibiting a larger amount of variance in C_{dl}. This indicates that the high frequency data points have not been weighted enough. Application of the weighting function $F(\omega)=1/|Z_{data}(\omega)|$ yields an optimization that is capable of providing both clean behavior for C_{dl} and consistent values for Q^o and α. This weighting function appropriately weights the low frequency and high frequency data enough to ensure that the optimization is effective over the entire considered frequency range.

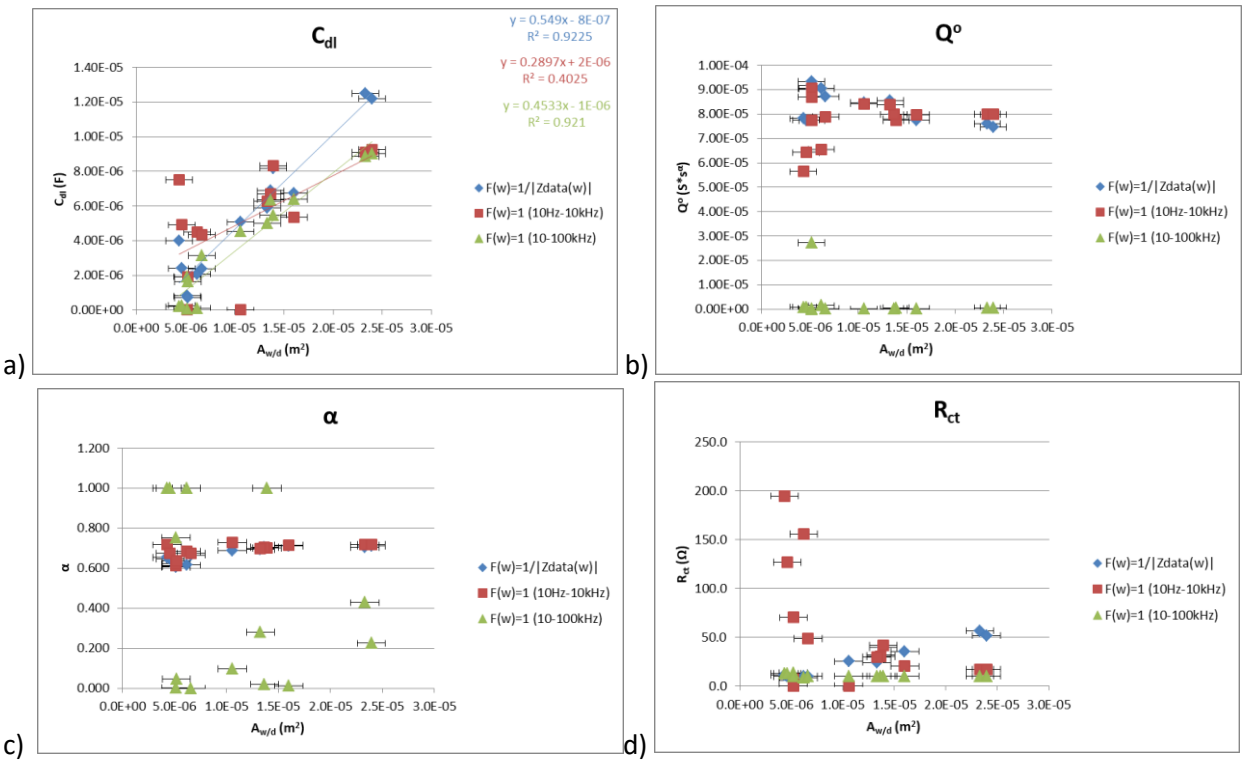

Figure 4.19: Impact of either weighting the optimization function or only considering high frequency data on the optimization performance.

While optimizing over only the high frequency data (10-100 kHz) without application of a weighting function was able to yield more sensitive results for C_{dl}, it did so at a cost of sensitivity for the CPE parameters Q^o and α. With the inclusion of $F(\omega)=1/|Z_{data}(\omega)|$ in the optimization function, the optimization is able to obtain sensitive results for C_{dl}, Q^o, and α for the entire considered frequency range of 10 Hz-10 kHz. This can be seen in Figure 4.19, which depicts how the output of the four optimization variables behave when $F(\omega)=1/|Z_{data}(\omega)|$ is included in the optimization function and when it is excluded and the optimization is run over different frequency ranges. Inclusion of the weighting function and consideration of only the high frequency data are both methods capable of producing sensitive results for C_{dl}; however, inclusion of the weighting function also yields clean behaviors for α and Q^o that are in agreement with what was seen when running the optimization over the entire frequency range with no weighting function. As a result, the weighting function $F(\omega)=1/|Z_{data}(\omega)|$ enables the optimization to obtain sensitive results for both the CPE parameters and C_{dl}.

An interesting result of applying the weighting function $F(\omega)=1/|Z_{data}(\omega)|$ to the optimization is the resulting change in behavior observed for R_{ct} as seen in Figure 4.19d. To study this in greater detail, impedance pseudo-data was generated using the average values obtained from the weighted optimization conducted over f=10Hz-10kHz for $(C/A)_{w/d}$, Q^{o}, and α as given in Table 4.3. R_{sol} and $A_{w/d}$ were taken to be the values appropriate for Test 8. Impedance pseudo-data was generated for R_{ct}=0 and 100 Ω, and the behavior of $|Z(R_{ct}=0)-Z(R_{ct}=100)|$ with frequency was plotted as in Figure 4.20. The large values of $|Z(R_{ct}=0)-Z(R_{ct}=100)|$ in the low frequency regime show that the model is most sensitive to changes in R_{ct} at low frequencies. Thus, in order to obtain the greatest sensitivity to R_{ct}, the impedance data should be optimized over a frequency range of roughly 10-100 Hz.

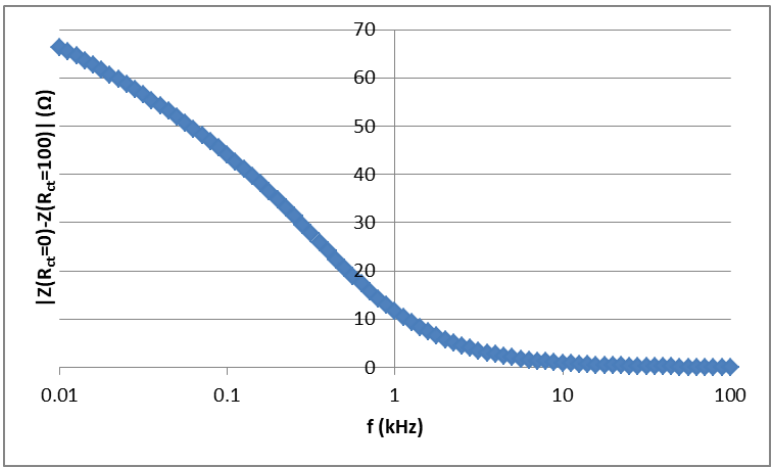

Figure 4.20: Sensitivity of model to changes in R_{ct}. The large values of $|Z(R_{ct}=0)-Z(R_{ct}=100)|$ at low frequencies indicates that the model is most sensitive to changes in R_{ct} at low frequencies.

With this knowledge, the MATLAB optimization script was modified to specify values of C_{dl}, Q^{o}, and α as given in Table 4.3, leaving R_{ct} as the only variable in the optimization function. With these changes made, the optimization was run over a frequency range of 10-100 Hz for each test and the output value of R_{ct} was recorded. The result of this methodology is shown by the blue data series in Figure 4.21. Note that the red and green series do not specify C_{dl}, Q^{o}, and α in the optimization and

instead leave them as variables to be solved for (i.e. these series match the purple circles in Figure 4.18d and the red squares in Figure 4.14, respectively). By determining R_{ct} using the above described method, the behavior reverts to a similar behavior seen when optimizing over the entire frequency range without application of a weighting function. This suggests that the different behavior of R_{ct} seen when applying the weighting function to an optimization conducted over f=10Hz-10kHz is a result of numerical error. Like the determination of Q^{o}, α, and C_{dl} in Table 4.3, tests with low sensitivity during data collection are omitted from the determination of R_{ct} due to the increased amount of error in these tests. Because R_{ct} should equal zero when the interfacial area is zero, the line of best fit shown in Figure 4.21 is constrained to pass through the origin.

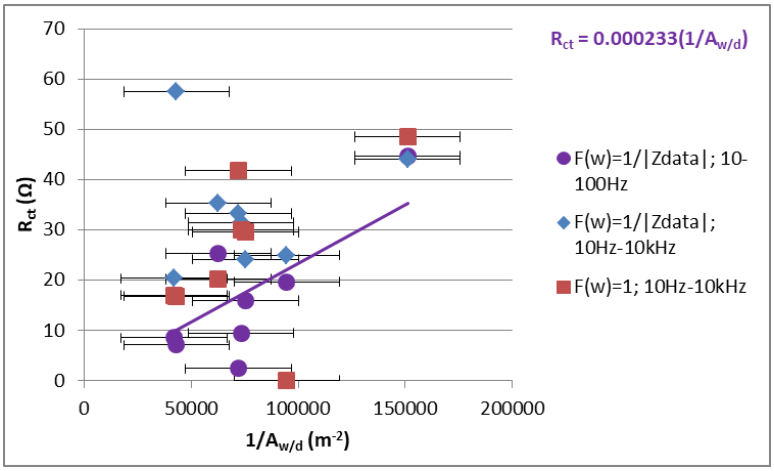

Figure 4.21: Improved behavior of R_{ct} upon consideration of optimizing with a weighting function over a frequency range of 10-100 Hz.

Using the above described method to determine R_{ct} yields a loosely linear behavior with the inverse of the water/DCE interfacial area. This is in agreement with what is given for the resistance of a length of fluid as given by Equations 4.3 and 2.2. In an electrolyte solution, the electrical resistance is a measure of how difficult it is for ions carrying charge to travel over a length of fluid when subjected to an applied potential. Because the charge transfer resistance is a measure of how difficult it is for charge to transfer from the aqueous phase to the organic phase (i.e. move across the ITIES), it makes sense that it would behave in a similar manner as the resistance of an electrolyte solution.

Nyquist plots were generated for each test over a frequency range of 10 Hz-10 kHz to compare the impedance fit given by the optimization variables listed in Table 4.3 with the raw data impedance of each test. The plots for Tests 4, 7, 13, and 14 are shown in Figure 4.22, with Nyquist plots over 1-10 kHz also provided. While Test 13 has a noticeably worse fit, this can be attributed to the reduced sensitivity of the 4192A during data collection for these tests as discussed in Section 4.2.1. Nyquist plots of data collected for tests with greater sensitivity during data collection (such as Tests 7 and 14) are fit by the transfer effects equivalent circuit model incredibly well over the entire considered frequency range of 10 Hz-10 kHz. Within the 1-10 kHz frequency range, C_{dl} dominates the impedance behavior of the system as evident by the nearly vertical lines present in the Nyquist plots. In all cases, the impedance fits given by the model variables listed in Table 4.3 accurately characterize the impedance behavior of the water/DCE ITIES.

a)

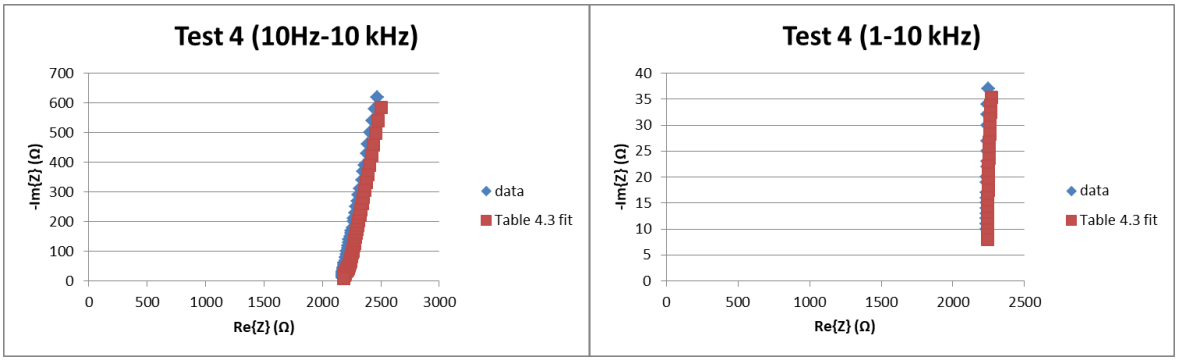

b)

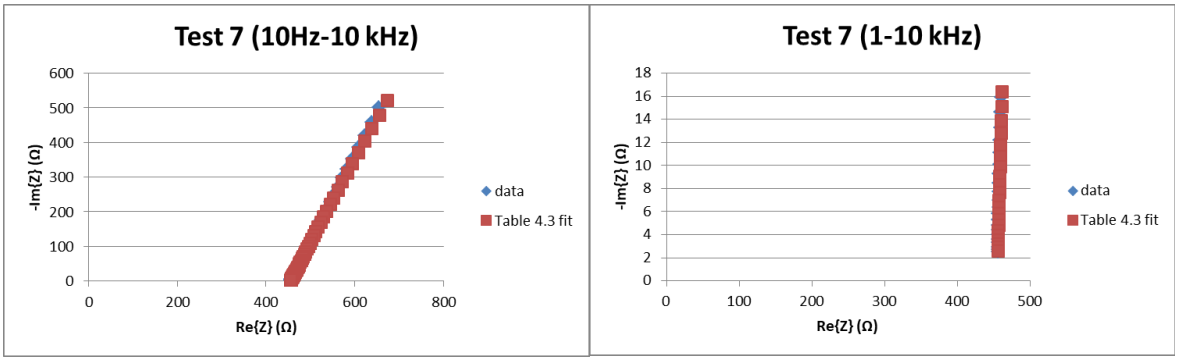

c)

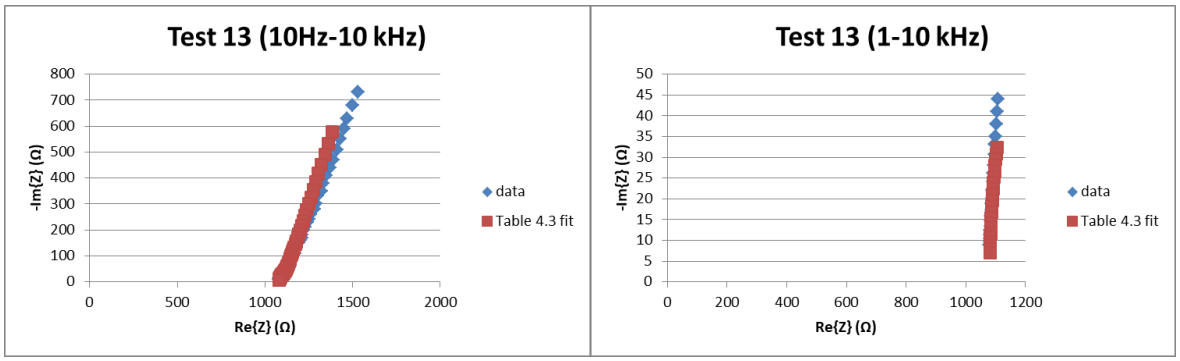

d)

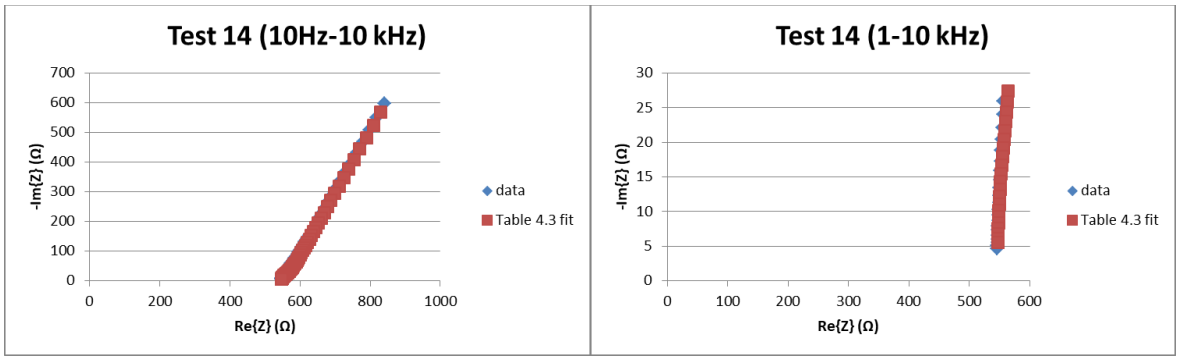

Figure 4.22: Nyquist plots comparing the impedance fit given by the optimization variables listed in Table 4.3 with the raw data impedance for Tests **(a)** 4, **(b)** 7, **(c)** 13, and **(d)** 14. Tthe worse fit in Test 13 can be attributed to the reduced sensitivity of the 4192A during data collection for this test.

In summary, application of the weighting function to the MATLAB optimization eliminates the CPE sensitivity issue seen when only considering the high frequency data points, and, as a result, including the weighting function $F(\omega)=1/|Z_{data}(\omega)|$ in the optimization is a significantly better solution for modifying the MATLAB optimization script than only considering the high frequency data. Further, the impedance phase output by the optimization is in good agreement with that of the data. With this optimization method, the water/DCE interface can be effectively characterized using the transfer effects model given in Figure 4.2. The final optimization parameters that effectively characterize the water/DCE ITIES are given in Table 4.3. Note that the low sensitivity data tests were omitted from the determination of these parameters due to the larger error present within these tests. The tolerance for $(C/A)_{w/d}$ is expected to be within 10% and the tolerances for Q^{o}, and α are expected to be within one standard deviation. Tolerance for R_{ct} is believed to be within 30%.

Table 4.3: Characterization Parameters for the Water/DCE ITIES

$C_{dl}/A_{w/d}$ (F/m^2)	Q^o	α	R_{ct}*
0.4186±0.042	8.04E-5±3.50E-6	0.699±0.015	$R_{ct}=(232.8\pm69.84)(1/A_{w/d})$

*For R_{ct} in Ω and $A_{w/d}$ in mm^2

While it was suggested that Q^o doesn't depend on the water/DCE interfacial area, this may not truly be the case. Note that as an insulator, the permittivity of the glass will be noticeably smaller than that of the water and DCE solutions. This creates a sharp corner effect where the water/DCE ITIES contacts the glass wall. It is well known in electrostatics that the electric field concentration is increased in sharp corners, resulting in a higher concentration of ions within this corner region. Further away from the corner (i.e. towards the center of the tube), the electric field regains its uniform behavior.

With this description, the pseudo-capacitance of the entire water/DCE ITIES can be broken up into many smaller components, as shown in Figure 4.23. Note that all of these pseudo-capacitances are in parallel with one another. As a result of the increased concentration of ions near the edges of the interface, it is possible that the anomalous effects causing CPE behavior will be enhanced, leading to large Q^o's for each of the segments around the tube perimeter. Additionally, it has been shown that near solid surfaces, the liquid state is significantly more ordered than it is in the bulk, resulting in the occurrence of anomalous diffusion [88].

If the perimeter of the glass tube is divided into n segments, then the total pseudo-capacitance around the perimeter of the tube can be expressed as

$$Q^o_{edges} = Q^o_1 + Q^o_2 + \cdots + Q^o_n \quad (4.8).$$

Because the electric field concentration is uniform near the center of the tube, it is assumed that the anomalous effects that cause CPE behavior are not as pronounced. As a result, $Q^o_{center} << Q^o_{edges}$. Because of this, the total pseudo-capacitance of the interface will be

$$Q^o_{ITIES} = Q^o_{center} + Q^o_{edges} \approx Q^o_{edges} \quad (4.9).$$

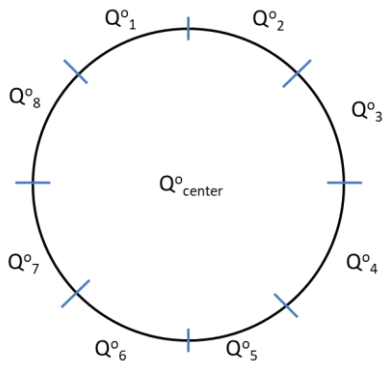

Figure 4.23: Q^o of the water/DCE ITIES broken up into many smaller components, each of which are in parallel to the others. Q^o's around the edges of the glass tube are expected to be larger than Q^o_{center} due to the higher concentration of electric field lines present due to corner effects where the ITIES contacts the tube.

Note that increasing the inner diameter of the tube would increase the magnitude of Q^o_{edges}. Q^o_{edges} is then expected to be proportional to the perimeter of the tube used to form the water/DCE ITIES and since $Q^o_{ITIES} \approx Q^o_{edges}$, the value of Q^o obtained by the MATLAB optimization would then be expected to then be proportional to the perimeter of the tube. Since the tube diameter remained unchanged for all of the 'Big Electrode' apparatus tests, it would then make sense why Q^o obtained from the optimization remained constant in area. Under this hypothesis, the effects of anomalous diffusion that cause CPE behavior are not so important near the center of the ITIES but are very important at the edges of the ITIES. More testing would need to be performed to confirm or disprove this hypothesis, and is something that will be considered in future work.

Should this hypothesis hold, it would have a significant impact on the scaling behavior of the device. While Q^o_{center} scales with the area of the ITIES, Q^o_{edges} scales with perimeter. As a result, Q^o_{edges} would decrease more slowly than Q^o_{center} when the dimensions of the device are reduced, thereby becoming increasingly more dominant at smaller scales. This is altogether unsurprising, as an analogous situation occurs in the derivation of the capacitance of a parallel plate capacitor when considering edge effects. This derivation also shows that as the capacitor is reduced in size, the edge effects become

increasingly more important. Additionally, since C_{dl} depends linearly on $A_{w/d}$, it is expected that Q^o will become increasingly important at the microscale, although shielding of the CPE by R_{ct} may mitigate this effect.

Section 4.2.4: Summary of Results

Two preliminary apparatuses were constructed to probe the water/DCE ITIES. Both of these devices showed that the area of the NPAu/liquid interfaces needed to be made larger in comparison to the water/DCE ITIES, enabling greater sensitivity to the ITIES. A third apparatus was constructed with this in mind. It was assumed for this apparatus that the NPAu/liquid interfaces were large enough such that $Z_{Au/L}$ could be taken as 0 Ω without negatively impacting the characterization of the water/DCE ITIES.

The transfer effects model shown in Figure 4.2 was applied to the impedance data collected for the water/DCE ITIES. This data was run through the MATLAB optimization over a frequency range of 10 Hz-10 kHz. It was found that unlike for the Au/liquid interfaces in Chapter 2, R_{ct} plays an important role in the overall impedance behavior of the ITIES. It could be explicitly seen that C_{dl} and the CPE dominate over different frequency regimes when optimizing over different frequency ranges yielded either more or less sensitive results for the CPE parameters and C_{dl}. It was hypothesized that this was caused by a shift in sensitivity of the 4192A present in collecting the raw data. While the CPE dominated at low frequencies, C_{dl} dominated at high frequencies.

While Q^o was found to have little dependence on the water/DCE interfacial area, C_{dl} showed a clear linear dependence, and, as a result, could potentially be used as an effective measurement parameter in an ITIES-based sensing device. Because C_{dl} dominates within the high frequency regime, the optimization was conducted including only the data points within the high frequency range. This

resulted in greater sensitivity to C_{dl} but at the cost of reduced sensitivity to the CPE parameters Q^o and α.

In order to ensure that the optimization was able to effectively characterize the water/DCE ITIES over the entire considered frequency range, the optimization function was multiplied by three separate weighting functions, taking on the form of Equation 4.7. These weighting functions were chosen to either increase the impact of the high frequency data points or decrease the impact of the low frequency data points so that the entire frequency regime would be equally important during the optimization. It was found that a weighting function of $F(\omega)=1/|Z_{data}(\omega)|$ enabled the optimization to effectively describe both the CPE and C_{dl} components of the transfer effects equivalent circuit model applied to the water/DCE ITIES over the entire considered frequency range of 10 Hz-10 kHz. Further, Nyquist plots of the fit showed good agreement with the data, indicating that this optimization method was capable of effectively capturing not only the impedance magnitude of the system but its phase as well. As a result, this optimization method was used to perform the final characterization of the water/DCE ITIES, obtaining a double layer capacitance per unit area of 0.4186±0.042 F/m^2. Parameters obtained for this final characterization are given in Table 4.3.

The value obtained for $(C/A)_{w/d}$ can be compared to other values obtained in the literature. Geblewicz *et. al.* found that for their water/DCE ITIES formed with 0.05M LiCl (a) and 0.05M Tetrabutylammonium Tetraphenylborate (TBATPB) (o) had C/A values in the range of 0.1-0.2 F/m^2 for applied potentials of 210-440 mV [89]. Hou *et. al.* reported a C/A of roughly 0.15 F/m^2 obtained from impedance spectroscopy for their 10 mM solutions of various alkali-chlorides (a) with 5 mM ammonium tetrakis(pentafluorophenyl) borate (o) [39]. Extrapolation of data collected by Yufei *et. al.* to an applied potential of 50 mV yields a value of C/A in the range of 0.3-0.4 F/m^2 [90]. Their interface consisted of 1M solutions of various alkali-metal chlorides (a) and 1M TBATPF (o). This range is in much better agreement with the C/A=0.4186±0.042 F/m^2 obtained in this work. Further, Yufei's work shows

significant variation in C/A values obtained for the same applied potential for the different aqueous salts considered and their salt concentrations in each phase match those used in this work [90]. As a result, it is plausible that the lower values obtained in [39] and [89] are caused by either the lower salt concentrations used or the different salts used between studies.

Chapter 5: Conclusions and Future Work

Section 5.1: Summary of Work and Conclusions

This work focused on experimental setups and data analysis techniques that permit the characterization of the water/DCE ITIES through the use of electrochemical impedance spectroscopy. In order to isolate the impedance contribution of the water/DCE ITIES, it was necessary to first characterize the Au/water and Au/DCE interfaces present within the ITIES device so that their impedances could be effectively subtracted from the system impedance. Three different equivalent circuit models were applied to the collected data of the different Au/water and Au/DCE tests. The first of these models was a pure CPE which, while able to fit the impedance magnitude quite well, was unable to effectively capture the phase of the impedance data. A second model based on the Randles equivalent circuit, dubbed the 'Transfer Effects' model accounted for effects of charge transfer across the double layer, ion transport within the double layer, and the effects of charge buildup at the outer and inner edges of the double layer. It was found that charge transfer did not play a significant role in the impedance behavior of the double layer so the charge transfer resistance could be removed for these interfaces.

While the Transfer Effects model was able to fit the imaginary component and magnitude of the impedance fairly well, there was a significant amount of error present in the real component, R. This suggested that there was some other resistive effect that was not accounted for in the model. A third model that accounted for the effects of ion adsorption on the electrode surface was then developed. While this model yielded noticeably less error in R at low frequencies, the error in R within the mid frequency range was noticeably greater. Consideration of the Nyquist plots for both the Transfer Effects and Adsorption models showed that the Adsorption model worked best at low frequencies while the Transfer Effects model performed better in the mid to high frequency range. In terms of which model

better fit the impedance data of the Au/water and Au/DCE interfaces, it was concluded that it ultimately depends on the frequency range being considered.

With a method in place for modeling the Au/water and Au/DCE interfaces, it was then considered whether the water/DCE ITIES interfacial impedance could be accurately determined using conventional gold electrodes. It was found that for a simple ITIES device, the water/DCE ITIES made up only 50% of the system's resistance and 14% of the system's reactance. Because the water/DCE interface contributed such a small portion of the system's overall impedance, any errors associated with subtracting out the Au/water and Au/DCE impedances would be compounded. Additionally, upon subtracting out the impedance contributions of the Au/liquid interfaces and solution resistance from data obtained in other impedance spectroscopy tests on the same device negative values of the resistance and positive values of the reactance were found over parts of the frequency range. This indicated that too much resistance and reactance were being subtracted out from the data. As a result, it was concluded that it would be difficult to obtain adequate sensitivity to the ITIES impedance using conventional gold electrodes.

The results from these preliminary water/DCE tests indicated that the area of Au/water and Au/DCE interfaces needed to be made significantly larger in comparison to the water/DCE ITIES. This was accomplished through the manufacturing of nanoporous gold electrodes from white gold leaf sheets. Because the area of the NPAu/liquid interfaces could not be optically determined as in the 'flat' electrode tests, the interfaces were modeled as a pure CPE and a value of C/A for each interface as determined from the pure CPE model of the flat Au/liquid interface tests was used. While the NPAu/liquid interfaces were expected to be dynamically more complex than a simple CPE model, this model was used to estimate any transient change in the impedance present as a result of the fluids penetrating further into the pore structure over time. By studying these results, an estimate of the waiting time necessary for a device to reach a quasi-steady behavior was obtained.

The impact of several different manufacturing parameters on pore structure and impedance behavior was considered. All electrodes in these tests were etched in a 70% Nitric acid, 30% DI water solution to selectively remove the silver from the gold leaf. Studying the effect of initial gold concentration showed that 6 karat gold leaf could not form a fully porous structure that covered the entire substrate. Instead, it formed regions of porous islands separated by regions of exposed substrate. 12 karat gold leaf showed regions of remaining alloyed material present with a lack of an interconnected pore structure throughout. Regions where pores were present showed a pore structure of discrete pinholes instead of a fully interconnected pore structure. 9 karat gold leaf formed a fully porous structure throughout. These results were in good agreement with those reported in [68]. Further, it was seen that the pure CPE model was able to effectively fit the impedance data for the NPAu/water and NPAu/DCE interfaces. While this does not necessarily mean that transfer and adsorption effects do not occur at the NPAu/liquid interfaces, it suggests that they are dominated by the anomalous effects that are responsible for CPE behavior.

The impact of electrode thickness was shown to have no impact on the surface pore structure for electrodes formed of 1 sheet, 3 sheet, and 6 sheet thick 9 karat electrodes. Each sheet was roughly 120 nm thick before etching. While no changes to pore structure were observed, increasing the thickness of the electrode drastically reduced the impedance associated with the NPAu/liquid interfaces. This was due to the pore structure being thicker, allowing for the liquid to penetrate further into the pore structure which enabled a significantly larger NPAu/liquid interfacial area.

Lastly, the impact of etch time on pore structure was studied. Etch times of 5, 10, 15, 30, 45, 60, and 90 minutes were studied. SEM imaging showed that coarsening of the ligaments occurred with increasing etch time. Additionally, for etch times over 45 minutes, the ligaments appeared to move further apart from one another. DiameterJ was used to determine average ligament size and percent porosity on the surface. Ligament diameter was found to increase from 9.3±3.4 nm for a 5 minute etch

time to 11.5±9.9 nm for a 90 minute etch time. While the behavior of porosity was seen to be more complicated, it increased from 19.6% for a 5 minute etch to 47.9% after 90 minutes of etching. Analysis of etch time, electrode thickness, and initial gold concentration showed that 9 karat electrodes etched for 10 minutes in a 70% HNO_3, 30% DI water solution would be ideal for use in probing the water/DCE ITIES. It was also seen that roughly 40-50 minutes were needed for the impedance behavior of the system to be treated as quasi-steady.

With a means of drastically increasing the area of the electrode/liquid interfaces available, attention was then focused on the characterization of the water/DCE ITIES. Because the NPAu/liquid interfacial areas could not be optically determined, impedance data collected from the water only and DCE only NPAu electrode tests for 9 karat 6 sheet thick electrodes etched for 10 minutes was multiplied by an area factor based on the geometric area of the electrodes to account for the different planar electrode areas present in the different tests. While this method for subtracting out the NPAu/liquid impedances was rather inexact, it was expected that the impedance contributions of these interfaces would be significantly smaller than the water/DCE ITIES impedance, thereby mitigating any error introduced as a result of accounting for the NPAu/liquid impedances in this way. Preliminary results from two separate apparatuses showed that these devices were still not sensitive enough to the water/DCE interface. This could explicitly be seen in the Nyquist plots, which showed $R_{w/d}$ bending back on itself in the low frequency regime, indicating that too much resistance had been subtracted out.

The NPAu/water and NPAu/DCE interfacial areas were increased further in relation to the water/DCE ITIES through the 'Big Electrode' apparatus. It was shown that for this apparatus, $Z_{NPAu/L}$ could be approximated as 0 Ω without introducing significant error into the characterization of the water/DCE ITIES. The water/DCE interfacial area was measured using the ImageJ contact angle plugin and the Transfer Effects model was applied. Unlike for the 'flat' Au/liquid interfaces though, R_{ct} was shown to have an impact on overall system behavior and could not be removed. Optimization through MATLAB

over a frequency range of 10 Hz-10 kHz showed clean results for Q^o and α but significant variance in C_{dl}. Further, Q^o appeared to show minimal dependence on $A_{w/d}$. It was explicitly seen that the CPE dominated at low frequencies while C_{dl} dominated impedance behavior at high frequencies.

Because C_{dl} could be seen to noticeable change with $A_{w/d}$, it was considered as the main candidate to use as a potential measurement parameter in an ITIES-based sensing device. To this end, a more accurate determination of C_{dl} was required. Since C_{dl} was shown to dominate at high frequencies, the optimization was run over several high frequency ranges including 1-10 kHz and 10-100 kHz. While this did output more consistent values for C_{dl}, it did so at the cost of reduced sensitivity in Q^o and α.

The system impedance is largest at low frequencies and as a result, the optimization was found to favor low frequency data points over high frequency data points. This problem was addressed through the addition of a frequency-dependent weighting function to the optimization criterion. The weighting function was chosen in a way to decrease the impact of low frequency data and increase the impact of high frequency data to ensure that the entire frequency range would be important in the optimization. A weighting function of $F(\omega)=1/|Zdata(\omega)|$ was found to work best. With this choice, consistent values for C_{dl}, Q^o, and α were obtained when optimizing over a frequency range of 10 Hz-10 kHz. Nyquist plots of data fit using this optimization showed that the Transfer Effects model was capable of matching both impedance magnitude and phase. With this optimization method, $(C/A)_{w/d}$ was found to be 0.4186 F/m^2. Other characterization parameters for the water/DCE interface are given in Table 4.3.

Section 5.2: Future Work

It was stated previously that C_{dl} for the water/DCE ITIES was a prime candidate for potential use in an ITIES-based sensing device. This is due to its clear dependence on the ITIES interfacial area. The next step for this research is to demonstrate that the ITIES interfacial area can be coupled to an applied

mechanical input signal and that changes in this area can be measured via changes in device impedance. This would likely require a change in device design to ensure that contact angle hysteresis would not have a major impact as discussed in Chapter 1. While designs such as the 'Concentric Tube' and 'Big Electrode' apparatuses described in Chapter 4 may work due to the pinning of the contact line, the 'Single Tube' apparatus described in Chapter 2 would certainly suffer from the effects of contact angle hysteresis. Additionally, it was hypothesized that the lack of dependence of Q^o on $A_{w/d}$ in the 'Big Electrode' apparatus was due to the higher concentration of electric field present where the water/DCE interface contacts the glass wall of the tube. In order to confirm or disprove this hypothesis, 'Big Electrode' apparatuses using different sized tubes to form the water/DCE ITIES could be constructed and tested using the same analysis methods described in Section 4.2.

With the above issues solved, an applied pressure would be a logical initial mechanical signal to couple to the water/DCE C_{dl} to. This choice of mechanical signal would allow the apparatus to remain stationary during testing and could easily be accomplished through the implementation of a microfluidic pump or a flexible reservoir wall in the device. In the former case, turning on the pump would result in an applied pressure on the interface. In the latter case, bowing in the wall by slowly pressing a screw into the flexible wall would provide the pressure change. In both cases, the applied pressure could be backed out by the change in curvature of the interface through use of the Young-Laplace Equation. By studying this for multiple applied pressures, a relationship between the interfacial capacitance and applied pressure can be developed.

With a value for C/A determined for the water/DCE interface, it is important to note that frequency sweeps no longer need to be performed. Instead, a single frequency can be chosen to measure the change in impedance and thus the change in capacitance when the input signal is applied. While it is expected that since C_{dl} dominates at higher frequencies that a frequency above 1 kHz would be ideal for operation, further testing would need to be performed to confirm this hypothesis.

Once the change in interfacial capacitance is able to be effectively coupled to an input mechanical signal, the next step would be the reduction in size down to the microscale. This process will introduce several different challenges associated with device design and manufacturing. First, NPAu electrodes cannot be effectively fabricated from etching of white gold leaf in the microscale. Instead, a different method for fabrication of these electrodes must be considered. An obvious choice would be the simultaneous magnetron sputtering of gold and silver followed by etching in an acid solution. This would also require the use of photolithography to ensure that the electrodes only form in the desired locations. Further, it is unknown how drastically reducing the size of the electrode would impact the effect of etch time on pore structure, requiring further tests to be conducted. Increasing the thickness of the NPAu electrode further beyond what was used in Chapter 4 would help ensure that the impedances of the NPAu/liquid interfaces remain small with respect to the water/DCE interfacial impedance.

Another design issue that would need to be solved is how to load the devices in a way that the electrodes only come into contact with the desired fluid phase. Additionally, the contact line of the water/DCE interface would need to be pinned in order to mitigate the impact of contact angle hysteresis. While no suggestions as to what may work best can currently be made, a thorough review of microfluidics fabrication techniques is expected to provide a wealth of inspiration. It is important to note that a design that may be good in sensing changes in pressure may not be good at measuring changes in acceleration or other mechanical signals. As a result, design considerations would likely vary based on the mechanical input that will be applied.

Finally, the microscale design must be developed in a way that allows for visualization of the water/DCE ITIES. This would be required to back out the applied pressure from the Young-Laplace Equation as a means to check whether the sensor is correctly determining the applied pressure. This can be accomplished through the use of cameras with specialized optics. Further, the device must be designed in a way that provides a clear visual path to the ITIES. Addition of a fluorescent dye to the

aqueous phase could potentially be used in conjunction with a laser to illuminate the ITIES, allowing for cleaner images to be obtained; however, introduction of dyes runs the risk of altering the electrochemical behavior of the ITIES. Various dyes would need to be studied in detail to ensure that its introduction would not alter the chemistry occurring at the ITIES.

Appendix A: Use of ImageJ Software in Interfacial Area Analysis

This appendix is meant for those who have little to no exposure to ImageJ and will cover in detail the process of determining areas through brightness threshold analysis. ImageJ is a free, open source Java-based image analysis and processing software [91]. It is useful for a wide range of analyses, particularly particle size distributions. A wide range of additional plugins have been developed, including one for the determination of contact angles which will be discussed in Appendix A2. The base software as well as the contact angle plugin are available on the ImageJ webpage [92,93].

Appendix A1: Determination of the Au/liquid Interfacial Area Using ImageJ Brightness Threshold Analysis

Determining the Au/liquid interfacial area begins with opening the image that is to be analyzed in ImageJ. Note that a scale will need to be set so it is important to have some sort of marker in the image to accurately judge distance. Further, it is important to know the aspect ratio of your image as this will impact the distances calculated by ImageJ after you set the scale. The aspect ratio of the image can be adjusted by clicking “Analyze” -> ”Set Scale”

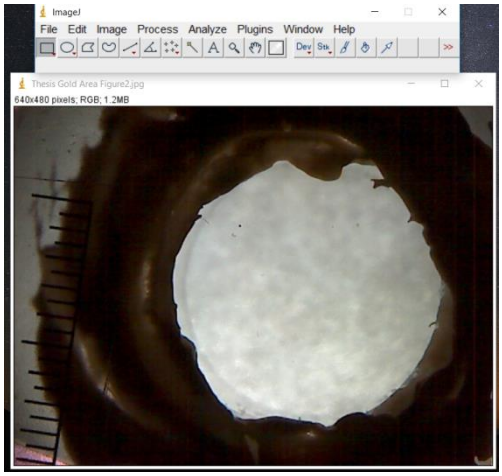

Figure A1: Base image opened in imageJ

To set the scale, zoom in on the marker that is being used to judge distance. Select the straight line icon and click and drag along the known distance as shown in Figure A2.

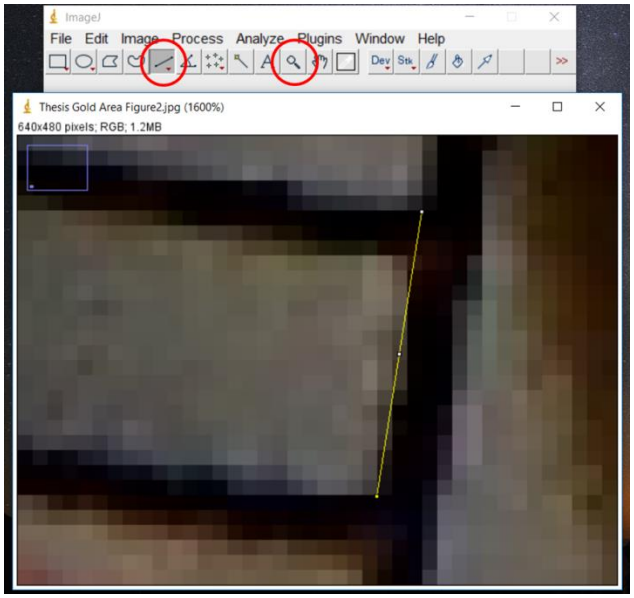

Figure A2: Zoomed in image to obtain an accurate distance to set the scale. Your position on the whole image is depicted in the blue square in the upper left corner.

Click the “Analyze” tab followed by set scale. In the “Set Scale” window, input the known distance you are using and set the appropriate units. The image aspect ratio can also be adjusted here. The scale is

shown at the bottom of the window. Select “OK” to apply the scale to the image. After the scale is set, use the magnifying glass icon to zoom back out to the whole image.

a) 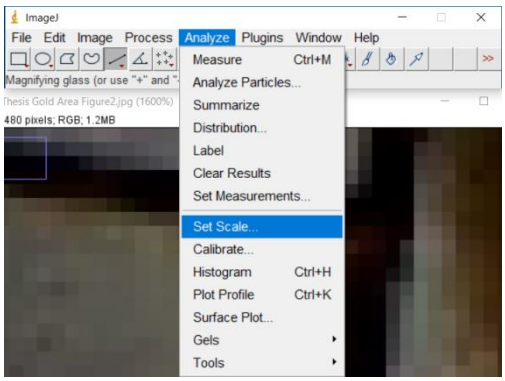

b) 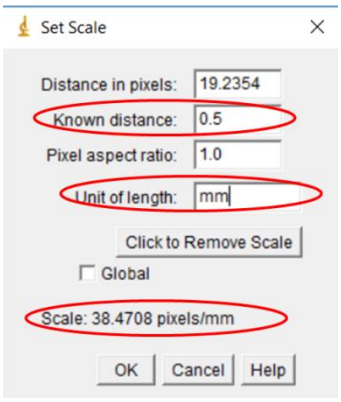

Figure A3: Setting the image length scale

In order to perform brightness threshold analysis, ImageJ requires the image to be in grayscale. This is accomplished by selecting the “Image” tab and selecting the “8-bit” option under “Type”. This process as well as the resulting change in the image is recorded is shown in Figure A4.

a) 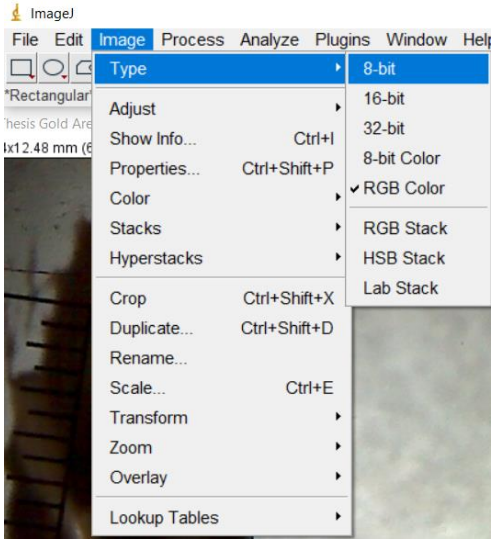

b)

Figure A4: (a) Conversion of the base image to grayscale and **(b)** the resulting effect on the image

With the image in grayscale, threshold analysis can now be conducted. This is done by selecting the “Image” tab followed by “Threshold” under “Adjust”. Alternatively, the keyboard command Ctrl+Shift+T can be used. The threshold analysis works as follows: the software measures the brightness of each pixel in the image and assigns a value based on that brightness. Adjusting the brightness threshold will then change which pixels are considered within the threshold. Pixels that are within the threshold turn bright red, as depicted in Figure A5c.

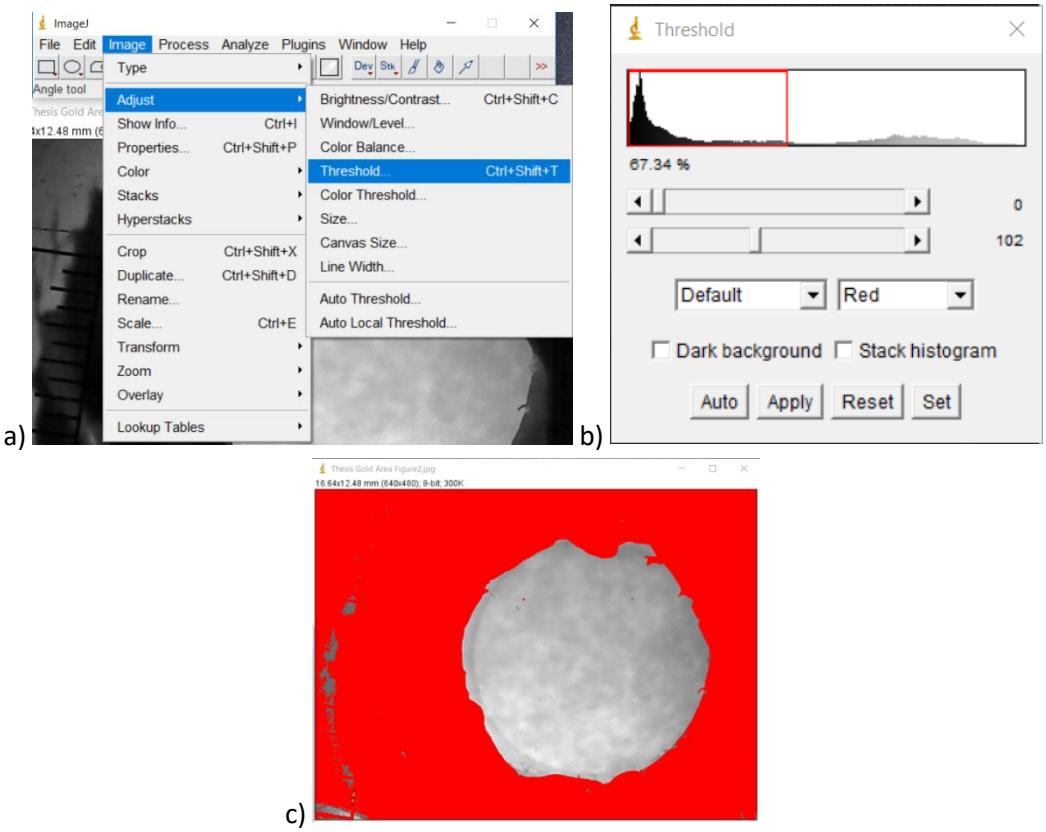

Figure A5: (a) How to open the threshold analysis tool. **(b)** The window in which the threshold can be adjusted. **(c)** Changes made to the image based on the threshold. Pixels that are red are within the assigned threshold.

The threshold is adjusted by using the two sliders shown in Figure A5b. The threshold needs to be adjusted so that the area corresponding to the Au/liquid interface is within the threshold. Once this is done, select “Apply” to apply the selected threshold to the image.

a) 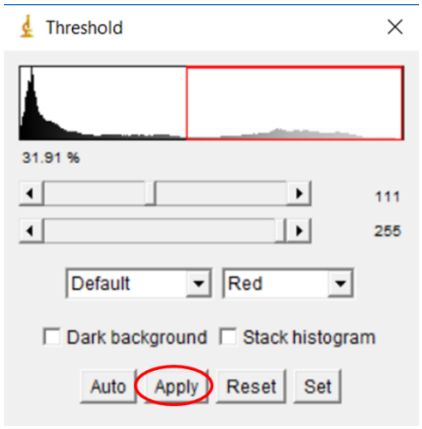

b)

Figure A6: Image after the appropriate threshold has been selected.

After the threshold has been applied, the image is converted to binary, with black regions indicating that the region was within the specified threshold. To determine the resulting area, use the freehand selection tool to draw a circle around the region corresponding to the interfacial area. It is important to try to exclude any smaller black regions that may be near the desired area. This will reduce clutter and ensure accurate measurement later.

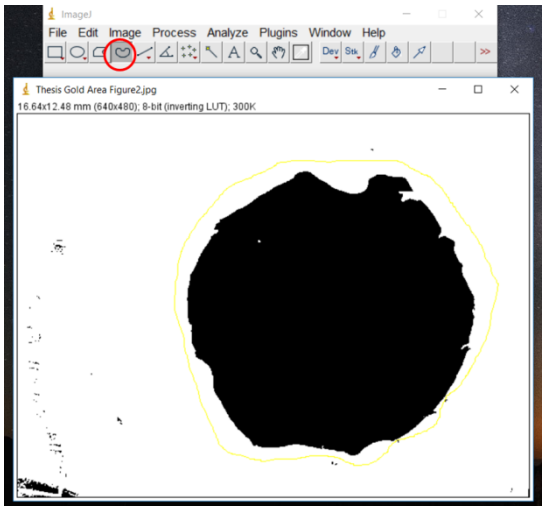

Figure A7: Image after the threshold has been applied. The freehand selection is denoted by the yellow curve around the large black region.

Next the desired measurements need to be set. To do this, select “Set Measurements” under the “Analyze” tab. This causes a window to pop up. For this analysis, only the area is desired so check the “Area” box as shown in Figure A8.

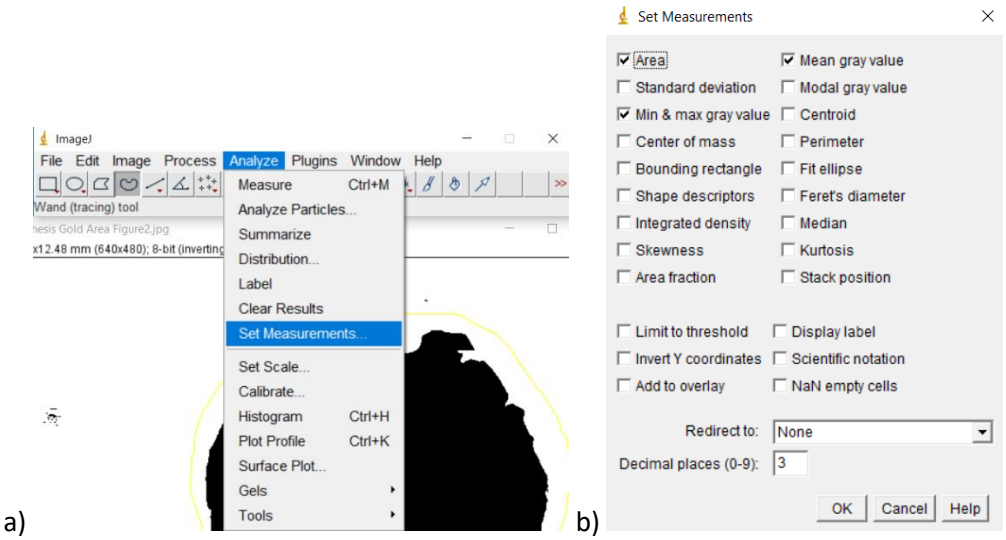

Figure A8: Setting measurements for the software to determine

After the desired measurements are selected, click “Analyze Particles” under the “Analysis” tab to open up another window as shown in Figure A9. In this window, a size threshold can be included to limit “particles” included to a specified size range. The “Show” drop down tab has several options that will change what the program shows you after conducting the measurement. The “Outline” option is the easiest to see if the correct area is being measured. This option shows an outline of each of the particles measured. Note that only “particles” within the region within the yellow curve drawn earlier will be included in the measurement. If no curve is drawn, the entire image is considered. Make sure the “Display Results” option is ticked and select OK to run the measurement.

a) 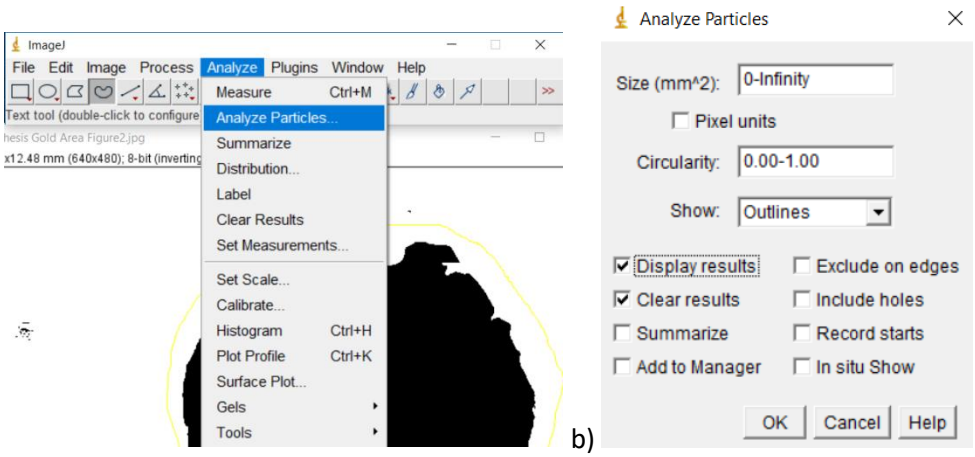

b)

Figure A9: (a) How to navigate to the measurement window and **(b)** the options available for the measurement.

After the measurement is run, two new windows appear as shown in Figure A10. The first shows the results of the measurement. The second shows the outline of the measured particles only if "Outlines" was selected in the "Show" drop down tab in Figure A9b. If more than one "particle" is measured, all their measurements will appear in the results window. Note that the numbers on the outline image correspond to the particle number in the results window.

a) 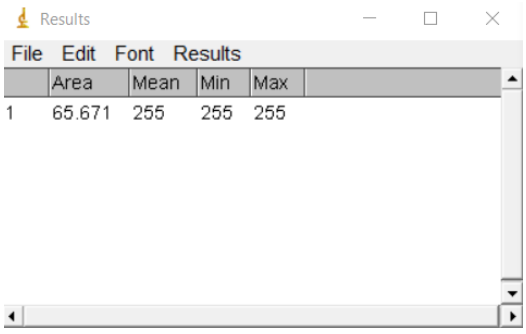

b) 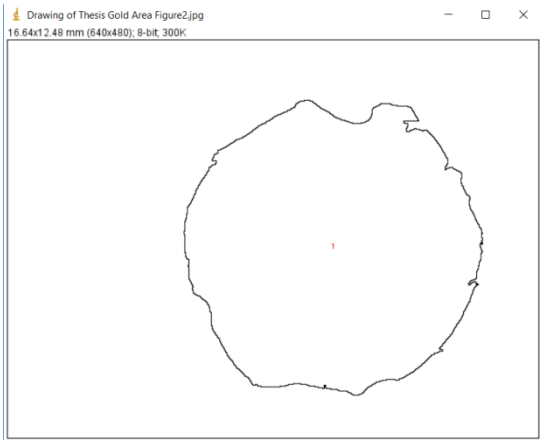

Figure A10: (a) Area results of the "particle" corresponding to the Au/liquid interface. **(b)** Outline of the Au/liquid interface.

Appendix A2: Determination of the Water/DCE Interfacial Area Using the ImageJ Contact Angle Plugin

In order to effectively characterize the water/DCE interface, it is imperative that the area of the interface can be accurately determined. To this end, the contact angle plugin for ImageJ was utilized. Through the use of this software and some simple geometry, the water/DCE interfacial area can be determined. Both ImageJ and the contact angle plugin are available in reference [92,93].

As in Appendix A1, it is important to determine the aspect ratio of the image before setting the scale. Once this ratio is known, the base image is opened in ImageJ as in Figure A11. The interface can be zoomed in on by using the magnifying glass icon in the main toolbar.

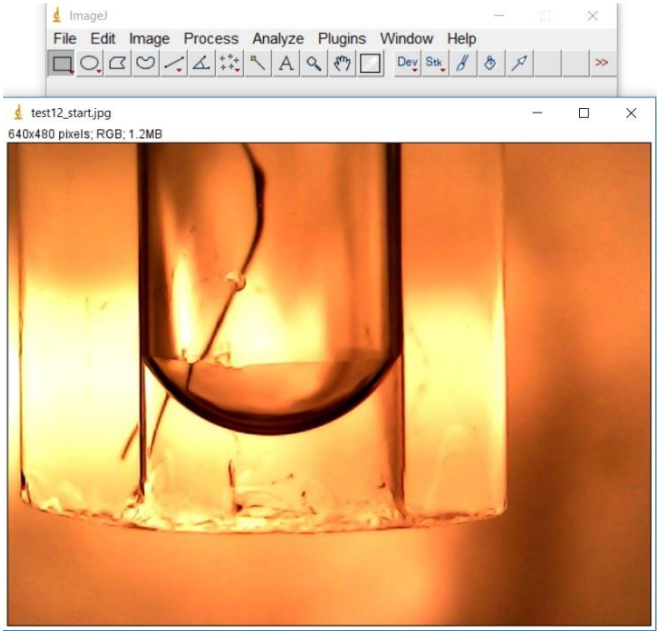

Figure A11: Base image of the water/DCE interface. The water solution is on top and DCE solution is on the bottom.

The contact angle plugin is accessed through the "Plugins" tab as shown in Figure A12a. Upon initiating the plugin, the image is automatically converted to grayscale and the user interface in the top bar changes as shown in Figure A12b.

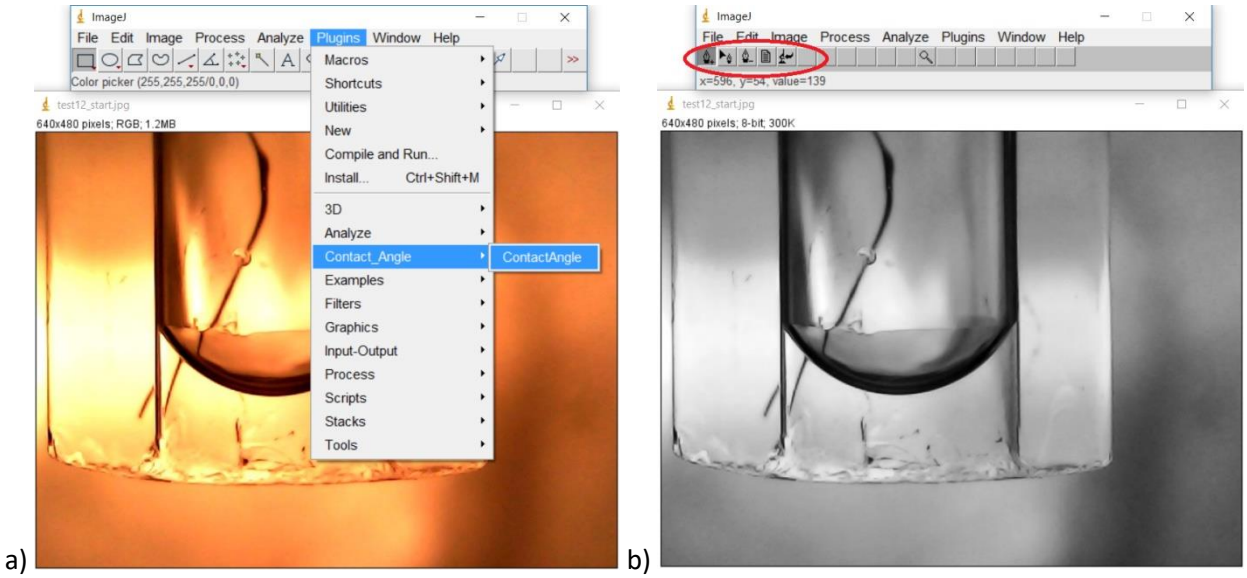

Figure A12: (a) Menu navigation to access the contact angle plugin. **(b)** Changes to the main user interface upon accessing the plugin.

The leftmost icon circled in Figure A12b is the point selection tool. This allows you to select points along the contour of the surface you are interested in. To the right of this is the “Move Crosses” option, which allows for added points to be moved once placed in case of misplacement or the need to fine-tune. The third option is the “Remove Crosses” icon, which allows for the removal of placed crosses by clicking on them. Alternatively, pressing the ‘Delete’ key will remove points in the reverse order they have been added. The fourth option, denoted by the page icon is the “Plugin Preferences” and is depicted in Figure A13. This window is where the contact angle analysis is conducted. The fifth and final option returns the interface back to the base interface for ImageJ that has been used up until this point.

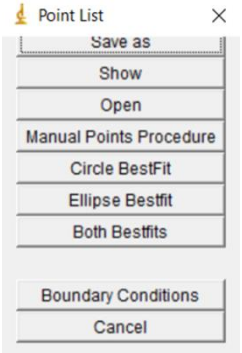

Figure A13: Plugin preferences available within the contact angle plugin. There are a total of four methods the plugin can use to determine contact angle.

As shown in Figure A13, the plugin has several options available for determining the contact angle. The “Manual Points Procedure” requires the user to manually place crosses along the contour of the interface. The first two points should be placed at the points where the interface contacts the glass wall, as depicted in Figure A14a. A minimum of three additional points along the drop surface are required for the plugin to run this method. In order for the plugin to work correctly, it is important that the points are selected moving in a clockwise or counterclockwise direction around the drop. This method automatically runs both the ellipse and circle analyses so it is up to the user to decide which is best for their application. The three “Bestfit” options automatically attempt to map the surface of the interface. As such, a good contrast between the interface and its surroundings is required to make effective use of these options. The rest of this appendix will continue assuming that the user has opted for the “Manual Points Procedure.” An example of what the image should look like after all crosses have been placed is shown in Figure A14b.

a) 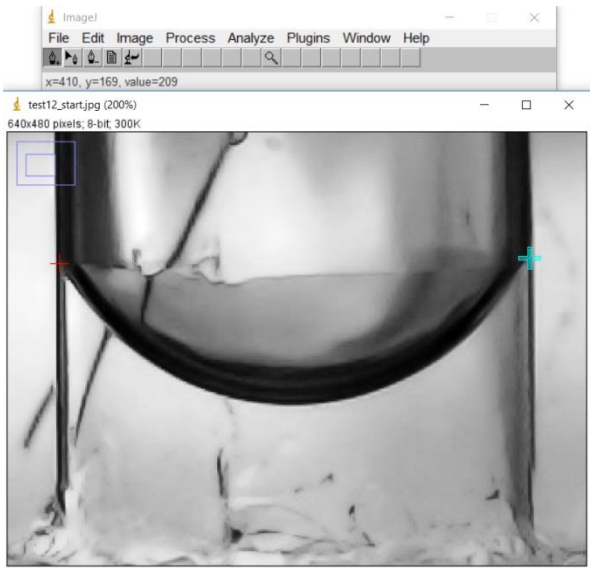

b) 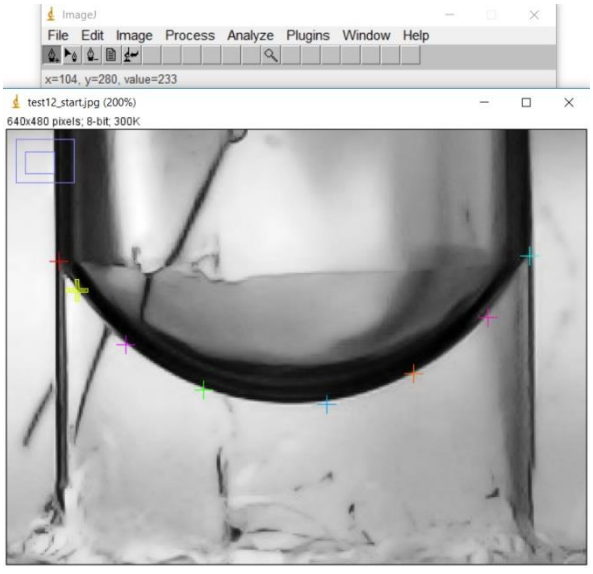

Figure A14: (a) When using the Manual Points Procedure, the initial two points must be at the ends of the baseline of the interface. **(b)** At least three more points in addition to those shown in (a) must be placed along the surface. Points should be added in a clockwise or counterclockwise order to ensure the plugin runs properly.

The image after running the Manual Points Procedure is shown in Figure A15. It has now been overlain with an ellipse and a circle that the plugin calculated to be the best fit of the shape of the interface based on the points selected by the user. Both the major and minor axes of the ellipse are included as well as the line connecting the first two points selected at the base of the interface. The two external lines that slowly come together at the bottom of the image denote the contact lines.

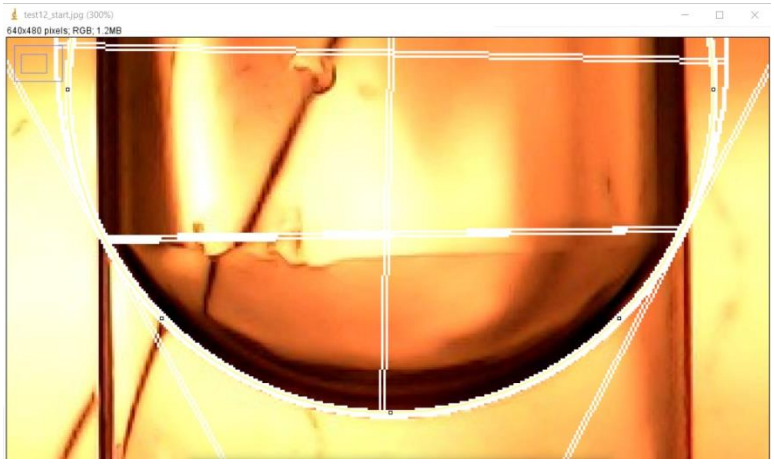

Figure A15: Base image after running the Manual Points Procedure. The lower of the two horizontal lines in the ellipse is the baseline formed between the initial two points selected in the Manual Points Procedure.

By analyzing the geometry of the inscribed circle, the surface area of the interface can be determined by approximating it as a spherical cap, as shown in Figure A16. In this image, r_{cap} is the radius of the base of the spherical cap which is also equal to the radius of the inner diameter of the tube. h is the height of the spherical cap, and r is the radius of the prescribed circle.

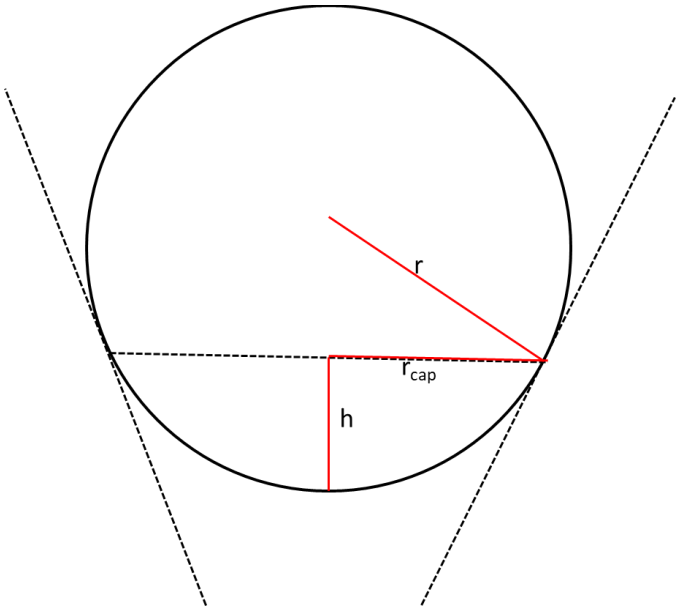

Figure A16: Geometric representation of Figure A15. r is the drop radius, h is the height of the spherical cap, and r_{cap} is the radius of the base of the spherical cap which should be equal to the radius of the tube.

Before proceeding further, a length scale must be established to ensure that ImageJ is measuring proper distances. To do this, the user interface is returned to the base ImageJ interface using the 'microscope' button in the contact angle plugin toolbar. A scale is set using the same method described in Appendix A1; however, this time around, there is no ruler to indicate a length scale in the image. Instead, notice that the edges of the inside of the tube wall appear darker than their surroundings. This is due to total internal reflection of the light passing through the device. These edges can be used as a point of reference to set the image's scale since the inner diameter of the tube is known. Note that the image's aspect ratio should be set at the same time the length scale is set.

With the length scale set, the three values r, r_{cap}, and h (depicted in Figure A16) that need to be determined to calculate the water/DCE interfacial area can be measured. It is often useful to measure r_{cap} first, as this value should be similar to that of the radius of the inner diameter of the tube. If, upon measuring, the two values are not similar, it is likely that the aspect ratio of the image is set incorrectly. Note that the inner diameter of the tube used in this test was measured to be 2.22 mm. Once the

desired length has been selected using the straight line tool, the length measurement can be conducted by either clicking the “Analyze” tab followed by “Measure” or by pressing “Ctrl+M” for Windows. The measurement of r_{cap} is shown in Figure 2.17. The magnifying glass tool should be used to ensure that the length being measured is as close to the desired pixel as possible.

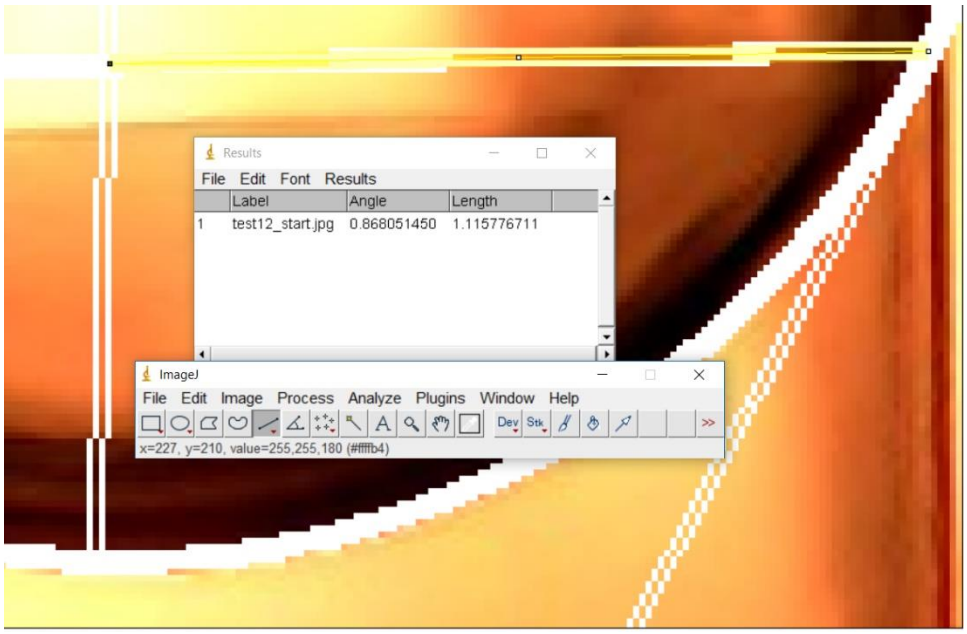

Figure 2.17: Measurement of r_{cap}. Note that this value should be similar to the inner diameter of the tube. If it is not, the aspect ratio of the image was likely set incorrectly.

This process can be repeated to measure h and the diameter of the inscribed circle. The diameter of the circle should be measured in multiple directions to ensure that a similar value is obtained for each. If not, the aspect ratio was likely set incorrectly.

With r, r_{cap}, and h known, the surface area of the water/DCE interface can be calculated in two ways using two different equations for the surface area of a spherical cap:

$$SA_{w/d} = 2\pi r r_{cap} \quad \text{(A1a)}$$

$$SA_{w/d} = \pi(r_{cap}^2 + h^2) \quad \text{(A1b)}$$

For interfaces that bulge out of the tube and form more than a hemisphere as shown in Figure 5._b, an additional step must be performed. In these cases, the surface area of the water/DCE interface is given by

$$SA_{w/d} = SA_{sphere} - SA_{cap} \quad \text{(A2)}$$

where SA_{sphere} is the surface area of the inscribed sphere given by the contact angle plugin and is equal to $4\pi r^2$. SA_{cap} is the surface area of the spherical cap formed by the top of the glass tube and the top of the inscribed sphere given by the contact angle plugin (i.e. the part of the sphere that is inside the tube).

Appendix B: MATLAB Optimization Scripts for Characterization of the Au/Liquid and Water/DCE Interfaces

This appendix shows the MATLAB-based optimization models used to characterize the 'flat' Au/water and Au/DCE interfaces (Appendix B1) and the NPAU/water and NPAu/DCE interfaces (Appendix B2). Because the same equivalent circuit model is used to describe the water/DCE ITIES as in the 'flat' Au/liquid interfaces, a separate Appendix for the water/DCE ITIES is omitted. The reader is instead directed to Chapter 4 for a description of how the water/DCE ITIES model varies from the 'flat' Au/Liquid model. A line-by-line description of each model is given followed by the script.

Appendix B1: 'Flat' Au/Water and Au/DCE Optimization

The optimization script shown below is for the 'flat' water only and DCE only tests described in Chapter 2. Several different equivalent circuit models were used to describe the Au/water and Au/DCE interfaces in Chapter 2, and slight modifications must be made to the script to account for these different models. In particular, the optimization function given in Line 15 will change based on the model used as given below:

Pure CPE model (x(1)=α and x(2)=$Q^{o}_{Au/l}$):

```
fun=@(x)(sum(abs(Zdata-1./(x(2).*((1i.*w).^x(1)))-Rsol)))
```

Transfer Effects Model with R_{ct} excluded (x(1)=C_{dl}, x(2)=Q^{o}, x(3)=α):

```
fun=@(x)(sum(abs(Zdata-1./(x(1)*1i.*w+x(2)*((1i.*w).^x(3)))-Rsol)))
```

Transfer Effects Model with R_{ct} included ($x(1)=C_{dl}$, $x(2)=R_{ct}$, $x(3)=Q^{o}$, $x(4)=\alpha$):
fun=@(x)(sum(abs(Zdata-1./(x(1)*1i.*w+(1./(x(2)+1./(x(3)*((1i.*w).^x(4))))))-Rsol)))

Adsorption Model ($x(1)=C_{dl}$, $x(2)=R_{ad}$, $x(3)=Q^{o}$, $x(4)=\alpha$):
fun=@(x)(sum(abs(Zdata-1./(x(1)*1i.*w+1/x(2)+x(3)*(1i.*w).^x(4))-Rsol)))

The upper bounds, lower bounds, and starting positions in Lines 27-29 must also be changed based on the model being used. These are summarized in Table B1. The outputs in lines 35-39 will likewise be adjusted.

Table B1: Upper Bounds, Lower Bounds, and Starting Points for The MATLAB Optimization of Different Equivalent Circuit Models for the Flat Au/water and Au/DCE Interfaces

Model	Interface	Variables	Upper Bounds	Lower Bounds	Starting Points
Pure CPE	Au/water Au/DCE	x=[α,Q^{o}]	[1,5E-2] [1,1E-2]	[0,0] [0,0]	[0.8,1E-6] [0.6,1E-6]
Transfer Effects (R_{ct} included)	Au/water Au/DCE	x=[C_{dl}, R_{ct}, Q^{o}, α]	[1E-2,1E7,1E-2,1]	[0,0,0,0]	[1E-5,10,1E-6,0.8]
Transfer Effects (R_{ct} excluded)	Au/water Au/DCE	x=[C_{dl}, Q^{o}, α]	[1E-2,1E-2,1]	[0,0,0]	[1E-5,1E-6,0.8]
Adsorption	Au/water Au/DCE	x=[C_{dl}, R_{ad}, Q^{o}, α]	[1E-2,1E7,1E-2,1]	[0,0,0,0]	[1E-5,1E6,1E-6,0.8]

Line Description of the Optimization Script:

Note that the script shown below uses the Transfer Effects model with R_{ct} included.

1-2: Clear workspace and command window
5: Read in name of file containing raw data
8-10: reads in angular frequency (w), Resistance (ReZ), and Reactance (ImZ) from the filename specified in line 4. The letters B, D and E refer to the columns w, ReZ, and ImZ occupy in the excel spreadsheet. 2:62 reads in the data over the frequency range of 10 Hz-10 kHz. These numbers can be changed to consider any specific frequency range data was collected over if desired by noting that there are 20 data points per decade.
11: Defines the complex impedance of the raw data in the form Z_{data}=ReZ+i*ImZ, where "i" is the imaginary number.
12: Reads in the solution resistance from the raw data as being the raw data resistance at 10 kHz.
15: Defines the function used in the minimization. The current function is set up for the model depicted in Figure 2.14c.
16: Shows what variables make up which elements of x
19-23: Defines parameters for fmincon. This minimization has no present inequalities or nonlinear constraints so each option is left empty
24: Sets options for fmincon. The options present in the code are setting the various tolerances and creating a plot that shows the function value against the iteration number. The algorithm used in fmincon can be changed in this line from the default interior-point algorithm if desired.

27-29: Sets starting points, upper bounds, and lower bounds for each of the variables in the function to be minimized. These values might change based on whether a water only or DCE only test is being run
32: Runs the optimization for the specified starting points and bounds.
35-39: Defines the physical function variables from the elements of x obtained by the minimization. Units for C_{dl} are Farads, R_{ct} and R_{sol} are Ohms, and Q_{cpe} is $S*s^{\alpha}$.

```
1   clear all
2   clc
3
4
5   filename='Excel_Spreadsheet.xlsx';
6
7   %read in data from model file
8   w=xlsread(filename,'B2:B62');
9   ReZ=xlsread(filename,'D2:D62');
10  ImZ=xlsread(filename,'E2:E62');
11  Zdata=ReZ+1i.*ImZ;
12  Rsol=xlsread(filename,'D62:D62');
13
14  %Minimization function
15  fun=@(x)(sum(abs(Zdata-1./(x(1)*1i.*w+(1./(x(2)+1./(x(3)*(1i.*w).^x(4)))))-Rsol)));
16  %x(1)=Cdl, x(2)=Rct, x(3)=Qcpe, x(4)=alpha
17
18  %set minimization parameters
19  A=[];
20  b=[];
21  Ceq=[];
22  beq=[];
23  nonlcon=[];
24  options=optimoptions(@fmincon,'Display','iter','OptimalityTolerance',1E-8,'StepTolerance',1E-
        8,'ConstraintTolerance',1E-8,'PlotFcns',@optimplotfval);
25
26  %Variable Bounds
27  lb=[0,0,0,0];
28  ub=[1E-2,1E7,1E-2,1];
29  x0=[1E-5,10,1E-6,0.8];
30
31  %run minimization
32  x=fmincon(fun,x0,A,b,Ceq,beq,lb,ub,nonlcon,options)
33
34  %Output
35  Cwd=x(1);
36  Rct=x(2);
37  Qcpe=x(3);
38  alpha=x(4);
39  x(5)=Rsol;
```

Appendix B2: NPAu/Water and NPAu/DCE Optimization

This Appendix shows the optimization script used to model the NPAu/water and NPAu/DCE interfaces as described in Chapter 3. The equivalent circuit model used was that of a pure CPE in series with a solution resistance. As such, the optimization is a function of three variables: α, A_{eq}, and R_{sol}. See Section 3.2.2 and Equations 3.1 and 3.2 for details on how the optimization function was obtained.

Line Description of the Optimization Script:

Note that the script shown below is set up for an 'NPAu/DCE Only' test.

1-2: Clear workspace and command window
4: Read in name of file containing raw data
7-9: reads in angular frequency (w), Resistance (ReZ), and Reactance (ImZ) from the filename specified in line 4. The letters B, D and E refer to the columns w, ReZ, and ImZ occupy in the excel spreadsheet. 2:82 reads in the data over the entire frequency range of 10 Hz-100 kHz. These numbers can be changed to consider any specific frequency range data was collected over if desired.
10: Defines the complex impedance of the raw data in the form Z_{data}=ReZ+i*ImZ, where I is the imaginary number.
12-13: Defines the capacitance per unit area of the Au/water and Au/DCE interface. The values are assumed to be that of the flat Au/water and Au/DCE interfaces obtained in Section 2.2.1.
15-18: Defines the function used in the minimization (Equation 3.2). A separate function is defined for water and DCE due to the different Q^o/A values for their Au/liquid interfaces. Depending on the type of test being run (i.e. water only or DCE only), the other function is commented out.
19: Shows what variables make up which elements of x
22-26: Defines parameters for fmincon. This minimization has no present inequalities or nonlinear constraints so each option is left empty
27: Sets options for fmincon. The options present in the code are setting the various tolerances and creating a plot that shows the function value against the iteration number. The algorithm used in fmincon can be changed in this line from the default interior-point algorithm if desired.
31-37: Sets starting points, upper bounds, and lower bounds for each of the three variables in the function to be minimized. Different bounds and starting points are assigned for water only tests and DCE only tests. Depending on the type of test being run (i.e. water only or DCE only), the other bounds and starting points are commented out.
39: Runs the optimization for the specified starting points and bounds.
42-44: Defines the physical function variables A_{eq}, α, and R_{sol} from the elements of x obtained by the minimization as described in line 19. A_{eq} is given in m^2 and R_{sol} is given in Ω.

```
clear all
clc

filename='Excel_Spreadsheet.xlsx';

%read in data from model file
w=xlsread(filename, 'B2:B82');
ReZ=xlsread(filename, 'D2:D82');  %Real impedance interface
ImZ=xlsread(filename, 'E2:E82');  %Imaginary impedance interface
 Zdata=ReZ+1i.*ImZ;

 QoverAw=0.0965; %F/m^2; From water only tests on flat electrodes
 QoverAd=0.088; %F/m^2; from DCE only tests on flat electrodes

 %water
 % fun=@(x)(sum(abs(Zdata-1./(QoverAw*x(2).*((1i.*w).^x(1)))-x(3))));
 %DCE
 fun=@(x)(sum(abs(Zdata-1./(QoverAd*x(2).*((1i.*w).^x(1)))-x(3))));
 %x(1)=alpha, x(2)=Aeq, x(3)=Rsol

 %Define parameters for fmincon
 A=[];
 b=[];
 Aeq=[];
 beq=[];
 nonlcon=[]; %No nonlinear constraints (i.e. dependent on x and not x^2, etc)
 options=optimoptions(@fmincon, 'Display','iter','OptimalityTolerance',1E-6, 'StepTolerance',
     1E-6, 'ConstraintTolerance',1E-6, 'PlotFcns',@optimplotfval);

 % Bounds
 %Water
 % lb=[0,0,0]; %defines lower bounds for variables
 % ub=[1,1E-3,200]; %defines upper bound for variables
 % x0=[0.6,1E-7,100]; %defines starting point for minimization
 %DCE
 lb=[0,0,0]; %lower bounds
 ub=[1,1E-3,1000]; %upper bounds
 x0=[0.45,5E-7,1]; %starting points

 x=fmincon(fun,x0,A,b,Aeq,beq,lb,ub,nonlcon,options) %runs minimization

 %Output
 alpha=x(1)
 Aeq=x(2) %m^2
 Rsol=x(3) %Ohms
```

References

[1] J. Bryzek. “Impact of MEMS technology on society”. *Sensors and Actuators A*, 56(1-2):1-9, 1996.

[2] D. Bell, T. Lu, N. Fleck, and S. Spearing. “MEMS Actuators and Sensors: Observations on Their Performance and Selection for Purpose”. *J. Micromech. Microeng.*, 15(7):S153-S164, 2005.

[3] C. Acar, A. Schofield, A. Trusov, L. Costlow, and An. Shkel. “Environmentally Robust MEMS Vibratory Gyroscopes for Automotive Applications”. *IEEE Sensors Journal*, 9(12):1895-1906, 2009.

[4] D. Eddy and D. Sparks. “Application of MEMS Technology in Automotive Sensors and Actuators”. *Proceedings of the IEEE*, 86(8):1747-1755, (1998).

[5] R. Shawgo, A. Richards Grayson, Y. Li, and M. Cima. “BioMEMS for Drug Delivery”. *Current Opinion in Solid State and Materials Science*, 6(4):329-334, 2002.

[6] M. Zurcher, M. Semaan, C. Megerian, W. Ko, and D. Young. “A MEMS Capacitive Accelerometer Design as a Middle Ear Microphone Based on Ossicular Chain Micromechanic Characterization at Umbo for Fully Implantable Cochlear Prosthesis”. *Sensors and Materials*, 22(6):297-312, 2010.

[7] P. Abgrall and A-M Gué. “Lab-on-chip Technologies: Making a Microfluidic Network and Coupling it into a Complete Microsystem—a Review”. *J. Micromech. Microeng,* 17(5):R15-R49, 2007.

[8] P. Dittrich and A. Manz. “Lab-on-a-chip: Microfluidics in Drug Discovery”. *Nature Reviews Drug Discovery*, 5(3):210-218, 2006.

[9] C. Chin, V. Linder, and S. Sia. “Lab-on-a-chip Devices for Global Health: Past Studies and Future Opportunities”. *Lab Chip*, 7:41-57, 2007.

[10] S. Kim, T. Nam, and S. Park. “Measurement of Flow Direction and Velocity Using a Micromachined Flow Sensor”. *Sensors and Actuators A*, 114(2-3):312-318, 2004.

[11] N. Nguyen. “Micromachined Flow Sensors-a Review”. *Flow Meas. Instrum.*, 8(1):7-16, (1997).

[12] Y. Wang, C. Lee, and C. Chiang. “A MEMS-based Air Flow Sensor with a Free-standing Micro-cantilever Structure”. *Sensors*, 7(10):2389-2401, 2007.

[13] M. Kimura, S. Tung, C. Ho, F. Jiang, and Y. Tai. “Mems for Aerodynamic Control”. *Annu. Rev. Fluid Mech.,* 30(1):579-612, 1998.

[14] R. Bogue. “Recent Developments in MEMS Sensors: a Review of Applications, Markets and Technologies”. *Sensor Review*, 33(4):300-304, 2013.

[15] “A Comparative Analysis of 23 MEMS Devices from 13 Different Manufacturers!” announces Yole Développement. (2011). at < http://www.i-micronews.com/news/archives/140-archives-2011/mems-sensors/2735-a-comparative-analysis-of-23-mems-devices-from-13-different-manufacturers-announces-yole-developpement.html>

[16] mCube Redefines MEMS Sensor Innovation by Unveiling the World’s Smallest 1x1mm Accelerometer. (2015). at < https://www.i-micronews.com/mems-sensors/6329-mcube-redefines-mems-sensor-innovation-by-unveiling-the-world-s-smallest-1x1mm-accelerometer.html>

[17] C. Pereira, F. Silva, M. Sousa, K. Kontturi, and L. Murtomäki. “Capacitance and Ionic Association at the Electrified Oil/Water Interface: the Effect of the Oil Phase Composition”. *J. Electroanal. Chem.*, 509:148-154, 2001.

[18] P. Peljo and H. Girault. *Liquid/liquid Interfaces, Electrochemistry at*. Encyclopedia of Analytical Chemistry. 2012.

[19] B. Amini and F. Ayazi. “Micro-gravity Capacitive Silicon-on-insulator Accelerometers”. *J. Micromech. Microeng.*, 15(11):2113-2120, 2005.

[20] H. Helmholtz. “Studies of Electric Boundary Layers”. *Annalen der Physik*, 243(7), 1879.

[21] G. Gouy. “Constitution of the Electric Charge at the Surface of an Electrolyte”. *J. Phys. Theor. Appl.*, 9(1):457-467, 1910.

[22] D. Chapman. “LI. A contribution to the Theory of Electrocapillarity”. *Phil. Mag.*, 25(148):475-481, 1913.

[23] O. Stern. “The Theory of the Electrolytic Double-Layer”. *Z. Elektrochem.,* 30(508):1014-1020, 1924.

[24] J. Berg. *An Introduction to Interfaces and Colloids: The Bridge to Nanoscience*. 480-483 (World Scientific, 2010).

[25] J. Berg. *An Introduction to Interfaces and Colloids: The Bridge to Nanoscience*. 467-471 (World Scientific, 2010).

[26] H. Girault. In *Modern Aspects of Electrochemistry Volume 25*, 1-62 (New York: Plenum, 1993).

[27] J. Berg. *An Introduction to Interfaces and Colloids: The Bridge to Nanoscience*. 57-64 (World Scientific, 2010).

[28] F. Bashforth and J.C. Adams. *An Attempt to Test the Theories of Capillary Action*. (Univ. Press, Cambridge, 1883).

[29] P. Smith and T. Van De Ven. "Profile of Slightly Deformed Axisymmetric Drops". *Journal of Colloid and Interface Science*, 97(1):1-8, 1984.

[30] R. Allen and D. Williams. "Dynamic Effects at the Interface Between Two Immiscible Electrolyte Solutions (ITIES)". *Faraday Discuss.,* 104:281-293, 1996.

[31] L. Cunningham and H. Freiser. "Computer-Controlled Apparatus for Interfacial Electrochemical Studies". *Langmuir*, 1(5):537-541, 1985.

[32] A. Trojànek, A. Lhotský, V. Mareček, and Z. Samec. "Limited Agreement Between the Interfacial Tension and Differential Capacity Data for the Polarised Water|1,2-Dichloroethane Interface". *J. Electroanal. Chem.,* 565(2):243-250, 2004.

[33] Z. Samec, J. Langmaier, and A. Trojànek. "Polarization Phenomena at the Water|o-Nitrophenyl Octyl Ether Interface Part II. Role of the Solvent Viscosity in the Kinetics of the Tetraethylammonium Ion Transfer". *J. Electroanal. Chem.*, 426(1-2):37-45, 1997.

[34] J. Reid, P. Vanýsek, and R. Buck. "Potential Dependence of Capacitance at a Polarizable (Blocked) Liquid/Liquid Interface". *J. Electroanal. Chem.,* 161(1):1-15, 1984.

[35] L. Dang. "A Mechanism for Ion Transport Across the Water/Dichloromethane Interface: A Molecular Dynamics Study Using Polarizable Potential Models". *J. Phys. Chem.*, 105(4):804-809, 2000.

[36] Z. Samec, V. Mareček, and D. Homolka. "The Double Layer at the Interface Between Two Immiscible Electrolyte Solutions Part I. Capacity of the Water/Nitrobenzene Interface". *J. Electroanal. Chem.,* 126(1-3):121-129, 1981.

[37] E. Lenzi, J. de Paula, F. Silva, and L. Evangelista. "A Connection Between Anomalous

Poisson−Nernst−Planck Model and Equivalent Circuits with Constant Phase Elements". *J. Phys. Chem. C,* 117(45):23685-23690, 2013.

[38] C. Yufei, V. Cunnane, and D. Schiffrin. "Interfacial Capacitance and Ionic Association at Electrified Liquid/Liquid Interfaces". *J. Chem. Soc. Faraday Trans.,* 87(1):107-114, 1991.

[39] B. Hou, W. Bu, G. Luo, P. Vanýsek, and M. Schlossman. "Ion Distributions at Electrified Water-Organic Interfaces: PB-PMF Calculations and Impedance Spectroscopy Measurements". *J. Electrochem. Soc.,* 162(12):H890-H897, 2015.

[40] C. Melo Pereira, A. Martins, M. Rocha, C. J. Silva, and F. Silva. "Differential Capacitance of Liquid/Liquid Interfaces: Effect of Electrolytes present in Each Phase". *J. Chem. Soc. Faraday Trans.,* 90(1):143-148, 1994.

[41] P. Hájková, D. Homolka, V. Mareček, and Z. Samec. "The Double Layer at the Interface Between Two Immiscible Electrolyte Solutions: Capacity of the Water/1,2-Dichloroethane Interface". *J. Electroanal. Chem.*, 151(1-2):277-282, 1983.

[42] S. H. Yalkowsky, R. M. Dannenfelser. The AQUASOL dATAbASE of Aqueous Solubility. Fifth ed, Tucson, AZ: Univ Az, College of Pharmacy (1992).

[43] A. Horvath. Halogenated Hydrocarbons: Solubility-Miscibility With Water NY: Marcel Dekker (1982).

[44] National Center for Biotechnology Information. PubChem Compound Database; CID=11, at <https://pubchem.ncbi.nlm.nih.gov/compound/11>.

[45] C. Hsu and F. Mansfield. "Technical Note: Concerning the Conversion of the Constant Phase Element Parameter Y0 into a Capacitance". *Corrosion,* 57(9):747-748, 2001.

[46] A. Le Mehaute and G. Crepy. "Introduction to Transfer and Motion in Fractal Media- The Geometry of Kinetics". *Solid State Ionics,* 9-10(Part1):17-30, 1983.

[47] R. De Levie. "The Influence of Surface Roughness of Solid Electrodes on Electrochemical Measurements". *Electrochim. Acta,* 10(2):113-130, 1965.

[48] J. Bates, Y. Chu, and W. Stribling. "Surface Topography and Impedance of Metal-Electrolyte Interfaces". *Phys. Rev. Lett.,* 60(7):627-630, 1988.

[49] T. Pajkossy. “Impedance of Rough Capacitive Electrodes”. *J. Electroanal. Chem.,* 364(1-2):111-125, 1994.

[50] "Impedance Spectroscopy", J.R. Macdonald, ed., John Wiley, 1987. Sect. 2.2.3.4.

[51] J. Randles. “Kinetics of Rapid Electrode Reactions”. *Discuss. Faraday. Soc.,* 1(0):11-19, 1947.

[52] A. Pilla and G. Margules. “Dynamic Interfacial Electrochemical Phenomena at Living Cell Membranes: Application to the Toad Urinary Bladder Membrane System”. *J. Electrochem. Soc.,* 124(11):1697-1706, 1977.

[53] M. González-Fuentes, J. Manríquez, R. Antañ0-López, and L. Godínez. “Electrochemically Driven Transfer of Carboxyl-Terminated PAMAM Dendrimers at the Water/Dichloroethane Interface”. *Electrochem. Commun.,* 12(1):137-139, 2010.

[54] Z. Samec. “Electrical Double Layer at the Interface between Two Immiscible Electrolyte Solutions”. *Chem. Rev.,* 88:617-632, 1988.

[55] R. Kortschot, A. Philipse, and B. Erné. “Debye Length Dependence of the Anomalous Dynamics of Ionic Double Layers in a Parallel Plate Capacitor”. *J. Phys. Chem. C.,* 118(22):11584-11592, 2014.

[56] MathWorks MATLAB Documentation. “fmincon”. at < https://www.mathworks.com/help/optim/ug/fmincon.html>. (Accessed Jan. 2018).

[57] MathWorks MATLAB Documentation. “Constrained Nonlinear Optimization Algorithms”. at < http://www.mathworks.com/help/optim/ug/constrained-nonlinear-optimization-algorithms.html#brnpd5f>. (Accessed Jan. 2018).

[58] J. Erlebacher, M. Aziz, A. Karma, N. Dimitrov, and K. Sieradzki. “Evolution of Nanoporosity in Dealloying”. *Nature*, 410: 450-453, 2001.

[59] J. Erlebacher. “An Atomistic Description of Dealloying Porosity Evolution, the Critical Potential, and Rate-Limiting Behavior”. *Journal of the Electrochemical Society*, 151(10):C614-C626, 2004.

[60] J. Huang and I.-Wen Sun. “Fabrication and Surface Functionalization of Nanoporous Gold by Electrochemical Alloying/Dealloying of Au±Zn in an Ionic Liquid, and the Self-Assembly of L-Cysteine Monolayers”. *Adv. Funct. Mater.,* 15(6):989-994, 2005.

[61] F. Jia, C. Yu, Z. Ai, and L. Zhang. “Fabrication of Nanoporous Gold Film Electrodes with Ultrahigh Surface Area and Electrochemical Activity”. *Chem. Mater.,* 19(15):3648-3653, 2007.

[62] E. Rouya, M. Reed, R. Kelly, H. Bart-Smith, M. Begley, and G. Zangari. “Synthesis of Nanoporous Gold Structures via Dealloying of Electroplated Au-Ni Alloy Films”. *ECS Trans.,* 6(11):41-50, 2007.

[63] Q. Zhang, X. Wang, Z. Qu, Y. Wang, and Z. Zhang. “A benign route to fabricate nanoporous gold through electrochemical dealloying of Al–Au alloys in a neutral solution”. *Electrochim. Acta,* 26(1):6190-6198, 2009.

[64] C. Xu, X. Xu, J. Su, and Y. Ding. “Research on unsupported nanoporous gold catalyst for CO oxidation”. *J. Catal.,* 252(2):243-248, 2007.

[65] V. Zielasek, B. Jürgens, C. Schulz, J. Biener, A. Hamza, and M. Bäumer. “Gold Catalysts: Nanoporous Gold Foams”. *Angew. Chem. Int. Ed.,* 45(48):8241-8244, 2006.

[66] E. Seker, M. Reed, and M. Begley. “Nanoporous Gold: Fabrication, Characterization, and Applications”. *Materials,* 2(4):2188-2215, 2009.

[67] C. Ji and P. Searson. “Synthesis and Characterization of Nanoporous Gold Nanowires”. *J. Phys. Chem. B,* 107(19):4494-4499, 2003.

[68] X. Lu, T. Balk, R. Spolenak, and E. Arzt. “Dealloying of Au–Ag thin films with a composition gradient: Influence on morphology of nanoporous Au”. *Thin Solid Films*, 515(18):7122-7126, 2007.

[69] O. Okman, D. Lee, and J. Kysar. Fabrication of crack-free nanoporous gold blanket thin films by potentiostatic dealloying. *Scripta Mater.,* 63(10):1005-1008, 2010.

[70] Y. Ding, Y. Kim, and J. Erlebacher. “Nanoporous Gold Leaf: “Ancient Technology”/Advanced Material”. *Adv. Mater.*, 16(21): 1897-1900, 2004.

[71] D. Lee, X. Wei, X. Chen, M. Zhao, S. Jun, J. Hone, E. Herbert, W. Oliver, and J. Kysar. “Microfabrication and mechanical properties of nanoporous gold at the nanoscale”. *Scripta Mater.,* 56(5):437-440, 2007.

[72] H. Rösner, S. Parida, D. Kramer, C. A. Volkert, and J. Weissmüller. “Reconstructing a Nanoporous Metal in Three Dimensions: An Electron Tomography Study of Dealloyed Gold Leaf”. *Adv. Eng. Mater.,* 9(7):535-541, 2007.

[73] A. Mathur and J. Erlebacher. “Size dependence of effective Young’s modulus of nanoporous gold”. *Appl. Phys. Lett.,* 90(6):061910, 2007.

[74] L. Chen, X. Lang, T. Fujita, and M. Chen. “Nanoporous gold for enzyme-free electrochemical glucose sensors”. *Scripta Mater.*, 65(1):17-20, 2011.

[75] O. Shulga, K. Jefferson, A. Khan, V. D’Souza, J. Jiu, A. Demchenko, and K. Stine. “Preparation and Characterization of Porous Gold and its Application as a Platform for Immobilization of Acetylcholine Esterase”. *Chem Mater.*, 19(16):3902-3911, 2007.

[76] L. H. Qian and M. W. Chen. “Ultrafine nanoporous gold by low-temperature dealloying and kinetics of nanopore formation”. *Appl. Phys. Lett.,* 91(8):083105, 2007.

[77] Y. Chen-Wiegart, S. Wang, I. McNulty, and D. Dunand. “Effect of Ag–Au composition and acid concentration on dealloying front velocity and cracking during nanoporous gold formation”. *Acta Materialia*, 61(15):5561-5570, 2013.

[78] S. Parida, D. Kramer, C. A. Volkert, H. Rösner, J. Erlebacher, and J. Weissmüller. “Volume Change during the Formation of Nanoporous Gold by Dealloying”. *Phys. Rev. Lett.,* 97(3):035504, 2006.

[79] J. Biener, A. Hodge, and A. Hamza. “Microscopic failure behavior of nanoporous gold”. *Appl. Phys. Lett.*, 87(12): 1-3, 2005.

[80] E. Seker, M. Reed, and M. Begly. “A thermal treatment approach to reduce microscale void formation in blanket nanoporous gold films”. *Scripta Mater.*, 60(6):435-438, 2009.

[81] Y. Sun, K. Kucera, S. Burger, and T. John Balk. “Microstructure, stability and thermomechanical behavior of crack-free thin films of nanoporous gold”. *Scripta Mater.,* 58(11):1018-1021, 2008.

[82] M. Reed and W. Lye. “Microsystems for drug and gene delivery”. *Proc. IEEE*, 92(1):56-75, 2004.

[83] E. Seker, Y. Berdichevsky, K. Staley, and M. Yarmush. “Microsystems for drug and gene delivery”. *Adv. Healthcare Mater.,* 1(2):172-176, 2012.

[84] M. Hieda, R. Garcia, M. Dixon, T. Daniel, D. Allara, and M. H. W. Chan. “Ultrasensitive quartz crystal microbalance with porous gold electrodes”. *Appl. Phys. Lett.,* 84(4):628-630, 2004.

[85] N.A. Hotaling, K. Bharti, H. Kriel, C.G. Simon Jr.. “DiameterJ: A validated open source nanofiber diameter measurement tool”. *Biomaterials* 61:327-338, 2015.

[86] ImageJ Documentation. “DiameterJ”. at< https://imagej.net/DiameterJ>. (Accessed Feb. 2018).

[87] R. Nock and F. Nielsen. "Statistical Region Merging". *IEEE Trans. Pattern Anal. Mach. Intell.* 26(11):1452-1458, 2004.

[88] S. Pronk, E. Lindahl, and P. Kasson. “Dynamic Heterogeneity Controls Diffusion and Viscosity Near Biological Interfaces”. *Nat. Commun.*, 5(3034):1-7, 2014.

[89] G. Geblewicz, Z. Figaszewski, and Z. Kocorowski. “Study of the Impedance of the Water-1,2-Dichloroethane Interface: Influence of the Picrate Ion Transfer”. *J. Electroanal. Chem.,* 177(1-2):1-12, 1984.

[90] C. Yufei, V. Cunnane, and D. Schiffrin. “Interfacial Capactiance and Ionic Association at Electrified Liquid/Liquid Interfaces”. *J. Chem. Soc. Faraday Trans.,* 87(1):107-114, 1991.

[91] C. A. Schneider, W. S. Rasband, and K. W. Eliceiri. “NIH Image to ImageJ: 25 years of image analysis”. *Nature methods* 9(7): 671-675, 2012.

[92] ImageJ Documentation. “ImageJ Home”. at < https://imagej.nih.gov/ij/>. (Accessed Feb. 2018).

[93] M. Brugnara. ImageJ Documentation. “Contact Angle”. at <https://imagej.nih.gov/ij/plugins/contact-angle.html>. (Accessed Feb. 2018).